Optical and vibrational properties

Joanna M Urban

THÈSE

En vue de l'obtention du

DOCTORAT DE L'UNIVERSITÉ DE TOULOUSE

Délivré par : *l'Université Toulouse 3 Paul Sabatier (UT3 Paul Sabatier)*

Présentée et soutenue le *02/07/2019* par :
Joanna URBAN

Optical and vibrational properties of anisotropic layered materials

—

Propriétés optiques et vibrationelles de matériaux en couches minces anisotropes

JURY

Adnen MLAYAH	Professeur d'Université	Président du jury
Adam BABIŃSKI	Professeur d'Université	Rapporteur
Mark Oliver GOERBIG	Directeur de Recherche	Rapporteur
Michał BARANOWSKI	Docteur	Invité
Paulina PŁOCHOCKA-MAUDE	Directeur de Recherche	Directrice de Thèse

Optical and vibrational properties of anisotropic layered materials

Abstract: Atomically thin layered materials with low symmetry which leads to in-plane anisotropy of electronic and optical properties are particularly interesting from the point of view of applications. In this thesis, the optoelectronic properties of three layered materials with in-plane anisotropy, black phosphorus, rhenium disulfide and franckeite are investigated using optical spectroscopy.

Black phosphorus (BP), with a puckered orthorhombic structure, has significant in-plane anisotropy and a direct bandgap which varies strongly with the number of layers. A significant hindrance from the point of view of the realization of BP-based devices is its degradation in ambient conditions, which can be prevented by encapsulation, for example using hexagonal boron nitride (h-BN). We have investigated the vibrational properties of h-BN encapsulated black phosphorus using Raman spectroscopy and report the first experimental observation of a theoretically predicted new peak slightly above the A_g^1 mode. We explain its appearance by a difference of the mode frequencies in the inner and surface layers and discuss this effect in the context of the strong interlayer coupling in BP and the influence of the encapsulation on the lattice properties.

The second part of this thesis presents the results of photoluminescence studies of few-layer rhenium disulfide. The optical response of ReS_2 is dominated by two energetically nondegenerate anisotropic excitons X_1 around 1.55 eV and X_2 around 1.57 eV which can be observed in polarized absorption and emission. A controversy exists regarding the nature of the fundamental bandgap of ReS_2 , in particular the presence of a crossover from indirect to direct bandgap with changing thickness. We have studied the polarized emission related to the excitonic states at low temperature as a function of the number of layers and compared the experimental results with the predictions of a kinetic model describing the radiative recombination and scattering between excitonic states. We conclude that the features observed in photoluminescence arise due to hot emission from direct excitonic states and that a smaller, indirect bandgap and a related excitonic state are responsible for the depopulation of the direct states, the relatively weak emission intensity and the observed X_1 and X_2 emission ratio.

Franckeite, a complex sulfide mineral, has attracted attention as a natural type-II heterostructure composed of alternating pseudo-hexagonal and pseudo-tetragonal layers. The incommensurate character of the two lattices leads to one-dimensional rippling. The last part of this thesis describes our observation of anomalous polarization dependence of the Raman modes in exfoliated franckeite flakes, which suggested the presence of optical anisotropy and could be used as a rapid and non-invasive method to identify the rippling direction.

Propriétés optiques et vibrationelles de matériaux en couches minces anisotropes

Résumé : Les matériaux bidimensionnels avec une faible symétrie, conduisant à une anisotropie dans le plan des propriétés électroniques et optiques sont particulièrement intéressants du point de vue de l'application. Dans cette thèse, les propriétés optoélectroniques de trois matériaux stratifiés à anisotropie dans le plan, phosphore noir, disulfure de rhénium et franckéite, sont étudiées par spectroscopie optique.

Le phosphore noir (BP), avec une structure orthorhombique plissée, présente une anisotropie significative dans le plan et une bande interdite directe qui varie fortement selon le nombre de couches. Un obstacle important du point de vue de la réalisation de dispositifs basés sur BP est sa dégradation dans les conditions ambiantes, qui peut être évitée par encapsulation, par exemple en utilisant du nitrure de bore hexagonal (h-BN). Nous avons étudié les propriétés vibratoires du phosphore noir encapsulé dans le h-BN à l'aide de la spectroscopie Raman et nous présentons ici la première observation expérimentale d'un nouveau pic théoriquement prévu légèrement au-dessus du mode A_g^1. Nous expliquons son apparition par une différence des fréquences de modes vibratoires dans les couches internes et les couches de surface, et nous discutons de cet effet dans le contexte du fort couplage entre couches dans BP et de l'influence de l'encapsulation sur les propriétés du réseau cristallin.

La deuxième partie de cette thèse présente les résultats d'études de photoluminescence du disulfure de rhénium avec une épaisseur de quelques couches atomiques. La réponse optique de ReS$_2$ est dominée par deux excitons anisotropes énergétiquement non dégénérés X$_1$ autour de 1,55 eV et X$_2$ autour de 1,57 eV qui peuvent être observés en absorption et émission de la lumière polarisée linéairement. Une controverse existe sur le caractère de bande interdite de ReS$_2$, en particulier sur la présence d'un passage de gap direct à gap indirect avec la variation de l'épaisseur. Nous avons étudié l'émission polarisée liée aux états excitoniques à basse température en fonction du nombre de couches et comparé les résultats expérimentaux avec les prédictions d'un modèle cinétique décrivant la recombinaison radiative et la diffusion entre états excitoniques. Nous concluons d'une part que les caractéristiques observées en photoluminescence sont liées à l'émission des états excitoniques associés à une bande interdite directe, et d'autre part que la bande interdite fondamentale est indirecte. Nous proposons un modèle ou un état excitonique associé à une bande interdite indirecte de plus basse énergie assiste au dépeuplement des états excitoniques directs. Sa présence explique l'intensité d'émission relativement faible et le rapport d'émission X$_1$ et X$_2$ observé.

La franckéite, un minéral sulfuré complexe, a attiré l'attention en tant qu'hétérostructure naturelle de type II composée de couches alternées pseudohexagonales et pseudotétragonales. Le caractère incommensurable des deux réseaux mène à une ondulation unidimensionnelle. La dernière partie de cette thèse décrit notre observation de la dépendance de polarisation anormale des modes Raman dans les couches de franckéite exfoliées, ce qui suggère la présence d'une anisotropie optique. L'observation de cette dépendance de polarisation pourrait être utilisée comme une méthode rapide et non invasive pour identifier la direction des ondulations.

Acknowledgements

Contents

Chapter 1

Optical and electronic properties of two-dimensional materials

Contents

This chapter gives an overview of the optical and electronic properties of layered materials with strong in-plane anisotropy. The general properties and applications of low-dimensional layered compounds are presented. Next, the class of anisotropic materials is introduced and the structure and characteristics of the compounds investigated in this work, including black phosphorus, rhenium disulfide and franckeite are discussed in detail.

1.1 Introduction

The interest in two-dimensional materials has been sparked by the discovery of an easy way to produce single- and few-layer graphene by micromechanical exfoliation [Novoselov 2004]. Many other materials share the characteristic features of the layered structure of graphite with strong in-plane bonds and only weak van der Waals interactions between the planes [Novoselov 2005]. Since the demonstration of the fabrication of graphene via micromechanical cleavage various other compounds, such as metal chalcogenides, oxides, boron nitride or black phosphorus have been exfoliated down to mono- and few-layer sheets using this technique [Novoselov 2005, Geim 2013, Tan 2017a, Novoselov 2016]. Atomically thin layered materials are now an intensively studied class of compounds [Duong 2017].

The family of van der Waals layered materials includes monoelemental materials such as graphene, phosphorene, silicene, germanene, stanene, borophene, antimonene or black arsenic

[Pumera 2017, Chen 2018b] and binary compounds such as boron nitride, metal oxides and transition metal mono- (SnS, SnSe, GeS, GeSe) [Gomes 2015], di-(MoS_2, $MoSe_2$, WSe_2 WS_2) and trichalcogenides (TiS_3, ZrS_3, HfS_3, NiS_3) [Silva-Guillén 2017, Island 2017]. Group IV-V compounds such as GeP or SiP [Li 2018a] as well as certain hybrid perovskites [Thygesen 2017, Lédée 2017] can also be found in thin layer form.

Layered compounds include metals, semimetals, insulators and semiconductors and their characteristics can change depending on the number of layers [Duong 2017]. Their applications rely on specific features such as the tunability of the electronic structure, flexibility, optical transparency, in-plane mechanical strength, potentially high sensitivity as sensors due to high surface-to-volume ratio. Efforts to increase the computing efficiency of electronic systems create the need for new channel materials which could be scaled down beyond the limit of silicon technology, with high on/off ratios and large bandgaps. These needs can be met by layered semiconductors which have bandgaps ranging from the mid-infrared for bulk black phosphorus [Island 2016], through visible for transition metal dichalcogenides [Wurstbauer 2017], to UV for hexagonal boron nitride [Cassabois 2016]. The band structure can be tuned by applying strain to a much larger extent than for classical semiconductors [Roldán 2015] as well as via alloying which has been demonstrated for TMDs [Xie 2015]. This makes layered materials promising from the point of view of a wide range of optoelectronic applications, including light emitting devices, photodetectors, solar cells [Huo 2017, Das 2019, Mauro 2018], transistors [Kelly 2017], energy harvesting and storage [Zhu , Choi 2017]. Reduced dimensionality has a strong influence on the properties of layered materials and the properties for bulk may be drastically different from these of one- or few-layer samples [Novoselov 2005]. Due to interlayer coupling and quantum confinement effects the size and nature of the bandgap can be easily tuned by changing the number of layers, providing means to test, explore and control optoelectronic properties with high precision [Velický 2017a, Duong 2017]. Finally, as a consequence of the specific symmetry and band structure, transition metal dichalcogenide monolayers offer the possibility to control the valley degree of freedom [Zeng 2012, Mak 2012]. This can be used to realize valleytronic data storage and logic applications, where the valley index of the carriers is used to represent information [Schaibley 2016]. Assembling different 2D monolayers into complex van der Waals heterostructures allows designing structures with new properties and functionalities overcoming the limitations of lattice matching, a major hindrance in the case of group IV, III-V and II-VI semiconductors [Geim 2013, Liu 2016c].

1.2   Excitons in layered materials

The optical and electronic properties of single- or few-layer thick materials are dominated by excitonic effects, which are particularly robust due to the large exciton binding energies and large oscillator strengths [Velický 2017a].

When an electron in the conduction band and a hole in the valence band are bound via Coulomb interaction, they form a quasiparticle called a neutral exciton [Knox 1963, Fox 2010]. Depending on the binding energy and the spatial extent of the excitonic function within the crystal two types of excitons can be distinguished, the delocalized Wannier-Mott and the tightly bound Frenkel excitons [Fox 2010]. Excitons in semiconductors are usually of the Wannier-Mott type. The wave function of a Wannier exciton extends over many unit cells of the crystal and these excitons can freely move within the crystal. Frenkel excitons have a radius comparable

to the size of the lattice unit cell and are tightly bound and characteristic for insulators or molecular crystals [Fox 2010]. Figure 1.1 (a) shows the schematics of the two types of excitons.
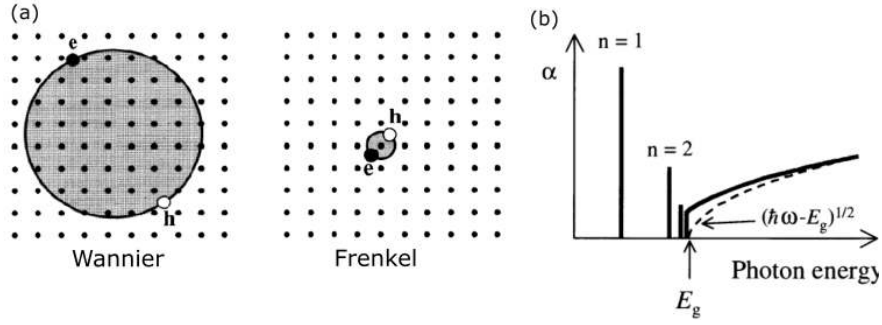
Figure 1.1: (a) Schematics of the Wannier and Frenkel excitons. (b) Absorption spectrum of a direct bandgap bulk semiconductor. The dashed line shows the band edge absorption spectrum in the absence of excitonic effects and the solid line the spectrum with excitonic effects included. After [Fox 2010].

The electron-hole pair can be compared to a hydrogen atom with the oppositely charged particles orbiting their center of mass. The masses of the electron and the hole contribute to the reduced mass of the exciton m_r^*:

$$\frac{1}{m_r^*} = \frac{1}{m_e^*} + \frac{1}{m_h^*} \tag{1.1}$$

The effective masses of the carriers are typically lower than the free electron mass m_0 and as a consequence the reduced mass of the exciton is also lower than m_0. For weakly bound Wannier excitons in bulk materials, the energies of the exciton bound states can be described by a hydrogen-like Bohr model:

$$E_n = -\frac{m_r^* e^4}{8h^2 \varepsilon_0^2 \varepsilon_r^2} \frac{1}{n^2} = R_y \frac{m_r^*}{m_0} \left(\frac{1}{\varepsilon_r}\right)^2 \left(\frac{1}{n}\right)^2 = R^* \left(\frac{1}{\varepsilon_r}\right)^2 \left(\frac{1}{n}\right)^2 \tag{1.2}$$

where $n \geq 1$ is the principal quantum number of the excitonic state [Fox 2010], e is the electron charge, ε_r the dielectric constant of the medium, m_0 is the electron mass and $R_y = -13.6eV$ the Rydberg constant. $R^* = E_{n=1}$ is the effective Rydberg constant. From equation 1.2 it can be seen that the binding energy is dependent on both the effective mass and the dielectric constant. In a crystal, we have $\varepsilon_r > 1$ because of the additional dielectric screening. Given that for typical materials $m_r^* < m_0$ the exciton binding energy is expected to be much smaller than for an electron and proton in a hydrogen atom. Typical exciton binding energies in bulk semiconductors are on the order of several to tens of meV, for example 23 meV for GaN, 4.2 meV for GaAs, 12 meV for CdTe and 2 meV for GaSb [Fox 2010]. The radius of the electron-hole orbit is given by [Fox 2010]:

$$r_n = \frac{m_0}{m_r} \varepsilon_r n^2 a_H \tag{1.3}$$

where a_H is the Bohr radius of the hydrogen atom. Again considering that $m_r^* < m_0$ and $\varepsilon_r > 1$, the radius of the exciton is larger than for a H atom. For example, the exciton Bohr

radius is 2.8 nm in bulk GaN [Rol 2007] and 10 nm in bulk CdTe [Nguyen 2004].

Excitons can be created in direct optical transitions at points of the Brillouin zone where the gradients of the conduction and valence bands are equal which means the group velocity of the electron and the hole are the same [Fox 2010]. For parabolic band dispersion, optically active excitonic states are formed at points corresponding the extrema of the conduction and valence band. The absorption spectrum of excitonic states consists of discrete lines at energies below the bandgap. Figure 1.1 (b) shows a schematic of the absorption spectrum of a direct bandgap bulk semiconductor. The solid line shows the spectrum including excitonic effects. Strong optical absorption lines appear below the fundamental bandgap at energies corresponding to [Fox 2010]:

$$E_n = E_g - \frac{R_X}{n^2} \tag{1.4}$$

In 2D materials, the reduced dimensionality can strongly modify the excitonic properties relative to the bulk. Due to the in-plane spatial confinement, the exciton binding energy is increased. Typical exciton binding energies observed in these materials are on the order of 0.1-1 eV [Duong 2017, Thygesen 2017]. As a consequence, excitonic effects are dominant even at room temperature because the exciton binding energy is larger than $k_B T$ which is around 25 meV at 300 K [Xiao 2017].

The exciton energy levels in an ideal 2D system relative to the exciton binding energy in the bulk E_n^{3D} can be described as [Zaslow 1967]:

$$E_n^{2D} = E_n^{3D} \cdot \frac{n^2}{(n - \frac{1}{2})^2} \tag{1.5}$$

For the ground state $n = 1$ this means a four times larger binding energy for the 2D case.

A further factor strongly influencing the exciton binding energies in atomically thin materials is the modified dielectric screening. As shown schematically in Fig. 1.2 (a), the bulk and 2D material are characterized by different effective dielectric constants ε_{3D} and ε_{2D}. The dielectric environment is different outside of the thin 2D layer, which leads to reduced screening in the typical case when the dielectric constant of the environment is lower than that of the material [Chernikov 2014]. The dielectric environment has a strong influence on the properties of thin materials because of the long-range nature of the Coulomb interaction [Florian 2018, Raja 2017]. Equation 1.5 derived from the hydrogen model cannot be used to describe the exciton energies for an inhomogeneous dielectric environment. Alternative models including a layer-dependent dielectric constant have been used to describe the deviation from the hydrogenic model in layered materials [Chernikov 2014]. The equation derived by Rytova [Rytova 1967] and Keldysh [Keldysh, L. V. 1979] describes the modified Coulomb potential energy for point charges in thin layers [Prada 2015]:

$$V_{2D}(r) = -\frac{e^2}{8\varepsilon_0 \bar{\varepsilon} r_0} \frac{\pi}{2} \left[H_0 \left(\frac{r}{r_0} \right) - Y_0 \left(\frac{r}{r_0} \right) \right] \tag{1.6}$$

where $\bar{\varepsilon} = (\varepsilon_1 + \varepsilon_2)/2$, $r_0 = d\varepsilon/(\varepsilon_1 + \varepsilon_2)$, ε_1 and ε_2 are the dielectric constants of the surrounding media, d is the thickness of the 2D material and ε is its bulk dielectric constant. H_0 and Y_0 are the Neumann and Struve Bessel functions. In this model, the Coulomb interaction increases strongly with decreasing film thickness for $\varepsilon_{2D} > \varepsilon_0$. Figure 1.2 (b) shows a comparison of the Rytova-Keldysh potential, 3D $1/r$ Coulomb potential, the logarithmic approximation of

equation 1.6 valid for $r << r_0$ and the potential suggested as an approximation of the Rytova-Keldysh potential by [Cudazzo 2011] as a function of r/r_0. The difference between the 3D Coulomb and other potentials becomes significant for r smaller than the screening length r_0 .
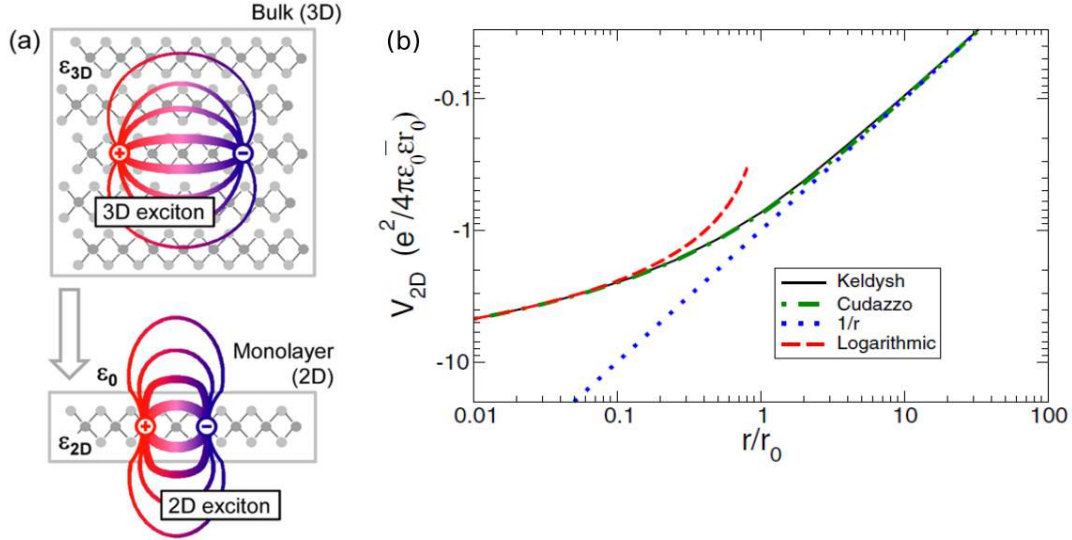
Figure 1.2: (a) Schematics of excitons in 2D and 3D systems. After [Chernikov 2014]. (b) Comparison of different binding potentials that can be used to describe the electron-hole interaction as a function of the ratio of the exciton radius r to the screening length r_0. After [Prada 2015].

Fig. 1.3 (a) shows the exciton energies as a function of the quantum number for monolayer WS_2, together with a fit to the 2D hydrogen model and energies calculated numerically for non-local screening of the Coulomb interaction according to Eq. 1.6 [Chernikov 2014]. The 2D hydrogen model fits the data relatively well for $n = 3$ and above while the behaviour for $n = 1, 2$ is clearly nonhydrogenic. Fig. 1.3 (b) shows a comparison of the 2D hydrogenic interaction potential and the interaction in the non-local screening model as well as the radial wave functions for the lowest exitonic states. While the wave functions for the higher excitonic levels probe mainly the asymptotic region where the potential approaches $1/r$ due to large spatial extent, this is not the case for the lowest states [Chernikov 2014]. For $n = 1$ or 2 the wave function is confined in the region where the interaction is significantly weakened relative to the 2D hydrogen model.

In ultrathin semiconductor layers, not only the exciton binding energy but also the quasiparticle bandgap is modified with respect to the bulk. The bandgap strongly varies as the electronic structure changes with the changing number of layers. In addition, the bandgap can also be modified by a change of the dielectric environment. The experimentally observed optical properties are a result of both the changing exciton binding energy and the bandgap energy. Fig. 1.4 (a) shows a schematics of excitons in a thin layered material partly covered by a dielectric layer and the change of the bandgap in response to the dielectric environment [Raja 2017]. Figure 1.4 (b) shows the optical absorption spectrum for the 2D and 3D case, with
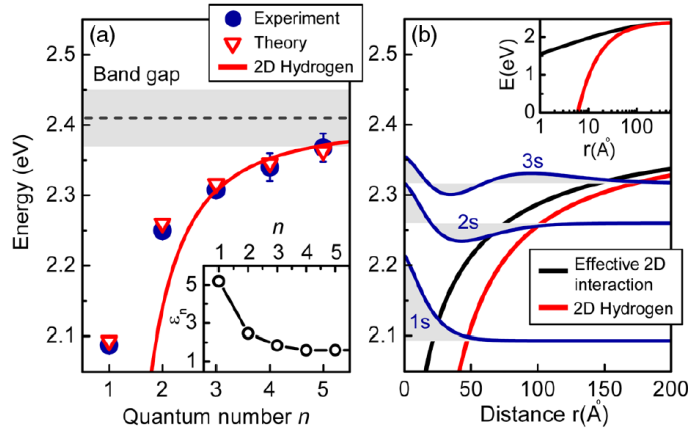
Figure 1.3: (a) Energies of the ground and excited exciton states in ML WS$_2$ determined experimentally and calculated theoretically, together with a fit of the 2D hydrogen model to the three highest states. The inset shows the effective dielectric constant. (b) Comparison of the nonlocal screening interaction potential (black) and the 2D hydrogen model (red) and the radial wave functions for the lowest exitonic states (blue). The inset shows the same dependence in semilogarithmic scale. After [Chernikov 2014].

the excitonic peak and band edge absorption both affected by the reduced dimensionality.
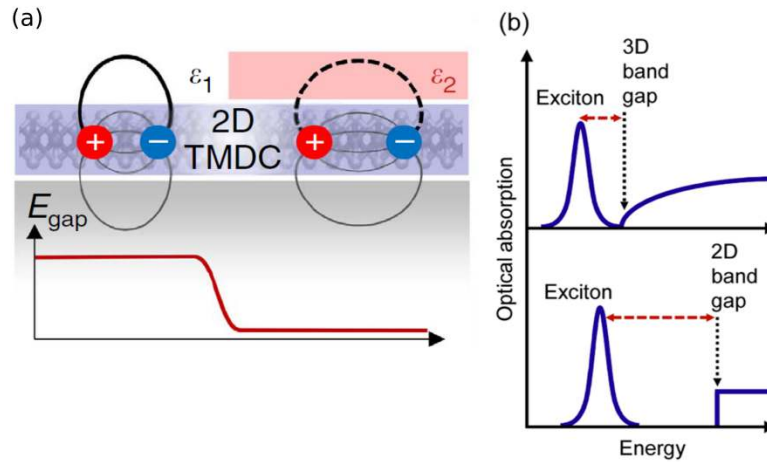
Figure 1.4: (a) Influence of the dielectric environment on the quasiparticle bandgap and the electron-hole interaction. After [Raja 2017]. (b) Optical absorption as a function of energy for bulk and 2D material. After [Chernikov 2014].

The large exciton oscillator strength in 2D materials results in very efficient absorption and

emission of light [Mueller 2018]. Even atomically thin layers can absorb a significant portion of the incoming light. The large binding energies lead to short exciton radiative lifetimes on the order of ps [Palummo 2015]. Due to the high sensitivity of the quasiparticle bandgap and exciton binding energy to the dielectric environment it is possible to tune the properties of layered materials by varying the substrate, forming van der Waals heterostructures or encapsulating the layers [Gupta 2017, Kistanov 2018, Thygesen 2017].

1.3 Anisotropic two-dimensional materials

For liquids and gases, as well as glasses and amorphous materials it can be assumed that their physical properties remain the same along all directions in space [Fox 2010]. This is not the case for crystals with lowered symmetry where non-equivalent axes can be defined. Anisotropy can also be induced in an isotropic crystal by strain or external fields. Due to low crystal symmetry some materials have direction-dependent optical, electronic, thermal and mechanical physical properties [Tian 2016]. Anisotropic phonon dispersion causes the anisotropy of thermal conductivity, while distinct effective masses along different directions can lead to anisotropic electrical conductivity [Qiao 2014, Tiong 1999]. Optical anisotropy can manifest itself via birefringence and dichroism [Yang 2017, Pankove, J. I. 1971].

In-plane anisotropy provides an additional degree of freedom to manipulate the already highly tunable properties of layered materials. Materials with a low-symmetry lattice with non-equivalent in-plane directions include monoelemental black phosphorus [Ling 2015], black arsenic [Chen 2018b], α-antimonene [Wang 2015a], GeSe [Yang 2018], GeS [Tan 2017b], $WTeS_2$ [Zhou 2018], ReS_2 and $ReSe_2$ [Hart 2016] or heterostructures in which the anisotropy results from stacking different materials with incommensurate lattices. They are particularly interesting from the point of view of various applications in electronic, plasmonic or optoelectronic devices [Shen 2018, Nemilentsau 2016, Liu 2017]. These include polarization-sensitive photodetectors [Yuan 2015, Venuthurumilli 2018, Li 2018b, Chen 2017] or anisotropic transistors [Na 2014, Luo 2014, Long 2016, Avsar 2015, Castellanos-Gomez 2014] and anistropic plasmonic devices [Liu 2016d, Hong 2018].

1.3.1 Black phosphorus

Phosphorus can crystallize in several allotropes with different crystal structure and physical properties. These include tetrahedral white phosphorus, amorphous red phosphorus, monoclinic violet phosphorus, orthorhombic black phosphorus and recently demonstrated blue phosphorus [Zhang 2016]. Black phosphorus (BP), and its monolayer form, phosphorene, with a puckered honeycomb lattice, is the most stable allotrope of phosphorus. BP has been first synthetized in 1914 from white phosphorus under high pressure conditions [Bridgman 1914]. Renewed interest in black phosphorus followed its rediscovery in monolayer and few-layer form, which was obtained via exfoliation [Xia 2014, Ling 2015]. Apart from the optoelectronic applications, BP is promising from the point of view of energy storage and thermoelectric devices [Qiu 2017b, Zhang 2017c].

In contrast to graphene and many other layered materials, the phosphorus atoms in BP undergo sp^3 hybridization and form a puckered honeycomb structure. Fig. 1.5 shows the structure of monolayer BP and a schematics of the atomic orbitals. Three valence electrons

form intra-layer bonds and lone electron pairs point into the interlayer region at an angle of around 45° with respect to the plane [Carvalho 2016, Luo 2015a, Hu 2016, Chaves 2017]. The presence of the lone electron pairs results in the formation of the characteristic puckered structure.
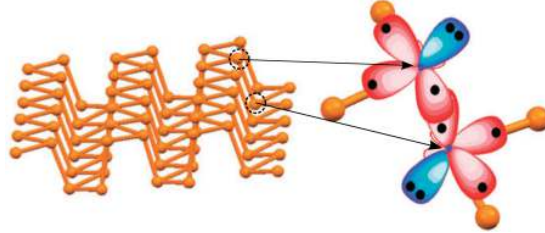
Figure 1.5: Atomic structure of monolayer BP and sketch of the hybridization of the orbitals. Red indicates σ orbitals and blue the lone electron pairs. Adapted from [Boukhvalov 2015].

Bulk black phosphorus belongs to the base-centered orthorhombic crystal system, while the monolayer has a simple orthorhombic structure. The phosphorus atoms lie in two parallel planes and two non-equivalent in-plane armchair and zigzag directions can be distinguished. Both bulk and monolayer BP have four atoms in their unit cell. Several stacking orders are possible [Chaves 2017, Dai 2014], but the lowest-energetic and most widely investigated structure is the AB stacking, presented in Fig. 1.6 (c). Figure 1.6 (a) and (b) shows the crystal structure and first Brillouin zone for monolayer and bulk BP. Γ indicates the center of the Brillouin zone.
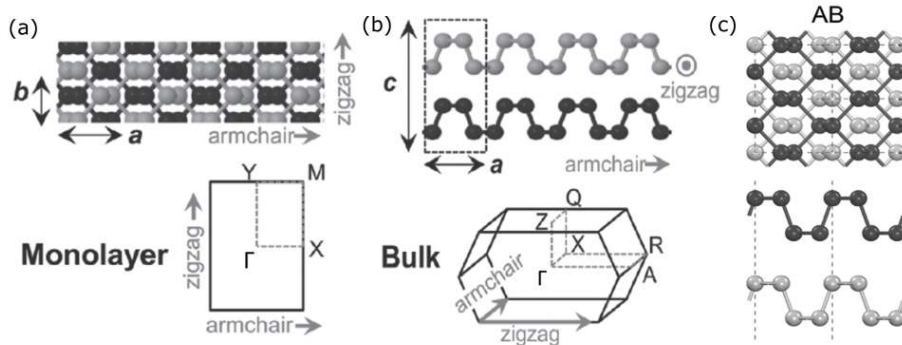
Figure 1.6: Side (left) and top (right) view of the BP crystal structure and the Brillouin zones of (a) monolayer and (b) bulk BP and (c) the most common AB stacking order. After [Chaves 2017].

BP is an ambipolar semiconductor with high mobilities reported both for electrons and holes, higher for the holes in both zigzag and armchair directions [Qiao 2014, Long 2016,

Li 2014, Xia 2014]. For few-layer thick BP a Hall hole mobility along the armchair direction of 1000 cm^{2}V^{-1}s^{-1} was measured at 120 K [Xia 2014]. In another work, mobilities of up to 1000 cm^{2}V^{-1}s^{-1} at room temperature were reported for FETs based on few-layer BP [Li 2014]. Typically, hole mobilities of several hundred to above a thousand cm^{2}V^{-1}s^{-1} have been reported in various studies of BP FETs, which is higher than for TMDs [Du 2015, Li 2014, Na 2014].

The bandgap of black phosphorus is direct for all thicknesses, in contrast to TMDs, where a crossover from indirect to direct bandgap with thickness is observed [Mak 2010, Zhang 2013, Sun 2016, Lezama 2015]. For monolayer BP, calculations predict a bandgap of 2.0 to 2.3 eV [Chaves 2017] which is in agreement with experimental data, for example the value of 1.98 eV obtained from electron energy loss spectroscopy measurements [Tan 2018]. Figure 1.7 (a) shows the band structure for monolayer, bilayer and trilayer BP obtained by *ab initio* calculations [Island 2016]. It can be seen that the fundamental bandgap is direct at the center (Γ point) of the Brillouin zone for all thicknesses and decreases with increasing thickness. Panel (b) shows a comparison of the bandgap energy based on theoretical results and the PL peak energy as a function of the number of layers [Island 2016]. Both theoretical and experimental results suggest a strong decrease of the bandgap from monolayer to bulk. This remarkable tunability of the bandgap with thickness is a consequence of the unusually strong interlayer interaction [Hu 2016, Shulenburger 2015].
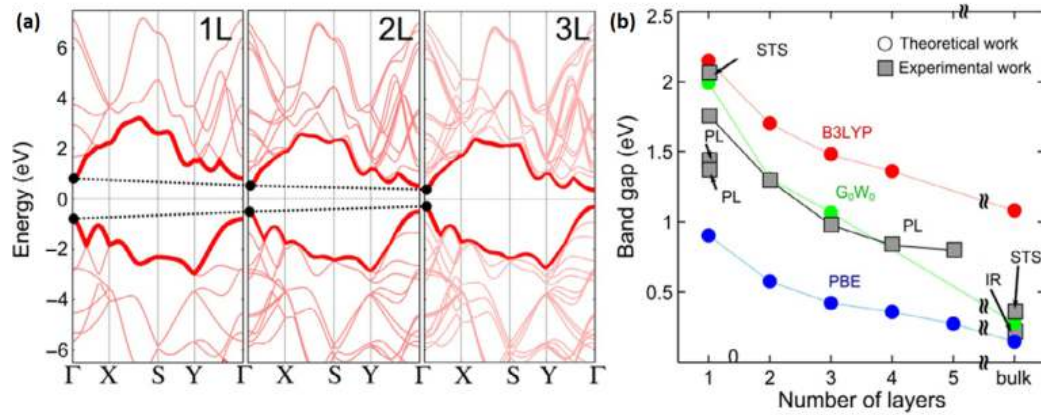
Figure 1.7: (a) Calculated band structure for different thicknesses of BP. (b) Energy of the bandgap obtained using different theoretical and experimental approaches. After [Island 2016].

From Fig. 1.7 (a) it can be seen that the band structure is asymmetric in the X and Y directions around the Γ point. The nonequivalency of zigzag and armchair directions is reflected by the physical properties. The different band dispersion in the k_x and k_y directions results in anisotropic effective masses for both electrons and holes. As a consequence, the electrical conductance and carrier mobilities are higher along the armchair direction [Liu 2017]. This causes the carrier transport to be more efficient along the k_y direction. Figure 1.8 (a) shows the preferred directions of heat and electron transport in the BP plane. The thermal conductivity in BP is around two times larger along the zigzag than along the armchair direction [Luo 2015b]. The electronic contribution to the thermal conductivity is very small and the phonon scattering

rates along the different crystal directions are nearly isotropic, so the observed thermal transport anisotropy can be attributed mainly to anisotropic phonon dispersion [Luo 2015b], shown in Fig. 1.9. For the acoustic phonons in the 5-15 meV range, which are mainly responsible for the thermal conductivity the bandwidths and group velocities are significantly different along the zigzag and armchair directions. Thermal conductivity depends on the number of conducting phonon modes per cross-sectional area of the material, which is significantly larger along the zigzag direction due to the larger phonon group velocity along this direction [Chaves 2017, Luo 2015b].
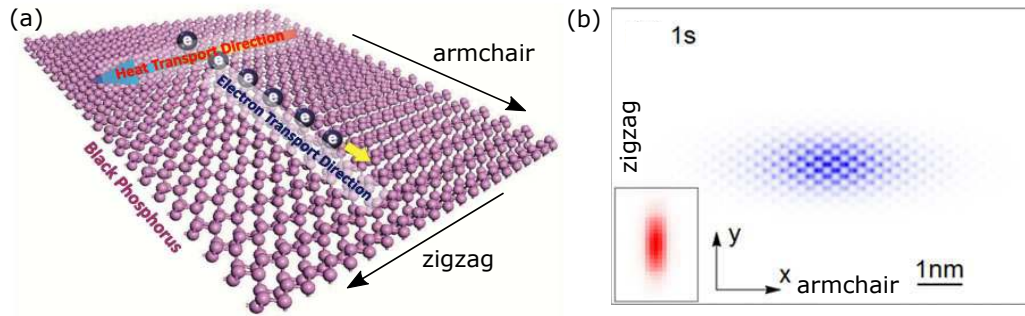
Figure 1.8: (a) Thermal and electronic transport anisotropy of BP along different crystal directions. After [Ling 2015]. (b) Top-view of the real-space wave function (blue) and reciprocal space distribution (inset, red) of the 1s exciton in monolayer BP. After [Tran 2015]

The dielectric function of BP is also strongly anisotropic [Tran 2015, Liu 2017] which results in strongly direction dependent optical absorption [Liu 2017]. The wave function of the $1s$ exciton state in monolayer phosphorene is shown in Fig. 1.8. The wave function is extended along the armchair, low effective mass, direction. The optical oscillator strength of the exciton is strongly direction-dependent [Tran 2015, Wang 2015b] and anisotropy of the emission attributed to the excitonic state was observed. Figure 1.10 shows the intensity of PL emission assigned to the lowest-energy exciton as a function of the detection linear polarization direction for different polarization directions of the linearly polarized excitation beam. Maximum intensity can be observed along the armchair direction independent of the polarization direction of the excitation light.

The specific hybridization of P atoms in black phosphorus leads to interlayer interaction much stronger than for most other layered materials. Due to significant wave function overlap in the interlayer region quasi-covalent electronic hybridization of lone-electron pairs occurs between the adjacent layers [Hu 2016, Qiao 2014, Chaves 2017]. Figure 1.11 (a) shows the differences of charge density in the interlayer and intralayer region for multi-layer black phosphorus, MoS_2 and graphene [Dong 2016]. It can be seen that the interlayer charge density is significantly larger for BP than for the other materials due to the hybridization of the P orbitals. This unusual electronic hybridization leads to an interlayer coupling much stronger than in the case of graphene and the majority of other two dimensional materials, where the stacking is governed only by weak van der Waals interactions [Hu 2016]. Figure 1.11 (b) shows the binding energy per BP atom as a function of the interlayer distance. The binding energy in BP has been reported as 80-120 meV per atom depending on the calculation method
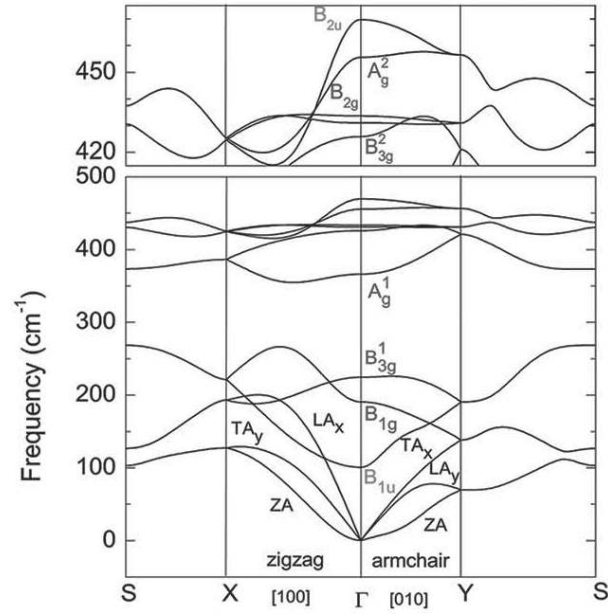
Figure 1.9: Phonon dispersion of phosphorene. After [Cai 2015a].
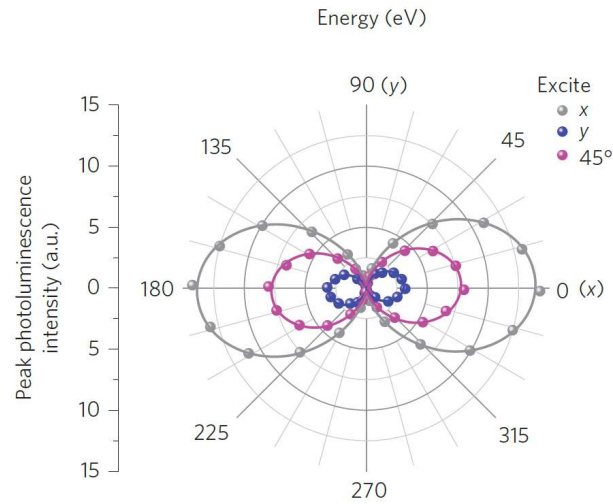
Figure 1.10: Intensity of the peak assigned to exciton photoluminescence of monolayer BP as a function of polarization detection angle for different polarization directions of the excitation light. After [Wang 2015b].

[Duong 2017, Shulenburger 2015], several times higher than in other 2D layered compounds. For example in graphite, the van der Waals interaction is in the range of 30-60 meV per atom

[Shulenburger 2015]. The strong interlayer interaction and covalent-like character of the bonds are responsible for the change of the lattice constant with the number of layers [Qiao 2014] and the emergence of layer-dependent lattice and vibrational properties [Hu 2016]. The exceptionally strong interlayer coupling is also a reason for the strong tunability of the bandgap energy of black phosphorus, one of the largest reported among two dimensional materials [Chaves 2017].
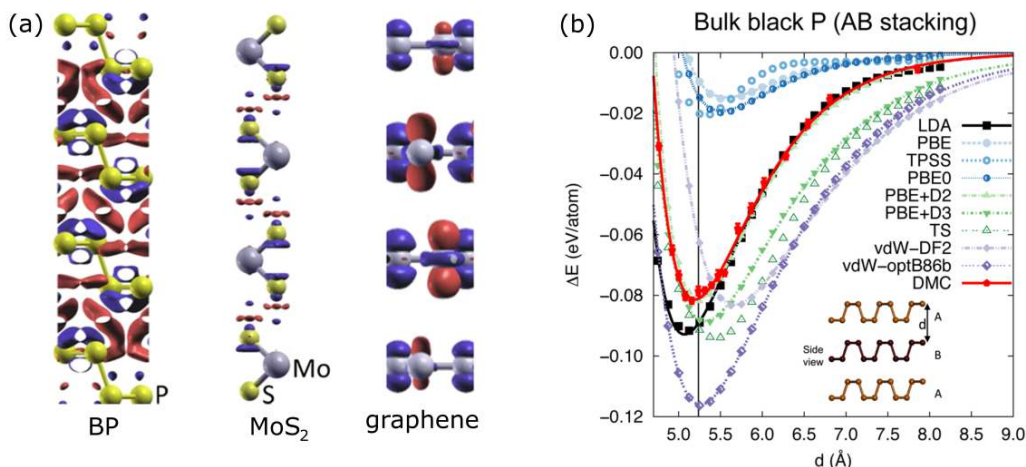
Figure 1.11: (a) Charge difference density calculated for BP, MoS_2 and graphene. Blue color denotes regions where electron density is depleted, purple - regions of increased electron density. Atoms are shown in yellow and gray. After [Dong 2016] (b) The binding energy per atom for bulk BP as a function of interlayer spacing. After [Shulenburger 2015].

A further consequence of the specific hybridization is the strong reactivity and environmental instability of BP, which is a significant hindrance from the point of view of producing functional devices. BP degrades quickly in the presence of water and oxygen [Castellanos-Gomez 2014, Wood 2014, Koenig 2014]. Due to the polar nature of the surface pristine BP layers are very hydrophilic and the surface is reactive in contact with oxygen and moisture [Castellanos-Gomez 2014, Luo 2015a, Kuriakose 2018, Huang 2016b, Island 2015]. Degradation of the material occurs via the formation of a surface oxide, often starting at intrinsic defect sites [Utt 2015]. This can react to form phosphoric acid [Edmonds 2015, Wood 2014], which dissociates and exposes further layers to degradation [Ziletti 2015]. BP degradation under ambient conditions has been monitored by AFM imaging [Koenig 2014] and optical spectroscopy [Alsaffar 2017]. Degradation is enhanced by light exposure [Favron 2015, Han 2017], since reactive oxygen species can form under illumination [Kuriakose 2018], especially in the ultraviolet range. This suggests that photo-oxidation is the main mechanism causing degradation [Ahmed 2017]. Various methods can be used to prevent the degradation of sensitive compounds under ambient conditions. A common approach is encapsulation in other chemically inert materials. The encapsulating material has to be highly impermeable to gases and liquids in order

to protect the encapsulated layers. Encapsulated BP heterostructures have been fabricated using graphene [Kim 2016], MoS$_2$ [Son 2017] and most commonly used hexagonal boron nitride (h-BN). h-BN is a mechanically strong, electrically insulating material with a large bandgap of around 6 eV [Zhang 2017a, Falin 2017], which assures that unwanted absorption will not hinder the functionality of the structure in the visible range, resistant to oxidation and corrosion in ambient atmosphere [Zhang 2017a]. A h-BN substrate or capping layer can provide an atomically smooth surface with no dangling bonds and surface charge traps [Doganov 2015]. h-BN encapsulation can improve the transport properties of 2D materials, e.g. carrier mobility, by reducing Coulomb scattering [Zhang 2017a, Doganov 2015]. h-BN has been widely used as a substrate and gate dielectric material [Zhang 2017a] as well as a passivation and protective layer and can be easily integrated with other 2D materials. In particular, h-BN/BP/h-BN heterostructures are stable under ambient conditions and exhibit improved electrical properties compared to non-encapsulated material [Cao 2015, Long 2016, Chen 2015]. Ultrahigh hole mobilities of around 45000 cm^{2}V^{-1}s^{-1} at cryogenic temperatures have been achieved in few-layer BP field effect transistors encapsulated in h-BN [Long 2016]. The superior transport quality has been confirmed by Hall measurements, which yielded a mobility of around 6000 cm^{2}V^{-1}s^{-1} and an independent estimation of mobility from the critical magnetic field for Shubnikov de Haas oscillations of around 5000 cm^{2}V^{-1}s^{-1} [Li 2016]. Shubnikov de Haas oscillations could be observed starting from a critical field of around 2 T, confirming high mobility $\mu \sim 1/B_C$ [Li 2016]. Figure 1.12 shows mangetotransport results for h-BN encapsulated BP [Li 2016]. Hall resistance shown in the left panel shows features of the quantum hall effect at high magnetic fields. At lower fields Shubnikov de Haas oscillations in the magnetoresistance are observed. Different curves present results obtained for different hole doping levels.

Figure 1.12: Hall resistance (left) and magnetoresistance (right) as a function of magnetic field for different hole concentrations. After [Li 2016].

Apart from protecting the layers, the encapsulating material may have a strong influence on the structural and electronic properties of the encapsulated crystal. For black phosphorus this effect may be particularly important because of the large charge density outside of the layer

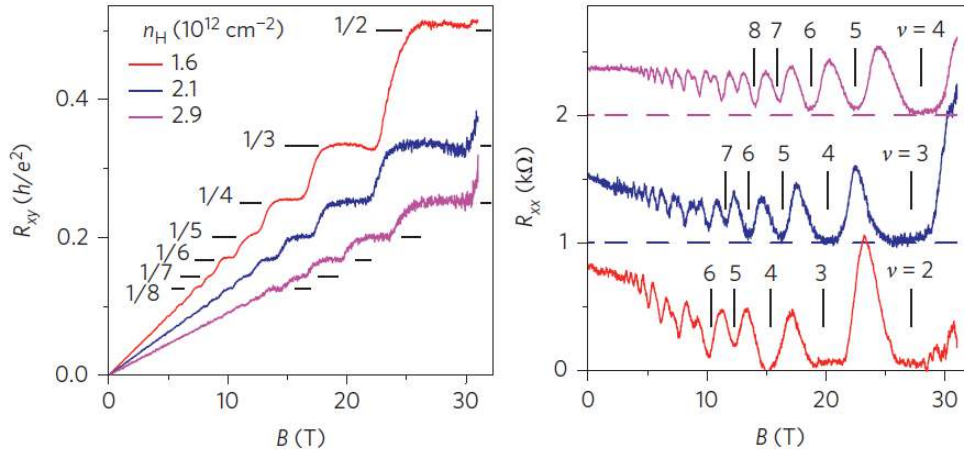plane due to the sp^3 hybridization. Lattice mismatch can lead to the appearance of strain at the interfaceand electronic properties could be modified in the surface layers relative to the bulk. Especially in a material with strong interlayer interactions significant changes of properties can be expected at the interface between the material and the environment which raises questions about interface bonding, charge transfer, changes of the bandgap and band alignment at interfaces in heterostructures [Cai 2015b]. It has been suggested that few-layer black phosphorus is sensitive to environmental screening and its optical properties can be dramatically affected by encapsulation in hexagonal boron nitride, in particular the excitonic effects in the spectra can be suppressed [Qiu 2017a]. It has also been suggested that the bandgap of BP changes upon contact with encapsulating Al_2O_3 due to interlayer charge transfer [Sun 2017] and this effect is strongly dependent on the number of BP layers as well as on the exact surface termination. Calculations predict a change in the distribution of electrostatic potentials within BP layers upon contact with the encapsulating graphene and h-BN [Cai 2015b]. DFT calculations [Birowska 2019] show that biaxial strain can be imposed by h-BN on the BP layer when the two different lattices are in contact. Since encapsulation is an inevitable step for the production of stable BP devices, it is crucial to understand its influence on the BP layers. In particular, in this work we focus on the vibrational properties of h-BN/BP heterostructures. An experimental study of h-BN encapsulated few-layer BP investigating the influence of encapsulation on the vibrational modes of BP is presented in Chapter 3.

1.3.2 Rhenium disulfide

Rhenium dichalcogenides are another example of layered materials with strong in-plane anisotropy. In contrast to group VI TMDs which form the H (hexagonal) or 1T (octahedral) structures, rhenium disulfide (ReS_2) and diselenide ($ReSe_2$) crystalize in the distorted 1T' phase with triclinic symmetry [Jariwala 2016, Tian 2016]. They are environmentally stable in ambient conditions, which makes them interesting from the point of view of applications. Fig. 1.13 shows the crystal structure of rhenium dichalcogenides. Metal atoms in group VII dichalcogenides have a d^3 electronic configuration, in contrast to the d^2 configuration of Mo and W chalcogenides [Fang 1997]. Two out of three metal d electrons form metal-metal bonds. The presence of the additional valence electron of the rhenium atom causes a disruption of the crystal symmetry along the in-plane direction, also called the Peierls distortion [Jariwala 2016, Rahman 2017]. Re atoms form diamond-shaped connected clusters aligned along the b crystal direction [Fang 1997].

The electronic and optical properties of ReS_2 and $ReSe_2$ are similar due to their isoelectronic character [Jariwala 2016]. The bandgap of $ReSe_2$, around 1.3 eV is slightly smaller than for ReS_2. The following paragraphs will focus on ReS_2, which was investigated in this thesis. The stacking order of multi-layer ReS_2 has been investigated theoretically and experimentally [He 2016, Qiao 2016]. In the work of [Qiao 2016], configurations with different relative orientation of the Re-Re bonds in the neighbouring layers were investigated. DFT calculations showed that the most stable configuration is the anisotropic-like (AI) stacking with the Re-Re bonds in adjacent layers rotated by 60° relative to each other. The second most stable configuration is the isotropic-like (IS) stacking for the Re-Re bonds in neighboring layers aligned along the a and b axes respectively. Fig. 1.14 (a) shows the schematic diagrams and top view of the crystal structure of the AI and IS polytypes calculated by [Qiao 2016].

The structural anisotropy of ReS_2 results in anisotropic thermal and electrical transport. Electric conductivity is higher along the rhenium chains [Lin 2015]. The ratio of the mobility
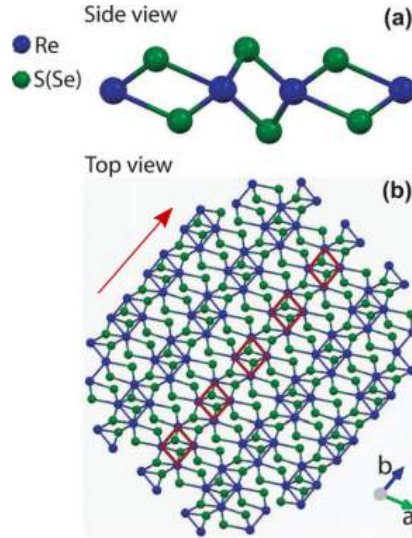
Figure 1.13: Schematics of the ReX$_2$ 1T' crystal structure (a) side view and (b) top view. Rhenium atoms are shown in blue and chalcogen atoms in green. The red arrow marks the direction of the Re atom chains. After [Jariwala 2016].
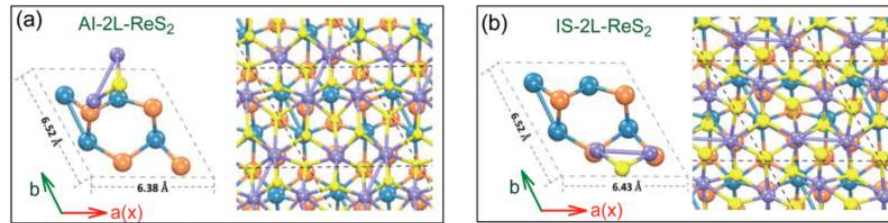
Figure 1.14: Schematic of the (a) AI-stacked and (b) IS-stacked bilayer ReS$_2$. After [Qiao 2016].

along the two different principle crystal axes was found to be 2.36 for electrons and 7.76 for holes, with higher mobility along the *b* direction [Yu 2016]. The thermal conductivity is also higher along the Re-chains direction [Jang 2017].

Rhenium disulfide has been used for the fabrication of electronic devices [Rahman 2017, Xiong], such as thin film transistors [Shim 2016, Liu 2016a] or digital inverters [Liu 2015]. Using encapsulated ReS$_2$ nanosheets in top-gated configuration allowed obtaining a very high on/off current ratio [Zhang 2015]. The anisotropy of the optical properties can be used for example in polarization-sensitive photodetectors [Liu 2016b, Zhang 2015].

Optical properties of ReS$_2$ are dominated by two energetically non-degenerate anisotropic excitons [Jariwala 2016]. Figure 1.15 shows the polarization-dependent absorption for a few-layer ReS$_2$ flake [Sim 2018]. Absorption depends strongly on the direction of the light polarization relative to the crystal. Two strong resonances with maximum intensity for different directions of light polarization are visible at energies around 1.53 eV and 1.57 eV, marked as X$_1$

and X_2. The left panel of Fig. 1.15 shows absorption as a function of the detection polarization angle and spectra for selected angles, the right panel the intensity of the absorption resonances as a function of detection angle. The polarization angle is measured with respect to the b axis. Polarization-resolved transient absorption has shown the anisotropy of the absorption coefficient, which is larger along the direction of the Re chains [Cui 2015]. The thermal [Jang 2017] and electrical conductivity [Ovchinnikov 2016, Wen 2017] are also higher along the b crystal direction. Theoretical calculations predicted the strong anisotropy of the dielectric tensor of ReS_2 [Echeverry 2018].
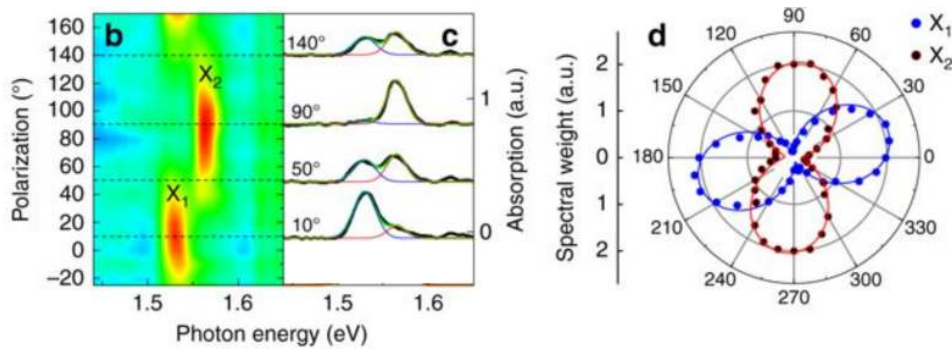
Figure 1.15: Absorption as a function of the direction of light polarization showing the two lowest energy X_1 and X_2 exciton resonances (left) and the spectral weights of the resonances based on fits for X_1 and X_2 (right). After [Sim 2018].

The two lowest-lying direct excitonic transitions visible in absorption can also be identified in photoluminescence. Fig. 1.16 (a) shows PL spectra acquired for two different detection polarization directions for a thick ReS_2 flake. The direct excitonic transitions E_1^{ex} and E_2^{ex} can be observed around 1.46 eV and 1.5 eV, as well as a lower-energetic emission interpreted as the indirect excitonic state around 1.4 eV and a higher-energetic emission around 1.59 eV [Ho 2017]. In Fig. 1.16 (b), the derivative of the reflectance contrast is compared with the unpolarized PL spectrum for bulk ReS_2. The direct transitions X_1 and X_2 can be identified in the reflectance spectrum, as well as a higher-energetic transition slightly below 1.6 eV, which has been interpreted as an excited excitonic state [Aslan 2016, Jadczak 2019]. Fig. 1.17 shows polarized μ-PL spectra of few-layer ReS_2 taken at 4 K for different detection polarizations for which the narrow linewidth allowed to identify five excitonic transitions [Ho 2019]. The PL spectra of the AI and IS polytype differ slightly, indicating differences in the electronic structure [Qiao 2016]. The maxima of the PL emission for the isotropic polytype are located at slightly lower energies, the PL peak is narrower and has higher intensity. A similar linear polarization dependence of the emission intensity has been observed for both ReS_2 polytypes [Qiao 2016].

The X_1 and X_2 transitions observed in photoluminescence show the same polarization dependence as the transitions in absorption. Fig. 1.17 (b) shows polarization-resolved photoluminescence spectra for different polarization directions for three-layer ReS_2. The X_1 and X_2 photoluminescence intensity is maximized for polarization along different directions. This energetic and linear polarization selectivity is unique for ReS_2 and $ReSe_2$. In contrast to for example SnS [Chen 2018a], for which PL emission peaks with orthogonal linear polarizations
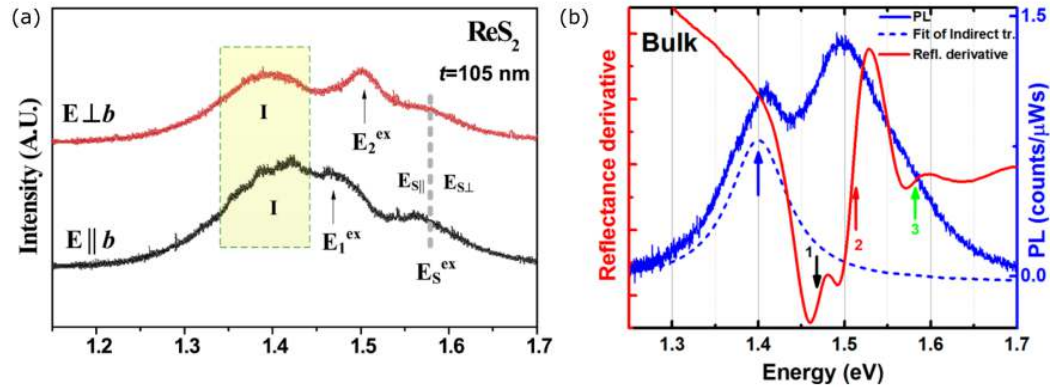
Figure 1.16: (a) μ-PL spectra for two different polarizations for thick ReS_2 with marked indirect transition (I), two lowest direct transitions E_1^{ex} and E_2^{ex} and a higher energetic excitonic transition E_S^{ex}. After [Ho 2017]. (b) Photoluminescence (blue) and a derivative of the reflectance (red) spectrum. Arrows indicate the positions of optical transitions. After [Aslan 2016].

originate from different valleys in the Brillouin zone, the linear dichroism in the Re dichalcogenides is not related to valley selectivity. Surprisingly, despite the different optical selection rules it was possible to observe quantum beats indicating quantum coherence between X_1 and X_2 states [Sim 2018].
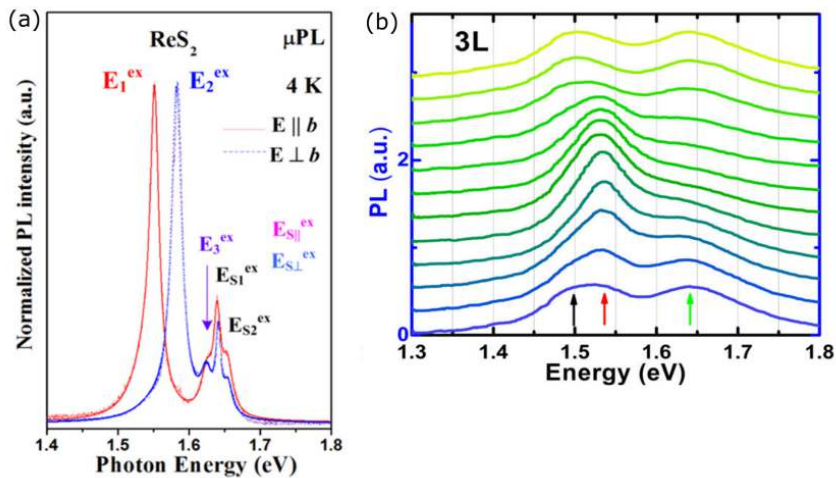
Figure 1.17: (a) Polarized PL spectra of few layer thick ReS_2 for detection polarization parallel (red) and perpendicular (blue) to the rhenium chains. After [Ho 2019]. (b) Polarization-resolved photoluminescence spectra measured at 15° intervals. After [Aslan 2016].

Figure 1.18 shows the first 3D Brillouin zone of bulk ReS_2. Despite intensive studies, contro-

versies remain regarding the electronic structure and the nature of the fundamental bandgap of this material. In particular, it has been brought into question if ReS_2 also undergoes an indirect to direct bandgap transition with decreasing thickness, similar to many other TMDs [Webb 2017]. For monolayer MX_2 compounds, the indirect bandgap becomes larger than the direct gap [Zhao 2013, Padilha 2014]. It is unclear if such an effect could also occur in ReS_2.
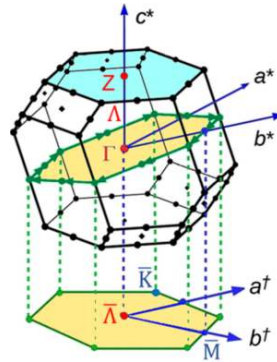
Figure 1.18: The Brillouin zone of ReS_2. a^*, b^*, c^* are the reciprocal lattice vectors and the high-symmetry Z-plane, Γ-plane and its projection on the k_z=constant plane are shaded [Webb 2017].

On one hand, calculations by A. Kuc and coworkers from the group of Prof. T . Heine ([Urban 2019]), which are discussed in Chapter 4, suggest the presence of an indirect fundamental bandgap which decreases with increasing ReS_2 thickness for all thicknesses apart from the bilayer, for which a direct gap was predicted. A similar theoretical result was obtained in the work of [Gehlmann 2017], where an indirect gap for more than > 2 layers and a direct gap at the Γ point for the bilayer were predicted. On the other hand, DFT calculations performed by [Tongay 2014] predicted a direct bandgap independent of the number of layers and [Zhong 2015] found that monolayer ReS_2 has a direct gap at the Γ point.

Experimental studies also provide contradicting evidence about the nature of the bandgap in ReS_2. Studies of the absorption edge in bulk ReS_2 indicate that the fundamental bandgap is indirect [Ho 1998, Ho 1997, Liang 2009]. Fig. 1.19 (a) shows $\sqrt{\alpha\hbar\omega}$ (α is the absorption coefficient and ω the photon frequency) as a function of photon energy determined experimentally for a series of temperatures and for different polarizations [Ho 1998]. The close to linear dependence observed in this plot suggests an indirect bandgap [Pankove, J. I. 1971]. The combination of photoacoustic and photoreflectance spectroscopy revealed the presence of energetically close-lying direct and indirect transitions for bulk ReS_2 [Zelewski 2017]. Fig. 1.19 (b) shows the bandgaps determined using both methods, in particular for ReS_2 the indirect bandgap is around 1.375 eV and the direct around 1.55 eV. Photoemission electron microscopy suggested a transition from an indirect bandgap in bulk ReS_2 to a direct bandgap in the bilayer and monolayer [Gehlmann 2017] and ARPES results suggested that bulk ReS_2 is marginally indirect [Webb 2017]. Transport studies of field effect transistors based on bulk crystals suggested an indirect bandgap of 1.41 eV [Gutiérrez-Lezama 2016]. In contrast, the observation of photoluminescence for ReS_2 thicknesses from monolayer to bulk could imply the direct nature of the bandgap independent of thickness [Ho 2017, Aslan 2016]. However, the photoluminescence quantum yields were shown to be very low and independent of the number of layers for

thicknesses from monolayer to seven layers [Mohamed 2018]. The PL intensity was observed to increase monotonically with material thickness [Mohamed 2018] which would suggest that there is no change of the bandgap nature.
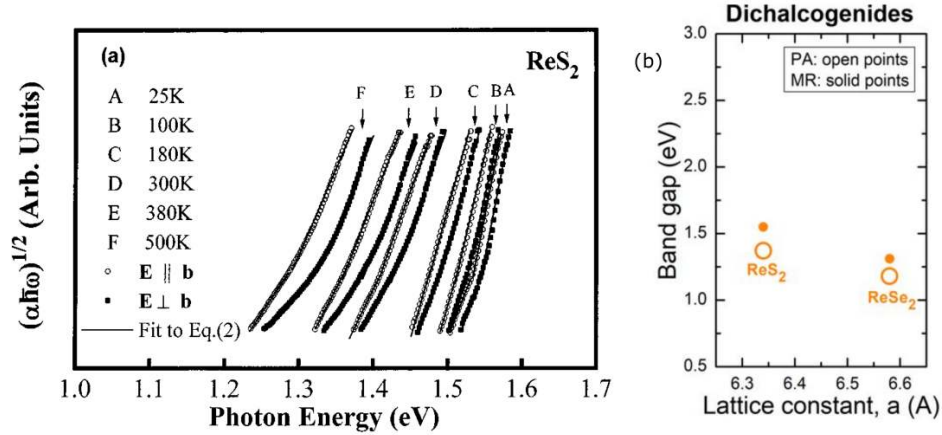
Figure 1.19: (a) Square root of the absorption coefficient α multiplied by photon energy as a function of photon energy for different polarization directions and temperatures. After [Ho 1998]. (b) The direct and indirect bandgaps for rhenium dichalcogenides determined using respectively modulated and photoacoustic reflectance. After [Zelewski 2017].

Chapter 4 of this thesis presents a detailed study of the absorption and photoluminescence properties of anisotropically stacked ReS$_2$ of varying thickness. Based on these results we draw conclusions about the nature of the photoluminescence and the underlying electronic structure of the material.

1.3.3   Anisotropic heterostructures

The possibility to integrate different 2D materials into multilayer stacks has inspired the rapidly expanding research field of van der Waals heterostructures [Wang 2014, Novoselov 2016]. Heterostructures can have new emergent properties and functionalities beyond those displayed by the constituent layers, providing an interesting platform for fundamental research and applications. For example, in transition metal dichalcogenide heterostructures, new excitonic phenomena such as the formation of spatially indirect excitons [Calman 2016] or the influence of the moiré potential on the intralayer exciton properties [Zhang 2018] can be observed.

The emergence of new properties in van der Waals heterostructures is caused by the electronic and structural changes induced by the neighbouring layers in each other [Novoselov 2016]. Depending on the symmetries and dimensions of the lattices of the layers and their relative alignment, the heterostructure can be described either as a commensurate or incommensurate superlattice [Yao 2018]. Commensurate lattices are characterized by a large-scale moiré interference pattern. This kind of pattern has translational symmetry and can be formed when the superimposed lattices fulfil the condition: $ma_1^A + na_2^A = m'a_1^B + n'a_2^B$ where $a_{1,2}^{A,B}$ are the primitive lattice vectors for the A and B layers and n, m, n', m' are integers. On the other hand, incommensurate, nonperiodic heterostructures are formed when this condition is not fulfilled.

Fig. 1.20 shows the schematics of the two different types of heterostructures formed by bilayer graphene stacked at different twisting angles. The incommensurate superlattice has rotational, but not translational symmetry and quasicrystalline order. Incommensurate structures are harder to stabilize and thus less common in nature [Yao 2018].
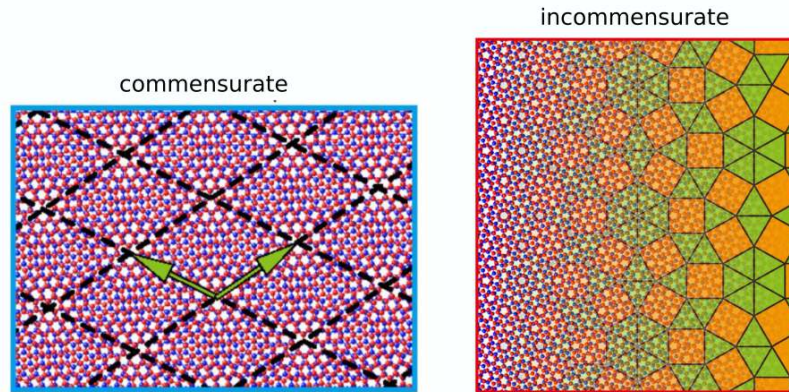
Figure 1.20: Schematics of commensurate and incommensurate heterostructures formed by bilayer graphene with different twisting angles. The arrows mark the moiré reciprocal lattice vectors of the commensurate superlattice. The patterns of the dodecagonal quasicrystal are shown on the lattice in the right side of the schematics. After [Yao 2018].

Heterostructures can be formed artificially, by bottom-up synthesis [Jung 2014] or deterministic placement of the individual layers on top of each other [Frisenda 2018]. The deterministic placement approach allows engineering structures with custom composition and properties but suffers from the risk of contamination and introducing unwanted adsorbates. It is also technically challenging to control the correct alignment of the layers, crucial for the properties of the heterostructure [Liao 2018, Nayak 2017]. A promising alternative approach is the top-down exfoliation of natural heterostructures. Several naturally occurring minerals crystallize in a layered form with different types of layers alternating in the stacking direction and held together via van der Waals forces. These include complex compounds from the sulfosalt family. In particular, this group includes minerals with SnS-like and Pb-S like weakly bound alternating layers, such as cylindrite, coiraite, potosiite or franckeite [Williams 1988]. The different compounds have a different number of atomic planes in the alternating layers as well as different atomic composition [Moelo 1997]. For example the PbS-like layer of franckeite is composed of four atomic layers as opposed to two layers in cylindrite. Natural heterostructures have attracted attention because of the superconducting transitions [Lafond 1997] and topological insulator properties [Momida 2018] observed in $[(Pb,Sb)S]_{2.28}NbS_2$ and $(PbSe)_5(Bi_2Se_3)_6$. The recent rediscovery of natural heterostructures is related to the development of various exfoliation methods. Few-layer and single unit layer thick heterostructures were obtained via mechanical and liquid phase exfoliation [Prando 2017, Molina-Mendoza 2017]. Franckeite, investigated in this work, is a naturally occuring mineral which was first discovered at the end of the XIXth century [Stelzner 1893]. An approximate chemical formula of the material is $FeSn_3Pb_5Sb_2S_{14}$ although the exact composition may vary [Wang 1995, Heitz 1961]. Fig. 1.21 shows the sim-

plified crystal structure of franckeite. The heterostructure is composed of pseudo-tetragonal (referred to as Q or t) and pseudo-hexagonal (H) layers stacked in a HQHQ sequence. The pseudo-hexagonal (H) layer has a NX_2 structure, where N=Sn (majority of atoms) or Fe and X=S. The pseudo-tetragonal layer (Q) is composed of MX compounds, M=Sn or Sb and Pb and X=S [Gusmao 2018, Spiece 2018]. The stoichiometry can vary within a single Q or H layer.
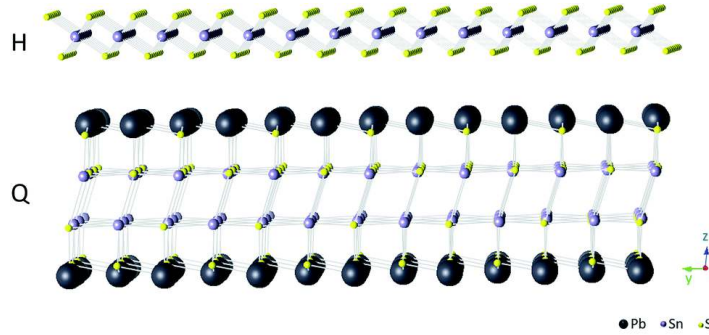
Figure 1.21: Simplified schematics of the H and Q layers of franckeite viewed along the in-plane direction. After [Gusmao 2018].

Franckeite is generally a p-type semiconductor [Burzuri 2018] with a narrow bandgap of 0.65 eV determined experimentally by diffuse reflectance spectroscopy [White 1998]. The observed onset of absorption in the near-infrared region is consistent with the small bandgap energy [Molina-Mendoza 2017]. DFT calculations of the electronic bandstructure performed using a simplified stoichiometry of Pb_3SbS_4 for the Q layer and SnS_2 for the H layer pointed to a 0.36 eV direct bandgap in the Q layer and a 1.48 eV indirect bandgap in the H layer. The approximate calculations for the Q-H heterostructure predicted an indirect gap of 0.35 eV [Velický 2017a]. Calculations by [Molina-Mendoza 2017] using an even more simplified PbS and SnS_2 stoichiometry suggested an indirect gap of 1-2 eV for the H layer and a narrower gap of 0.5-0.75 eV at the X point of the Brillouin zone for the bulk franckeite crystal (Fig. 1.22). The edge of the valence band lies closer to the Fermi level which suggests p-type doping of the material [Molina-Mendoza 2017]. The vast majority of layered semiconducting materials, including MoS_2 and $MoSe_2$, generally are n-type. P-type materials are less common among layered materials and include WSe_2 and environmentally unstable black phosphorus, which makes p-type franckeite interesting from the point of view of devices [Molina-Mendoza 2017]. According to DFT calculations the valence band is composed mainly of H layer orbitals while the conduction band is composed of the wave functions of the Q layer and as a consequence franckeite is a type-II heterostructures [Molina-Mendoza 2017]. Fig. 1.22 shows the calculated band structure of franckeite and the Q and H layers. Heterostructure with type-II band alignment have recently gained interest due to their ability to host interlayer excitons where electrons and holes are spatially separated in the different layers [Meckbach 2018].

Franckeite has shown a photoresponse over a wide spectral range, consistent with the calculations of the dielectric function of the crystal [Ray 2017, Molina-Mendoza 2017]. It was suggested that the photocarrier generation and recombination is strongly dominated by trap states in the bandgap [Ray 2017]. Fig. 1.23 (a) shows the calculated imaginary part of the
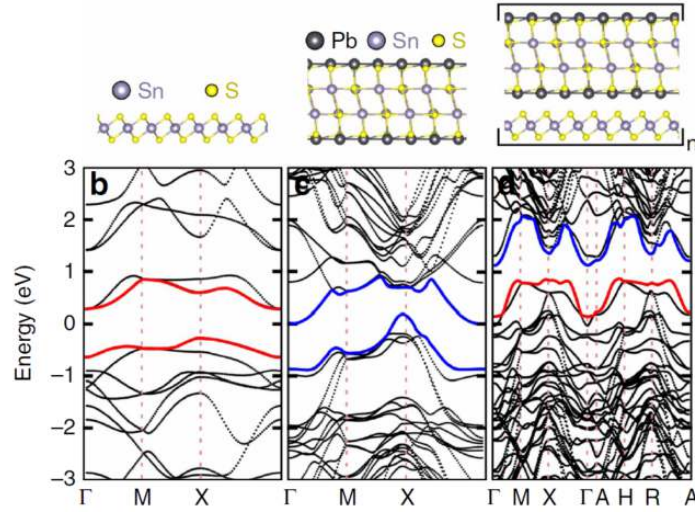
Figure 1.22: Band structure of the H layer (left), Q layer (middle) and of the franckeite crystal (right). The band states originating from the H layer are marked in red, the band states originating from the Q layer in blue. After [Molina-Mendoza 2017].

dielectric function of the Q and H layers and bulk franckeite. Fig. 1.23 (b) shows the photocurrent as a function of wavelength, after [Ray 2017]. Two peaks around 590 nm and 740 nm correspond to the bandgaps of SnS_2 and Sb_2S_3. Franckeite is stable under ambient conditions [Prando 2017]. Stability, in addition to the moderate bandgap and photoresponsivity over a broad wavelength range makes franckeite interesting for near-IR photodetector and photodiode applications [Prando 2017]. Exfoliated franckeite has been used in electrocatalytic energy reactions and showed very high hydrogen evolution performance [Gusmao 2018]. Strong anisotropic third harmonic generation has been observed in franckeite, suggesting potential for applications in nonlinear optical devices [Steinberg 2018].

To describe the crystal structure of franckeite we can adopt a notation of [001] for the out-of-plane direction and [100] and [010] for the perpendicular in-plane directions. The Q and H layers are incommensurate along the in-plane [010] direction [Velický 2017a]. The incommensurability of two neighbouring layers introduces strain which can be relaxed via structural deformation. This leads to a characteristic feature of franckeite and other misfit layered compounds, the in-plane rippling with a periodicity along the [010] direction, revealed by transmission electron diffraction and HRTEM [Williams 1988] as well as AFM and STM [Henriksen 2002] measurements. Fig. 1.24 shows the AFM and HRTEM images of franckeite layers where the sinusoidal long-range modulations can be seen.

Modulation has been observed also in high-angle, annular, dark-field (HAADF) microscopy which is sensitive to atomic composition [Wang 1995]. This suggests that the modulation has both a structural and stoichiometric component. Fig. 1.25 shows the top and side projections of the franckeite structure. A sinusoidal height variation is accompanied by the substitution of lead for lighter Sn or Sb cations in the concave regions of the Q layer [Makovicky 2011]. The modulation in franckeite has a wavelength of typically 4.7 nm [Wang 1995]. Interestingly, some
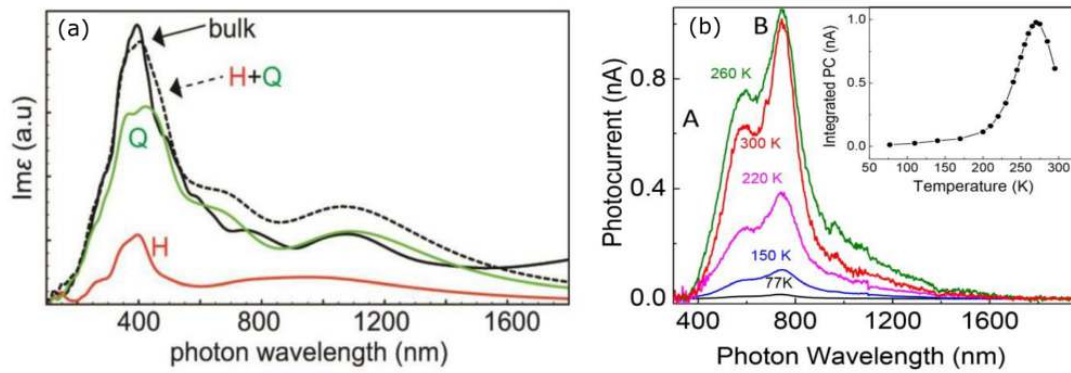
Figure 1.23: (a) Calculated imaginary part of the dielectric function of isolated H and Q layers, their sum and of bulk franckeite. (b) Photo-current spectra for different temperatures and the integrated intensity as a function of temperature (inset). After [Ray 2017].
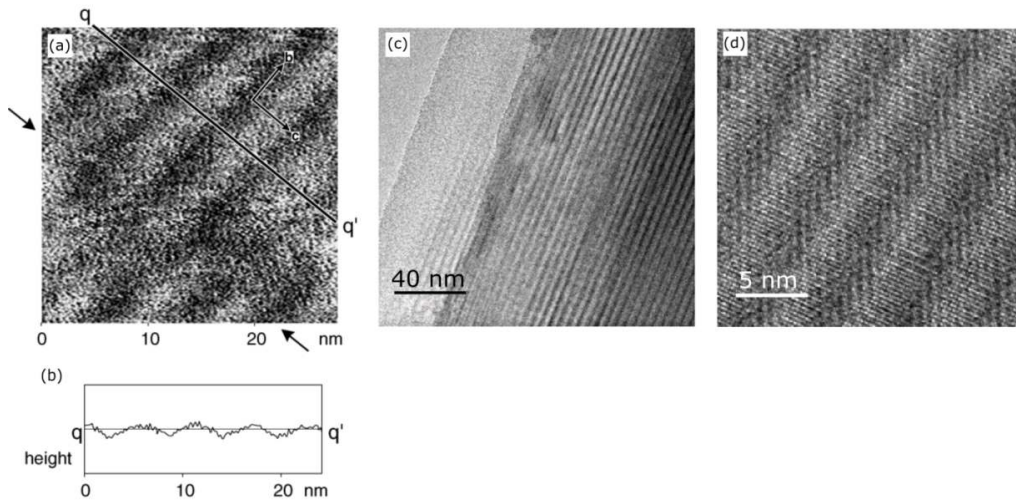
Figure 1.24: Height mode AFM image (top) and cross-section taken along the qq' direction. After [Henriksen 2002]. (b) and (c) HRTEM micrographs of franckeite layers. After [Molina-Mendoza 2017]. All the images present a top-down view on the basal plane.

different modulation wavelengths have also been observed for natural franckeite samples with slightly varying chemical composition, in particular the Pb/Sn ratio [Henriksen 2002]. Fig. 1.26 shows the comparison of the rippled structure of cylindrite and franckeite. Smaller curvature and larger wavelength of the ripples can be observed for the franckeite, possibly due to the larger stiffness of the thicker Q layer [Wang 1991, Makovicky 2011].

The in-plane anisotropy and strain induced by rippling can have a strong influence on the optoelectronic properties of the material, leading to linear dichroism or conductance anisotropy
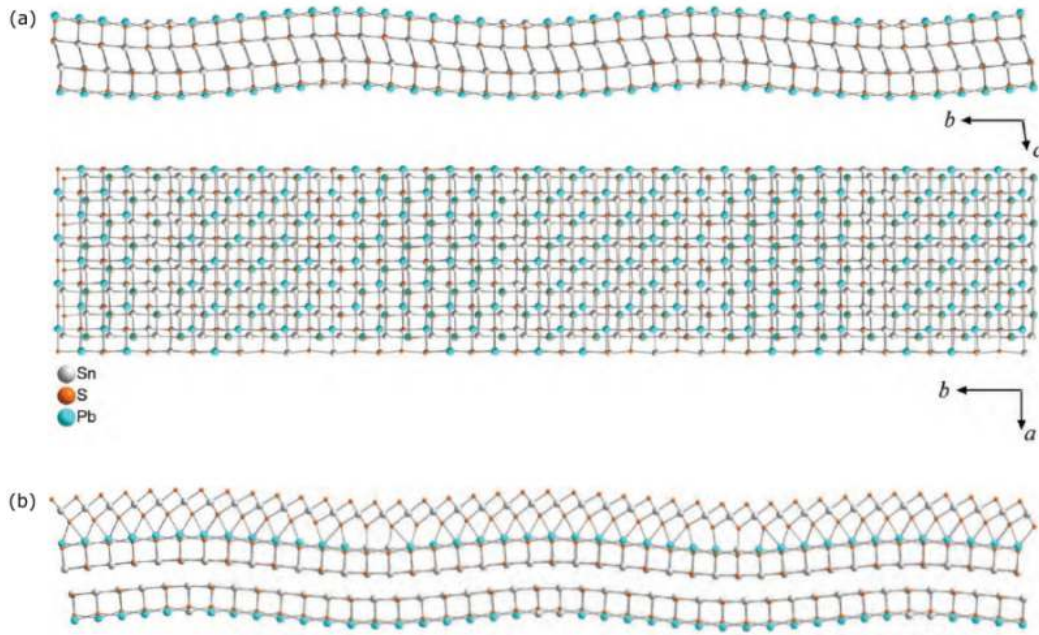
Figure 1.25: (a) Structure of the Q layer in the [100] and [001] projection. (b) Q-H layer pair structure in the [100] projection. The substitution of Pb cations for Sn or Sb cations in the concave region of the structure is visible. After [Makovicky 2011].
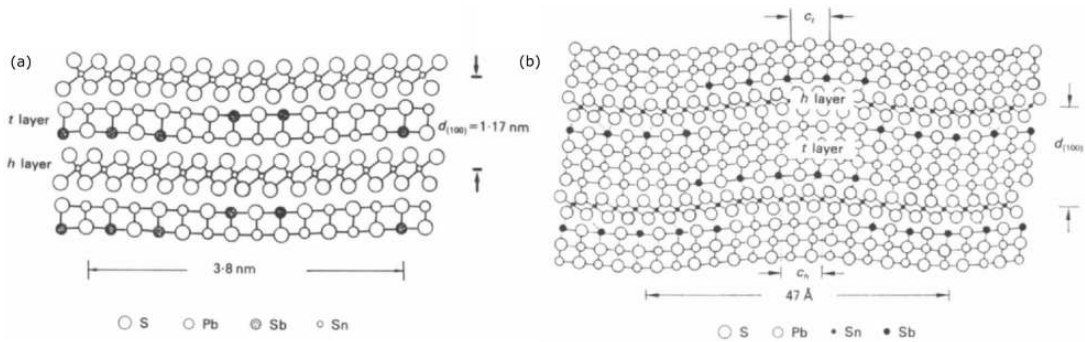
Figure 1.26: A structure model of (a) cylindrite and (b) franckeite in the [100] projection. *t* marks the pseudo-tetragonal layer, *h* the pseudo-hexagonal layer. After [Wang 1991].

[Quereda 2016]. Therefore, it is important to determine the rippling direction of the flakes. In this work, we will show how this can be achieved using polarized Raman spectroscopy, which, in comparison with AFM and TEM is a rapid and non-invasive method requiring minimal sample preparation which can be used to determine the orientation of anisotropic materials.

Chapter 2

Experimental methods

Contents

This chapter introduces the spectroscopic methods used to investigate the optoelectronic and vibrational properties of the samples investigated in this thesis. The first part describes the optical properties of anisotropic materials. In the following sections, the microspectroscopy setup and its adaptations for the particular spectroscopic methods are described.

2.1 Introduction

The optical properties of a crystal reflect the electronic band structure, the energy and symmetry of vibrational modes and the properties of excitonic states [Dresselhaus 2018]. Transmission and reflectance spectroscopy allow to determine the frequency-dependent dielectric function and the energies of the excitonic transitions or determine the bandgap. Photoluminescence spectroscopy can provide information about the recombination mechanisms, sample composition, impurities and defect states. Raman spectroscopy is a sensitive probe of the vibrational properties of the lattice. In this thesis, a combination of these spectroscopic methods was used to investigate the properties of atomically thin samples.

2.1.1   Optical properties of anisotropic materials

When electric field passes through a medium, a polarization is induced in the material and the vector of electric displacement $\mathbf{D}$ can be defined as:

$$\mathbf{D} = \varepsilon_r \varepsilon_0 \mathbf{E} = \varepsilon_0 (1 + \chi_e) \mathbf{E} = \varepsilon_0 \mathbf{E} + \mathbf{P} \tag{2.1}$$

where ε_r is the dielectric constant of the medium, ε_0 is the vacuum permittivity, χ_e is the dielectric susceptibility, $\mathbf{P}$ is the polarization and $\mathbf{E}$ is the electric field strength. The polarization field $\mathbf{P} = \varepsilon_0 \chi_e \mathbf{E}$ accounts for the displacement of charges in the medium. The complex electric susceptibility and dielectric function can be used to describe the material response during a periodic variation of $\mathbf{E}$ in time, for example for an electromagnetic wave propagating in a crystal [Dressel 2002]:

$$\tilde{\chi} = \chi_1 + i\chi_2 = \left(\frac{\tilde{\varepsilon}}{\varepsilon_0} - 1 \right) \tag{2.2}$$

$$\tilde{\varepsilon} = \varepsilon_1 + i\varepsilon_2 \tag{2.3}$$

This approach allows us to describe both the changes in magnitude of the $\mathbf{D}$ and $\mathbf{E}$ fields and the phase shift between them. The refractive index n and the extinction coefficient k can be used to describe the propagation and dissipation of electromagnetic waves in a medium. They correspond to the real and imaginary component of the complex refractive index:

$$\tilde{n} = n + ik \tag{2.4}$$

Components of $\tilde{n}$ can be expressed in terms of the real and imaginary part of the complex dielectric constant:

$$n^2 = \frac{1}{2} \left(\sqrt{(\varepsilon_1^2 + \varepsilon_2^2)} + \varepsilon_1 \right) \tag{2.5}$$

$$k^2 = \frac{1}{2} \left(\sqrt{(\varepsilon_1^2 + \varepsilon_2^2)} - \varepsilon_1 \right) \tag{2.6}$$

In an isotropic material, χ_e is a scalar and $\mathbf{P}$ and $\mathbf{E}$ are parallel and the magnitude of the polarization vector does not depend on the direction of the incident electric field. In anisotropic materials, the susceptibility can be represented in the form of a tensor which can be reduced to a diagonal form:

$$\hat{\chi}_e = \begin{pmatrix} \tilde{\chi}_{xx} & 0 & 0 \\ 0 & \tilde{\chi}_{yy} & 0 \\ 0 & 0 & \tilde{\chi}_{zz} \end{pmatrix} \tag{2.7}$$

where at least one of the eigenvalues $\tilde{\chi}_{ii}$ is not equal to the remaining ones. The polarization is then given as:

$$\mathbf{P} = \varepsilon_0 \tilde{\chi}_{xx} E_x \hat{\mathbf{x}} + \varepsilon_0 \tilde{\chi}_{yy} E_y \hat{\mathbf{y}} + \varepsilon_0 \tilde{\chi}_{zz} E_z \hat{\mathbf{z}} \tag{2.8}$$

Anisotropy of the susceptibility results in the direction dependent character of the absorption and propagation of light in the medium. In an anisotropic medium, $\mathbf{P}$ and $\mathbf{E}$ do not have to be colinear. The refractive index and as a consequence the speed of light $v = c/n$ depends on the

propagation and polarization directions of light. If for example $\tilde{\chi}_{xx} = \tilde{\chi}_{yy} \neq \tilde{\chi}_{zz}$, the crystal is uniaxial with two different refractive indices for light polarized in the xy plane and for light polarized along the z direction. If a light wave propagates along z and the electric field vector is only in the xy plane, the propagation speed will not depend on the polarization. This direction in the crystal is called an optical axis. However, if the direction of propagation is different so that orthogonally polarized components of the light beam experience different refractive indices, the beam will be split in two rays which refract at different angles in a phenomenon called birefringence. If all $\tilde{\chi}_{ii}$ are unequal, the crystal is biaxial with two different optical axes. Dichroism refers to the property of a material when one of the polarization components of light is absorbed more strongly as a result of the anisotropy of k. The ability of the crystal to absorb different wavelengths of light depending on the polarization leads to pleochroism, observed as changes of the color of the material when viewed at different angles.

Optical transitions in a semiconductor can be described in a phenomenological way by the Lorentz model of driven damped oscillators. This model applies the concept of a classical oscillator to the interaction of the medium with an electromagnetic wave to model the dielectric constant on a microscopic level. Inside the material the electromagnetic wave can induce polarization due to different mechanisms, such as interaction with bound and free carriers, excitons or ions in the lattice. Each of these processes will contribute to the total electric displacement, which can be expressed as:

$$\mathbf{D} = \varepsilon_0 \mathbf{E} + \mathbf{P}_{background} + \mathbf{P}_{resonant} \tag{2.9}$$

$\mathbf{P}_{background}$ is the background polarization and $\mathbf{P}_{resonant}$ is the term related to the resonant interactions of the different dipoles in the medium with the oscillating electric field. The frequency-dependent dielectric constant includes contributions related to the different oscillators in the medium:

$$\varepsilon_r(\omega) = 1 + \chi_{background} + \sum_n \chi_n(\omega) = 1 + \chi_{background} + \sum_n \frac{A_n}{\omega_{0n}^2 - \omega^2 + i\Gamma_n\omega} \tag{2.10}$$

where ω_{0n} is the resonance frequency, Γ_n the width of the resonance of the n-th oscillator (related to the damping constant in the Lorentz model) and A_n a phenomenological parameter called the oscillator strength related to the intensity of the n-th transition.

In anisotropic materials, the oscillator strength of resonant transitions depends on the direction of polarization of the absorbed or emitted light. This can be understood by relating the phenomenological parameter A_n to the transition matrix elements describing the radiative transition probabilities in the quantum model of light-medium interaction. Coupling of a single-electron atom to a time-dependent electromagnetic field can be described using the Hamiltonian:

$$\hat{H} = \frac{1}{2m}(\hat{\mathbf{p}} + e\mathbf{A}(\mathbf{r}, t))^2 - e\phi(\mathbf{r}, t) + V(\mathbf{r}) \tag{2.11}$$

where $\hat{\mathbf{p}}$ is the momentum operator, $\mathbf{A}$ is the magnetic vector potential, m is the effective mass, e the elementary electric charge, ϕ the electric scalar potential and $V(\mathbf{r})$ is the binding Coulomb potential of the atomic nucleus. The term:

$$\hat{H}_{para} = \frac{e}{m}\mathbf{A}(\mathbf{r}, t) \cdot \hat{\mathbf{p}} \tag{2.12}$$

describes the paramagnetic term of the coupling of the electron to the electromagnetic field, related to single photon emission and absorption. The rate of spontaneous optical transitions can be described by Fermi's Golden Rule [Fermi 1932]. The $\hat{H}_{para}$ can be treated as a time dependent perturbation and the transition probability between two states a and b per unit time will be given as:

$$\Gamma_{a \to b}(t) = \frac{2\pi}{\hbar^2} | < \psi_b | \hat{H}_{para} | \psi_a > |^2 \delta(E_b - E_a) \tag{2.13}$$

where E_b and E_a are the energies of the final and initial state. In the electric dipole approximation, $e^{-i\vec{k}\vec{r}} \approx 1$, that is assuming that the wavelength of the incident light is much larger than atomic dimensions, the interaction term can be written as:

$$\hat{H}_{para} \approx e\hat{\mathbf{E}}(\mathbf{r}, t) \cdot \mathbf{r} = \hat{\mathbf{E}}(\mathbf{r}, t) \cdot \hat{\mathbf{d}} \tag{2.14}$$

where $\hat{\mathbf{d}}$ is the dipole moment related to the transition. If the time dependence of the electric field has an oscillating form $\mathbf{E}(\mathbf{r}, t) = cos(\omega t)$, the transition probability becomes

$$\Gamma_{a \to b}(t) = \frac{2\pi}{\hbar^2} | < \psi_b | \hat{\mathbf{E}}(r) \cdot \hat{\mathbf{d}} | \psi_a > |^2 \delta(E_b - E_a - \hbar\omega) \tag{2.15}$$

corresponding to the absorption of the radiation of frequency $\hbar\omega$. The matrix element:

$$|\hat{\mathbf{M}}_{ab}|^2 = | < \psi_b | \hat{\mathbf{E}}(\mathbf{r}, t) \cdot \hat{\mathbf{d}} | \psi_a > |^2 \tag{2.16}$$

depends on the relative orientation of the transition dipole moment, the electric field vector and the symmetries of the wave functions of the initial and final states. All these factors can contribute to the dependence of the oscillator strength, which is proportional to the transition matrix element $A_{ab} \propto |\hat{\mathbf{M}}_{ab}|^2$, on the polarization direction of resonantly absorbed or emitted light. The anisotropy of the oscillator strength for different transitions contributes to the effective anisotropy of the dielectric constant of the medium.

2.1.2   Reflectivity

Reflectance measurements are a useful method to investigate interband and excitonic transitions in semiconductors. Light falling on an optical boundary can be reflected or propagate in the medium, where it can be transmitted, scattered or absorbed. The reflectivity R, absorbtance A, transmittance T and energy losses due to scattering L fulfil the energy conservation law for the radiation reflected from and propagating in a material:

$$A + L + R + T = 1 \tag{2.17}$$

Reflectance at the boundary of different optical media is defined as the ratio of reflected to incident optical power. Reflection at the surface of an optical medium can be defined by the complex reflection coefficient $\tilde{r}$ which is equal to the ratio of the amplitudes of the electric fields of the reflected and incident wave. Reflectivity R is the square of its modulus $R = |\tilde{r}|^2$. For normal incidence R can be expressed as a function of the indices of refraction n_1 (entrance medium), n_2 (reflecting medium) and extinction coefficients k_1 and k_2:

$$R = \frac{(n_2 - n_1)^2 + (k_2 - k_1)^2}{(n_2 + n_1)^2 + (k_2 + k_1)^2} \tag{2.18}$$

Reflectivity depends on both the real and imaginary part of the dielectric function. For thin layered media, effects related to multiple internal reflection and interference can modify the observed reflectance spectrum of the sample. In such cases reflectance is not the same as reflectivity, which describes the reflection for a simple, homogenous, flat interface, and can strongly depend for example on the sample thickness. Anisotropy of the complex dielectric constant can result in the observation of polarization dependent features in the reflectance spectrum.

2.1.3 Photoluminescence

Photoluminescence (PL) is a process in which light is emitted after the material is excited by optical radiation. Fig. 2.1 shows the schematics of processes that lead to luminescence emission in a semiconductor [Dresselhaus 2018]. The first type of transitions involves defect and impurity states. The second are interband transitions, including band edge emission and higher energetic hot luminescence involving non-thermalized higher energy carriers. The last type of emission is related to the intraband relaxation of higher energetic carriers. Finally, recombination can occur from excitonic states below the bandgap (Fig. 2.1 (g)). The energy of the emitted photons corresponds to the energy difference between the excited and ground state. If the emitted light has a lower energy than the absorbed photons, the energy difference between the absorption and emission maxima, which depends on the relaxation mechanisms, for example vibrational relaxation or the presence of trap states, is referred to as the Stokes shift.
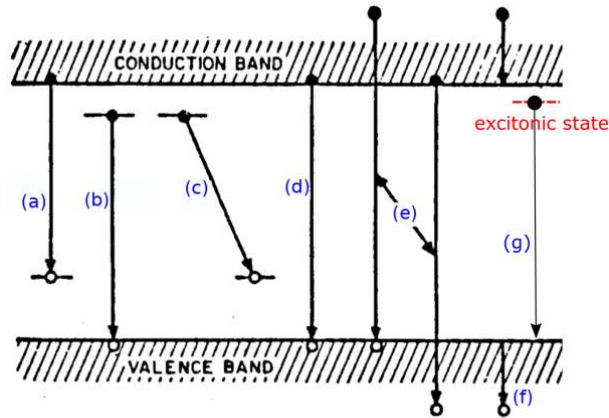
Figure 2.1: Luminescence recombination processes in a semiconductor: (a) conduction band to acceptor, (b) donor to valence band, (c) donor to acceptor, (d) band edge emission, (e) hot PL emission, (f) intraband relaxation processes, (g) recombination from an excitonic state. Adapted from [Dresselhaus 2018].

The photoluminescence spectrum can be a source of information about the electronic structure of the material, relaxation mechanisms in the crystal as well as the thermal distribution of electrons, holes and excitons. In an anisotropic crystal, the photoluminescence emission from excitonic states can be strongly linearly polarized due to the anisotropy of optical constants and excitonic wave functions.

2.1.4   Raman spectroscopy

2.1.4.1   Principle of Raman scattering

Raman spectroscopy, based on the phenomenon of scattering of light, is a non-invasive and versatile method to investigate the properties of crystalline materials. It can be used to obtain information about the electronic structure, phonon dispersion and electron-phonon interaction and doping, strain or number of layers of the material. Polarization-resolved Raman spectroscopy can be used to determine the symmetries of vibrational modes and the crystalline orientations of layered materials with in-plane asymmetry [Wu 2019].

Fig. 2.2 (a) shows a schematic illustration of the energy levels for different scattering processes. The incoming photon causes the system to transition from the ground state to an intermediate state, from which it relaxes emitting a photon of the same (elastic Rayleigh scattering) or different wavelength (Raman Stokes- and anti-Stokes scattering). For non-resonant Raman scattering the intermediate states are virtual, while for resonant scattering where the excitation energy matches an electronic transition in the material the states are real, which significantly enhances the observed intensity of the transitions [Cardona 1982]. Resonant Raman scattering can provide information about the electronic structure of the sample [Leite 1966, Scott 1969]. Energy is conserved during the scattering process: the change of the photon energy occurs due to interaction with phonons or other excitations in the crystal, for example electronic excitations (electronic Raman scattering [Cardona 1982]) or defects. For scattering involving phonons, the difference in energy between the initial and final state in the case of Stokes and anti-Stokes Raman scattering is equal to the energy of the phonon created or annihilated in the process. Momentum also has to be conserved during the scattering process, thus given the small momentum carried by a photon in the visible range only phonons at or near the center of the Brillouin zone can take part in first-order Raman scattering. Higher-order processes can involve modes from the whole Brillouin zone. Fig. 2.2 (b) shows the schematics of a typical first-order Raman spectrum with the Stokes, Rayleigh and anti-Stokes lines. The intensities of the Raman lines are lower than the intensity of the elastically scattered light. The Stokes and anti-Stokes line intensities are related by a temperature dependent factor due to the phonon statistics. The probabilities of both processes depend on the initial occupation of the phonon states. The average phonon occupation number $\langle n \rangle$ is given by the Bose-Einstein statistics:

$$\langle n \rangle = \frac{1}{\exp\left(\dfrac{\hbar\Omega}{k_B T}\right) - 1} \tag{2.19}$$

and is a function of the temperature T and phonon frequency Ω. Stokes scattering involves the creation and the anti-Stokes process the annihilation of a phonon. The intensity ratio of the

Stokes and anti-Stokes line is equal to:

$$\frac{I_{Stokes}}{I_{anti-Stokes}} = \frac{\langle n \rangle + 1}{\langle n \rangle} = \exp\left(\frac{\hbar\Omega}{k_B T}\right) \tag{2.20}$$
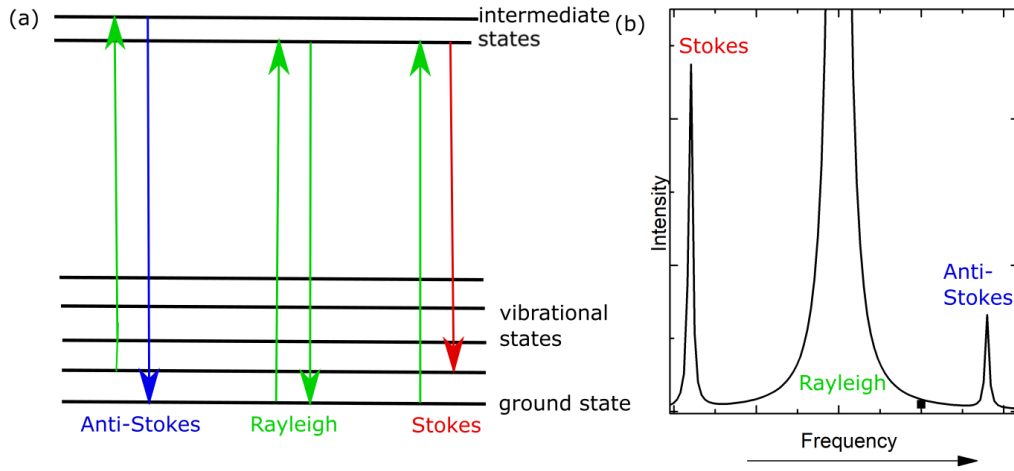
Figure 2.2: (a) The schematics of the energy levels in elastic and inelastic scattering processes. The arrows mark the incoming and scattered photons. (b) Schematics of a Raman spectrum showing the Stokes and anti-Stokes lines and the Rayleigh elastically scattered line.

The Raman scattering process can be described in the classical picture of an electromagnetic wave interacting with the material. The local dipole moment $\mathbf{p}$ induced in the material when a molecule or atoms in the crystal are subjected to external electric field and the electric field of the incident light are related by the polarizability $\hat{\alpha}$: $\mathbf{p} = \hat{\alpha} \cdot \mathbf{E}$. The Clausius-Mossotti relation relates the dielectric constant ε_r, which describes the dependence of the induced polarization on the incident electric field, to the atomic or ionic polarizabilities of the different species in the crystal α_i:

$$\frac{\varepsilon_r - 1}{\varepsilon_r + 2} = \sum_i \frac{N_i \alpha_i}{3\varepsilon_0} \tag{2.21}$$

where N is the density of the atoms or ions exhibiting polarization. In a general case, $\hat{\alpha}$ is a tensor, the elements of which are defined by the vibrational mode symmetry:

$$\hat{\alpha} = \begin{pmatrix} \alpha_{xx} & \alpha_{xy} & \alpha_{xz} \\ \alpha_{yx} & \alpha_{yy} & \alpha_{yz} \\ \alpha_{zx} & \alpha_{zy} & \alpha_{zz} \end{pmatrix} \tag{2.22}$$

From Eq. 2.21 it can be seen that the anisotropy of the dielectric constant and polarizabilities in the crystal are related. For an oscillating electric field of the incoming electromagnetic wave with the frequency ν_0:

$$\mathbf{E} = \mathbf{E}_0 \cos(2\pi\nu_0 t) \tag{2.23}$$

the induced dipole moment can be approximated as:

$$\mathbf{P} = \hat{\alpha_0}\mathbf{E}_0\cos 2\pi\nu_0 t + \frac{1}{2}\mathbf{E}_0 Q_k^0\Big(\frac{\partial\hat{\alpha}}{\partial Q_k}\Big)_0\Big[\cos 2\pi(\nu_0 + \nu_k)t + \cos 2\pi(\nu_0 - \nu_k)t\Big] \qquad (2.24)$$

where ν_k is the frequency of the k-th vibrational mode involved in the scattering process, $\hat{\alpha}$ is the polarizability tensor and Q_k is the displacement along the normal coordinate. The oscillating dipole moment is the source of the scattered radiation. The term describing oscillations with ν_0 frequency is related to elastic scattering. The presence of the terms with $(\nu_0 + \nu_k)$ and $(\nu_0 - \nu_k)$ frequencies is related to the anti-Stokes and Stokes processes, respectively. From Eq. 2.24 it can be seen that the condition for the appearance of bands with modified frequency is the nonzero value of $\partial\hat{\alpha}/\partial Q_k$ at the equilibrium position. This defines the Raman selection rules: while for an IR mode to be observed the net dipole moment has to change, for a mode to be Raman active a change of polarizability has to take place during the vibration. While the Rayleigh scattering is defined by the equilibrium polarizability of the molecule, for the inelastic scattering to occur the derivative of polarizability along the vibration direction has to be nonzero. The Raman tensor [Meyer 2010]:

$$\hat{R}(\nu) = \Big[\frac{\partial\hat{\alpha}(\nu)}{\partial Q}\Big]_{Q=0} \qquad (2.25)$$

is defined by the point group of the crystal and the symmetry of the vibrational mode.

Fig. 2.3 shows the normal vibrational modes of a linear triatomic molecule, such as CO_2, and the corresponding derivatives of the polarizability and dipole moment with respect to the normal vibration direction, after [Dietzek 2011]. For the symmetric stretch vibration, the polarizability changes monotonically as a function of nuclear displacement, leading to a nonzero derivative of $\hat{\alpha}$ around the equilibrium position. This mode is Raman active. For the antisymmetric stretching and bending vibrations, the dipole moment changes sign around the equilibrium position. These modes do not contribute to Raman scattering, but due to the nonzero derivative of the dipole moment they are IR-active.

2.1.4.2 Polarized Raman spectroscopy

Polarized Raman spectroscopy is a useful method in the study of anisotropic materials [Wu 2019]. In particular, in materials with low symmetry it allows for the identification of the crystalline orientation of the sample relative to the measurement geometry, as has been demonstrated for example for black phosphorus, $MoTe_2$ or ReS_2 [Wu 2015, Chenet 2015, Song 2017]. Resonant Raman scattering measurements on few layer WS_2 have shown that taking into account the polarization dependence of the mode intensity is necessary to reach correct conclusions when using the relative shift of the Raman peaks to determine the number of layers [Mitioglu 2014].

The Raman scattering efficiency is dependent on the form of the Raman tensor and the scattering geometry. If the incident and scattered photons have polarizations in the directions of unit vectors e_i and e_s, the scattering efficiency is given by the equation [Loudon 2001]:

$$S = A\Big[\sum_{\rho,\sigma=x,y,z} e_i^\sigma R e_s^\rho\Big]^2 = A|e_i \cdot R \cdot e_s|^2 \qquad (2.26)$$

where $\hat{R}$ is the Raman tensor, A a proportionality constant, and e_i^σ and e_s^ρ are the components
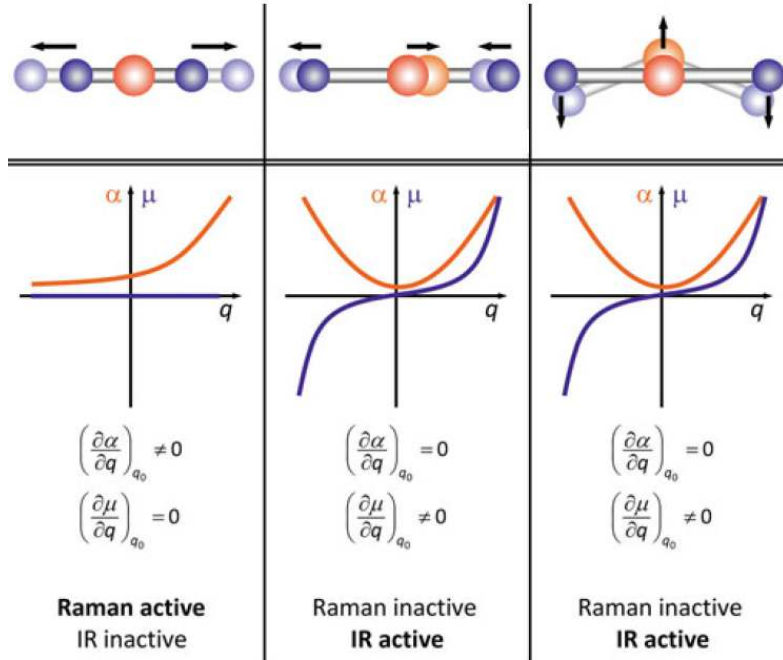
Figure 2.3: Normal modes of a three-atomic molecule. The orange curve shows the derivative of the polarizability with respect to the vibration direction and the blue curve, the derivative of the dipole moment. After [Dietzek 2011].

of the unit vectors along the σ and ρ axes. $\hat{R}$ is defined in the $\sigma\rho$ coordinate system related to the crystalline axes directions.

To describe the scattering intensities observed in the geometry of the experimental setup, the $\hat{R}$ tensor has to be transformed from the coordinate frame related to the crystalline directions. If the incident and scattered light propagate along the z axis, perpendicular to the sample, and the angle between e_i and the crystalline orientation in the xy plane is θ, the Raman tensor in the measurement coordinates can be defined as $\hat{R}' = r\hat{R}r^t$. r is the transformation matrix [Wu 2019]:

$$r = \begin{pmatrix} \cos\theta & \sin\theta & 0 \\ -\sin\theta & \cos\theta & 0 \\ 0 & 0 & 1 \end{pmatrix} r^t = \begin{pmatrix} \cos\theta & -\sin\theta & 0 \\ \sin\theta & \cos\theta & 0 \\ 0 & 0 & 1 \end{pmatrix} \tag{2.27}$$

The observed Raman intensity depends on the angle θ. Typically, in a polarization-resolved Raman scattering experiment the direction of the excitation polarization will be rotated in-plane relative to the sample and the scattered light will be detected in two polarizations: the co- and cross- detection polarization, when the incident light and detection polarization directions are respectively parallel or perpendicular. In the parallel configuration, the Raman intensity is dependent only on the diagonal elements of the transformed $\hat{R}'$ Raman tensor. In the cross-polarized configuration, the intensity is determined by the off-diagonal elements of

$\hat{R}'$ [Wu 2019]. This can be demonstrated for example for the A_1 mode in triclinic crystals, as shown in the example of WTe$_2$ [Song 2016b]. The Raman tensor for the A_1 mode before and after the transformation to measurement coordinates has the form:

$$R = \begin{pmatrix} a & 0 & 0 \\ 0 & b & 0 \\ 0 & 0 & c \end{pmatrix} R' = \begin{pmatrix} a\cos^2\theta + b\sin^2\theta & (b-a)\sin\theta\cos\theta & 0 \\ (b-a)\sin\theta\cos\theta & a\sin^2\theta + b\cos^2\theta & 0 \\ 0 & 0 & c \end{pmatrix} \tag{2.28}$$

and the angular dependence of the intensity in the co- and cross-polarized configurations is given by:

$$I_{co} \propto a^2 \left(1 + \left(\frac{b}{a} - 1 \right) \sin^2(\theta) \right)^2 \tag{2.29}$$

$$I_{cross} \propto \frac{1}{4} a^2 \left(\frac{b}{a} - 1 \right)^2 \sin^2 2(\theta) \tag{2.30}$$

which results in the characteristic two-lobed or four-lobed shape in the polar plot of intensity, as shown in Fig. 2.4. The degree of in-plane anisotropy is reflected in the difference between the a and b coefficients of the Raman tensor. For $a = b$, there is no in-plane asymmetry and the intensity in co-polarization does not depend on the polarization angle, while no scattered light can be observed in the cross-polarization. Fig. 2.5 shows the calculated angular dependence of the A$_1$ mode for different a/b ratios to illustrate the effect of anisotropy.
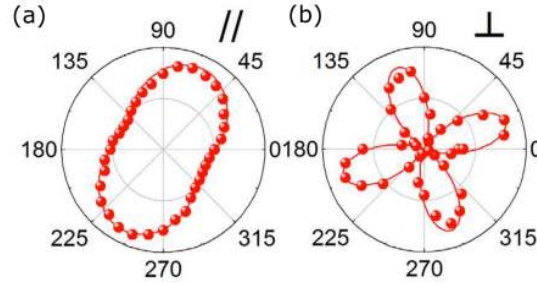
Figure 2.4: Polarization direction dependence of the Raman intensity for the 80 cm^{-1} A$_1$ mode in WTe$_2$ in the (a) parallel and (b) perpendicular configuration. After [Song 2016b].

In absorptive materials the elements of the Raman tensor are complex, which leads to more complicated polarization dependences. A detailed discussion is presented in Chapter 5. Observing the changes of the Raman mode intensities as a function of the in-plane direction of the linear polarization of the excitation beam can be a method to determine both the symmetry of the vibrational mode and the orientation of the crystalline axes of the sample.
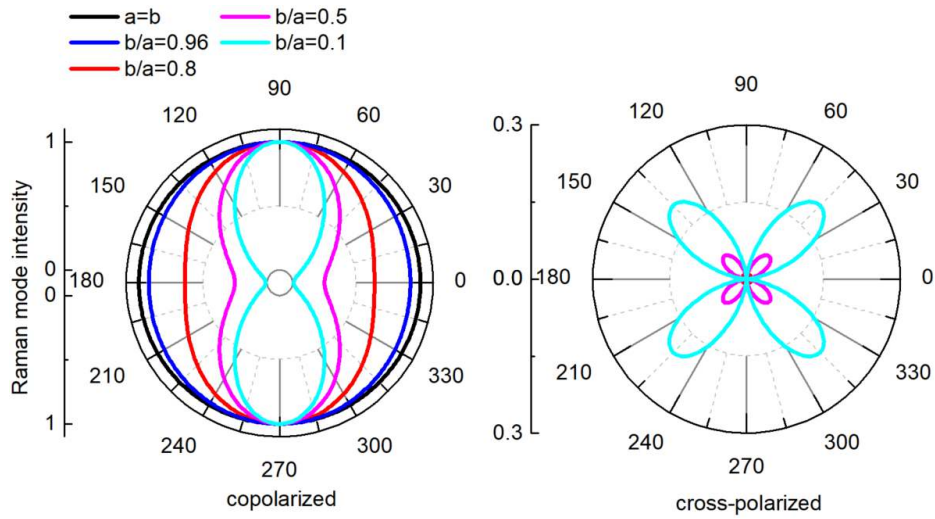
Figure 2.5: Calculated Raman mode intensity in the co- (left) and cross-polarization (right) for different ratios of the a/b A_1 mode Raman tensor elements.

2.2 Experimental setups

All of the spectroscopy measurements in this work were performed in backscattering geometry. Fig. 2.6 shows the general schematics of the excitation and detection path in this configuration. The light coming to the sample along the excitation path is reflected from a beamsplitter and directed towards the sample at a normal incidence angle. Light reflected or emitted from the sample along the normal direction passes through the beamsplitter and is directed towards the spectrometer, where it is dispersed and detected. The same lens or objective focuses the incident light and collects the signal.
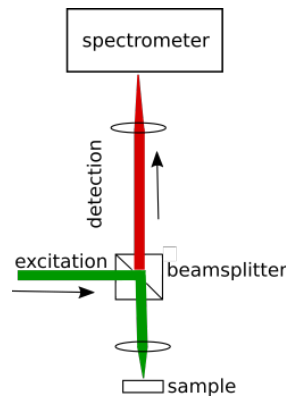
Figure 2.6: Schematics of a setup in backscattering geometry.

The scheme of the experimental setup at the LNCMI Toulouse is shown in Fig. 2.7. The μ-spectroscopy setup at the Institute of Physics of the Polish Academy of Sciences which was used for some of the reflectivity measurements was built according to a similar principle. The samples are placed in a helium flow cryostat equipped with a temperature controller and *xy* translation stages. The incident light is directed to either a dichroic mirror or a cube beamsplitter. In particular a 50/50 nonpolarizing cube beamsplitter was used for all polarization-resolved measurements to avoid artifacts related to the polarizing properties of the dichroic mirror. The light is then focused on the surface of the sample using a long working distance 50 x objective with 0.66 N.A. A long working distance objective is necessary because of the separation between the sample and the optical window. The collected signal passes back through the objective and through the beamsplitter and is directed by mirrors towards the spectrometer.

For photoluminescence measurements, a CW solid state or gas laser or the pulsed output of a tunable optical parametric oscillator pumped by a mode-locked Ti:Sapphire laser in free beam geometry was used. For reflectivity measurements, white light from a halogen lamp was coupled into an optical fiber which was mounted on a collimator in the optical path. Flip mounts on which mirrors and collimators are mounted allow to alternate between the different excitation sources. Typically the setup is used in the μ-spectroscopy configuration where the excitation beam passes through a spatial filter composed of two lenses and a pinhole aperture placed in between. The pinhole aperture is placed in the foci of both lenses. This allows to probe the sample with a diffraction limited spot and obtain high spatial resolution. Alternatively, for macro-reflectivity measurements or optical imaging of the sample surface the light from the lamp can be coupled into the excitation path without passing through the pinhole.

In the detection path, a lens is used to focus the signal on the monochromator entrance slit. For photoluminescence and Raman measurements a long-pass filter and/or edge filter is placed in front of the monochromator to reject elastically scattered light from the laser. Inside the monochromator, the light is dispersed using diffraction gratings and directed to the detector, a nitrogen-cooled CCD camera. To obtain an optical image of the sample surface, which enables positioning the excitation spot on the region of interest, a mirror on a flip mount can be used in the detection path to direct the reflected white light in the macro configuration to a small CCD camera.

For linear polarization resolved measurements, polarizing optics were placed in the excitation and/or detection path. For controlling the excitation polarization relative to the sample, a Glan-Taylor polarizer was placed in the excitation beam to clean the polarization and a $\lambda/2$ waveplate was used to rotate the polarization direction. Similarly, for polarization-resolved detection in PL and reflectivity measurements a linear polarizer was fixed in the detection path to assure the same relative orientation of the polarization direction of the signal and the diffraction gratings inside the spectrometer, which are sensitive to polarization. A half waveplate was rotated in front of the polarizer to sample different polarization directions of the incoming light.

The same setup that has been used for the μ-PL and reflectivity measurements has been adapted for the Raman measurements in different polarization configurations. Fig. 2.8 shows the simplified layout of the setup used for polarized Raman measurements. A linear polarizer and half-waveplate placed in a rotating motorized mount in the excitation beam were used to control the excitation polarization direction. A nonpolarizing 50/50 cube beamsplitter was used and a linear polarizer was placed in the detection path before the spectrometer. For every position of the $\lambda/2$ waveplate in the excitation beam, the linear polarizer was rotated so that light polarized parallel or perpendicular to the polarization direction of the excitation beam
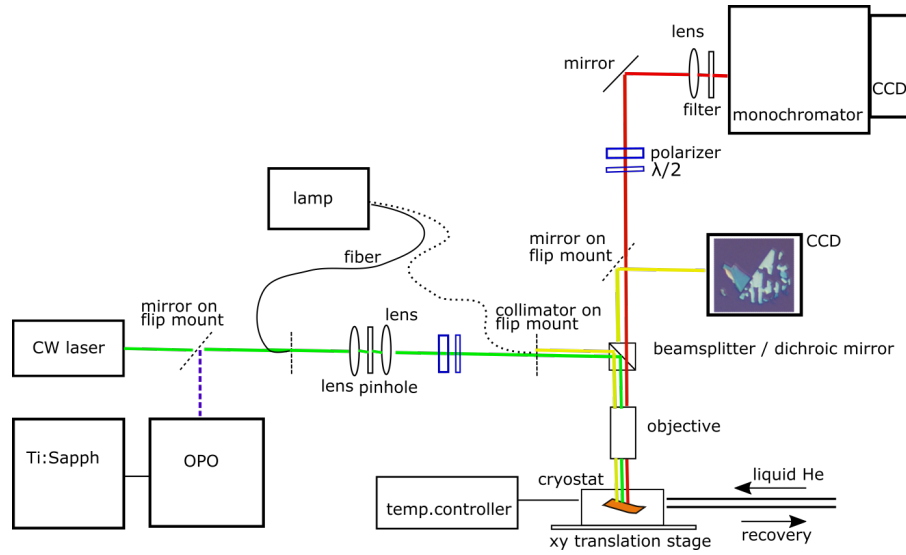
Figure 2.7: The general layout of the μ-spectroscopy setup at the LNCMI-Toulouse.

could be detected. In this configuration, to account for the polarizing properties of the gratings inside the spectrometer, the spectra had to be normalized by the intensity of the laser line in the copolarized configuration.
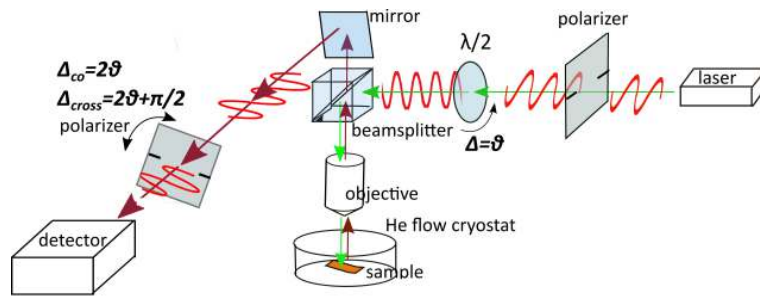
Figure 2.8: Schematics of the setup for polarized Raman scattering measurements.

Raman mapping measurements were performed in the Institute of Physics of the Polish Academy of Sciences in Warsaw in collaboration with D. Włodarczyk and Prof. A. Suchocki. A commercial Raman microscope system, MonoVista CRS+ from Spectroscopy and Imaging GmbH equipped with a Trivista Triple Raman Spectrometer and a CCD detector was used. The sample was placed on a motorized XYZ stage driven by a stepper motor and piezo actuators which enabled precise point by point mapping. The 532 nm and 785 nm lines of CW lasers were used as excitation. The power could be adjusted by neutral density filters. The microscope system was equipped with a 100 x objective with N.A. 0.9, enabling the focusing of the beam to a spot of around 1 μm diameter on the sample.

Chapter 3

Vibrational properties of encapsulated black phosphorus

Contents

In this chapter, we present a study of the influence of h-BN encapsulation on the vibrational properties of few layer black phosphorus. In the first part, Raman scattering in black phosphorus is discussed. Section 3.2 describes the investigated h-BN encapsulated BP samples and section 3.3 presents the results of μ-Raman characterization of the samples. We observe a theoretically predicted new Raman mode at energies slightly higher than the A_g^1 mode in few-layer samples. We explain the appearance of this mode by a change of the phonon frequencies in the surface layers relative to the frequencies in the inner layers. We discuss this effect in the context of interlayer coupling and strain and changes of the lattice properties in the outer layers. We also observe a narrowing of the Raman lines in encapsulated material and the absence of photoluminescence, which confirms the good quality of encapsulated BP and the effective protection against degradation. The content of this chapter has been partially published in [Urban 2017].

3.1 Raman scattering in black phosphorus

Raman spectroscopy has been extensively used to investigate the vibrational properties of black phosphorus [Castellanos-Gomez 2014, Lu 2014, Favron 2015, Phaneuf-L'Heureux 2016]. Both

monolayer and bulk black phosphorus belong to the D_{2h} point group [Ribeiro 2018]. The unit cell of phosphorene contains 4 atoms, resulting in 12 phonons at the center (Γ point) of the Brillouin zone:

$$\Gamma = 2A_g \oplus B_{1g} \oplus B_{2g} \oplus 2B_{3g} \oplus A_{1u} \oplus 2B_{1u} \oplus 2B_{2u} \oplus B_{3u} \tag{3.1}$$

The calculated phonon dispersion of monolayer BP is shown in Figure 3.1. The 12 phonon branches include 3 acoustic (B_{1u}^1, B_{2u}^1 and B_{3u}) and 9 optical phonons. Six of the optical modes with even parity are Raman active: B_{1g}, B_{2g}, $2B_{3g}$ and $2A_g$ while five modes with odd parity are infrared (IR) active : $2B_{1u}$, $2B_{2u}$, B_{3u}. The A_u mode is optically inactive [Luo 2015a].
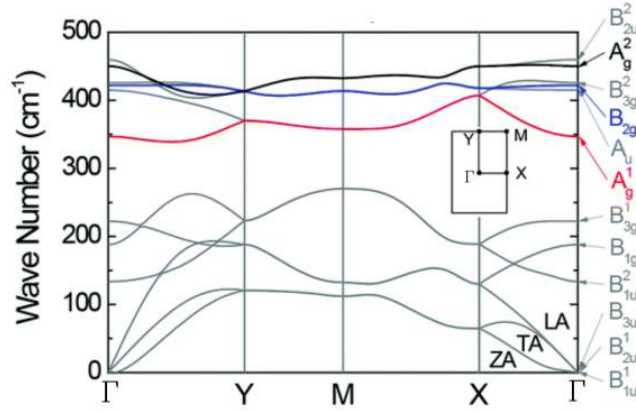
Figure 3.1: Phonon dispersion of monolayer BP after Hu et al. [Hu 2016]. The black, blue and red colors mark Raman-active modes observed in backscattering geometry. LA, TA and ZA label the acoustic modes.

In the coordinate system where the y direction is perpendicular to the crystal plane, x corresponds to the armchair, and z to the zigzag direction, the Raman tensors of the active modes have the following form [Ribeiro 2018]:

$$R(A_g) = \begin{bmatrix} a & \cdot & \cdot \\ \cdot & b & \cdot \\ \cdot & \cdot & c \end{bmatrix}, R(B_{1g}) = \begin{bmatrix} \cdot & d & \cdot \\ d & \cdot & \cdot \\ \cdot & \cdot & \cdot \end{bmatrix}$$

$$R(B_{2g}) = \begin{bmatrix} \cdot & \cdot & f \\ \cdot & \cdot & \cdot \\ f & \cdot & \cdot \end{bmatrix}, R(B_{3g}) = \begin{bmatrix} \cdot & \cdot & \cdot \\ \cdot & \cdot & g \\ \cdot & g & \cdot \end{bmatrix} \tag{3.2}$$

In the backscattering geometry light propagates perpendicularly to the layer planes, so that the polarization of the incident and scattered light is only in the xz plane. As a consequence, only the A_g and B_{2g} symmetry modes can be observed in this geometry [Ribeiro 2018].

Figure 3.2 (a) shows the schematics of the three Raman modes which are observed in the backscattering geometry with the directions of the movement of atoms marked by arrows and (b) a typical Raman spectrum we measured on a thick BP flake on Si substrate using 532 nm excitation. The A_g^1 mode around 365 cm^{-1} corresponds to the movement of the atoms in the out-of-plane z direction, the A_g^2 around 470 cm^{-1} to the movement mainly along the x (armchair) direction and B_{2g} around 440 cm^{-1} for movement along the y (zigzag) direction.
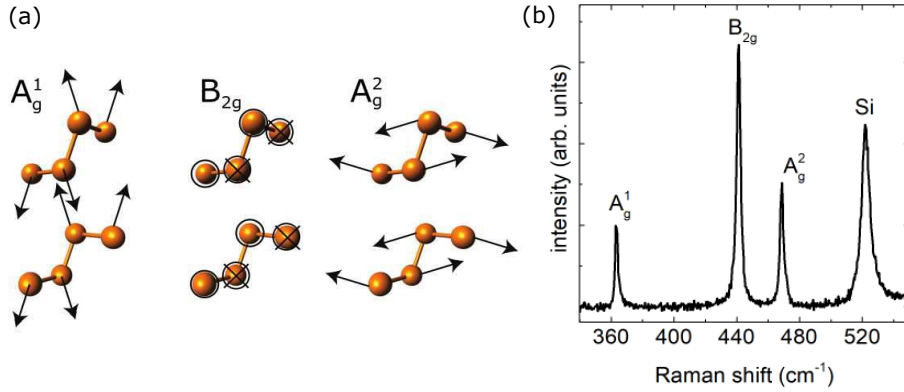
Figure 3.2: (a) The vibrational Raman-active modes A_g^1, A_g^2 and B_{2g}. Arrows mark the directions of the displacement of the atoms. (b) typical Raman spectrum (532 nm excitation) of a thick BP flake on Si/SiO$_2$ substrate.

Changes relative to the monolayer spectrum can be observed for few-layer crystals. Figure 3.3 (a) shows the Raman B_{2g} and A_g^2 modes of BP for a varying number of layers [Ribeiro 2018]. The B_{2g} peak shows only very small changes in energy while the A_g^2 shows a more clear redshift with increasing thickness. For bilayer and thicker BP a second peak appears on the high-energy side of the A_g^2 mode. In contrast to monolayer and bulk crystals, in few layer material the translational symmetry along the out-of-plane direction is broken. As a consequence, the unit cell of a few-layer BP flake contains $4n$ atoms. This leads to the appearance of $12n$ vibrational modes which can be considered as the in-phase and out-of-phase combinations of monolayer modes in opposed layers [Phaneuf-L'Heureux 2016]. Flakes with an even (with inversion symmetry) and odd (without inversion symmetry) number of layers belong to different space groups. The change in symmetry can lead to the emergence of new Raman-active modes via the mechanisms of Davydov splitting and mode conversion [Ribeiro 2018, Luo 2013a]. If the new Raman-active modes can be resolved spectrally, the appearance of a larger number of modes at frequencies slightly different from the frequency of the original mode due to the effect of coupling between the layers is referred to as Davydov splitting. The generation of IR active modes from the out-of-phase combinations of Raman modes, as well as the generation of Raman-active modes from a combination of IR modes is referred to as Davydov mode conversion. In BP, the frequency of the IR-active B_{2u} mode is very close to that of the Raman-active A_g^2 mode. A combination of two B_{2u} IR modes $B_{2u} \otimes B_{2u}$ gives rise to the $A_g^2(B_{2u})$ mode, approximately 4 cm^{-1} above the A_g^2 mode. The relative intensity of the $A_g^2(B_{2u})$ mode is stronger for a

small number of layers where the thickness of the material does not exceed the interaction range of a single layer with its neighbours [Phaneuf-L'Heureux 2016]. The $A_g^2(B_{2u})$ mode is particularly strong for bilayer and its relative intensity decreases with increasing thickness before disappearing completely in bulk, as can be seen in Fig. 3.3 (a).
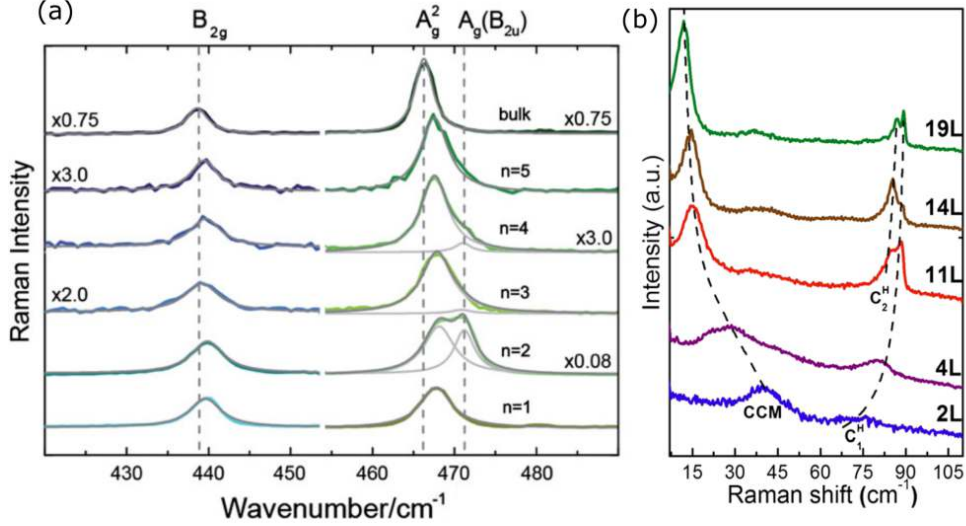
Figure 3.3: (a) Raman spectra of BP showing the B_{2g} and A_g^2 modes for a different number of layers. After [Ribeiro 2018]. (b) Low frequency branches of Raman interlayer compression modes as a function of the number of layers, after [Dong 2016].

With increasing thickness from phosphorene to bulk BP, the varying lattice parameters lead to changes of the mode energies [Hu 2016]. In conventional weakly coupled layered materials, the interlayer interaction is expected to cause an increase in the optical mode frequencies with thickness, as described by the classical coupled harmonic oscillator model [Lu 2014, Wieting 1972]. The interlayer van der Waals forces are expected to increase the restoring forces experienced by the atoms. This can lead to a blueshift of the Raman peaks with increasing thickness, as has been previously observed for example in MoS_2 [Lee 2010]. In addition, long-range electrostatic interaction can strongly modify the lattice dynamics, which has been demonstrated for example in β-GaSe [Wieting 1972] and more recently for MoS_2, $MoSe_2$, WS_2 and WSe_2 [Lee 2010, Luo 2013a, Tonndorf 2013, Lee 2015, Molina-Sánchez 2011]. In these materials, an anomalous behaviour has been observed, namely a blueshift of the A_g^1 and a redshift of the E_{2g}^1 modes with increasing thickness. The redshift of the in-plane E_{2g}^1 mode was explained via an enhancement of the dielectric screening with thickness [Lee 2015, Lee 2010]. In black phosphorus, a noticeable redshift of the A_g^2 mode and slightly smaller redshift of the B_{2g} mode was observed. The A_g^1 mode does not shift significantly with thickness [Favron 2015]. This behaviour of the modes indicates the presence of effects related to strong interlayer interaction in BP. In the work of [Phaneuf-L'Heureux 2016], a mode slightly above the A_g^1 mode was observed in the spectrum of the monolayer, but could not be clearly distinguished in thicker

flakes. A similar observation of additional modes in the proximity of the A_g^1 and A_g^2 peaks for few-layer BP was made by [Favron 2018]. The newly observed modes were interpreted as related to defect-activated second-order Raman processes and their presence was not correlated directly to changes of thickness.

Low energy shear and breathing interlayer modes appear in the Raman spectrum of few-layer 2D materials [Ribeiro 2018]. Figure 3.3 (b) shows the low-frequency Raman modes for different BP thicknesses. Observing their evolution with thickness can be a method of determining the interlayer force constants, because the frequency of the modes depends on both the number of layers and the strength of the interlayer coupling [Tan 2012, Luo 2015a]. The changes of these low-frequency interlayer Raman mode frequencies with thickness are much larger for BP than for other materials such as MoS_2 and WSe_2 due to the significantly stronger interlayer coupling [Luo 2015a, Hu 2016].

The vibrational properties of thin layered materials, reflected by the Raman spectrum, are sensitive to factors such as external environment or strain [Ribeiro 2018]. Changes of the Raman spectral features, such as intensity variations and the emergence of a new mode with respect to the pristine material have been observed in stacked heterostructures, including h-BN-TMD systems [Ding 2018]. The vibrational properties of layers neighbouring with another material differ from the properties of isolated layers [Ding 2018, Hu 2016]. In the following sections, our experimental results, in particular an analysis of the changes of the vibrational properties of BP in contact with h-BN, will be presented.

3.2   Samples characterization

The following section describes the preparation of the investigated h-BN encapsulated BP samples and their characterization using AFM imaging.

3.2.1   Preparation of encapsulated samples

The samples investigated in this work were few-layer thick BP flakes encapsulated in multilayer h-BN and deposited on Si/SiO_2 substrates. The samples were prepared at the Hong Kong University of Science and Technology in the group of Prof. Ning Wang by Gen Long and Dr Yang Wang. The detailed technique of producing the encapsulated heterostructures is described in reference [Chen 2015]. A schematics of the used polymer-free van der Waals transfer technique is presented in Figure 3.4 (a). Thin BP flakes were micro-mechanically cleaved from a bulk single crystal and deposited on Si/SiO_2 substrates. Two h-BN flakes were deposited respectively on another Si/SiO_2 substrate and on a PMMA film. The BP flake was then picked up by the h-BN flake placed on the polymer film and the h-BN-BP heterostructure was deposited on top of the h-BN flake on the Si/SiO_2 substrate to form a h-BN/BP/h-BN heterostructure as presented in Fig. 3.4 (b).

Optical micrographs of the samples allowed us to identify interesting few-layer flakes. Figure 3.5 shows an optical image of one of the investigated flakes. Different optical contrast in the microscopic images indicates different thickness of BP and h-BN.
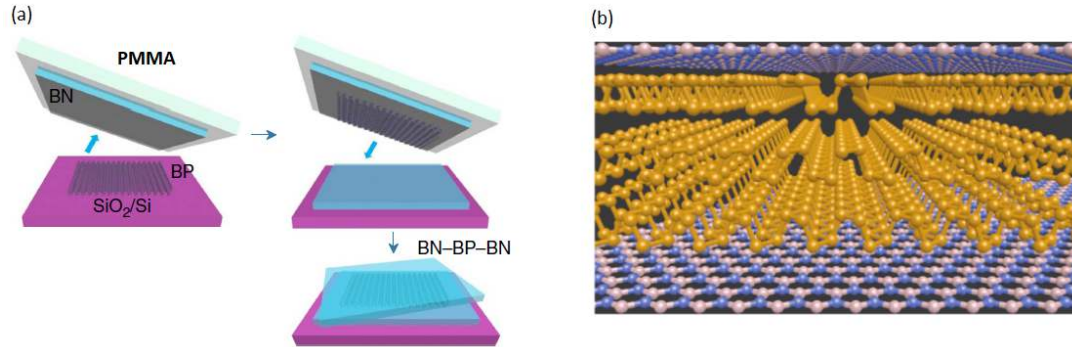
Figure 3.4: (a) Schematic of the encapsulated sample fabrication process, after [Chen 2015] and (b) crystal structure of BP encapsulated in h-BN.
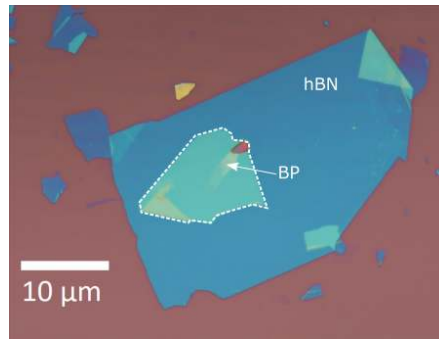
Figure 3.5: Optical micrograph of the investigated h-BN encapsulated black phosphorus flake on Si/SiO$_2$ substrate. The area where the top and bottom h-BN are overlaid is marked by a dashed line.

3.2.2   Thickness determination by AFM

AFM imaging was used to determine the number of BP layers in the investigated flakes. The AFM measurements were performed by Dr Marta Aleszkiewicz at the Institute of Physics, Polish Academy of Sciences in Warsaw. A contact-mode topographic image of a flake (referred to later as flake 2) as well as height profiles extracted from the image and fitted with sigmoid functions are presented in Figure 3.6. Based on the AFM measurements it was possible to obtain qualitative information about the relative thickness of the sample regions. From profiles 2,3 and 4 height differences of of 16.6 nm, 4.4 nm and 5 nm respectively could be determined. The AFM image clearly indicates that the thinnest region present in flake 2 is the one corresponding to profile 1 with a height of 3.3 nm, which was later identified as a bilayer using Raman spectroscopy. Exact determination of the number of layers using AFM is not possible because we do not precisely know the thickness of the encapsulating h-BN.
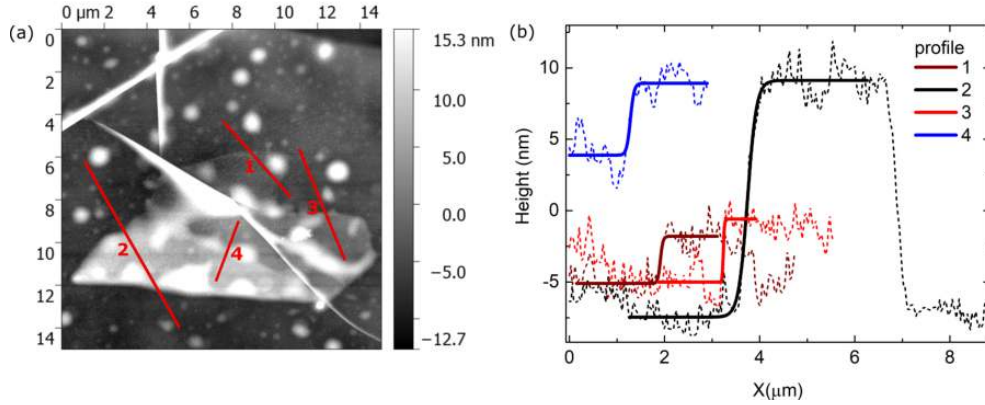
Figure 3.6: (a) AFM height image of flake 2 and (b) height profiles with fitted sigmoidal curves to determine the height.

3.3 μ-Raman studies of encapsulated BP flakes

Spatially resolved μ-Raman spectroscopy measurements were used to characterize all of the investigated flakes. I performed the measurements in the Institute of Physics, Polish Academy of Science in Warsaw together with Damian Wlodarczyk. The experimental setup is described in detail in Chapter 2. All measurements were carried out at room temperature and under ambient conditions. A 532 nm laser line at 630 μW power was used for excitation. The polarization of the laser was randomly oriented relative to the sample and no polarizing optics was used. We used a 100× objective with a numerical aperture of 0.9. The typical excitation spot size was of a diameter of around 1 μm. The spectral resolution was nominally 0.18 cm^{-1}. Several flakes of the size of several tens of micrometers were mapped with a spatial step between 1 μm and 2 μm (varying between different measurement series).

Figure 3.7 shows optical micrographs of two exemplary flakes and Raman spectra acquired at positions where different thicknesses could be expected based on the optical contrast. Significant changes in the energy, shape and relative intensity of the peaks were observed for the different positions on the flakes. The bilayer can be easily identified based on the high intensity of the $A_g^2(B_{2u})$ mode which appears on the high-energy side of the A_g^2 peak [Ribeiro 2018, Phaneuf-L'Heureux 2016]. In the bilayer, the intensity of the $A_g^2(B_{2u})$ and A_g^2 peaks is comparable and significantly higher than for the B_{2g} and A_g^1 mode. The relative peak positions and intensities are slightly different depending on the position on the flake. In certain spectra, an additional peak at the high energy side of the A_g^1 and A_g^2 modes can be observed.

To obtain quantitative information from the Raman data, we fitted each spectrum with a single Lorentzian for the B_{2g} mode and double Lorentzians for the A_g^1 and A_g^2 modes to account for the weaker peaks present on the high-energy side of both of these peaks. An example of the fitting is shown in figure 3.8 (a) for a spectrum acquired on a thin region of the flake. We extracted the peak positions, widths and intensities from the fits.
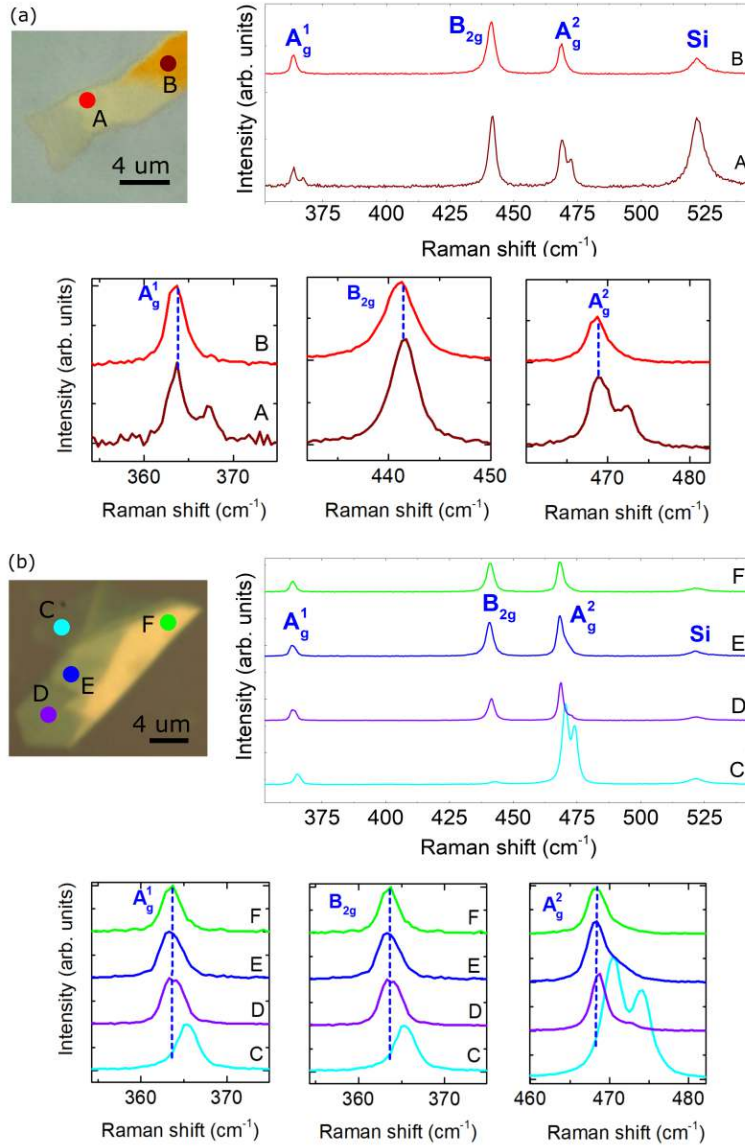
Figure 3.7: Raman spectra showing the three Raman active modes of BP and the Raman mode around 520 cm^{-1} from the Si substrate normalized to the A_g^1 mode intensity, optical micrographs of flakes with marked spots at which representative spectra were taken and the A_g^1, B_{2g} and A_g^2 Raman peaks in larger scale for two different flakes (a) and (b).

3.3.1 Thickness determination

Thanks to the anomalous behaviour of the Raman peaks with thickness, the relative difference between the A_g^2 and B_{2g} mode frequencies ΔE can provide a measure of the number of layers [Lu 2014]. For all four flakes on which we performed Raman mapping, ΔE was determined as the difference between B_{2g} and the lower energetic component of the A_g^2 mode. We then used a multiexponential function to fit the experimental $\Delta E(A_g^2 - B_{2g})$ dependence on the number of BP layers n previously observed by Lu *et al.* [Lu 2014]:

$$n = a + b_1 \cdot \exp\left(-\frac{\Delta E}{w_1}\right) + b_2 \cdot \exp\left(-\frac{\Delta E}{w_2}\right) + b_3 \cdot \exp\left(-\frac{\Delta E}{w_3}\right) \tag{3.3}$$

Parameters obtained from the fit $a = 1.96$, $w_1 = 0.467$ cm^{-1}, $w_2 = 0.519$ cm^{-1}, $w_3 = 0.571$ cm^{-1}, $b_1 = 5.05 \cdot 10^{25}$, $b_2 = 1.40 \cdot 10^{23}$, $b_3 = 1.13 \cdot 10^{21}$ were used to calculate the number of layers based on the observed $\Delta(A_g^2 - B_{2g})$ shift for all the spectra from our dataset for three and more layers. The form of the function was adapted to best reproduce the experimental data and the parameters do not have any physical meaning. In Fig. 3.8 (b), red points show experimentally determined ΔE from ref. [Lu 2014] and the dashed line shows the inverse of the fitted $n(\Delta E)$ function described by equation 3.3.

Fig. 3.9 (a) shows the number of layers calculated according to the formula 3.3 for all the collected BP spectra as a function of ΔE. The errors of ΔE are derived from the uncertainties of the positions of the B_{2g} and A_g^2 peaks obtained from fitting the spectra. The error of the calculated number of layers has been obtained according to the propagation of error formula taking into account the uncertainty of ΔE (the uncertainties of the parameters used in Eq. 3.3 are negligibly small). Within our dataset, points for $n \pm 0.5$ around each integer n value were grouped together to obtain averaged values for the different number of layers. Fig. 3.9 (b) shows the arithmetic means and standard deviations of n and E (in red) as well as the weighted means and their uncertainties (in black) for points group in this way for thicknesses between 3 and 10 layers. It can be observed that due to the shape of the $\Delta E(n)$ dependence a certain error of determining the shift ΔE will result in a larger uncertainty of n for thicker samples. The number larger number of spectra collected for a particular thickness also results in a smaller uncertainty of the estimated values. Finally, Fig. 3.10 shows a comparison of $\Delta E(n)$ as determined in the work of Lu *et al*, the fitted function and the values estimated for our dataset based on the weighted averages of the grouped points for 3-10 layers. We could unambiguously identify the bilayer based on the large intensity of the $A_g(B_{2u})$ mode. The two data points marked for the bilayer correspond to the $\Delta E(A_g^2 - B_{2g})$ and the $\Delta E(A_g(B_{2u}) - B_{2g})$ frequency differences. The value determined by [Lu 2014] for the bilayer corresponds approximately to the average of these two values which could be explained by the fact that these two modes were not spectrally resolved in the work of Lu and coworkers.

Fig. 3.11 shows the optical micrographs of all the investigated flakes and the maps of the number of layers calculated based on the $\Delta(A_g^2 - B_{2g})$ shift, the intensity ratio of the A_g^1/Si modes as well as the intensity of the Si Raman mode from the substrate. It can be seen that a lower number of layers correlates with an increased intensity of the mode from the substrate and lower A_g^1/Si ratio, both of which indicate smaller BP thickness. The A$_g^1$/Si 520 cm^{-1} mode ratio has been previously suggested as a measure of the number or layers [Castellanos-Gomez 2014]. However, due to the dependence of the Si mode intensity on the relative orientation of the crystal and the incident laser polarization, the A$_g^1$/Si mode ratio cannot be directly used to
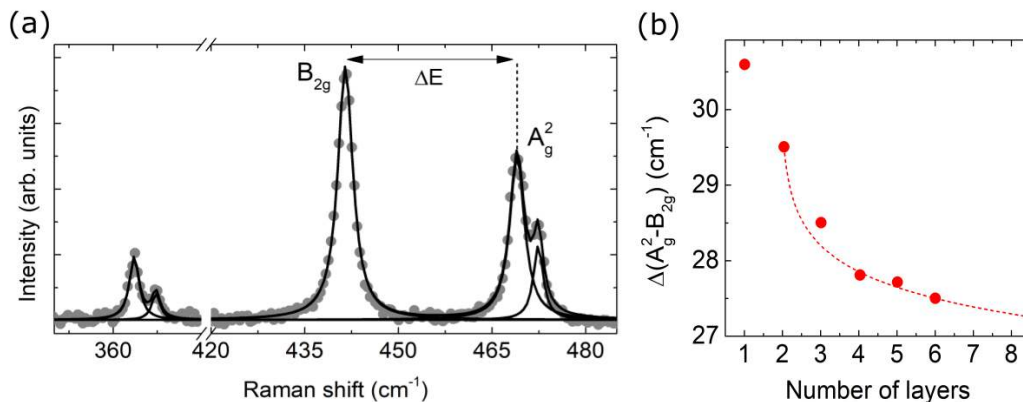
Figure 3.8: (a) Raman spectrum of a thin BP flake (points) and Lorentzian fits (solid lines). ΔE is marked with arrows. (b) $\Delta(A_g^2 - B_{2g})$ energetic separation of the modes as a function of the number of layers. Red points represent digitalized data from [Lu 2014], the dashed line shows the function fitted according to Eq. 3.3.
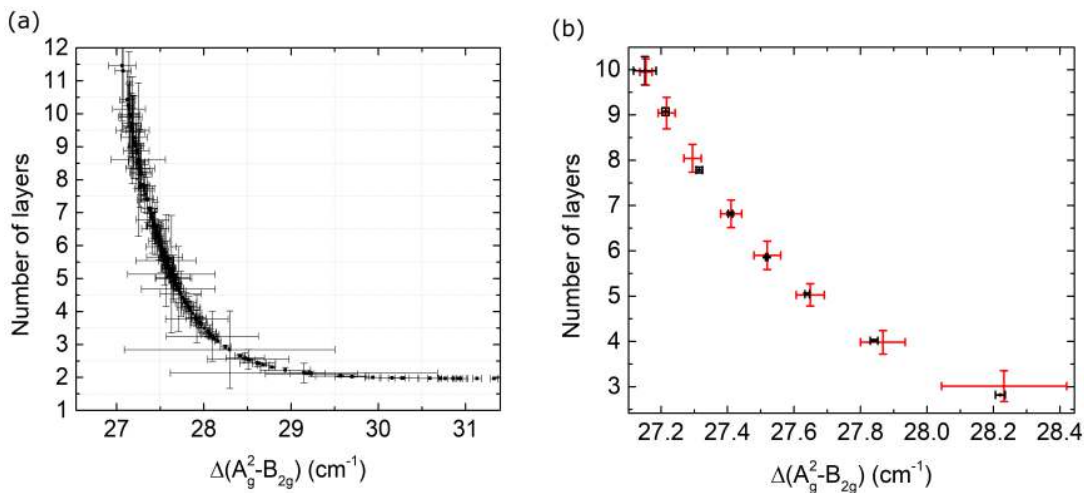
Figure 3.9: (a) The calculated number of layers as a function of the ΔE shift for all the Raman spectra acquired on different flakes. (b) The n and ΔE average arithmetic means and standard deviations (red) and weighted means and their uncertainties (black) calculated for the data points grouped around the integer number of layer values for 3-10 layers.

estimate the thickness without determining the relative orientation of the crystal directions of the substrate and the BP flakes first. Fig. 3.12 shows the A_g^1/Si intensity ratio as a function of the number of layers for one chosen flake. It can be seen that a larger thickness correlates with a higher A_g^1/Si ratio. The assignment of the number of layers based on the $\Delta(A_g^2 - B_{2g})$ frequency difference is used for all further analysis.
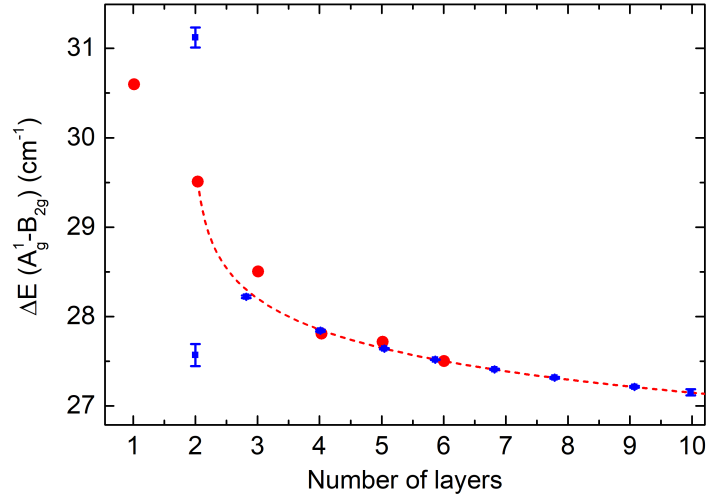
Figure 3.10: The shift ΔE as a function of the number of layers based on data from the work of [Lu 2014] (red points), the fitted function (dashed line) and the weighted mean values obtained for our data (blue). The data points for the bilayer were unambigously assigned based not on the energy shift but on the large intensity of the Davydov-converted mode.

3.3.2   Observation of the A_g^1 surface mode

In the following section we will discuss the emergence of modes on the high energy side of the A_g^1 and A_g^2 peaks for multilayer BP. The peak on the high energy side of A_g^2 has been observed before and can be assigned as the $A_g^2(B_{2u})$ mode arising due to Davydov conversion of two infrared active modes [Sugai 1985, Phaneuf-L'Heureux 2016, Ribeiro 2018]. In Fig. 3.7 this mode can be clearly seen in the spectrum corresponding to point C.

Surprisingly, a relatively weak mode showing a clear dependence on the number of layers appears around 3-4 cm^{-1} to the high energy side of the main A_g^1 peak. This new mode could be observed for three-layer and thicker samples, but not for the bilayer. Figure 3.13 (a) and (b) shows the Raman modes as a function of the number of layers and the fitted Lorentzian functions. The $A_g^2(B_{2u})$ mode can be resolved for all measured thicknesses. The additional peak on the high energy side of A_g^1 peak can be seen for three layers and larger thicknesses while no clear splitting could be resolved for the B_{2g} mode.

The intensity of the newly observed mode relative to the main A_g^1 component decreases as a function of the number of layers. The peak intensities obtained from the fitting were used to calculate the intensity ratio of the high energy peak to the sum of the high energy peak and the main A_g^1 component. The result is presented as a function of the number of layers in Fig. 3.14. The different colored points show results for a given number of layers and the black points the mean values for a given number or layers. Another interesting feature is the absence of this
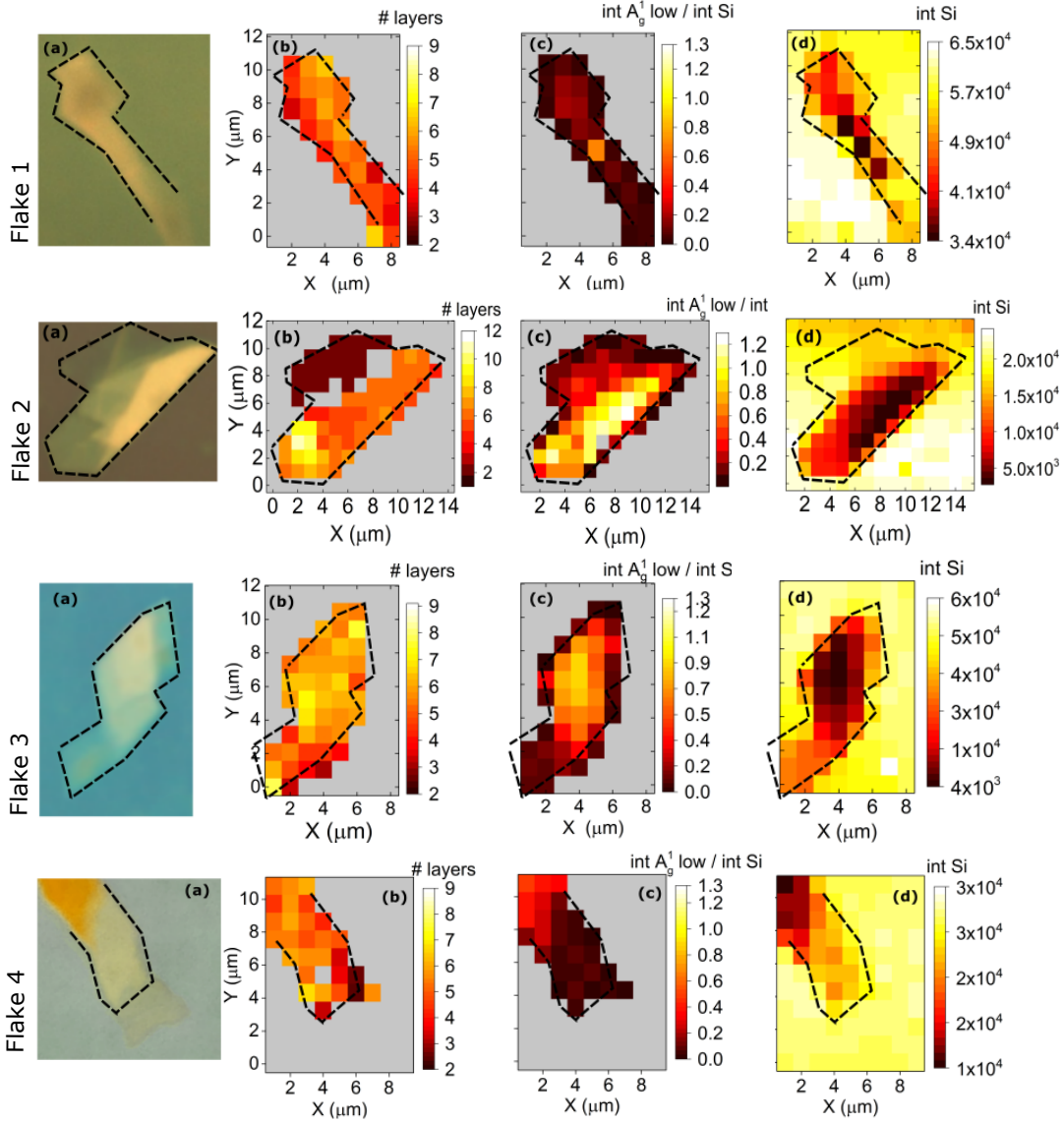
Figure 3.11: (a) Optical micrograph of the flakes, (b) calculated number of layers, (c) $A_g^1//\mathrm{Si}$ peak intensity ratio and (d) Si 520 cm^{-1} peak intensity for four different investigated flakes.

mode for the bilayer.

A change of the Raman mode frequencies in the surface layers of few-layer BP relative to the bulk has been predicted theoretically for bare BP [Hu 2016]. Calculations suggested a splitting of the mode frequencies for thicknesses starting from three layers (Fig. 3.15) for the A_g^1 and B_{2g} modes but not in the case of A_g^2 mode (Fig. 3.15). The calculated splitting of the B_{2g}
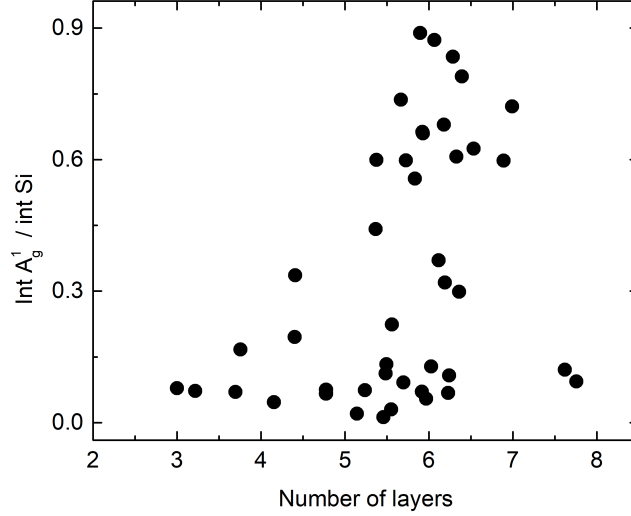
Figure 3.12: The intensity of the lower energetic A_g^1 component divided by the Si peak intensity as a function of the calculated number of layers for the third flake .

mode is very small, less than 1 cm^{-1} for 6 layers while the splitting of the A_g^1 mode is larger, on the order of 4-5 cm^{-1}. The effect is related to different motion of the atoms in the surface and inner layers. The intralayer interactions are predicted to be stronger in the surface layer and lead to higher frequency vibrations [Hu 2016].

This result is surprising since typically in a 2D layered material lower restoring forces and lower vibrational frequencies could be expected in the surface layer. The anomalous behaviour in BP can be explained considering the hybridization of the lone electron pairs between different layers. Charge transfer to the interlayer space causes an anomalous redshift of the A_g^1 mode in multi-layer BP compared to the monolayer [Hu 2016]. The optical phonon modes soften because of a weakening of the interaction between P atoms within the same layer. In the surface layer, the charge transfer from within the layer to the interlayer space is weaker, since there is only one neighbouring layer in contrast to two for the inner layers and more charge is conserved inside the layer. This leads to stronger bonding and higher phonon frequencies in surface layers [Hu 2016].

Based on these observations we suggest that the newly observed mode originates from the surface layers of BP which are in contact with the encapsulating h-BN while the low-energy component is related to the inner layers (Figure 3.16). The vibrational properties of the surface and inner layers differ and as a consequence the A_g^1 mode has slightly different energy for the surface and for the bulk. This could explain the absence of an additional mode in the bilayer, since there both layers are in contact with h-BN and should have identical vibrational properties, leading to the presence of only one peak. This interpretation is also in agreement with the observed decrease of relative intensity of the higher energetic mode with increasing
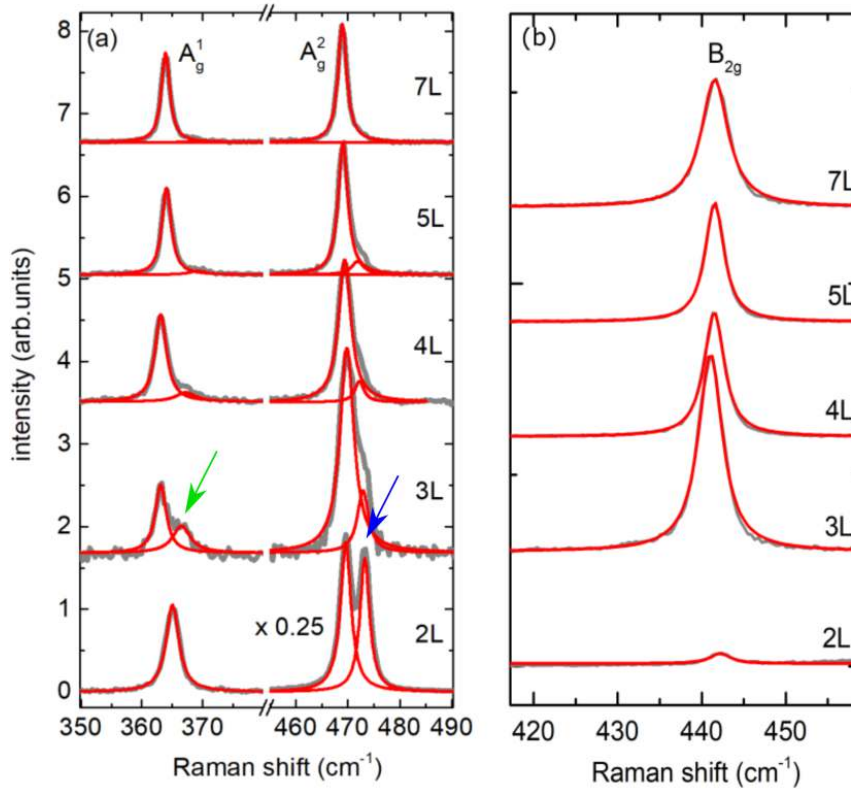
Figure 3.13: The (a) A_g^1 and A_g^2 and (b) B_{2g} modes as a function of the number of layers. Experimental data is shown in gray and the Lorentzian fits in red. The green arrow marks the newly observed mode, the blue arrow - the mode arising due to Davydov splitting.

thickness. For three layers, two layers are in contact with h-BN and one layer can be considered as an 'inner layer'. For larger thicknesses, the number of the 'inner' layers increases relative to the two 'surface' layers which explains the changes of the intensity ratio. Figure 3.16 shows a schematics of the encapsulated few-layer BP with marked surface and inner layers and the corresponding Raman peaks.

Not only the interlayer interaction, but also the changing lattice parameters can contribute to the changes of the vibrational frequencies with material thickness. Simulations predict a decrease of both the interlayer distance as well as the layer thickness (understood as the bond length of the puckered structure in the direction perpendicular to the plane) at the surface of non-encapsulated multi-layer black phosphorus [Hu 2016]. To verify this hypothesis and understand the influence of h-BN encapsulation on the structural properties of BP we have collaborated with the group of Magdalena Birowska and Neville Gonzalez-Szwacki from the Faculty of Physics, University of Warsaw who performed first-principles theoretical calculations of the structural and vibrational properties of few layer black phosphorus with and without encapsulation in boron nitride. The change of the lattice constants can be seen as equivalent to exerting external uniaxial stress [Hu 2016, Birowska 2019]. Calculations suggest that the
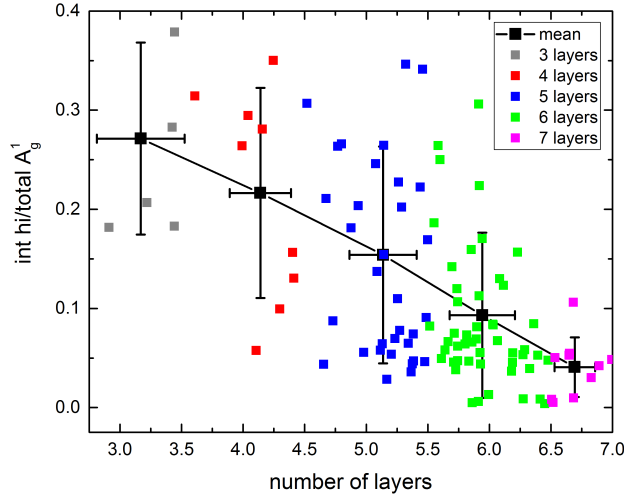
Figure 3.14: Intensity ratio of the high energy peak to the total intensity (sum of the high- and low-energy component intensities) for the A_g^1 mode as a function of the number or layers. The black points with error bars show mean values for each number of layers.
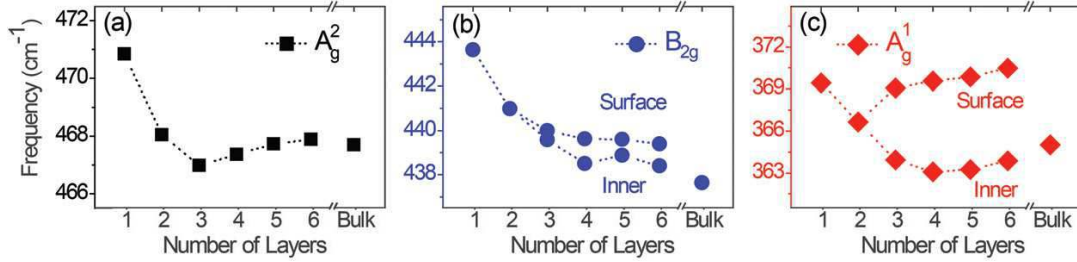
Figure 3.15: Raman peak frequencies as a function of the number of layers for the A_g^2, B_{2g} and A_g^1 modes showing the inner and surface branches. After [Hu 2016].

lattice constant along the zigzag direction increases while the lattice constant along the armchair direction decreases with the number of layers for bare black phosphorus [Birowska 2019]. For encapsulated BP, the lattice constant along the zigzag direction is larger than for bare material for all thicknesses and decreases slightly with the number of layers. The lattice constant along the armchair direction decreases with the number of layers for bare BP and shows only a slight change with thickness for encapsulated material [Birowska 2019]. As a consequence, h-BN encapsulation causes a decrease of the lattice constant in the armchair direction for a monolayer and an increase for larger thicknesses relative to bare material as can be seen in Fig. 3.17. The panels (a) and (b) show the lattice constant along the armchair and zigzag
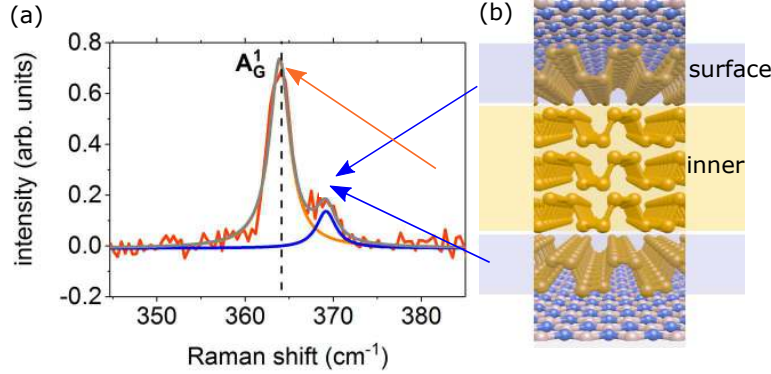
Figure 3.16: (a) Raman spectrum showing the high and low energy components of the A_g^1 mode and (b) schematics of the encapsulated BP crystal structure demonstrating the origin of the inner and surface modes observed in the spectrum.

direction for bare and encapsulated BP as a function of the number or layers, while the panels (c) and (d) show the strain along two different lattice directions. When h-BN and BP layers are in contact, the encapsulating h-BN is slightly compressed while the BP material is stretched with the exception for a monolayer in the armchair direction [Birowska 2019].

Figure 3.18 (a) shows the energies of the 'inner' and 'surface' A_g^1 mode as a function of the number of layers obtained from the Lorentzian fits to our data (red), as well as calculated energies based on [Hu 2016] (black) and [Birowska 2019] (green and blue) for bare and encapsulated BP. The error bars for the experimental points represent scattering of the values within a group of points assigned to a given number of layers. Theoretical calculations [Birowska 2019] suggest that encapsulations leads to a decrease of the energy of the modes. This is in contrast to what is observed experimentally based on the comparison of Raman spectra for bare and encapsulated BP. This can be explained considering the strain that can be introduced in BP placed on SiO_2/Si substrate which causes the redshift of the Raman modes [Birowska 2019]. The energy difference between the 'inner' and 'surface' modes is comparable for the experimental data and the different theoretical approaches. In panel (b), the relative positions and intensities are compared for our experimental data and the calculations for bare and encapsulated BP after [Birowska 2019]. The heights of the Lorentzians representing experimental data and of the bars showing calculated values have been normalized to the main A_g^1 component while the mode frequency has been shifted so that the frequency of the main peak corresponds to 0. Both theory and experiment show a decrease of the relative intensity of the higher to lower energy mode with increasing thickness. The calculated splitting in energy is slightly larger according to theory than the value based on experiment and slightly increases with the number of layers.

To confirm the surface-related origin of the newly observed mode, we should also exclude other possible reasons for its appearance in the spectra of few-layered black phosphorus. A mechanism that can lead to the observation of additional Raman modes for multi-layered 2D materials is Davydov splitting and mode conversion [Song 2016a, Staiger 2015, Gołasa 2017, Ribeiro 2018, Tonndorf 2013, Phaneuf-L'Heureux 2016]. In black phosphorus, Davydov mode conversion is the origin of the prominent peak that appears on the high energy side of the
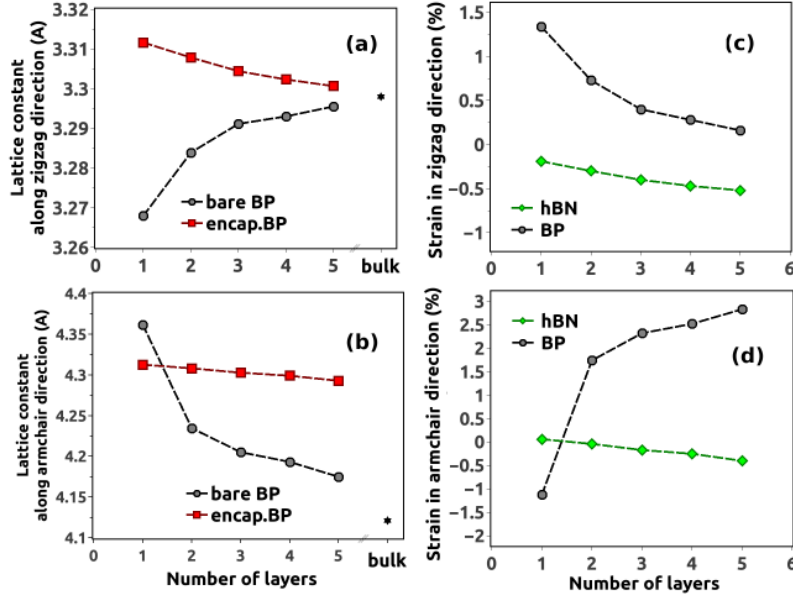
Figure 3.17: Changes of the lattice constant along the (a) zigzag and (b) armchair directions as a function of the number of layers calculated for bare and encapsulated BP, strain in (c) zigzag and (d) armchair directions as a function of the number of BP layers for encapsulated BP and encapsulating h-BN after [Birowska 2019].

A_g^2 mode for bilayer and thicker samples. Davydov mode conversion can be excluded as the origin of the new peak on the high energy side of the A_g^1 mode based on both theoretical and experimental evidence. Firstly, from the phonon dispersion for monolayer BP (Fig. 3.1) it can be seen that there is no IR active mode at energies close to the A_g^1 mode which could undergo Davydov conversion to a Raman active mode. Secondly, the presence of only two A_g^1 components regardless of the number of layers and their relatively unchanging positions are strong arguments against the Davydov splitting or mode conversion as the origin of the additional peak.

The presence of a mode on the high energy side of the A_g^1 peak has been reported in some previous studies. In the work of Phaneuf-L'Hereux et al. [Phaneuf-L'Heureux 2016] it was assigned to a second-order Raman process. Interestingly, in this work the mode was also observed for a monolayer flake, and no clear dependence of the intensity on the thickness could be observed. A splitting of the A_g^1 mode into 'two sharp components' has been observed by Favron et al., where the authors mentioned that this peak is present only sometimes and its appearance depends on the substrate and the preparation protocol and is possibly linked to local sample inhomogeneities [Favron 2015]. A recent work by Favron et al. [Favron 2018] identifies the origin of additional modes observed in the proximity of the A_g^1 and A_g^2 peaks as defect-activated second-order processes. However, the authors observe the additional mode on the high energy side of A_g^1 also for the bilayer and no systematic dependence of the relative mode intensity on thickness is observed, contrary to our observations. Moreover, in our case, we do not
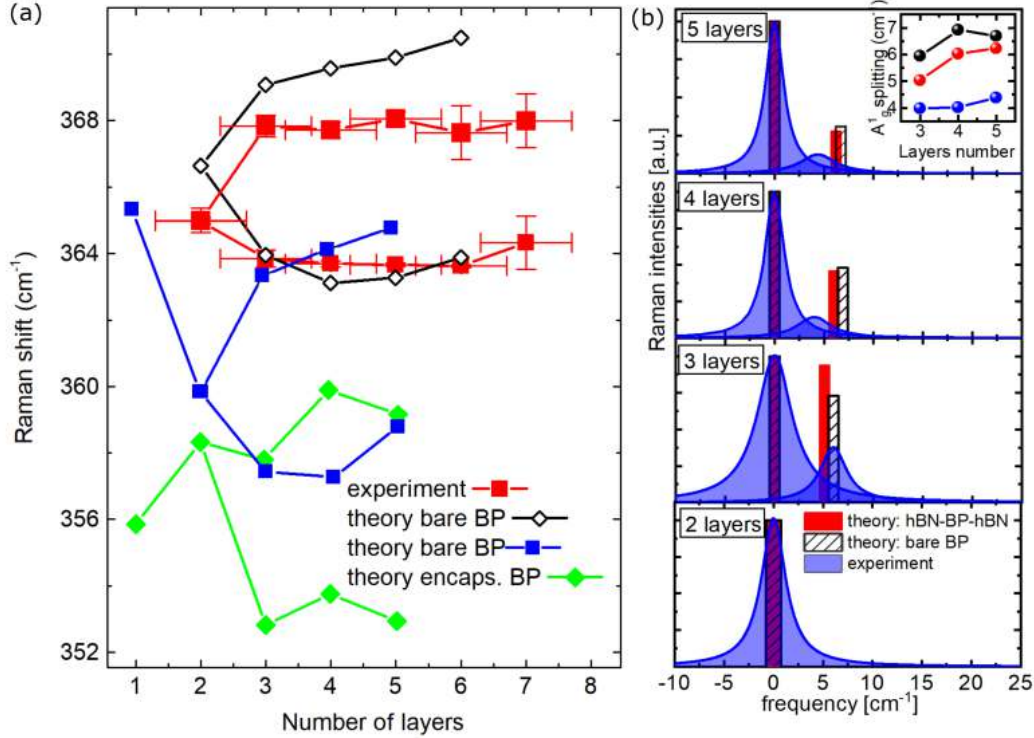
Figure 3.18: (a) Energies of the inner and surface branches of the A_g^1 vibration as a function of the number of layers based on averaged values obtained from our data (red) and theoretical predictions from [Hu 2016] (black) and [Birowska 2019] (blue - bare BP and green - h-BN encapsulated BP). (b) Relative intensity and splitting of the A_g^1 mode as a function of the number of layers based on our experimental data (Lorentzian peaks, the intensities are normalized to the main A_g^1 component, widths correspond to average peak FWHM, the frequency of the main component is set to 0) and calculations for bare (black bars) and encapsulated (red bars) BP. The inset shows the energy difference between the inner and surface peaks as a function of the number of layers. After [Birowska 2019].

expect a significant intensity of defect-related modes because of the absence of defects related to degradation in ambient conditions thanks to the protection of BP layers via encapsulation.

A splitting due to different vibrational frequencies in the inner and surface layers has been also predicted for the B_g^2 mode of BP [Hu 2016]. In contrast to the A_g^1 mode, the predicted splitting is very small, on the order of 1 cm^{-1}. In our experimental data, the B_g^2 mode shows little variation with thickness, apart from a strongly decreased relative intensity for the bilayer (Fig. 3.13). No splitting can be resolved, but the observed width of this mode is larger than for the A_g modes (Fig. 3.19). Thus, it is possible that a surface-inner mode splitting is also present for the B_g^2 mode but could not be resolved spectrally.

It is worth mentioning that the splitting of mode frequencies due to surface effects has been previously reported for few layered transition metal dichalcogenides [Terrones 2014], including MoTe$_2$ [Froehlicher 2015, Grzeszczyk 2018] and MoS$_2$ [Luo 2013b]. The surface effects in

these compounds refer to the changes of the metal-chalcogen bond length in the outer layers [Froehlicher 2015] and the larger force constants resulting from the lack of one neighboring adjacent layer for the topmost and bottommost layer [Luo 2013b]. The modes involving atomic vibrations in the exterior layers have higher energies than the modes related to the interior layers and the surface-related modes dominate for thinner TMD samples [Froehlicher 2015].

3.3.3 Effect of encapsulation on BP stability and Raman modes

Given the large number of Raman studies on few layer BP, it is surprising that the surface-bulk splitting of the A_g^1 mode has never been clearly observed before. A possible explanation is the influence of the encapsulation on the material quality. Figure 3.19 shows a comparison of the linewidths obtained from the fitting for the three Raman modes in our work and for non-encapsulated BP based on ref. [Phaneuf-L'Heureux 2016]. It can be seen that the linewidths observed by us are smaller, with the exception of the B_{2g} mode for the bilayer. For the bilayer however the B_{2g} intensity is very small and the FWHM could not be defined as precisely. Also in the work of Favron *et al.* [Favron 2015], the FWHMs reported are larger than observed by us, for A_g^1 mode decreasing from around 6 cm^{-1} for the monolayer to around 4 cm^{-1} for 6 layers.
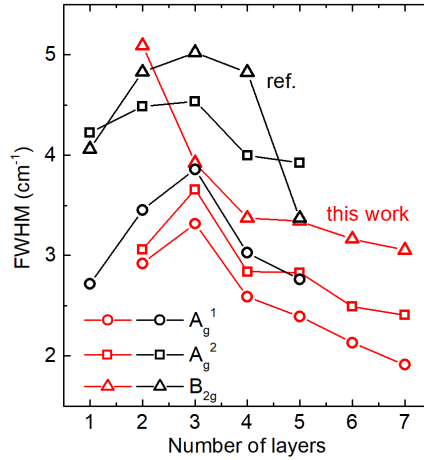
Figure 3.19: Full width at half maximum of the Raman modes as a function of the number of layers. Experimental data obtained in this work are shown in red, while the black points show values from ref. [Phaneuf-L'Heureux 2016].

The width of a Raman peak consists of contributions due to homogeneous and inhomogeneous broadening. Homogeneous broadening of a mode is related to finite natural phonon lifetime τ, $\Gamma = \hbar/\tau$ [Sun 2013]. Intrinsic (phonon-phonon) scattering due to the potential anharmonicity as well as extrinsic scattering related to defects or interfaces can reduce phonon lifetime [Luo 2015a]. Inhomogeous broadening is related for example to spatial variations across the sample, e.g. local degradation. The broadening is very small in the investigated samples, sug-

gesting a very good material homogeneity, low number of defects and no significant scattering on the h-BN/BP interface. This confirms the effective protective effect of h-BN.

To monitor the samples for possible signs of degradation we also performed Raman measurements on the same flake before and after a time of exposure to ambient conditions. During Raman mapping, the sample was exposed to ambient conditions for several hours, accompanied by laser irradiation The acquisition time on a given spot was several tens of seconds, the excitation power used was 630 μW. In between the measurements, the sample was kept for a week under N_2 atmosphere and then mapping of the same region under identical experimental conditions was repeated. Figure 3.20 shows spectra acquired on approximately the same positions on flake 2 for the two consecutive measurements and no significant difference can be noticed in peak width, position or relative intensity.
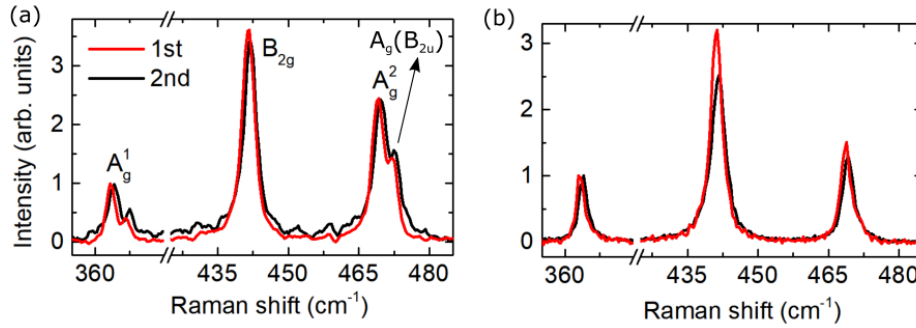
Figure 3.20: Typical Raman spectra acquired on a (a) thin and (b) thick region of flake 2 taken at the beginning of the measurements and after a week, including several hours of exposure to ambient conditions.

It is worth noting that we did not observe photoluminescence in the visible range from the encapsulated flakes. While this is not surprising for the thickest material, since the bulk BP has a bandgap of around 0.3 eV, PL emission could be expected to occur in the visible range for the thinner regions. Emission assigned as neutral and charged exciton has been previously observed in the 1.8 - 2 eV range for non-encapsulated ML BP under 532 nm excitation [Surrente 2016]. Zhang and coworkers observed exciton-related polarized photoluminescence above 1.3 eV, redshifting with increasing thickness [Zhang 2014]. A PL emission at around 1.6 eV, stronger than the Raman peaks has been observed for bilayer BP under 514 nm excitation [Castellanos-Gomez 2014]. PL emission for amorphous phosphorus is expected at energies of 1.18-1.36 eV and for chemically degraded material a peak appears around 2-2.1 eV [Castellanos-Gomez 2014]. However, according to the authors degradation was observed during the measurement which raises questions about the nature of the 1.6 eV emission [Castellanos-Gomez 2014]. A previous study by Cao *et al* found that photoluminescence was completely absent in h-BN encapsulated BP and significant PL intensity at around 1.65 eV was observed only for thin flakes of BP that have been exposed to air [Cao 2015]. The authors concluded that the disorder introduced upon degradation in air is necessary for the observation of PL emission. In light of this interpretation the lack of photoluminescence provides further proof for the effective protection of the BP layers. However, changes of the BP band structure

due to h-BN encapsulation, leading to the absence of luminescence, cannot be ruled out.

3.4 Conclusion

In this chapter we have presented a Raman spectroscopy study of h-BN encapsulated black phosphorus showing the influence of the encapsulating material on the vibrational properties of BP surface layers. For the first time, we have observed a theoretically predicted splitting of the A_g^1 mode into 'inner' and 'surface' branches for three-layer and thicker flakes. The change of the frequency of Raman modes in the surface layers can be explained via changes of both lattice parameters and of the intralayer coupling in the surface layers relative to the bulk. The increase of the vibrational frequencies for the surface layer confirms a theoretical prediction of stronger intralayer interactions in the surface layer [Hu 2016]. We also observe a narrowing of the Raman lines, a signature of reduced scattering and improved material quality. The results suggest that encapsulation, while being an effective means of protecting the material, can also have a significant influence on the material properties, especially for the thinnest samples.

Chapter 4

Non-equilibrium anisotropic excitons in ReS$_2$

Contents

This chapter presents optical studies of few-layer rhenium disulfide. The first part introduces the motivation for our study, the controversy concerning the nature of the bandgap. The following sections describe the determination of thickness and stacking order of the investigated samples using Raman spectroscopy together with the μ-reflectivity and μ-PL measurements performed to study the excitonic transitions. Based on these results we conclude that the observed photoluminescence is hot emission related to direct excitonic states. The last part of this chapter describes a kinetic model which can be used to explain the experimental observations and supports the conclusions about the indirect nature of the fundamental bandgap. The content of this chapter has been partially published in [Urban 2019].
'

4.1   Introduction

Contradicting experimental and theoretical results can be found in the literature concerning the nature of the fundamental bandgap of ReS$_2$. Our study of the photoluminescence properties of few-layer ReS$_2$ presented in this chapter was motivated by theoretical calculations of A. Kuc and coworkers from the group of Prof. T. Heine predicting the indirect character of the bandgap for all ReS$_2$ thicknesses apart from bilayer. The DFT calculations shown in Fig. 4.1 suggest a decrease of the direct gap at the Γ point from around 1.5 eV in monolayer to 1.2 eV for four layers, and the presence of a smaller indirect bandgap for all thicknesses apart from the bilayer. The indirect bandgap lies several tens of meV below the direct gap. In this work, we investigated the changes of the PL spectrum with the number of ReS$_2$ layers to verify the presence of the indirect to direct bandgap transition and the nature of the excitonic states which are the source of the PL emission.
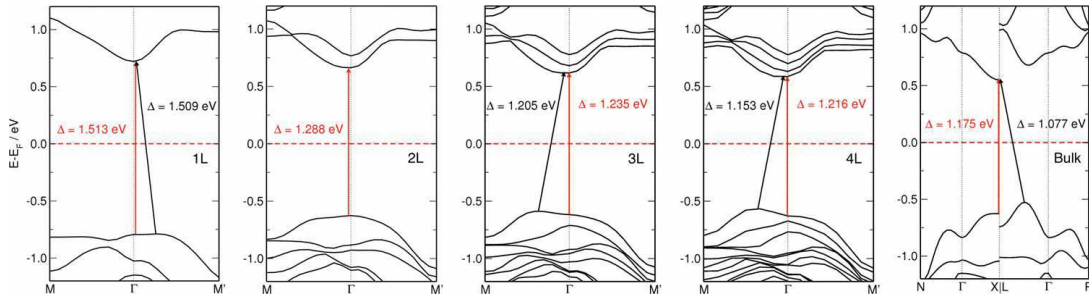
Figure 4.1: Calculated band structure for several layer ReS$_2$. The red arrows mark the direct bandgap, the black arrows the fundamental bandgap. After [Urban 2019].

4.2   Raman spectroscopy in ReS$_2$

Raman spectroscopy has been used to determine the stacking order and number of layers of the investigated ReS$_2$ flakes. The following section describes the Raman spectrum of ReS$_2$ and its characteristics useful for the determination of the number of layers.

Bulk and monolayer ReS$_2$ belongs to the C_i point group and triclinic crystal system [Wu 2019]. The units cell contains 4 rhenium and 8 sulphur atoms, 12 in total, which gives rise to 36 vibrational modes [Feng 2015]. In the center of the Brillouin zone there are 18 Raman-active A_g modes and 18 A_u modes [Wu 2019, Feng 2015]. The A_u modes include 15 infrared-active optical modes and 3 optically inactive acoustic modes. Due to low symmetry all the Raman-active and infrared-active modes are non-degenerate. All of the 18 first-order Raman modes have been previously observed experimentally [Feng 2015, Chenet 2015, Pradhan 2015]. Fig. 4.2 (a) and (b) shows the phonon dispersion for monolayer ReS$_2$ together with its Raman spectrum.

The first-order Raman-active modes can be observed in the 100-450 cm^{-1} range. The in-plane mode around 155 cm^{-1} which involves the vibrations of both Re and S atoms is labelled as A_g^1 [Pradhan 2015]. The atom displacements for this mode are shown in Fig. 4.2 (c). Two

other modes with distinct directions of vibrations, the out-of-plane modes above 400 cm^{-1} are labelled as A_g^2 and A_g^3. After previous work, we adopt a notation where the remaining modes involving vibrations of the atoms at different angles relative to the plane are numbered in the order of increasing frequency as A_g^i [McCreary 2017, Feng 2015, Pradhan 2015]. Fig. 4.2 (c) shows the atom displacements for the lowest energetic, A_g^4 mode, which has a predominantly out-of-plane character. Fig. 4.3 shows the typical Raman spectra measured on a thick ReS$_2$ flake for two different excitation wavelengths. The lower-energetic modes below 250 cm^{-1} are related mainly to vibrations involving the heavier Re atoms and the modes above 250 cm^{-1} are mainly related to vibrations of the lighter S atoms [Feng 2015].
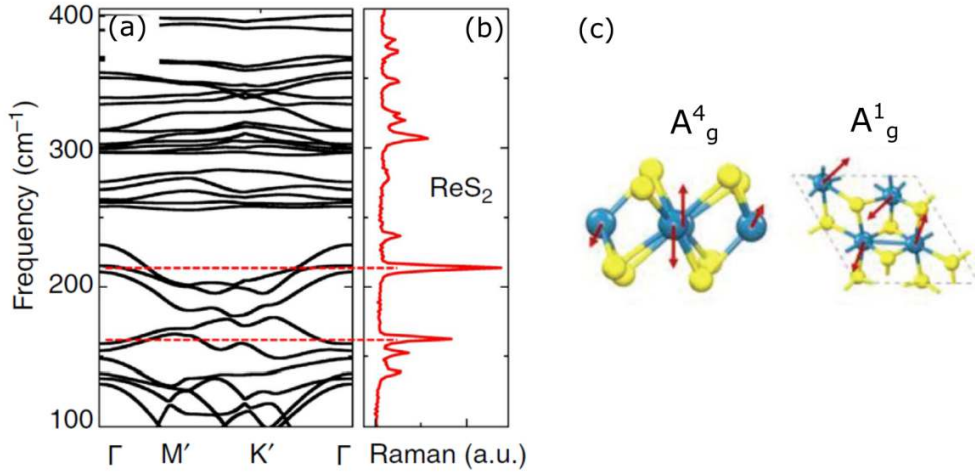
Figure 4.2: (a) Phonon dispersion for monolayer ReS$_2$ and (b) Raman spectrum measured on monolayer ReS$_2$ using 488 nm excitation. After [Tongay 2014]. (c) Atom displacements for the A$_g^1$ (in-plane) and A$_g^4$ (predominantly out-of-plane) modes. After [Qiao 2016].

The presence of low-frequency interlayer shear and breathing modes in the 5-50 cm^{-1} range confirms the non-negligible interlayer coupling in ReS$_2$ and the detailed studies of theses modes allowed the identification of two different polytypes with isotropic and anisotropic stacking order [Lorchat 2016, Nagler 2016, He 2016, Qiao 2016]. Fig. 4.4 shows the ultralow-frequency spectra of a monolayer and two differently stacked bilayer ReS$_2$ flakes. Three peaks could be assigned to interlayer modes due to their absence in the monolayer spectrum. Only one shear mode is observed for the isotropic (IS) stacking, while two nondegenerate peaks related to shear modes appear in the spectrum of the anisotropically (AI) stacked polytype. Some of the high-energy intralayer Raman modes also show changes in energy and intensity with the number of ReS$_2$ layers [Qiao 2016, McCreary 2017, Nagler 2016]. Fig. 4.5 (a) shows the evolution of the lowest-energetic Raman modes from monolayer to four layer ReS$_2$ and Fig. 4.5 (b) the energies of the modes as a function of the number of layers determined in the work of Chenet [Chenet 2015]. The first and third mode (A$_g^4$ and A$_g^1$) show opposite trends with increasing thickness and their relative separation decreases by 4 cm^{-1} from monolayer to bulk. Interestingly, Qiao and coworkers could identify two opposite trends for different investigated ReS$_2$ flakes, either an increase or decrease of the A$_g^4$ and A$_g^1$ mode separation with thickness
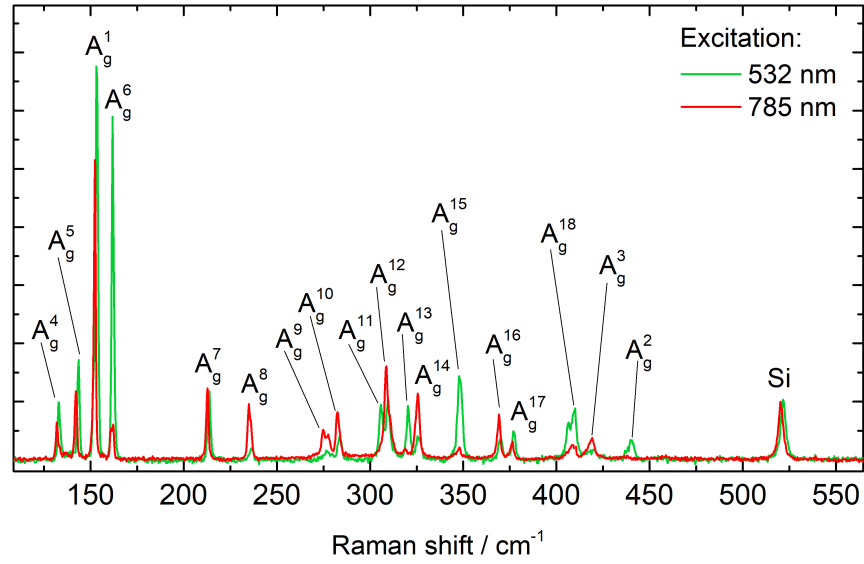
Figure 4.3: Our Raman spectra measured on a thick part of the investigated ReS$_2$ flake for 532 nm and 785 nm excitation. The mode assignment has been done according to [McCreary 2017].

(Fig. 4.4 (c)). Comparing the high- and low-frequency Raman spectra allowed correlating the difference in the behaviour of the high-energy modes with different stacking of the few-layer ReS$_2$. For the isotropic-like stacking, a blueshift of the A$_g^1$ mode and a redshift of the A$_g^4$ mode are observed for increasing thickness and an opposite trend is seen for anisotropically stacked flakes.
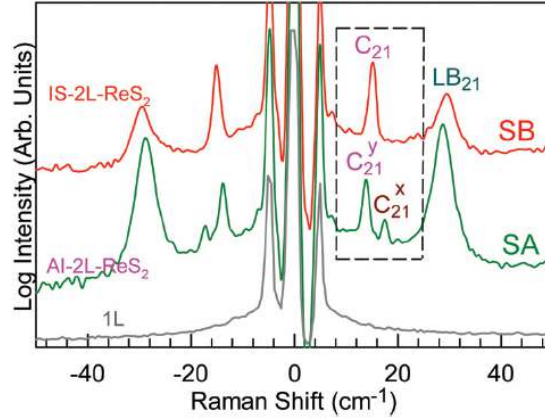
Figure 4.4: Raman spectra (showing the Stokes and anti-Stokes lines) of the isotropic and anisotropic bilayer polytype and monolayer ReS$_2$ in the ultralow-frequency range. C$_{21}$ are the shear modes and LB$_{21}$ the layer breathing modes. After [Qiao 2016].
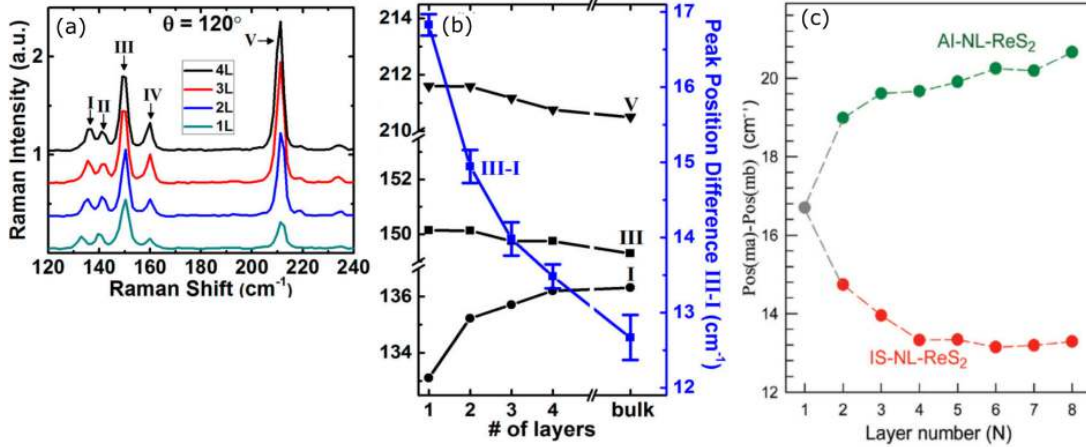
Figure 4.5: (a) Raman spectra for 1-4 layer thick ReS$_2$ showing the lowest-energetic modes after [Chenet 2015]. The peaks marked as I-IV correspond to the A_g^4 - A_g^6 modes, peak V to the A_g^7 mode. (b) Energies of the A_g^4 (peak I), A_g^1 (peak III) and A_g^7 (peak V) modes and the $E(A_g^1) - E(A_g^4)$ distance as a function of the number of layers [Chenet 2015]. (c) Relative shift between the A_g^1 and A_g^4 modes as a function of the number of layers for two different stacking polytypes: anisotropic (AI) and isotropic (IS). After [Qiao 2016].

4.3   Investigated samples

4.3.1   Sample preparation

We investigated mono- and few-layer ReS$_2$ flakes prepared by scotch tape exfoliation. The flakes were deposited on a substrate of degenerately doped Si covered with 270 nm of SiO$_2$. The samples were prepared in the group of Prof. Andras Kis at the Laboratory of Nanoscale Electronics and Structures at EPFL, Lausanne.

4.3.2   Raman characterization

Raman spectroscopy measurements were performed in the Institute of Physics, Polish Academy of Sciences in Warsaw in collaboration with Damian Włodarczyk and Prof. Andrzej Suchocki. The experimental setup is described in more detail in Chapter 2 and 3. $\mu-$Raman measurements were performed under ambient conditions at room temperature for an arbitrary orientation of the flakes relative to the polarization direction of the incident laser beam. Two different laser lines were used for excitation, 532 nm and 785 nm at powers of 630 μW and 1.7 mW, respectively. We first performed several measurements at different positions on one of the ReS$_2$ flakes using both excitation wavelengths to observe any dependence of the Raman spectrum on the flake thickness and excitation energy. Subsequently, we performed spatially-resolved Raman mapping over the area of several tens of μm using $\lambda_{exc} = 532$ nm on two different flakes. In our analysis, we focused on the four Raman modes in the 130-170 cm^{-1} range and fitted the spectra in this region using four Lorentzian peaks.

Figure 4.6 (a) shows Raman spectra acquired on different positions on the first investigated flake using 532 nm excitation in the 130-170 cm^{-1} spectral range where the four lowest-energetic modes A_g^4, A_g^5, A_g^1 and A_g^6 can be observed. The peak energies around 135 cm^{-1}, 143 cm^{-1}, 152 cm^{-1} and 162 cm^{-1} for the monolayer correspond well to previous studies [Qiao 2016]. An optical image of the flake is shown in figure 4.6 (c). Different optical contrast indicates changing thickness. The spectra acquired on different parts of the sample are numbered in panel (a) according to the points marked in (c). In panel (b), the schematics of the vibrational modes A_g^1 and A_g^4 after [McCreary 2017] are shown. The A_g^1 mode is predominantly in-plane, while for the A_g^4 mode the atoms move along different directions with both an in-plane and out-of-plane component.

For different positions on the sample, changes in the position and intensity of the peaks can be observed. The A_g^1 and A_g^4 modes shift in opposite directions with changing thickness and the A_g^5 mode shifts in the same direction as the A_g^1 mode. With increasing separation between the A_g^1 and A_g^4 peaks, an increase of the A_g^6 mode relative intensity can be observed. The A_g^6 mode shows no significant energy changes. The exact positions of the peaks were extracted from Lorentzian fits. The average values observed for the thickest part of the flake, 132.6 cm^{-1} and 153.4 cm^{-1} were used as mode energies for the bulk. The two left panels in Fig. 4.7 show maps of the shifts of the A_g^4 and A_g^1 mode energies from the bulk values. The right panel in Fig. 4.7 shows the energy difference between these two modes as a function of the position on the sample. The peak separation clearly increases from the thinnest to the thickest region of the sample.

Fig. 4.8 (a) shows the spectra acquired on regions with different thicknesses on the first flake and the fit of four Lorentzians and the energy difference between the modes A$_g^1$ and A$_g^4$ ΔE.
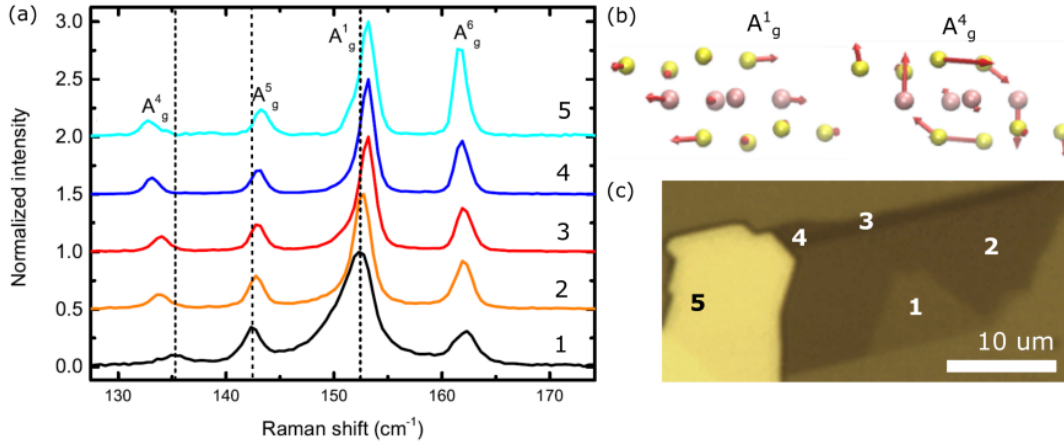
Figure 4.6: (a) Raman spectra acquired using 532 nm excitation on different positions on the ReS$_2$ flake showing the four characteristic peaks in the 130-170 cm^{-1} range. The spectra are normalized to the A_g^1 mode intensity. (b) Eigenvectors of the A_g^1 and A_g^4 Raman modes. Reproduced from [McCreary 2017]. (c) Optical image of the flake with marked positions where the spectra shown in panel (a) were acquired.
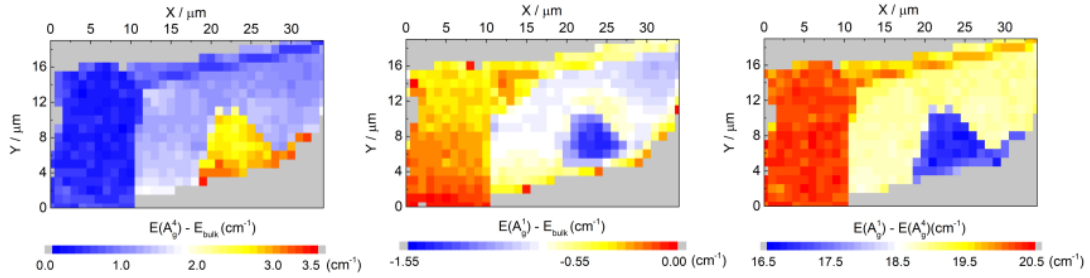
Figure 4.7: Raman maps of the flake shown in Fig. 4.6 (c) showing the shifts of the A_g^4 (left) and A_g^1 (middle) relative to the bulk values as well as the distance between these modes (right) as a function of the position on the sample.

ΔE was compared with the relative shift of the modes as a function of the number of layers determined by [Qiao 2016] for the anisotropic and isotropic ReS$_2$ polytype. The shift observed for spectra acquired on regions 1 and 2 of the sample (Fig. 4.6 (c)) corresponds very well to the shift for a monolayer and anisotropically stacked bilayer. Fig. 4.8 (b) shows ΔE as a function of the number of layers determined by [Qiao 2016] for the anisotropic and isotropic polytype together with data points obtained based on spectra acquired on different regions of the sample. For the larger thicknesses (> 2 layers) and ΔE the number of layers was assigned by comparing the observed shift with the dependence observed by [Qiao 2016]. An exponential function was fitted to the experimental data and based on this dependence the estimated number of layers was calculated for all the spectra from the Raman map. Fig. 4.8 (c) shows the shift of the A_g^1

and A_g^4 modes from the bulk value as a function of the calculated number of layers extracted from all the spectra from the Raman map of the first flake. Figure 4.9 shows the optical images of both mapped flakes and corresponding maps of the calculated number of layers. For both measured flakes the shifts of the modes indicated anisotropic stacking.

As an alternative method of determining the thickness, the optical contrast observed in microscopic images was calibrated with atomic force microscopy images for a flake containing different relevant thicknesses [Benameur 2011] and subsequently used to estimate the thickness of other investigated flakes. The regions 1 and 2 on the optical image were identified as mono- and bilayer using this method, which is consistent with the Raman results and confirms the thickness and polytype assignment.
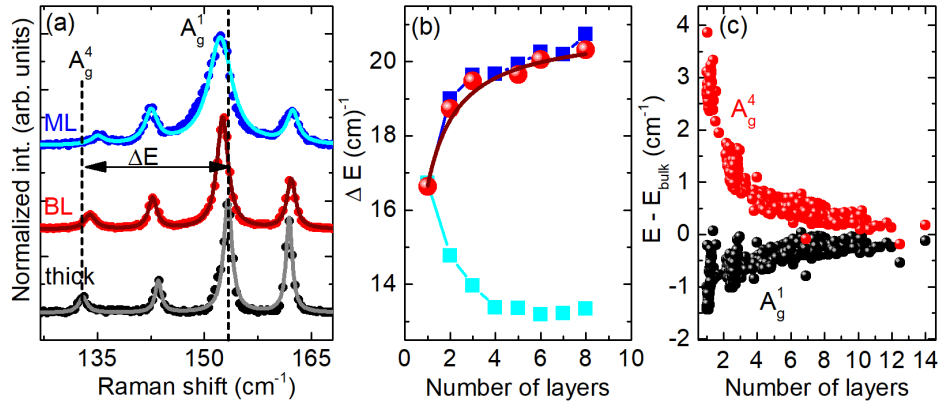
Figure 4.8: (a) Raman spectra showing the A_g^1 and A_g^4 mode for different thicknesses, (b) relative shift between the A_g^1 and A_g^4 peaks as a function of the number of layers for the isotropic (light blue) and anisotropic (dark blue) stacking order from ref. [Qiao 2016], experimental data points from this work (red) and a fitted exponential function (c) the shifts of the A_g^1 and A_g^4 peak energies from the bulk values as a function of the calculated number of layers based on the Raman map.

Fig. 4.10 shows the energy of the A_g^1 mode as a function of the energy of the A_g^4 mode. What can be clearly seen from the distribution of the data points for the mono- and bilayer is that while the averaged mode energies for a given number of layers show opposite trends with thickness, within the group of points for certain thickness a simultaneous blueshift of both peaks can be observed. This could be attributed for example to the effect of strain and can cause an error in the determination of ΔE since the shifts of the different modes under strain can be different. On the other hand, it could also be observed that the ratio of the intensities of the A_g^6 and A_g^1 mode is sensitive to materials thickness. In Fig. 4.10 (b), $I(A_g^6)/I(A_g^1)$ is shown as a function of ΔE. While ΔE shows some scattering within a group of points assigned to the mono- and bilayer, possibly due to the effects of strain, the intensity ratio shows smaller scatter and could potentially provide a more accurate measure of the number of layers. Fig. 4.10 (c) shows the intensity ratio as a function of the number of layers calculated based on ΔE and Fig.
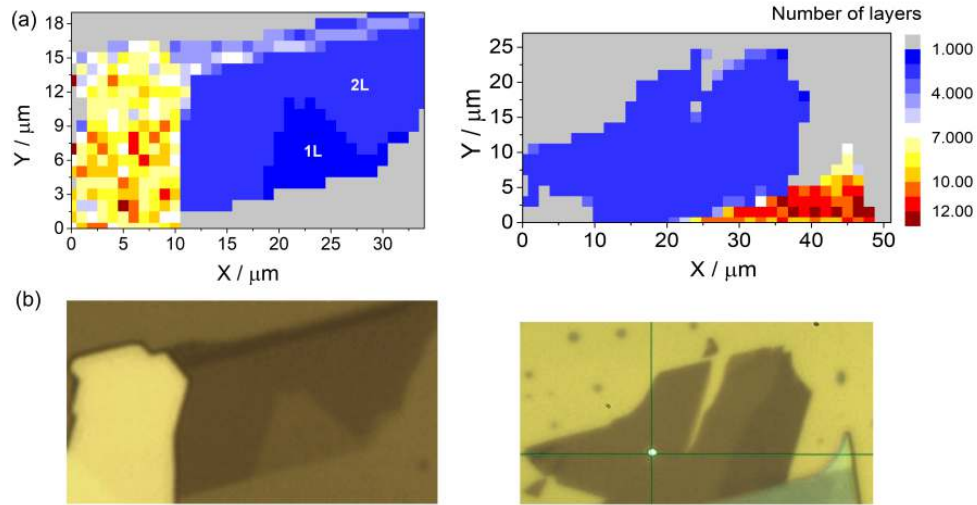
Figure 4.9: (a) Maps showing the calculated number of layers compared with (b) optical images of the flakes.

4.10 (d) the map of the intensity ratio. This could provide an alternative way of determining the material thickness, independent of local strain variations.

We compared Raman spectra measured at different excitation energies to verify if the estimation of the number of layers based on the relative shifts of the modes can be done independent of the excitation wavelength. Fig. 4.11 (a) shows the Raman spectra for a monolayer and thick flake measured for 532 nm and 785 nm excitation wavelength. The spectra are normalized to the A_g^1 mode intensity. Fig. 4.11 (b) shows the relative shifts of the modes obtained by [Qiao 2016] and determined by us for 532 nm and 785 nm excitation. The number of layers has been first determined for the 532 nm data and then the relative shift of the modes was determined for a spectrum measured on the same spot using $\lambda_{exc} = 785$ nm. ΔE is the same within the experimental error for both excitation energies, indicating that it is possible to use this method of thickness determination for different λ_{exc}. At the same time, significant differences in the relative intensities of some of the modes can be seen for different excitation energies, in agreement with what has been previously observed in other work for excitation wavelengths between 488 and 633 nm [Jariwala 2016, McCreary 2017]. This suggests that an assignment of the number of layers based on the relative peak intensity ratio can only be done for a defined λ_{exc}.
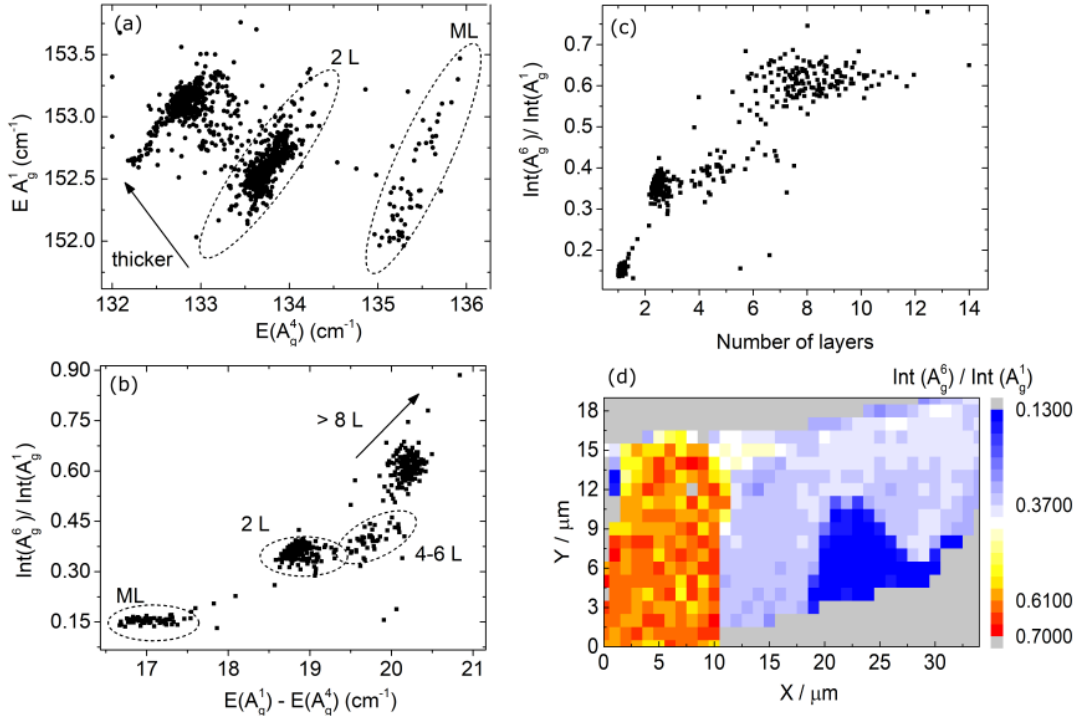
Figure 4.10: (a) Energy of the A_g^1 versus the energy of the A_g^4 mode with marked groups of points corresponding to the mono- and bilayer (b) Intensity ratio of the A_g^6 and A_g^1 mode as a function of the relative shift of the A_g^1 and A_g^4 mode. (c) The intensity ratio as a function of the calculated number of layers. (d) Map of the intensity ratio.

4.4 Photoluminescence and reflectivity studies of excitonic transitions in ReS$_2$

Photoluminescence and reflectivity contrast measurements were performed to identify the excitonic transitions and characterize the absorption and emission as a function of the detection and excitation linear polarization, the number of ReS$_2$ layers and temperature.

4.4.1   Reflectivity

The absorption edge of ReS$_2$ is strongly anisotropic. Strong optical dichroism [Ho 2007, Cui 2015] and anisotropy of the features related to the excitonic transitions [Aslan 2016, Arora 2017] have been observed using a variety of optical methods. A dependence of the band gap energy and the intensities of band-edge excitonic transitions on the crystal direction was observed in multiple studies using polarization resolved absorption [Ho 2007, Ho 1998, Liu 2016b, Liang 2009, Ho 1997, Arora 2017, Sim 2016], reflectivity [Ho 1997, Aslan 2016] as well as photo- and piezoreflectance [Ho 2002, Liang 2009, Ho 2004] and saturable and excited-state absorption [Cui 2017, Meng]. Transient absorption measurements showed the anisotropy
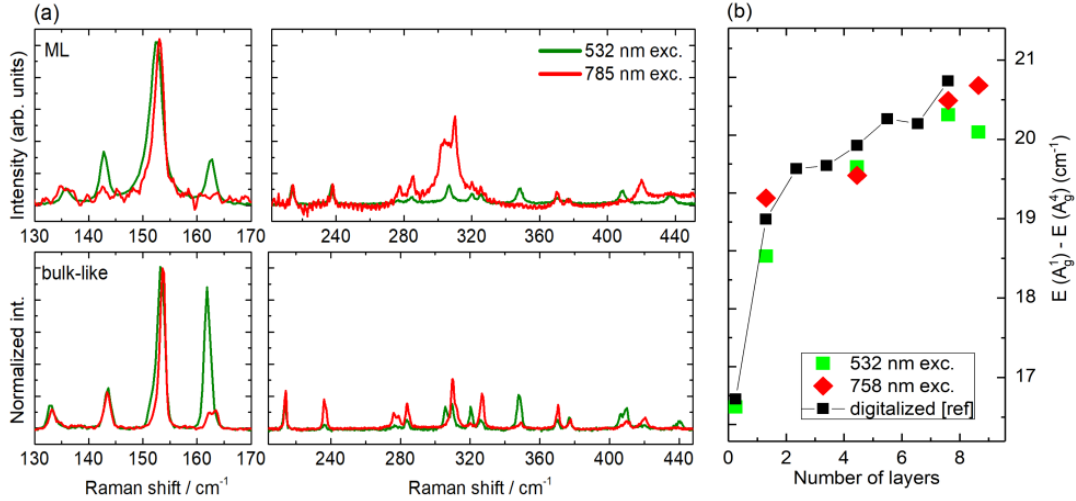
Figure 4.11: (a) Raman spectra for monolayer (top) and thick (bottom) flakes for different excitations wavelengths (b) Δ E for 532 nm, 785 nm excitation and after [Qiao 2016].

of both the absorption coefficient and transient behaviour [Cui 2015].

We have performed μ-reflectance measurements at the LNCMI Toulouse and in the Institute of Physics, Polish Academy of Sciences in Warsaw. The experimental setup is described in detail in Chapter 2. White unpolarized light from a tungsten-halogen lamp was used and a linear polarization analyzer was placed in the detection beam for polarization-resolved measurements. The sample was placed in a helium-flow cryostat equipped with translation stages. Reference spectra necessary to calculate the reflectivity contrast were acquired using the light reflected from the Si/SiO$_2$ substrate. In the case of polarization-resolved measurements, the reference spectrum was acquired for each polarization separately to compensate for artifacts related to the setup. All the reflectivity measurements presented in this section were performed on the thickest, bulk-like part of the ReS$_2$ flake.

Figure 4.12 (a) shows a typical unpolarized reflectivity contrast spectrum acquired at low temperature (10 K). The two lowest-lying X$_1$ and X$_2$ excitonic transitions can be identified at energies of around 1.55 eV and 1.57 eV. Two further transitions can be seen at higher energies, around 1.60 and 1.64 eV. Figure 4.12 (b) shows the derivative of the reflectivity contrast spectrum where the four transitions can be identified more clearly as minima as well as a weaker fifth transition around 1.69 eV.

Transitions energetically higher than the X$_1$ and X$_2$ transitions have been observed previously. Aslan and co-workers observed a third transition around 70 meV above the X$_2$ transition in bulk ReS$_2$ in reflectivity and PL which was interpreted as an excited excitonic state [Aslan 2016]. This transition possibly corresponds to the transition visible in Fig.4.12 (b) at around 1.6 eV. A dip in the reflectivity derivative above 1.6 eV, corresponding to the fourth transition observed by us, is also seen in the spectra presented by Aslan *et al.*, but not discussed further. Jadczak and coauthors observed four features at higher energies, in the 1.64 eV - 1.67 eV range, in PL and reflectivity contrast measurements, which were interpreted as the excited
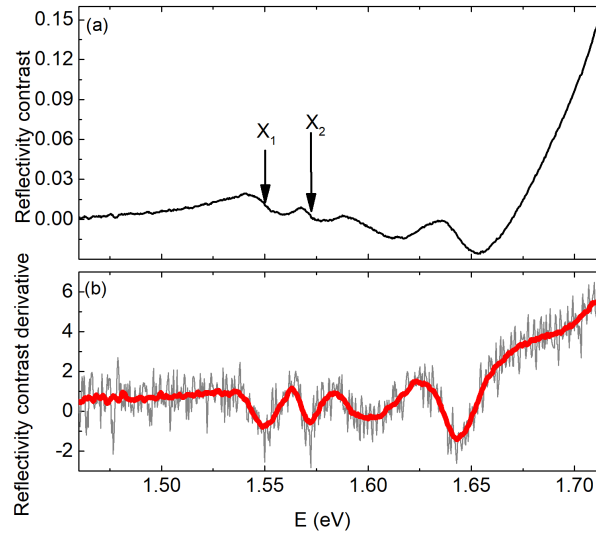
Figure 4.12: (a) Unpolarized reflectivity contrast spectrum measured on a thick ReS$_2$ flake. (b) Derivative of the reflectivity contrast calculated from the unpolarized spectrum (gray: raw data, red: smoothed).

states of both excitons X$_1$ and X$_2$ which follow the hydrogenic Rydberg series of energy levels [Jadczak 2019]. They suggested that the feature corresponding to the third transition observed by Aslan is a superposition of the X$_1$ and X$_2$ excited states. A similar series of features at higher energies were previously observed in photo- and piezoreflectance [Ho 2002, Liang 2009].

Fig. 4.13 shows a pseudo-color map of the reflectivity contrast derivative as a function of the linear polarization detection angle as well as two chosen curves for different linear polarization directions. The lowest energetic X$_1$ and X$_2$ transitions show clear linear polarization along different directions. The polarized spectra show the separation of the broad transitions around 1.60 eV and 1.64 eV into multiple features with maximum intensity at different polarization angles. The higher-energetic transitions are labelled as T_i with increasing transition energy. Two main polarization directions can be distinguished: T_3, T_5, T_7, T_9 features are linearly polarized along the same direction as the X$_1$ excitonic transition, while T_4, T_6 and T_8 show maximum intensity for the same polarization direction as X$_2$. Without further studies it is hard to conclude as to the origin of these transitions. In the work of Echeverry and coworkers [Echeverry 2018] the anisotropic optical absorption spectra were calculated based on solving the Bethe-Salpeter equation and absorption maxima corresponding to X$_1$, X$_2$, T_7 and T_8 energies observed by us have also been predicted. Linearly polarized interband excitonic transitions at higher energies have been observed previously in the 1.63-1.67 eV range in photoreflectance and interpreted as a Rydberg series of excited states [Ho 2002, Ho 2004, Liang 2009]. The energies of T_7 and T_8 and their energetic separation from X$_1$ and X$_2$ are consistent with the higher Rydberg states of X$_1$ and X$_2$ reported in these works, but the energies and spacings of the remaining features cannot be consistently explained within this model.

Reflectivity contrast spectra could be fitted using a Lorentzian oscillator model according
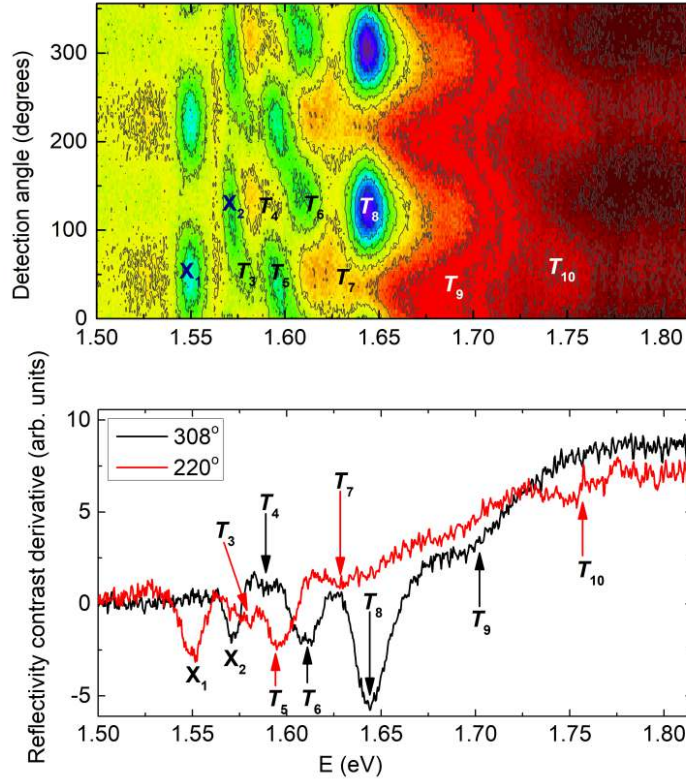
Figure 4.13: Pseudo-color map of reflectivity contrast derivative as a function of the detection polarization angle (top) and two representative curves (bottom) showing the reflectivity contrast derivative for different detection polarization directions with marked transitions identified as dip in the derivative curves.

to the formula [Korona 1996]:

$$R(E) = R_0 + \sum_x R_x \operatorname{Re}\left(\frac{hE_x - E + i\Gamma_x}{\Gamma_x^2 + (E - E_x)^2} e^{i\Theta} \right) \tag{4.1}$$

where R_x is an amplitude, E_x the energy, and Γ_x the broadening of the x-th excitonic transition, R_0 is the background and Θ is the phase factor. The spectra were fitted in the 1.525 - 1.635 eV range and transitions up to T_7 were included in the fit. The phase factor was fixed for all the transitions to reduce the number of fitting parameters. Energies and widths of the individual transitions were fitted for chosen spectra where the respective transition was the strongest and then fixed so that the final fitting was performed allowing only the offset and the amplitudes R_x to vary. Fig. 4.14 (a) shows the reflectivity contrast spectra acquired for different detection polarization angles and the fits. Fig. 4.14 (b) shows two exemplary spectra and fits and Fig. 4.14 (c) shows the intensities of the transitions as a function of the detection angle, defined as

the integrated moduli of the resonances:

$$A_X = \frac{R_X}{(E - E_X)^2 + \Gamma_X^2} \tag{4.2}$$

The polar plots were fitted with a function $I_0 + I_x \cos(\theta + \theta_0)$. The energies and polarization angles at which the maximum intensities of the six lowest energetic transitions are observed are listed in Table 4.1. The difference in orientation of the X$_1$ and X$_2$ transitions is $(64.1\pm0.9)°$, consistent with what has been observed previously for these excitonic features. The polarization directions obtained from the fit for the higher energetic transitions confirm the observation that two groups of transitions which have polarization directions close to those of X$_1$ and X$_2$ can be distinguished. The degree of linear polarization is 0.933 ± 0.007 for X$_1$ and 0.288 ± 0.007 for X$_2$.
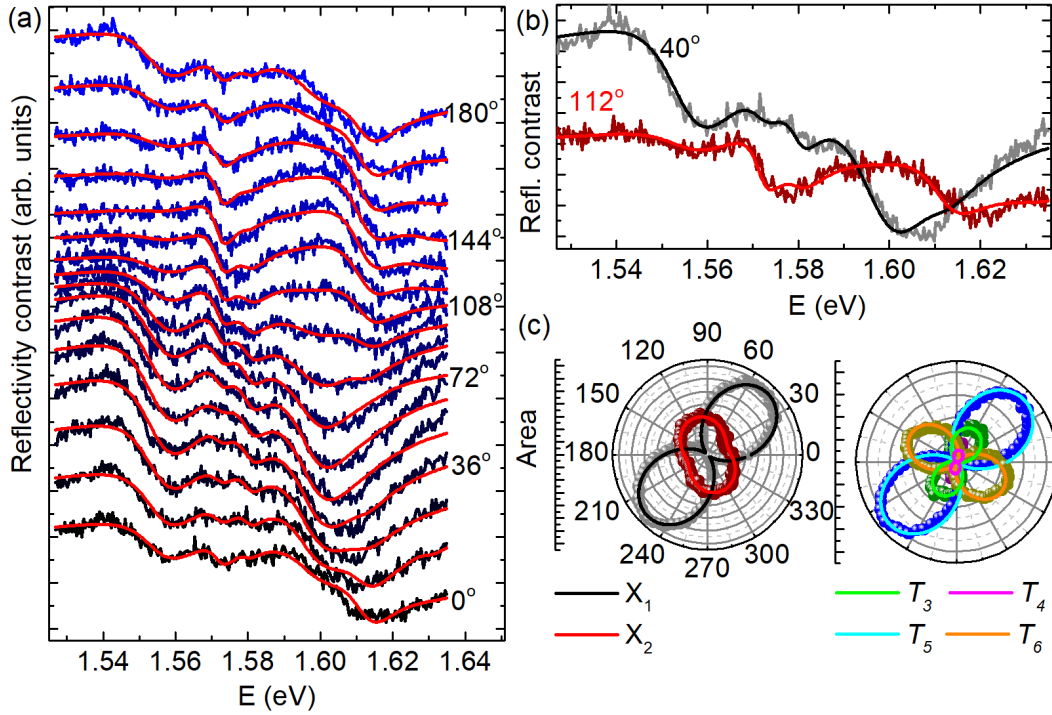
Figure 4.14: (a) Reflectivity contrast spectra for different detection polarization angles in the 0-180 ° range in 12° steps and fitted curves (red). (b) Two representative reflectivity contrast spectra and fitted curves for different polarization detection angles. (c) Polar plots showing the angular dependence of the intensity of the transitions.

Table 4.1: Energies of transitions observed in reflectivity contrast and linear polarization directions for which maximum transition intensities are observed.

	Energy (eV)	Polarization direction
X_1	1.555	45.7°
X_2	1.572	109.8°
T_3	1.58	61.8°
T_4	1.59	76.9°
T_5	1.5975	42.1°
T_6	1.612	148.8°

Measurements as a function of temperature were performed to determine the behaviour of the transitions with temperature. Fig. 4.15 (a) shows the reflectivity contrast spectra for a range of temperatures at which the excitonic transitions can be distinguished. Fig. 4.15 (b) shows the temperature dependence of the X_1 and X_2 transition energies.

The energies of the transitions at 0 K can be extrapolated as $E_{X1} = 1.557$ eV and $E_{X2} = 1.572$ eV and a redshift of around 7 meV can be seen for increasing temperature from 4.5 K to 100 K. Previous studies of temperature dependence of the absorption edges related to the indirect bandgap parallel and perpendicular to the rhenium chains have predicted a redshift of around 30 meV from 0 to 100 K for both polarizations with the shift slightly larger for the absorption edge for the polarization direction along the Re chains [Ho 1998]. The shift predicted based on fitting the temperature-dependent data for direct band-edge excitonic transitions for a larger range of temperatures in [Ho 2002] was around 13 meV from 0 to 100 K, larger than observed in this work. It is hard to exactly determine the energies of the broadened transitions which may partly explain the discrepancy.
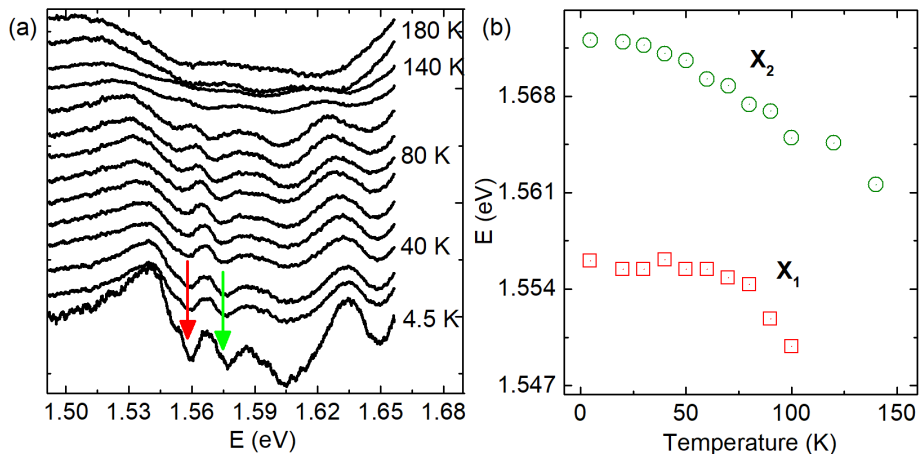
Figure 4.15: (a) Reflectivity contrast spectra as a function of temperature. Arrows indicate the X_1 and X_2 transitions. (b) Energies of the X_1 and X_2 transitions as a function of temperature.

Fig. 4.16 shows the reflectivity contrast spectrum measured at 4.5 K in the spectral range

corresponding to X$_1$ and X$_2$. For this lowest temperature, it can be seen that the two transitions in fact have a double nature and four transitions could be identified, X$_{11}$ at around 1.550 eV, X$_{12}$ at 1.558 eV, X$_{21}$ at 1.572 eV and X$_{22}$ at 1.576 eV. This fine structure could not be seen in the polarization-resolved measurements because of the coarser spectral resolution than the one used for the temperature dependent measurements. In the work of Arora *et al.* [Arora 2017], four excitonic transitions in the 1.372-1.404 eV range were identified in μ−transmission measurements for ReSe$_2$, two of them as distinctive features and the other two as lower-lying shoulders. They were interpreted as interband transitions with different combinations of spins, arising due to the twofold degeneracy of both the conduction and valence band. Bands with different spin are split by exchange interaction and the transitions with different combinations of spins have different energies. The energy difference between the spin-split transitions was around 10 meV in the studied case of ReSe$_2$. For ReS$_2$ a similar effect might be expected due to similar electronic structure, which could explain the observed double features.
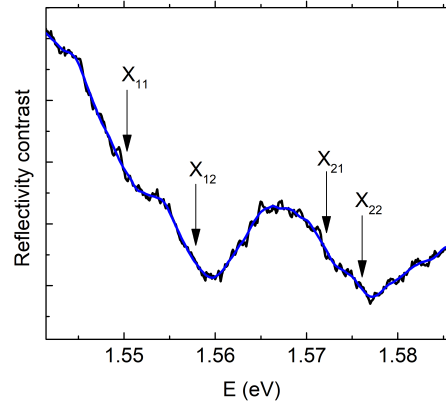
Figure 4.16: Reflectivity contrast spectrum for at 4.5 K (black) and the smoothed curve (blue). Arrows mark the areas of large slope of the curve corresponding to the approximate energy of the four spin-split transitions.

4.4.2 Photoluminescence

We have performed μ-PL measurements at LNCMI Toulouse. The setup is described in detail in Chapter 2. For excitation, the 532 nm line of a solid-state CW laser was used. The power used was in the 650-950 μW range and no changes in the spectral shape were noticed in this range. A half-waveplate and linear polarizer were used in the excitation or detection path for polarization-resolved measurements.

4.4.2.1 PL of bulk ReS$_2$

First, we characterized the PL emission from the thickest, bulk-like part of the flake at low temperature. Fig. 4.17 shows an unpolarized reflectivity contrast and photoluminescence spec-

trum of a thick ReS$_2$ flake at 4 K. The two lowest-lying excitonic transitions X$_1$ and X$_2$ can be identified in PL at energies of around 1.55 eV and 1.565 eV, with a Stokes shift of approximately 10 meV. The arrows mark the transitions in the PL spectrum, for the emission related to the X$_1$ excitonic state two close-lying maxima can be observed. This observation is in agreement with previous studies, where emission from the two ground state excitons as well as a transition at higher energy around 1.6 eV was reported [Aslan 2016, Tongay 2014, Gutiérrez-Lezama 2016, Ho 2017]. In the work of [Ho 2019] five transitions were identified, the two lowest-energetic X$_1$ and X$_2$ excitons as well as three transitions in the 1.62-1.66 eV range. It is hard to clearly identify higher-energetic transitions in our spectra due to the very broad shape of the emission.
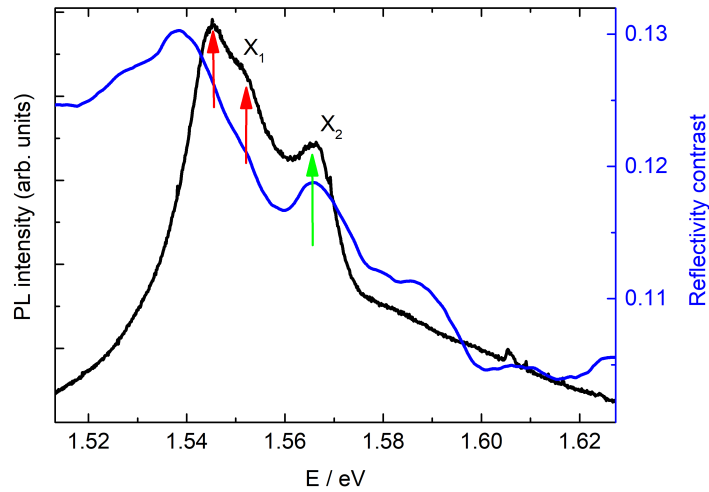
Figure 4.17: Unpolarized photoluminescence and reflectivity contrast spectra for a thick ReS$_2$ flake. Arrows mark the two peaks that can be distinguished in the X_1 emission and the X_2 emission peak.

Comparing absorption (or reflectivity) and photoluminescence spectra can provide information about the nature of the optical transitions. The observation of an indirect transition in absorption requires the presence of a phonon to compensate for the momentum mismatch. At low temperatures the population of thermally excited phonons in the crystal is very small and such a process is highly unlikely, therefore it is difficult to observe indirect transitions in low-temperature absorption or reflectivity spectra. The clear features observed in our reflectivity contrast spectra suggest the direct nature of the transitions.

Fig. 4.18 (a) shows the PL spectra of a thick flake measured for a fixed excitation polarization direction and different detection polarization directions. The X$_1$ and X$_2$ transitions can be clearly resolved in the polarization-resolved spectra, as shown in the pseudo-color PL intensity map in Fig. 4.18 (b). Maximum emission from the two direct states is observed for different detection angles. The two peaks which can be observed in the X$_1$ emission are polarized along the same crystal direction, consistent with what has been observed for the anisotropic

resonances in ReSe$_2$ [Arora 2017].
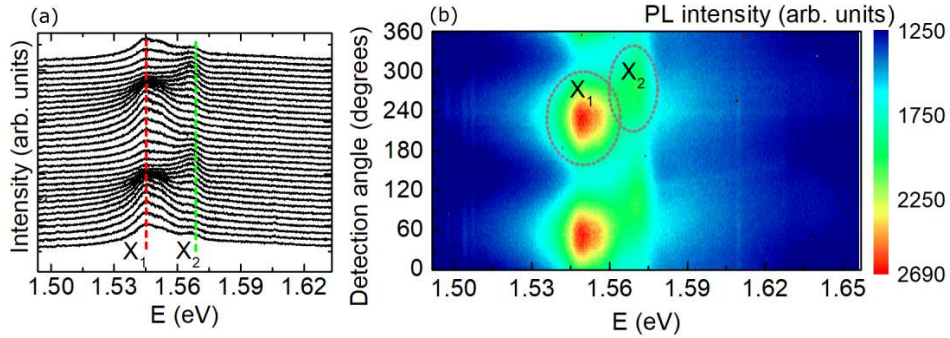
Figure 4.18: (a) Photoluminescence spectra of a thick ReS$_2$ flake for different polarization detection angles. The dashed lines mark the maxima of the X$_1$ and X$_2$ emissions. (b) Pseudo-color map of PL emission intensity as a function of energy and detection polarization angle.

The PL spectra were fitted with five Gaussian peaks, with the lowest energetic peak at 1.53 eV fit to the emission below X$_1$, possibly related to weak emission from the indirect states, two consequent peaks at 1.544 and 1.548 eV fit to the X$_1$ emission, a fourth peak at 1.567 eV fit to the X$_2$ emission and a broad peak centered at 1.569 eV used to fit the higher-energetic emission. The energies and widths of the peaks were fixed for all detection angles so only the peak intensity was allowed to vary. Fig. 4.19 (a) shows the spectra for two chosen detection angles and the fitted functions. Fig. 4.19 (b) shows the angular dependence of the X$_1$ and X$_2$ emission intensities, with X$_1$ as a sum of the two fitted peaks, and the $I_0 + I_x \cos(\theta + \theta_0)$ fits. Fig. 4.19 (c) shows the polar plot of the intensities of the two peaks used to fit the X$_1$ emission. The relative angle between the maxima of the X$_1$ and X$_2$ emission is $(67.5 \pm 0.2)°$ and the degree of linear polarization is 0.625 ± 0.002 for the X$_1$ and 0.457 ± 0.003 for the X$_2$ emission. This is similar to the polarization directions and degree of linear polarization observed for the X$_1$ and X$_2$ transitions in reflectivity. Peaks 2 and 3, related to the X$_1$ emission are linearly polarized along the same direction. The slight difference in the directions determined from the fit is possibly due to the overlap with other peaks. Fig. 4.20 shows two PL spectra for different detection angles where the double shape of the X$_1$ transition can be clearly seen. For X$_2$ any splitting is hard to distinguish due to lower intensity and overlap with X$_1$.

Fig. 4.21 (a) shows unpolarized PL spectra as a function of temperature. The changes of the spectral shape, in particular the slight increase of the X$_2$ to X$_1$ emission intensity ratio with increasing temperature are further discussed in the section describing the kinetics of the recombination processes. The emission peaks broaden and redshift with temperature. Fig. 4.21 (b) shows a comparison of the temperature dependence of the transitions seen in reflectivity and PL. Both the reflectivity features and the PL emission show a similar redshift with increasing temperature and the Stokes shift does not change significantly.

4.4.2.2   Thickness dependence

To investigate the evolution of the bandgap with the number of layers, we measured photo-luminescence spectra on different parts of the sample with different thickness. In particular,
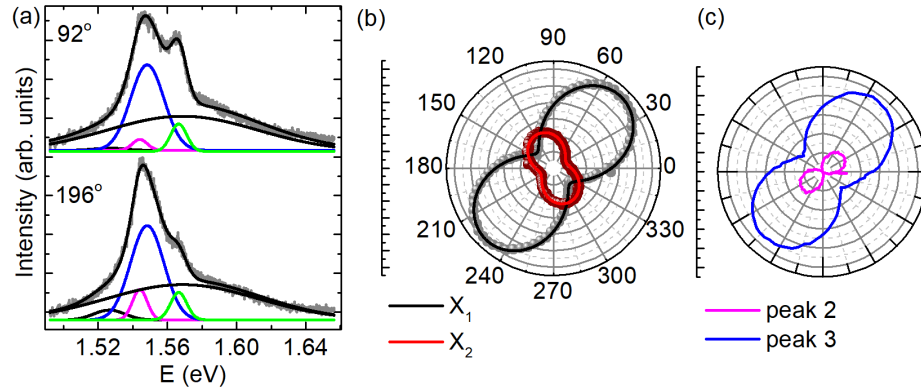
Figure 4.19: (a) Spectra for two different polarization detection angles and fits of the five peaks and the cumulative fit. Peak 1 and peak 2 (magenta and blue) correspond to the X$_1$ transition and peak 3 (green) to the X$_2$ transition. (b) Polar plot of the X$_1$ and X$_2$ transition intensities (X$_1$ intensity is a sum of the area of peak 1 and 2). (c) Polar plot of the intensity of peak 1 and peak 2 which correspond to the X$_1$ transition.
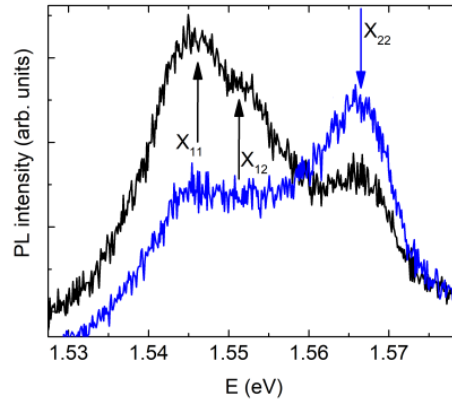
Figure 4.20: Photoluminescence spectra for two different polarization detection angles 0° (black) and 140° (blue). The arrows mark the approximate energies of the transitions.

we wanted to verify experimentally if a crossover from an indirect to a direct bandgap occurs for the bilayer, as predicted by DFT calculations. Fig. 4.22 (a) shows PL spectra acquired on regions with different thicknesses. A blueshift and decreasing intensity of the emission can be seen for decreasing thickness. Fig. 4.22 (b) shows the energies of the maxima of the X$_1$ and X$_2$ emissions and their relative separation as a function of the number of layers. For the bilayer, the emission was too weak to clearly identify the X$_2$ transition so the value was taken from [Aslan 2016]. The blueshift from bilayer to 8 layers is around 60 meV for X$_1$ and 100 meV for X$_2$.
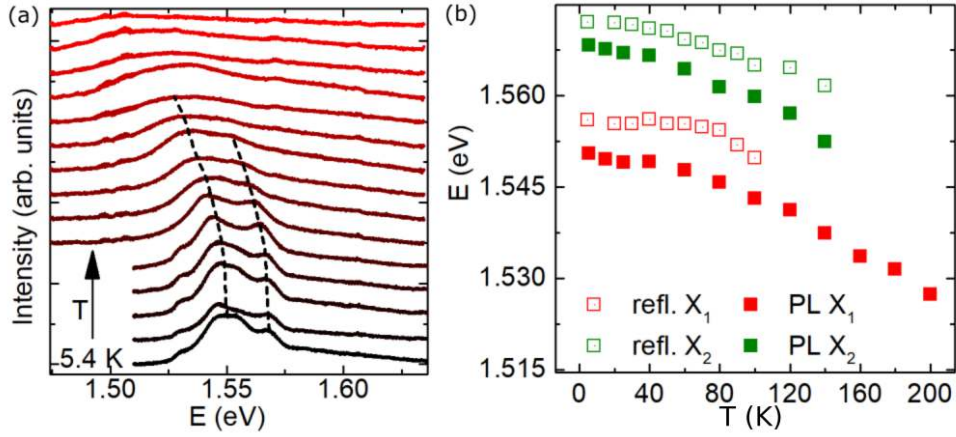
Figure 4.21: (a) PL spectra as a function of temperature from 5.4 K to 290 K. Dashed lines serve to guide the eye. (b) Energies of the maxima of the PL emission as a function of temperature. Empty symbols show the energies of transitions identified in reflectivity and full symbols the transitions seen in PL.

The relative separation of the emission peaks decreases from around 70 to 20 meV from bilayer to 8 layers. Our observation is in agreement with previous studies which have shown a monotonically decreasing PL intensity and blueshift of the PL emission with decreasing thickness [Tongay 2014, Aslan 2016, Cui 2016]. A blueshift of all excitonic PL features and decreasing intensity with decreasing thickness has also been observed for ReSe$_2$ [Arora 2017, Zhao 2015]. Aslan *et al.* reported blueshifts of 140, 170 and 300 meV for the X$_1$, X$_2$ and higher-energetic PL peaks with thickness changing from bulk to monolayer, which is larger than the shifts observed for direct transitions in other transition metal dichalcogenides (MoS$_2$, WS$_2$) but smaller than the shifts of the indirect transitions in these materials with thickness [Arora 2017]. This effect has been attributed to weaker electronic coupling and smaller exciton binding energy in ReS$_2$.

Fig. 4.23 (a) shows a map of the PL intensity integrated over the whole spectral range. A clear increase of the PL intensity with the number of layers can be seen. Fig. 4.23 (b) shows the integrated intensity as a function of the number of layers. The emission from the thickest region is around 13 times stronger than from the monolayer and the monotonic dependence suggests there is no change of the bandgap nature with thickness.

Polarization-resolved PL on bilayer and monolayer regions of the sample revealed linear polarization of the emission independent of thickness. Fig. 4.24 (a) shows the PL intensity as a function of the polarization detection angle for a bilayer flake. Fig. 4.24 (b) shows a polar plot of the PL intensity as a function of the detection angle, the intensity extracted from fitting single Gaussians to the X$_1$ and X$_2$ emissions. The angular separation of the X$_1$ and X$_2$ maxima is 69±1°. Figure 4.25 shows the map of PL emission intensity for monolayer ReS$_2$. The map shows the spectral region corresponding to X$_1$ emission. The emission for X$_2$ was too weak to be clearly observed. The emission is linearly polarized and has maximum intensity around 1.6 eV. This results confirm previous observations of a linear polarization of the emission for a range of thicknesses [Zhao 2015, Aslan 2016]. In the work of Aslan, the
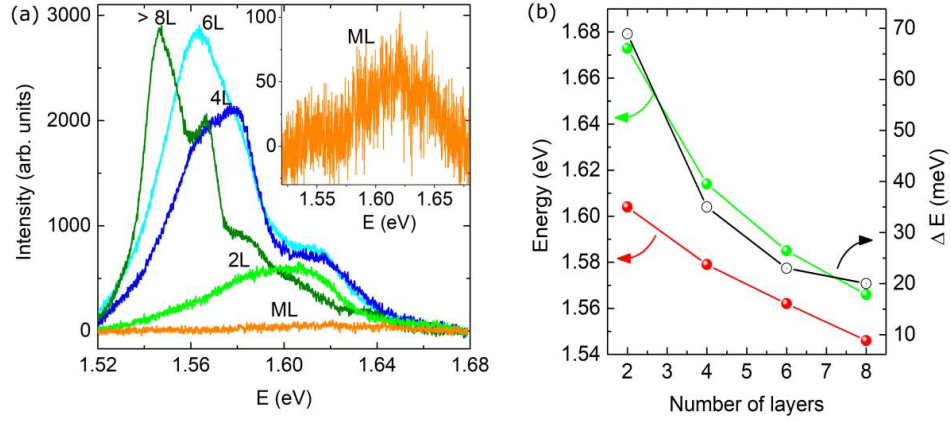
Figure 4.22: (a) PL spectra for different thicknesses of ReS$_2$. (b) The energies of the maxima of the X$_1$ and X$_2$ emissions and their relative energetic separation as a function of the number of layers.
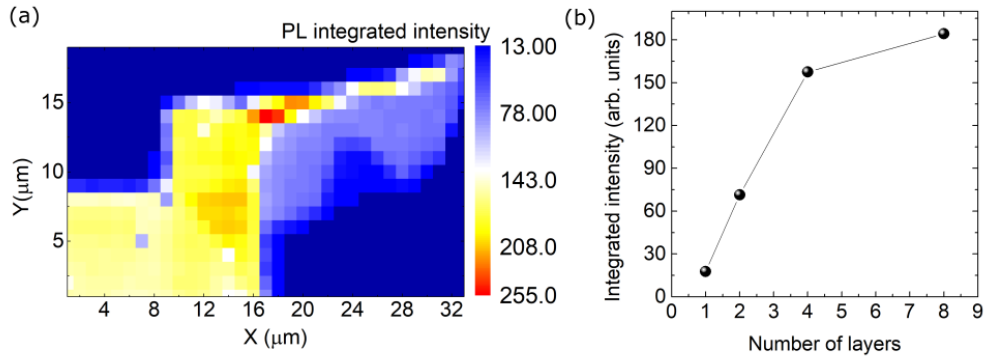
Figure 4.23: (a) Integrated PL intensity in the whole measured spectra range as a function of spatial position. (b) Integrated PL intensity as a function of the number of layers.

orientation of the X$_1$ emission relative to the Re-Re chain direction was observed to remain the same from monolayer to bulk, while the angle between this crystal direction and the direction of maximum X$_2$ emission increased from around 50° for the monolayer to almost 90° for bulk. In our case, the relative orientation of X$_1$ and X$_2$ remains the same for bulk and bilayer.

4.4.2.3 Effect of excitation polarization

Due to the strong absorption anisotropy, we expect the photoluminescence emission intensity to strongly depend on the excitation polarization. Fig. 4.26 (a) and (b) show maps of the PL emission intensity as a function of the excitation polarization direction for two different detection polarization directions maximizing the X$_1$ or X$_2$ emission measured on the thickest
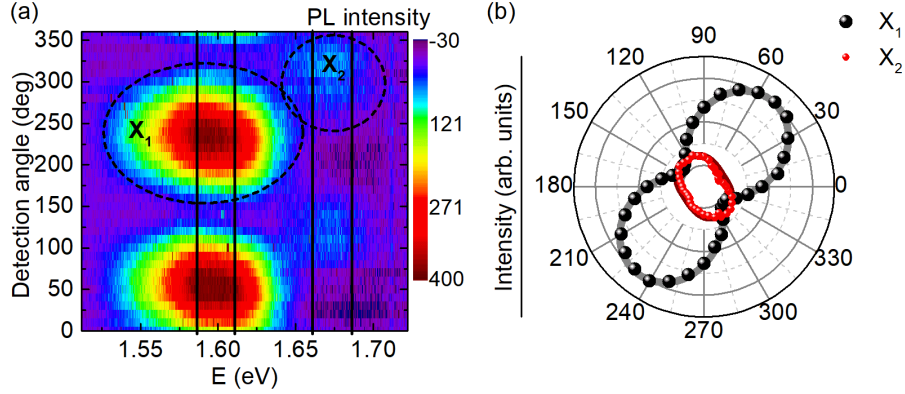
Figure 4.24: Pseudo-color map of PL emission intensity for bilayer ReS$_2$ in the spectral region corresponding to X$_1$ and X$_2$ emission as a function of the detection angle and (b) polar plot of the intensity.
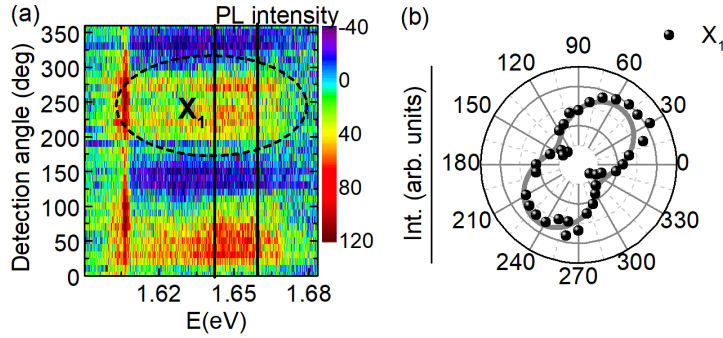
Figure 4.25: (a) Pseudo-color map of PL emission intensity for monolayer ReS$_2$ in the spectral region corresponding to X$_1$ emission as a function of the detection angle and (b) polar plot of the emission intensity, integrated in the spectral region indicated by the straight lines in panel (a), as a function of detection angle.

part of the flake. The intensity changes depending on the excitation polarization direction. Emission at higher energies, in the 1.58 - 1.62 eV range which follows the same polarization dependence as the X$_1$ and X$_2$ peaks can be observed as a broadened feature in the spectra where detection is set to maximize X$_1$ emission and as a series of distinct lines for the other detection polarization. This emission most probably originates from excited excitonic states [Jadczak 2019, Ho 2002].

Fig. 4.27 shows spectra for perpendicular excitation polarization directions for a detection angle maximizing (a) the X$_1$ and (b) the X$_2$ emission after subtraction of linear background. The relative variation of the X$_1$ emission intensity is much stronger than for X$_2$ and the higher-energetic transitions can be better resolved in the detection configuration maximizing X$_2$ emission. Fig. 4.28 shows the same set of spectra normalized to the maximum intensity
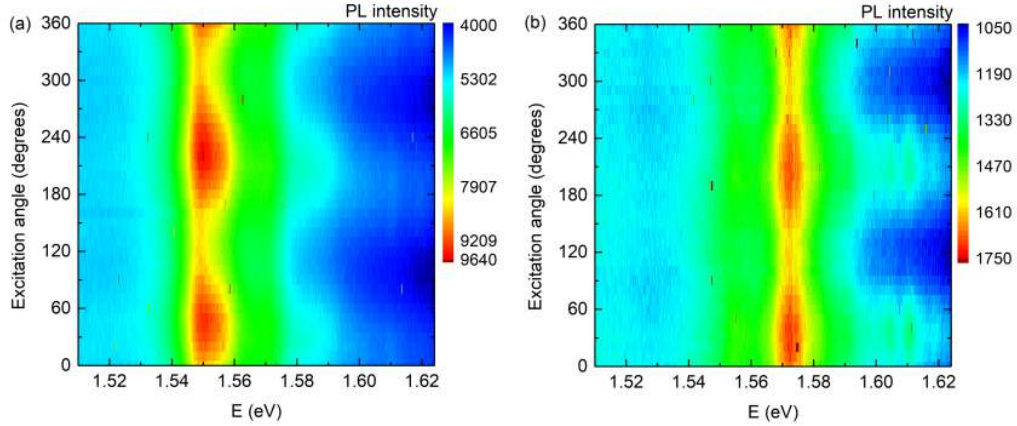
Figure 4.26: Pseudo-color maps of polarization intensity as a function of the excitation angle for the detection angle corresponding to (a) maximum of the emission for X_1 and (b) maximum of the emission of X_2.

to demonstrate changes of the spectral shape. For both detection polarizations the X_1 emission seems slightly blueshifted for the 230° excitation polarization. The X_3 emission is also stronger for this excitation polarization direction. Based on this measurement alone it hard do conclude on the nature of this effect, but the changes in spectral shape, i.e. the apparent blueshift of the X_1 peak could be related to a larger intensity of one of the peak components due to optical alignment of spin-split excitonic sublevels by the linearly polarized excitation beam [Ivchenko 1995]. The stronger changes of the X_1 emission intensity in response to the polarization direction as compared to X_2 could be understood considering the different relaxation mechanisms within the framework of the kinetic model which is discussed in the following section.

4.5 Kinetic model

To describe our results in a quantitative way and explain the nature of the observed PL emission, we propose a kinetic model describing the generation, scattering and recombination of excitons in the X_1 and X_2 states. We calculate the number of excitons in both direct states and the radiative recombination probabilities in the presence and absence of a lower-lying state related to the indirect bandgap.

4.5.1 Direct versus indirect bandgap model

A schematic of the excitonic states is shown in Fig. 4.29. Two direct excitonic states X_1 and X_2 lie above a state X_I related to an indirect bandgap. The presence of a smaller, indirect bandgap has been, as described previously, suggested by experimental studies of the absorption edge [Ho 1998] and photoacoustic and modulated reflectance measurements which defined its
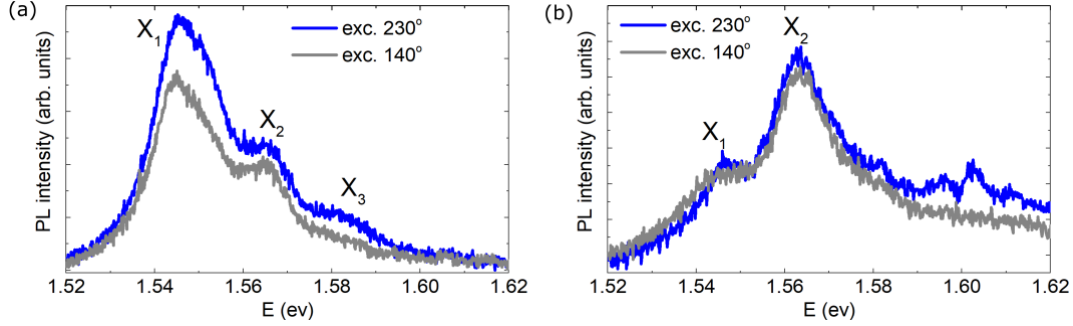
Figure 4.27: (a) Spectra taken at excitation angles corresponding to the minimum and maximum intensity of X$_1$ for a detection angle maximizing the X$_1$ emission. (b) Spectra taken at excitation angles corresponding to the minimum and maximum intensity of X$_1$ for a detection angle maximizing the X$_2$ emission.
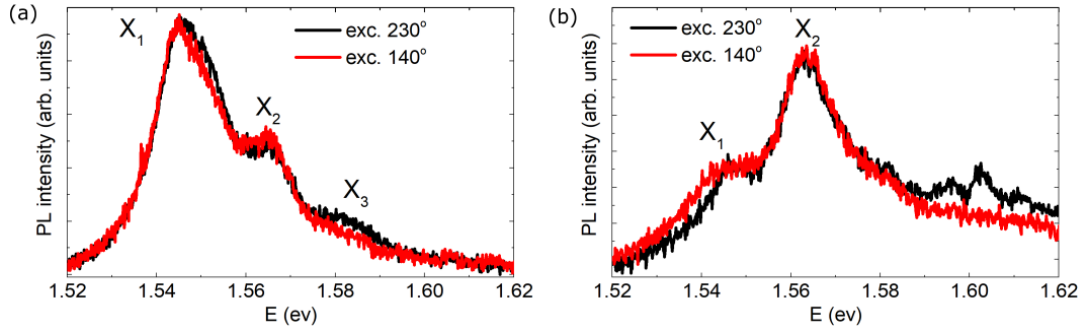
Figure 4.28: (a) Normalized spectra taken at excitation angles corresponding to the minimum and maximum intensity of X$_1$ for a detection angle maximizing the X$_1$ emission. (b) Normalized spectra taken at excitation angles corresponding to the minimum and maximum intensity of X$_1$ for a detection angle maximizing the X$_2$ emission.

energy as 180 meV smaller than that of the direct gap for bulk ReS$_2$ [Zelewski 2017]. DFT calculations by A. Kuc and coworkers [Urban 2017] also suggested the presence of an indirect bandgap around 100 meV below the direct gap in bulk.

Under optical CW excitation, excitons are created with a generation rate g in the two higher, direct excitonic states. We assume the generation rate to be the same for X_1 and X_2. An exciton in the X_2 state can decay via radiative recombination, described by a time constant τ_r as well as scatter to the lower-lying direct state X_1 with a time constant τ_X or to the indirect state with a time constant τ_s. An exciton in the X_1 state can also decay radiatively or scatter to the indirect state. The rates of these two processes are assumed to be the same for excitons in state X_1 and X_2 and no scattering from the lower to the higher direct state is considered, which is a valid assumption at 4 K where the energy difference between the states is larger than $k_B T$. Recombination from the indirect state occurs with a time constant τ_I.
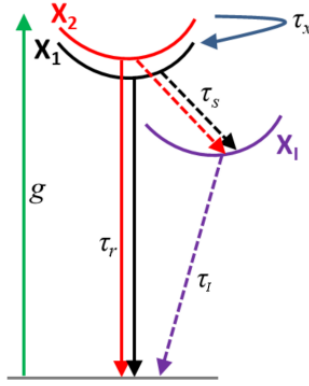
Figure 4.29: The proposed model of the excitonic states. X_1 and X_2 are the direct excitonic states and X_I is the excitonic state related to the indirect bandgap.

We can describe the generation and decay processes in terms of rate equations describing the changes of the exciton population in the three states, N_1, N_2 and N_I.

$$\begin{cases} \dfrac{\mathrm{d}N_2}{\mathrm{d}t} = -\dfrac{1}{\tau_s}N_2 - \dfrac{1}{\tau_x}N_2 - \dfrac{1}{\tau_r}N_2 + g \\[3mm] \dfrac{\mathrm{d}N_1}{\mathrm{d}t} = -\dfrac{1}{\tau_s}N_1 + \dfrac{1}{\tau_x}N_2 - \dfrac{1}{\tau_r}N_1 + g \\[3mm] \dfrac{\mathrm{d}N_I}{\mathrm{d}t} = \dfrac{1}{\tau_s}N_1 + \dfrac{1}{\tau_s}N_2 - \dfrac{1}{\tau_{nr}}N_I \end{cases} \tag{4.3}$$

$1/\tau_s$ corresponds to the scattering rate from X_1 and X_2 to X_I, $1/\tau_x$ to the scattering rate between the direct excitonic states, $1/\tau_r$ to the radiative recombination rate and $1/\tau_I$ describes the recombination of the excitons in the indirect state. We can easily solve the equations assuming a steady state is reached under CW excitation, i.e. $\dfrac{\mathrm{d}N_2}{\mathrm{d}t} = \dfrac{\mathrm{d}N_1}{\mathrm{d}t} = \dfrac{\mathrm{d}N_I}{\mathrm{d}t} = 0$. This allows us to obtain relations between the number of excitons in the different states as a function of the decay rates:

$$\frac{N_1}{N_2} = \frac{\dfrac{2}{\tau_x} + \dfrac{1}{\tau_s} + \dfrac{1}{\tau_r}}{\dfrac{1}{\tau_s} + \dfrac{1}{\tau_r}} \tag{4.4}$$

$$\frac{N_I}{N_2} = \frac{\tau_{nr}}{\tau_s}\left(1 + \frac{\dfrac{2}{\tau_x} + \dfrac{1}{\tau_s} + \dfrac{1}{\tau_r}}{\dfrac{1}{\tau_s} + \dfrac{1}{\tau_r}}\right) \tag{4.5}$$

It is convenient to write these equations as a function of only the ratios of the different decay times τ_r/τ_x and τ_x/τ_s, so that conclusions can be reached without making assuptions

about their exact values:

$$\frac{N_1}{N_2} = \frac{\dfrac{\tau_r}{\tau_x}\left(2 + \dfrac{\tau_x}{\tau_s}\right) + 1}{\dfrac{\tau_r}{\tau_s} + 1} \tag{4.6}$$

$$\frac{N_I}{N_2} = \frac{\tau_{nr}}{\tau_s}\left(1 + \frac{\dfrac{\tau_r}{\tau_x}\left(2 + \dfrac{\tau_x}{\tau_s}\right) + 1}{\dfrac{\tau_r}{\tau_x}\dfrac{\tau_x}{\tau_s} + 1}\right) \tag{4.7}$$

The observed PL intensity depends on the number of excitons in a given state as well as on the probability of the radiative recombination from this state. The recombination probability is expressed as the ratio of the radiative recombination rate to the sum of the rates of all possible recombination processes. The expected intensity ratio of the PL emission from X_1 and X_2 states is proportional to the ratio of the emission probabilities from these states P_1 and P_2:

$$\frac{I_1}{I_2} = \frac{N_1}{N_2} \cdot \frac{P_1}{P_2} \tag{4.8}$$

The ratio of these probabilities can again be expressed in terms of the ratios of the decay times:

$$\frac{P_1}{P_2} = 1 + \frac{\dfrac{\tau_r}{\tau_x}}{\left(1 + \dfrac{\tau_r}{\tau_s}\right)} \tag{4.9}$$

Figure 4.30 shows the calculated ratio of the number of excitons in states X_1 and X_2 (N_1/N_2), the radiative recombination probability ratio P_1/P_2 and the predicted PL intensity ratio $I_1/I_2 = N_1 P_1/N_2 P_2$ from the two direct excitonic states as a function of τ_r/τ_x. In each case, the dependence has been calculated for different values of τ_x/τ_s. In particular, setting $\tau_s = \infty$ and as a consequence $\tau_x/\tau_s = 0$ (red curves in Fig. 4.30) is equivalent to assuming the absence of the indirect state in the model, making the recombination from X$_1$ a ground state transition. For $\tau_s = \infty$ the predicted PL intensity ratio quickly diverges with τ_r/τ_x. It can be seen from panel (c) that the PL intensity ratio I_1/I_2 lower than 10 observed experimentally could be reproduced in the absence of scattering to the indirect state only for $\tau_r/\tau_x < 1$. This would mean that the radiative decay is faster than scattering between the two direct excitonic states, which is typically not expected in semiconductors [Bonch-Bruevich 1968]. On the other hand, it can be seen that for $\tau_x/\tau_s = 0.1$ and higher the PL intensity ratio approaches a constant value for $\tau_r/\tau_x > 1$. In this case, the lifetimes of excitons in the X$_1$ and X$_2$ states are determined mainly by the relaxation to the lower lying indirect state and the PL emission intensity from the direct states becomes comparable.

The exact determination of the experimental value of the intensity ratio I_1/I_2 is difficult due to the overlap of the peaks and the presence of emission from higher-energetic states, but it can be estimated to be in the range from 5 to 10. This value could be reproduced well for τ_x/τ_s between 1 and 10 for large τ_r/τ_x. For a given τ_r/τ_x, the larger the τ_x/τ_s ratio, that is for increasing relative probability of scattering to the indirect state, the stronger the emission from X_2 compared to X_1. For $\tau_s \ll \tau_x$ the I_1/I_2 ratio approaches 1.
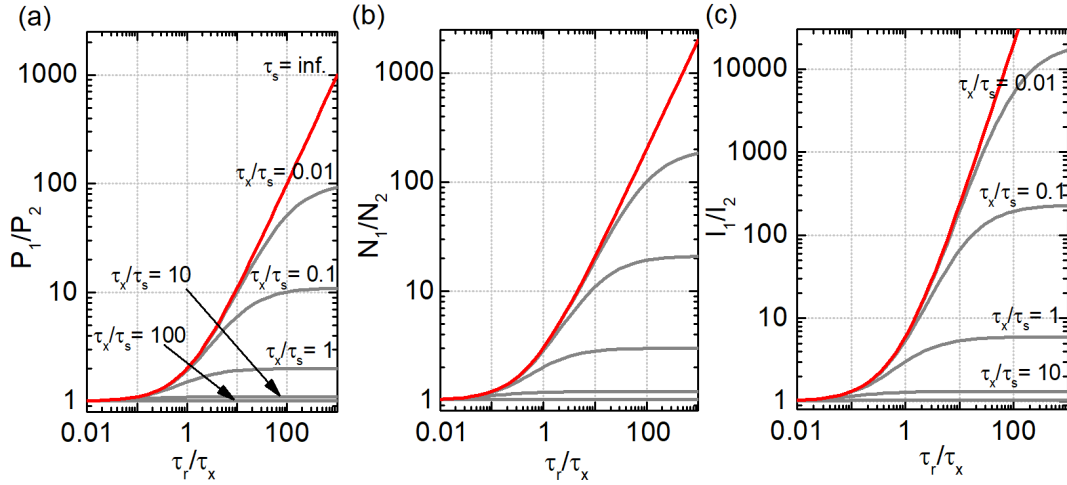
Figure 4.30: (a) Probability of radiative emission from state X_1 and X_2, (b) the number of excitons in state X_1 and X_2 and (c) predicted PL intensity ratio from state X_1 and X_2 as a function of τ_r/τ_x. The red line represents the prediction for the direct bandgap ($\tau_s = \infty$) while the grey lines show predictions for the indirect bandgap case for different ratios of scattering time between the direct excitonic states and the indirect state τ_x/τ_s. In all three panels, curves for τ_x/τ_s=0, 0.01, 0.1, 1, 10 and 100 are shown.

Intraband relaxation of excitons is usually a very fast process. In ML and few-layer MoS$_2$ it has been shown to be shorter than 500 fs and to dominate other relaxation processes [Kozawa 2014]. Exciton-exciton scattering on the timescale of 500 fs [Kozawa 2014] and intra- and inter-valley scattering on the ps timescale have been reported [Moody 2016]. Exciton-phonon scattering was shown to occur on the timescale of 70 ps in thin MoS$_2$ [Kozawa 2014]. At low temperatures, reported radiative recombination lifetimes for direct excitons in thin layered materials are usually on the order of sub-ps [Robert 2016, Moody 2016] to hundreds of ps [Kozawa 2014]. Based on the values observed for other thin layered materials we can estimate the recombination time from the direct excitonic states in ReS$_2$ τ_r to be in the ps time range and τ_x and τ_s in the tens to hundreds of fs range, giving an estimate of $\tau_r/\tau_x > 10$. Therefore, we conclude that for a reasonable set of parameters the suggested model including an indirect bandgap can explain the comparable emission intensity from X$_1$ and X$_2$.

The observed PL emission intensity from the direct states is relatively weak, which suggests that the scattering to the indirect state is faster than radiative recombination and can effectively depopulate the direct states. Based on the experimentally detected number of counts per second we estimate the PL to be 2 orders of magnitude weaker than for typical direct band gap TMDs, suggesting $\tau_s/\tau_r \approx 100$. Consequently, both scattering times τ_s and τ_x could be considered comparable and on the order of tens to hundreds of fs.

A very short radiative lifetime of X$_1$ and X$_2$ excitons is confirmed by time resolved spectroscopy. Figure 4.31 (a) shows a streak camera image of time-resolved PL measured acquired at

10 K on a thick flake of ReS$_2$. Panel (b) shows the vertical cross-section taken at the energy of 1.54 eV. The decay time of the PL is below the time resolution of our setup which is in the range of 5 ps. This is in line with previous observations of decay times around 3-5 ps for MoS$_2$, MoSe$_2$ and WSe$_2$ monolayers at low temperatures limited by the experimental time resolution [Robert 2016].
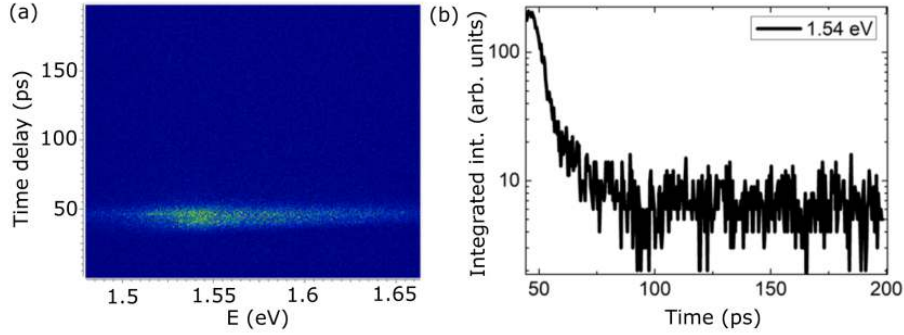
Figure 4.31: (a) Streak camera image of time-resolved PL emission measured at 10 K for a thick flake of ReS$_2$. (b) Time profile profile showing the decay at 1.54 eV.

Within the rate equation model we can also calculate the number of excitons in the indirect state N_I relative to N_2. The number of excitons in X_I state relative to the number of excitons in the higher direct state increases for slower recombination from X_I and for faster scattering to this state. Radiative recombination from an indirect exciton state requires the emission or absorption of a phonon and is a less probable and slower process than radiative recombination from a direct state. Lifetimes related to indirect emission have been shown to be on the order of several ns [Kozawa 2014]. In particular, for τ_x/τ_s in the experimentally observed range and assuming $\tau_I/\tau_x \approx 1\,\text{ns}/100\,\text{fs} = 10^4$ we can predict the number of excitons in the indirect state to be larger by a factor of almost 10^5 compared to the number of excitons in the higher-energetic direct state. This would be consistent with the weak observed intensity of the PL from the direct excitonic states.

4.5.2   Temperature dependence

Fig. 4.32 (a) shows the photoluminescence spectra as a function of temperature in the 5-80 K range, where both transitions can still be clearly resolved, normalized to the X$_1$ intensity and shifted in energy to overlap at the X$_1$ maximum at E=0. The I_1/I_2 emission intensity ratio decreases with increasing temperature. A possible reason could be the increasing probability of thermal excitation from the lower-lying X$_1$ to X$_2$ with increasing temperature which is negligible at the lowest temperatures. It is complicated to predict how the ratios of the recombination times τ_r/τ_x and τ_x/τ_s evolve with temperature, since the effective radiative lifetime for direct excitons is expected to increase with temperature by 1-10ps/K [Moody 2016, Korn 2011] and on the other hand, scattering by phonons, which is a possible mechanism of the transition from the direct to indirect state, is predicted to become more likely with increasing temperature, leading to a decrease of τ_s.

The thermal activation from X_1 to X_2 can be included in the kinetic model with a time constant τ_{therm}:

$$\begin{cases} \dfrac{dN_2}{dt} = -\dfrac{1}{\tau_s}N_2 - \dfrac{1}{\tau_x}N_2 - \dfrac{1}{\tau_r}N_2 + \dfrac{1}{\tau_{therm}}N_1 + g \\[3mm] \dfrac{dN_1}{dt} = -\dfrac{1}{\tau_s}N_1 + \dfrac{1}{\tau_x}N_2 - \dfrac{1}{\tau_r}N_1 - \dfrac{1}{\tau_{therm}}N_1 + g \end{cases} \tag{4.10}$$

Solving these equations assuming a steady state leads to an expression for the predicted photoluminescence intensity ratio:

$$\frac{I_1}{I_2} = \frac{\dfrac{\tau_r}{\tau_x}\left(2 + \dfrac{\tau_x}{\tau_s}\right) + 1}{1 + \dfrac{\tau_r}{\tau_s} + \dfrac{\tau_r}{\tau_{therm}}} \cdot \left(1 + \frac{\dfrac{\tau_r}{\tau_x} + \dfrac{\tau_r}{\tau_{therm}}}{1 + \dfrac{\tau_r}{\tau_s}}\right) \tag{4.11}$$

For simplicity it can be assumed that τ_r, τ_x and τ_s do not depend on the temperature and that τ_{therm}, the inverse of the scattering rate from the lower to the higher direct state can be expressed as:

$$\tau_{therm} = \frac{1}{v\exp\left(-\dfrac{(E_2 - E_1)}{k_B T}\right)} \tag{4.12}$$

where $(E_1 - E_2)$ is the energy difference between the two direct excitonic states and v is a constant describing the rate of the activation process [Baranowski 2018]. The normalized PL spectra for different temperatures have been fitted with three Gaussian peaks to account for X_1 and X_2 emission and the background. Fig. 4.32 (b) shows the spectra and fits for 4.5 K and 80 K. The intensity ratio and the energy difference $(E_2 - E_1)$ have been determined from the fits. Fig. 4.32 (c) shows the experimentally determined I_1/I_2 ratio for temperatures up to 80 K. I_1/I_2 decreases from almost 9 at 4.5 K to around 2 at 80 K.

Substituting τ_{therm} in equation 4.11 by the expression given in equation 4.12 and using $(E_2 - E_1)$ determined experimentally it is possible to calculate the predicted PL intensity ratio for different values of τ_r/τ_x, τ_x/τ_s and $\tau_r/\tau_{therm} = \tau_r \cdot v$. It can also be assumed that $\tau_x = v^{-1}$. This means that the transition 'attempt' rate can be described by a rate constant v and each attempt is succesful for scattering from the higher to the lower state, while the probability of the scattering from the lower to the higher state is governed by the thermal Boltzmann factor. Fig. 4.33 shows the PL intensity ratio I_1/I_2 as a function of temperature calculated assuming $\tau_x = v^{-1}$, $\tau_r/\tau_x = 100$ and for different values of τ_x/τ_s. The experimental observation cannot be reproduced well using these assumptions, but a decrease of the PL intensity ratio with temperature is also observed. The relative intensity change with temperature is larger for lower τ_x/τ_s. Finally, it should be stressed the I_1/I_2 ratio determined from fitting of the experimental temperature-dependent data is only approximate and it is hard to directly compare it with results of the calculations.

4.5.3 Emission intensity as a function of excitation polarization

As shown in the previous section, the experimentally observed variation of the PL intensity with the changing direction of the excitation polarization was much stronger for the X_1 emission than
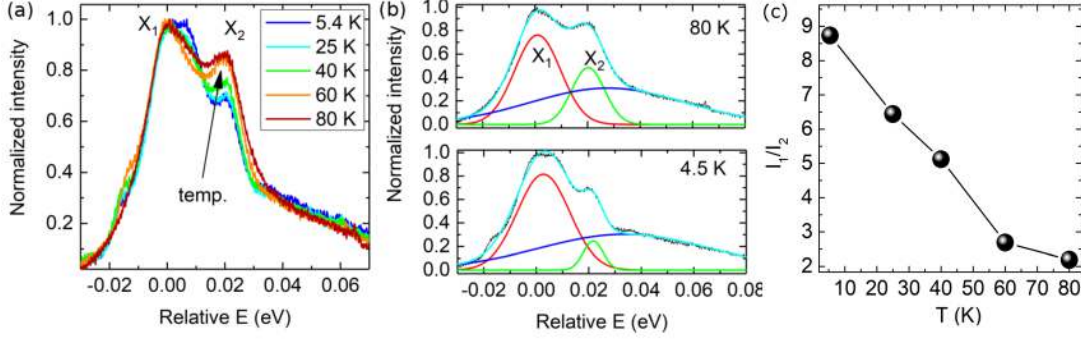
Figure 4.32: (a) PL spectra of a thick ReS$_2$ flake showing the X$_1$ and X$_2$ emission, normalized to the X$_1$ intensity and shifted in energy to overlap at the X$_1$ maximum for a range of temperatures. (b) PL spectra for 4.5 K and 80 K and three Gaussian peaks used to fit the data as well as the cumulative fit. The peak fit to X_1 is shown in red, the peak fit to X_2 in green and the Gaussian peak used to fit the background in dark blue. (c) The experimentally observed PL intensity ratio I_1/I_2 as a function of temperature.

for X$_2$.

Considering Eq. 4.3 and assuming steady state, we can express the number of excitons in both direct states as a function of the decay times and the generation rate g:

$$
\begin{cases}
N_2 = \dfrac{g}{\dfrac{1}{\tau_s} + \dfrac{1}{\tau_x} + \dfrac{1}{\tau_r}} \\[3ex]
N_1 = \dfrac{g + \dfrac{N_2}{\tau_x}}{\dfrac{1}{\tau_s} + \dfrac{1}{\tau_r}}
\end{cases}
\tag{4.13}
$$

The generation rate depends on the absorption coefficient for linearly polarized light and changes with the changing excitation polarization direction. The change of the number of excitons in each state with g can be defined as:

$$
\begin{cases}
\dfrac{\mathrm{d}N_2}{\mathrm{d}g} = \dfrac{1}{\dfrac{1}{\tau_s} + \dfrac{1}{\tau_x} + \dfrac{1}{\tau_r}} \\[3ex]
\dfrac{\mathrm{d}N_1}{\mathrm{d}g} = \dfrac{1 + \dfrac{1}{\tau_x}\dfrac{\mathrm{d}N_2}{\mathrm{d}g}}{\dfrac{1}{\tau_s} + \dfrac{1}{\tau_r}}
\end{cases}
\tag{4.14}
$$

and is different for the two states. The larger $\mathrm{d}N_i/\mathrm{d}g$, the stronger the emission intensity changes will be as a function of the excitation polarization direction. It is worth noting that $\mathrm{d}N_1/\mathrm{d}g$ depends also on $\mathrm{d}N_2/\mathrm{d}g$, since the excitons can scatter from the higher to the lower
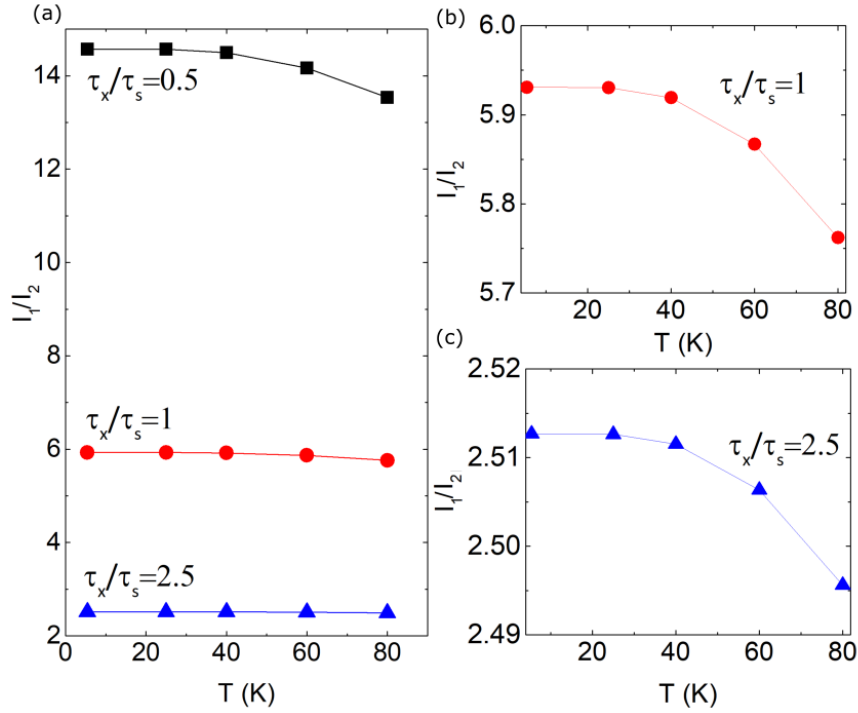
Figure 4.33: (a) PL intensity ratio I_1/I_2 as a function of temperature for different values of τ_x/τ_s, $\tau_x = v^{-1}$ and $\tau_r/\tau_x = 100$. (b) curve for $\tau_x/\tau_s = 1$ and (c) $\tau_x/\tau_s = 2.5$.

state. Fig. 4.34 shows the ratio $(\mathrm{d}N_2/\mathrm{d}g)/(\mathrm{d}N_1/\mathrm{d}g)$ as a function of τ_r/τ_x for different τ_x/τ_s ratios. For the radiative recombination slower than scattering between the states ($\tau_r/\tau_x >> 1$) depending in τ_x/τ_s the rate of change of the number of excitons with the generation rate can be almost the same for X_1 and X_2 ($\tau_x >> \tau_x$) or significantly smaller for X_2 ($\tau_x < \tau_x$). This means that the scattering from the higher to the lower excitonic state can explain the significantly smaller sensitivity of the X_2 PL emission intensity to the excitation polarization. The faster the scattering from the higher to the lower direct state relative to the scattering to the indirect state, the more pronounced this effect will be.

4.6 Conclusion

In this chapter, the properties of anisotropically stacked ReS_2 were investigated using Raman, reflectivity and PL spectroscopy. Linearly polarized features in emission and reflectivity corresponding to two previously described direct excitons were observed. A monotonic dependence of the PL intensity on ReS_2 thickness suggested that the nature of the bandgap does not change with the number of layers. The comparable intensity of the two lowest-lying excitonic states suggested the hot nature of the photoluminescence and the generally weak PL intensity pointed to the existence of scattering mechanisms responsible for depopulating the direct excitonic
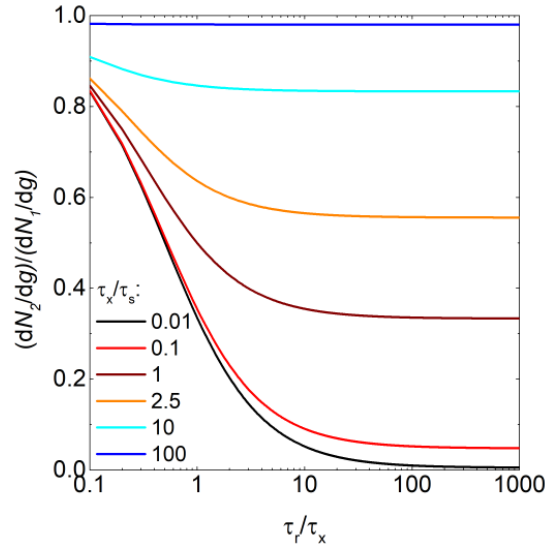
Figure 4.34: Ratio of the derivatives of the number of the number of excitons with respect to the generation rate g for state X$_2$ and X$_1$ as a function of τ_r/τ_x. Curves for different values of τ_x/τ_s are shown in different colors.

states. The presence of an excitonic state related to the narrower fundamental indirect bandgap was proposed and a kinetic model describing the exciton scattering and recombination allowed to partly explain the experimental observations.

Chapter 5

Anomalous polarization dependence of Raman scattering in franckeite

Contents

The first part of this chapter presents the motivation of our study, the observation of one-dimensional corrugation in exfoliated franckeite flakes, and describes the optical properties of franckeite. Next, our reflectivity and Raman spectroscopy measurements on exfoliated franckeite samples are described. Polarization dependent reflectivity measurements revealed slight linear anisotropy of the heterostructure. The polarization dependence of the Raman spectra was investigated and the intensity of the modes at 186 cm^{-1}, 253 cm^{-1} and 322 cm^{-1} was characterized as a function the polarization direction of the excitation beam. Anomalous polarization dependence, which could not be explained only by the mode symmetry, was observed. The presence of an anisotropy axis oriented along one of the flake cleavage directions suggests the anisotropy of the absorption and refraction indices with respect to the rippling direction of franckeite.

5.1 Introduction

Despite the two constituent lattices of franckeite being isotropic in-plane (with hexagonal and cubic symmetry for SnS_2 and PbS layers, respectively), anisotropy appears in the heterostructure due to their incommensurate character. Fig. 5.1 shows the TEM image of a suspended franckeite flake clearly showing one-dimensional rippling with a period below 5 nm. Preliminary transport measurements suggested strong anisotropy of conductivity along the directions parallel and perpendicular to the ripples.
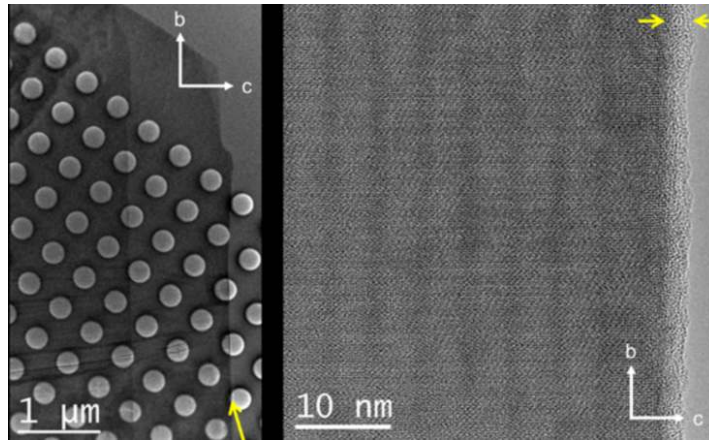
Figure 5.1: Optical microscopy image of a franckeite flake (left) placed on a TEM grid and TEM image (right) of a suspended part of the flake with clearly visible one-dimensional corrugation. The images were taken by our collaborators from the group of A. Castellanos-Gomez.

Because of the expected anisotropy of the optical and transport properties of franckeite induced by the one-dimensional rippling of the heterostructure, it is important to establish a fast and non-invasive method of identifying the orientation of the periodic pattern. Polarization dependence of the intensity of Raman modes in materials with optical anisotropy cannot be described based only on the classical real Raman tensor formalism. Here, we propose that the observation of the anomalous polarization dependence of the Raman modes can be used to identify the rippling direction.

5.2 Optical properties of franckeite

5.2.1 Raman spectrum

The Raman spectrum of franckeite consists of several bands in the 50-400 cm^{-1} spectral region. Their exact assignment is complicated due to the complex structure of the material. An assignment of the modes can be done based on the known Raman spectra of the constituent metal sulfides [Velický 2017b, Molina-Mendoza 2017]. Fig. 5.2 shows a comparison of Raman spectra of franckeite from several works. A lowest-lying band at around 66 cm^{-1} has been attributed to PbS [Molina-Mendoza 2017]. Two bands at around 143 and 185-200 cm^{-1} have

been assigned to the SnS_2 berndtite phase in the hexagonal layer and the PbS phase in the tetragonal layer [Molina-Mendoza 2017]. In all of the spectra a dominant peak can be seen at around 250-260 cm^{-1} together with a weaker shoulder at around 276-277 cm^{-1}. Both of these modes have been assigned to the stibnite Sb_2S_3 phase in the tetragonal layer. It has also been suggested that the peak at 250-260 cm^{-1} arises due to a combination of modes from the Q and H layers [Molina-Mendoza 2017]. A mode observed around 320 cm^{-1} has also been attributed to the berndtite phase. A detailed assignment of the modes can be found in the work of [Molina-Mendoza 2017]. Both stibnite and berndtite have larger bandgaps (1.72 eV and 2.1 eV, respectively) than PbS (0.37 eV). Consequently, they absorb less and scatter light more strongly than PbS at the 532 nm wavelength used for excitation, which explains the dominance of the features related to these compounds in the Raman spectra. No clear changes in the shape of the Raman spectrum with thickness can be seen and the intensity changes have been attributed to interference effects in multilayer material (Fig. 5.2 (b)). Spectra differ slightly for bulk franckeite powder concentrated colloidal liquid-phase exfoliated material.

Fig. 5.3 shows the Raman spectra of (a) SnS_2 and (b) Sb_2S_3. The spectrum of berndtite shows a single strong peak at 315 cm^{-1} and the spectrum of stibnite multiple peaks at frequencies at which features are observed also in the spectrum of franckeite. The spectra of Sb_2S_3 shown in Fig. 5.3 (b) were measured in two different polarization configurations and differences in the peak intensities can be noticed. The $\bar{x}(yy)x$ configuration corresponds to the backscattering geometry with parallel polarization, which was used in this work.
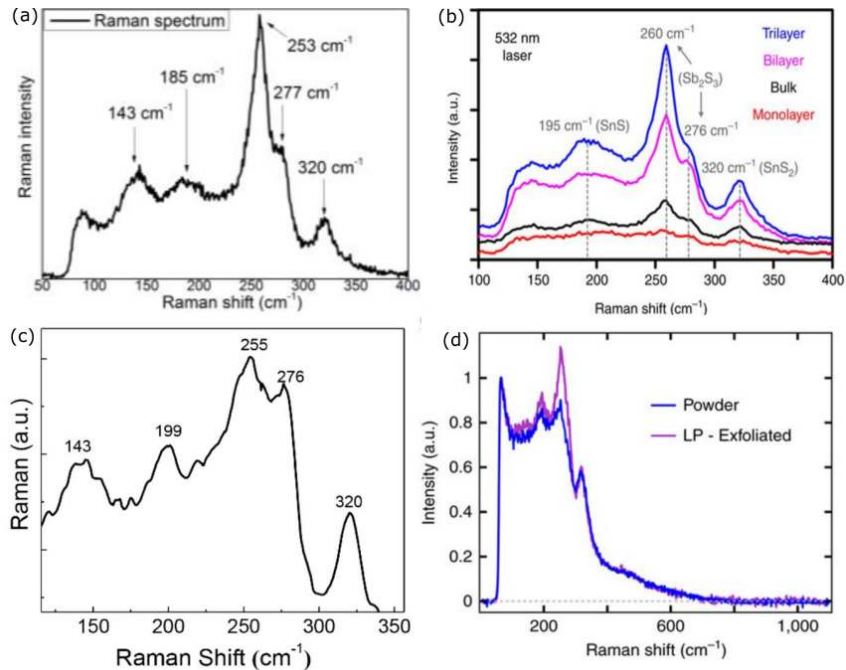
Figure 5.2: Comparison of Raman spectra of franckeite with marked characteristic peaks after (a) [Steinberg] (b) [Ray 2017] (c) after [Velický 2017b] (d) after [Molina-Mendoza 2017] .
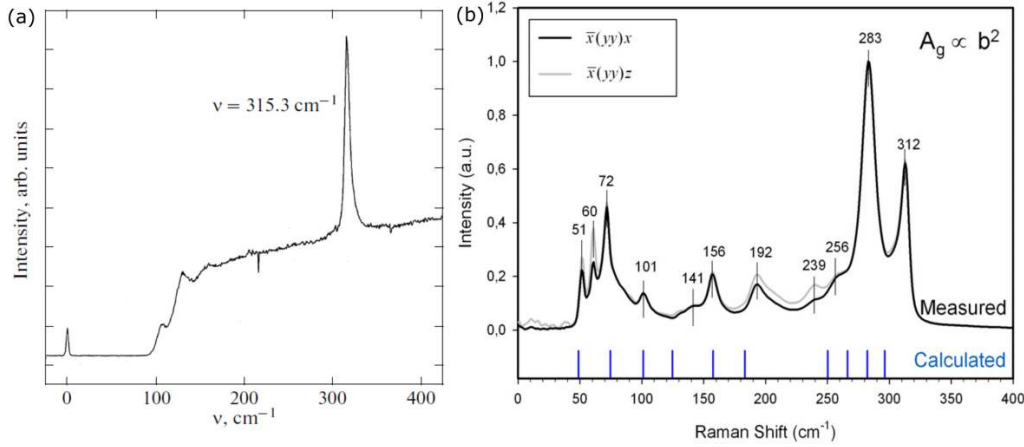
Figure 5.3: Raman spectra of (a) SnS_2 [Utyuzh 2010] (b) Sb_2S_3 [Sereni 2010]. The spectra of Sb_2S_3 shown in panel (b) have been measured in two different polarization configurations, the backscattering copolarized and 90° geometry.

5.2.2   Absorption and reflectivity

Diffuse reflectance spectroscopy measurements were performed to determine the bandgap of bulk franckeite [White 1998]. The spectra of franckeite and cylindrite, converted to absorbance, are shown in Fig. 5.4. The absorption edge onset is slow and not very sharp, making it difficult to determine whether the spectra represent the intrinsic shape of the band edge or also show contributions from impurity and defect states. The band gap, determined as the crossing point of the extrapolated base line and absorption edge, is 0.65 eV.

Optical contrast in the visible range was investigated for mechanically exfoliated nanosheets of different thickness using quantitative optical microscopy [Gant 2017]. Fig. 5.5 (a) shows the optical contrast spectra as a function of wavelength for a range of sample thicknesses and Fig. 5.5 (b) the optical contrast for a range of wavelengths as a function of flake thickness. A model based on the Fresnel law, accounting for the reflections and refractions of light at the air/franckeite, franckeite/SiO_2 and SiO_2/Si interfaces with the complex refractive index as the fitting parameter was used to explain the results. The shape of the spectrum can be used to identify thickness, but the substrate (i.e. the thickness of the SiO_2 layer) has to be taken into account. No excitonic features were observed, as expected, because the band edge is far from the measurement spectral range.

5.3   Investigated samples

The samples investigated in this work were prepared by P. Gant in the group of A. Castellanos-Gomez in Instituto de Ciencia de Materiales de Madrid. Thin franckeite flakes were prepared by mechanical exfoliation from bulk crystals originating from a natural rock (san José mine, Oruro, Bolivia). The flakes were exfoliated onto a PDMS substrate and deposited on a 292 nm SiO_2/Si substrate by an all-dry transfer technique [Gant 2017]. AFM characterization, also
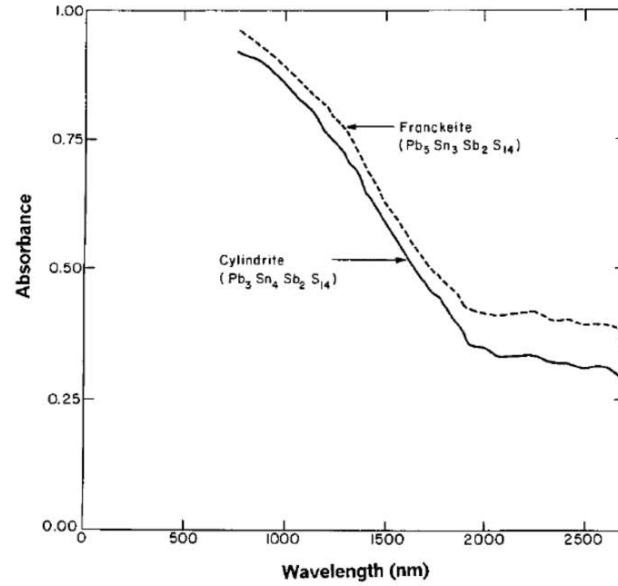
Figure 5.4: Absorption edge spectra of cylindrite and franckeite. After [White 1998].
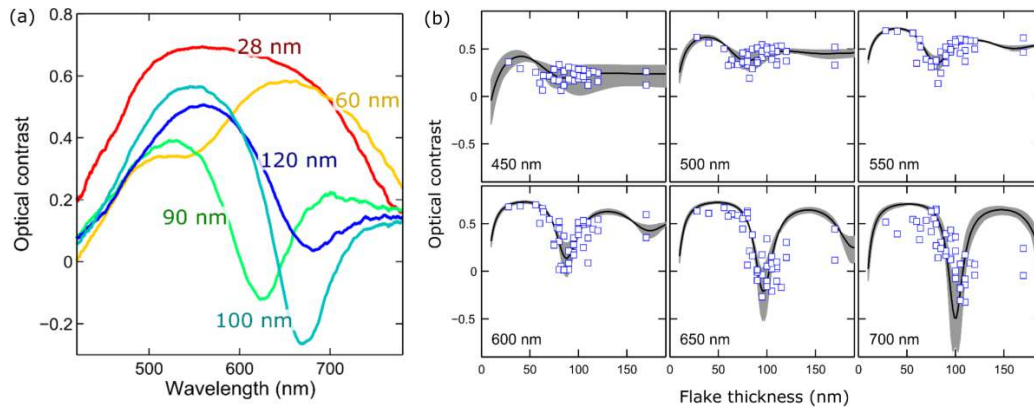
Figure 5.5: Optical contrast spectra for different thicknesses of franckeite on a 92 nm SiO_2/Si substrate. [Gant 2017] .

performed in the group of A. Castellanos-Gomez allowed to determine the thickness of the flake. The AFM topography image of the investigated flake is shown in Fig. 5.6 (a). A thicker and thinner part can be distinguished, which based on the two marked profiles could be identified as around 87 nm and 42 nm thick. This corresponds to around 47 and 23 repeating units consisting of a H and a Q layer, assuming a single unit cell thickness of 1.85 nm [Velický 2017b]. The optical image of the same flake is shown in Fig. 5.6 (b).
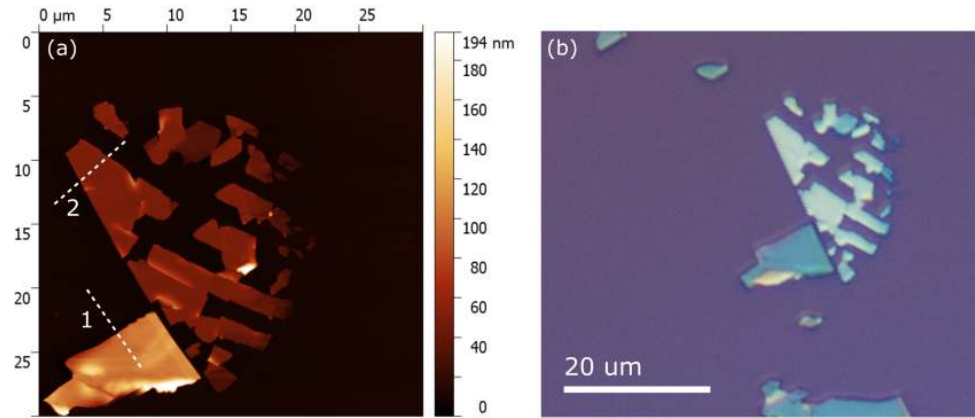
Figure 5.6: (a) AFM topography image of the investigated flake with marked profiles which were used to estimate thickness. (b) Optical micrograph of the same flake.

5.4   Reflectivity contrast measurements

Reflectivity contrast measurements were performed using the microspectroscopy setup at the LNCMI Toulouse. The measurements were made at room temperature. Fig. 5.7 (a) shows the spectra acquired on the thick and thin parts of the flake, panel (b) shows the optical contrast at 1.93 eV corresponding to the dip in the spectrum for the thick flake showing the regions of uniform thickness and panel (c) the micrograph of the flake with marked positions at which the spectra were acquired.
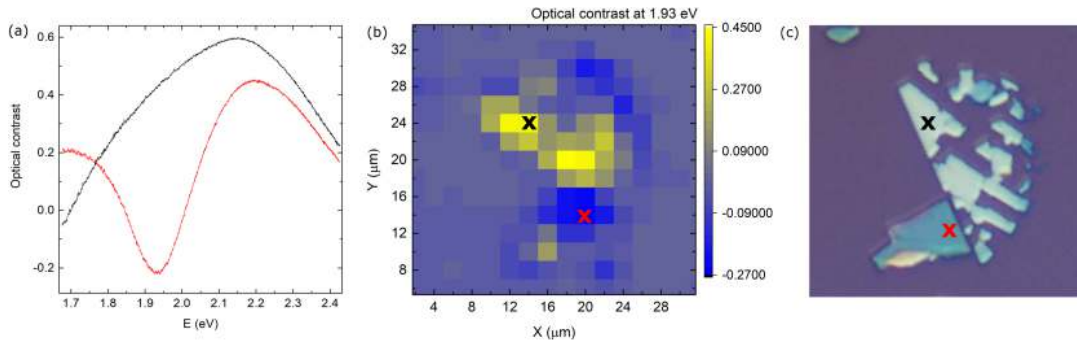
Figure 5.7: (a) Typical reflectivity contrast spectra acquired on the 87 nm (red) and 42 nm (black) thick regions of the flake. (b) Map of optical contrast at 1.93 eV. (c) Optical micrograph of the flake with marked positions at which the spectra were acquired.

Polarization-resolved reflectivity contrast measurements were performed on the thicker part of the flake. Fig. 5.8 (a) shows the optical contrast spectra for two perpendicular detection

polarization angles. Fig. 5.8 (b) shows the optical contrast as function of energy and linear polarization detection angle. Slight changes of the spectrum can be seen as a function of the detection angle, which suggests the presence optical anisotropy caused by the one-dimensional rippling of the heterostructure.
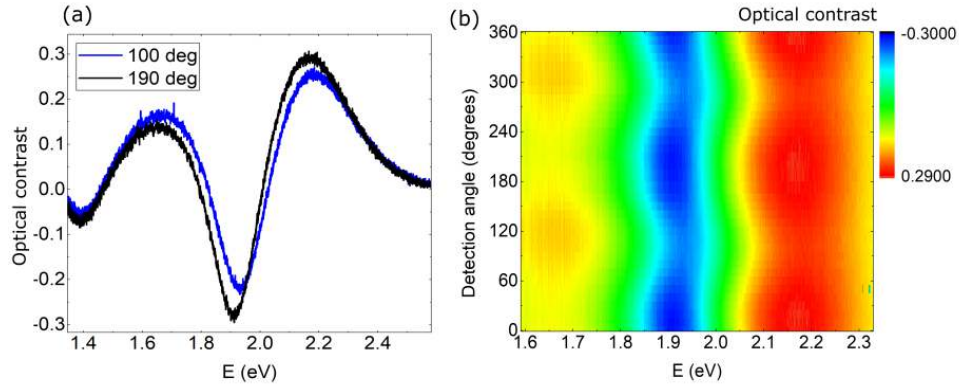
Figure 5.8: (a) Reflectivity contrast spectra acquired for two different detection polarization directions measured on the thick part of the flake. (b) Optical contrast as a function of energy and detection angle.

5.5 Raman spectroscopy

We performed Raman spectroscopy measurements at room temperature. For excitation, the CW 532 nm line of a solid state laser was used at 2 mW power. For the mapping of the sample a dichroic mirror was used to obtain better signal-to-noise ratio. For the polarization-resolved measurements, a nonpolarizing cube beamsplitter was mounted to avoid polarization artifacts introduced by the dichroic mirror.

5.5.1 Thickness dependence of unpolarized Raman spectra

Fig. 5.9 (a) shows the Raman spectra acquired on the substrate and on the thin 40 nm and the thicker 90 nm parts of the franckeite flake. The Raman features related to franckeite in the 200-400 nm range overlap with spectral features from silicon, including the 300 cm^{-1} 2TA mode [Spizzirri 2010], and the spectra have to be corrected for the contribution from the substrate [Velický 2017b]. The substrate spectrum has been rescaled so that the intensity of the 520 cm^{-1} Si peak matches with that of the franckeite spectrum and then subtracted from the other spectra as shown in Fig. 5.9 (b). Fig. 5.9 (c) shows the spectra of the thinner and thicker flake after background spectrum subtraction. While a change in the intensity can be noticed, no significant change of the spectral shape occurs with thickness.
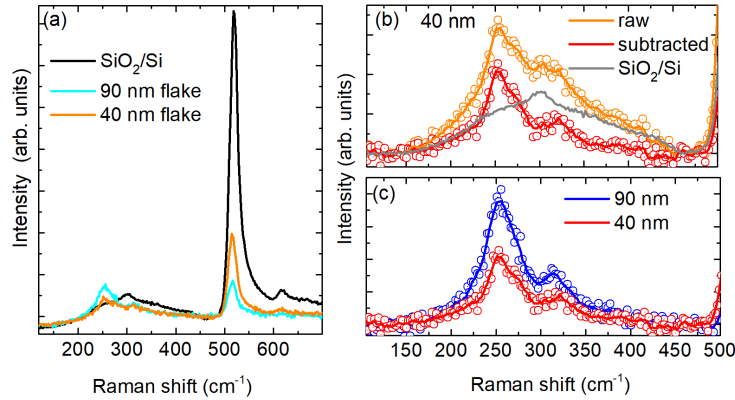
Figure 5.9: Raman spectra acquired on the SiO_2/Si substrate and on a 90 nm and a 40 nm thick franckeite flake. (b) Rescaled spectrum of the substrate and the spectrum of the thinner flake before (orange) and after (red) subtracting the substrate spectrum (c) Spectra of the 90 nm (blue) and 40 nm (red) franckeite flake before and after substrate spectrum subtraction. In panels (b) and (c) the points show raw data and the lines smoothed spectra.

5.5.2 Polarization-resolved measurements

Polarization-resolved Raman spectroscopy measurements were performed to identify the symmetry of the modes and investigate the optical anisotropy of the sample. The configuration of the setup is described in Chapter 2. The spectra were normalized by the intensity of the laser line to compensate for the polarizing characteristic of the diffraction gratings. Fig. B.22 shows spectra obtained by averaging the spectra measured on the thicker part of the flake for a full range of excitation angles acquired in the co-polarization and cross-polarization configurations. The most prominent feature is the peak at 253 cm^{-1} with a shoulder at 277 cm^{-1}. These peaks have been previously interpreted as modes related to the stibnite spectrum from the Q phase [Ray 2017]. The peak around 300 cm^{-1} most probably originates from the substrate. The position of the mode at 322 cm^{-1} corresponds to the energy of the A$_g^1$ vibration observed in SnS$_2$ [Molina-Mendoza 2017]. The assignment of the two lowest-energetic modes is not straightforward, as they have been previously attributed to different modes or their combinations from both the Q and H layer.

Fig. 5.11 shows the Raman intensity maps as a function of the excitation angle for the co- and cross-polarized configuration. The 0° angle corresponds to excitation polarization parallel to the horizontal direction on the flake micrograph shown in Fig. 5.13 (b). The modes show a strong modulation of intensity with the excitation polarization direction. In the copolarized configuration, a twofold periodicity can be observed for almost all of the modes (the polarization dependence is difficult to resolve for the 277 cm^{-1} peak because of the close-lying, stronger 253 cm^{-1} peak, as well as for the 144 cm^{-1} broad peak due to low intensity). In the cross-polarized configuration, for the 186 cm^{-1} and 253 cm^{-1} mode a fourfold symmetry of the polarization pattern can be seen. The 322 cm^{-1} mode is absent in the cross-polarized configuration. Fig. 5.12 shows chosen Raman spectra measured in the co- and cross-polarization as a function of
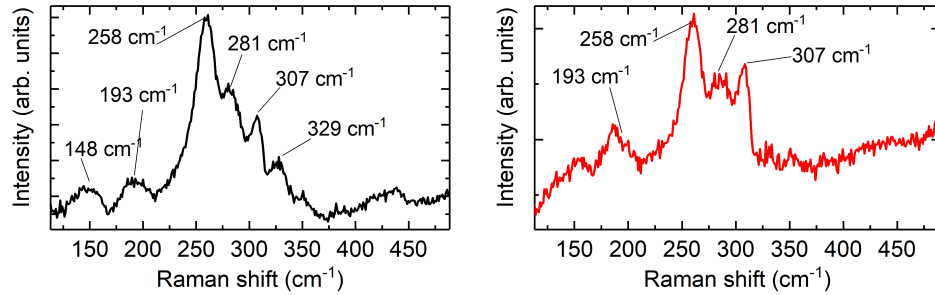
Figure 5.10: Raman spectrum of the thicker franckeite flake with marked characteristic modes for (a) co-polarized and (b) cross-polarized detection configurations and averaged over the full range of excitation directions.

the excitation angle.
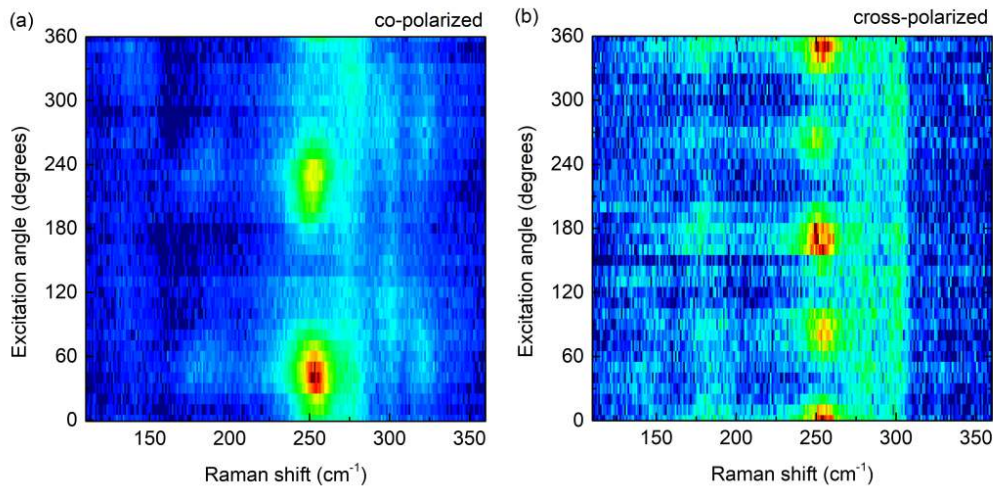
Figure 5.11: Maps showing the Raman mode intensity as a function of excitation angle for the (a) co- and (b) cross-polarization.

In order to quantitatively describe the polarization dependence, the spectra were fitted using six Gaussian peaks corresponding to the five franckeite modes and the mode originating from the substrate. The fit for the copolarized spectrum measured at 0° excitation polarization direction is shown in Fig. 5.13. The peak positions and widths were fixed and the peak height was extracted as a measure of intensity and plotted in Fig. 5.14 for the three franckeite modes at 186, 253 and 322 cm^{-1} for which a clear polarization dependence could be resolved. Fig. 5.15 shows the polar plots of peak height in co- and cross-polarization overlaid on one graph for the 186 cm^{-1} and 253 cm^{-1} modes The directions of the polarization axes observed in copolarization determined based on the polar plots are shown with arrows in Fig. 5.14 and
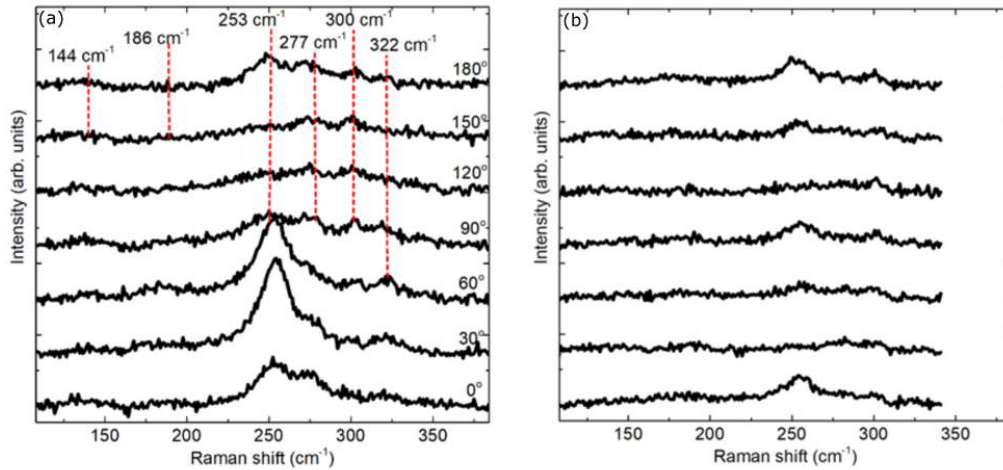
Figure 5.12: Chosen Raman spectra for different excitation angles at 30° intervals for the (a) co- and (b) cross-polarization configurations.

have been overlaid with the flake micrograph in Fig. 5.13 (b). This allowed us to compare the directions of the flake cleavage with polarization directions observed for the Raman modes. The polarization direction along which maximum intensity of the 322 cm^{-1} mode is observed in copolarization is parallel to the long edges of the thinner part of the flake. The polarization direction for the two remaining modes is parallel to one of the edges of the thicker part of the flake.
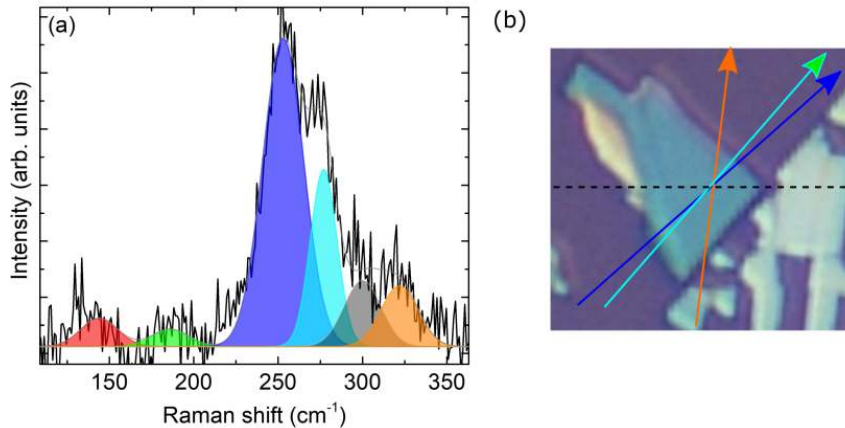
Figure 5.13: (a) Example of fitting for the spectrum for 0° excitation angle with Gaussian peaks fitted to the transitions. (b) Optical micrograph of the flake with marked 0° direction (dashed line) and the maximum intensity directions derived from the polar plots for the 186 cm^{-1} (green), 253 cm^{-1} (dark blue) and 322 cm^{-1} (orange) modes.
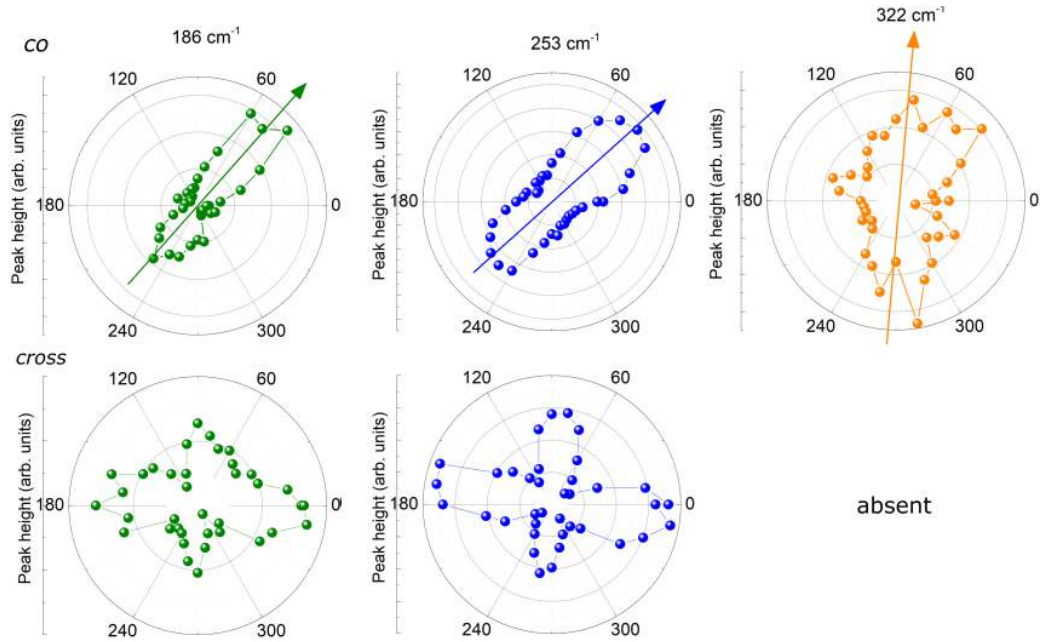
Figure 5.14: Polar plots showing the intensity of the 186 cm^{-1} (green), 253 cm^{-1} (dark blue) and 322 cm^{-1} mode as a function of excitation angle in the copolarized (top) and cross-polarized (bottom) configuration. The 322 cm^{-1} mode was not observed in the cross-polarization. The arrows mark the approximate directions of the maximum intensity.
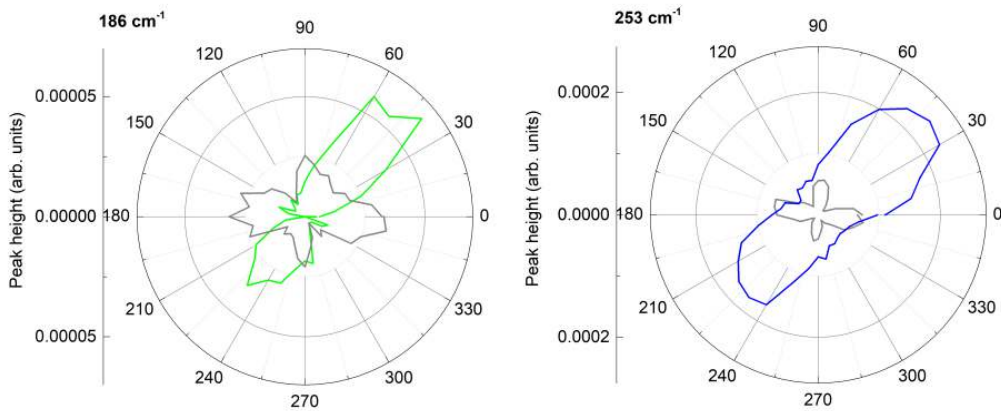
Figure 5.15: Raman mode height as a function of the excitation angle in the co- (color) and cross-polarization (grey) for the 186 cm^{-1} and 253 cm^{-1} modes.

Based on the observed polarization dependence, we can reach conclusions about the symmetry of the observed modes. In hexagonal SnS$_2$, the A_1 and E_2 modes are Raman active in

backscattering geometry. The Raman tensors of these modes have the form:

$$\hat{R}_{A_1} = \begin{pmatrix} a & 0 & 0 \\ 0 & a & 0 \\ 0 & 0 & b \end{pmatrix} \hat{R}_{E_2} = \begin{pmatrix} d & 0 & 0 \\ 0 & -d & 0 \\ 0 & 0 & 0 \end{pmatrix}, \begin{pmatrix} 0 & -d & 0 \\ -d & 0 & 0 \\ 0 & 0 & 0 \end{pmatrix}$$

The dependence of the intensity on the excitation polarization in co- and cross- detection polarization calculated based on Eq. 2.23 for these modes is shown in Fig. 5.16. A four-fold symmetry pattern in co- and cross- polarization is observed for both E_2 modes, with a relative difference in the orientation of the polarization axes of 45° (the dependence for only one of the modes is shown in Fig. 5.16). The calculated intensity dependence predicted based on the real Raman tensor for the A_1 mode is consistent with the absence of the 322 cm^{-1} mode in cross-polarization. However, this approach cannot explain the presence of twofold anisotropy observed in copolarization. A modified form of the A_1 mode tensor with unequal diagonal elements, which could be caused by a reduced in-plane symmetry of the hexagonal layer for example due to strain, could explain the anisotropy in copolarization, but on the other hand would result in the observation of nonzero intensity in cross-polarization.

The two remaining modes, for which a clear polarization dependence could be identified have been previously interpreted as a combination of phonons from the PbS and SnS$_2$ phase (253 cm^{-1} mode) and either an LO PbS phonon or E_g SnS$_2$ vibration (mode observed by us at 186 cm^{-1}) [Molina-Mendoza 2017]. In another work the 253 cm^{-1} mode was assigned to the Sb$_2$S$_3$ stibnite phase and the 186 cm^{-1} mode to the SnS$_2$ phase [Ray 2017]. The polarization dependence measured by us follows the same pattern for both peaks with twofold symmetry in copolarization and fourfold symmetry in cross-polarization. This excludes the assignment of these modes as E_g vibrations of the hexagonal lattice, which would result in a fourfold pattern in both the co- and cross-polarization. The symmetry of the observed polarization pattern could be explained considering the Raman tensor for an A_g vibration in an orthorombic lattice:

$$\hat{R}_{A_1} = \begin{pmatrix} a & 0 & 0 \\ 0 & b & 0 \\ 0 & 0 & c \end{pmatrix} \tag{5.2}$$

If orthorombic inclusions of Sb$_2$S$_3$ locally exist within the PbS symmetric cubic lattice, the A_1 vibration could be the origin of the observed mode. Interestingly, two of the lobes in cross-polarization have larger intensity, which cannot be explained only based on the form of the Raman tensor.

In materials with optical anisotropy, the observed polarization dependence of the intensity cannot be described only based on the symmetry of the modes described by the real elements of the Raman tensor. Anomalous dependence of the Raman mode intensity on polarization has been previously observed in materials with in-plane anisotropy such as black phosphorus [Kim 2015, Wang 2018], MoTe$_2$ [Song 2017], GaTe [Huang 2016a] or ReS$_2$ [Zhang 2017b]. Bi-refringence and anisotropic absorption lead to the observation of a more complex dependence of the scattering intensity on the polarization configuration [Kranert 2016]. For an absorbing material, the polarizability is complex and as a consequence, the Raman tensor has complex
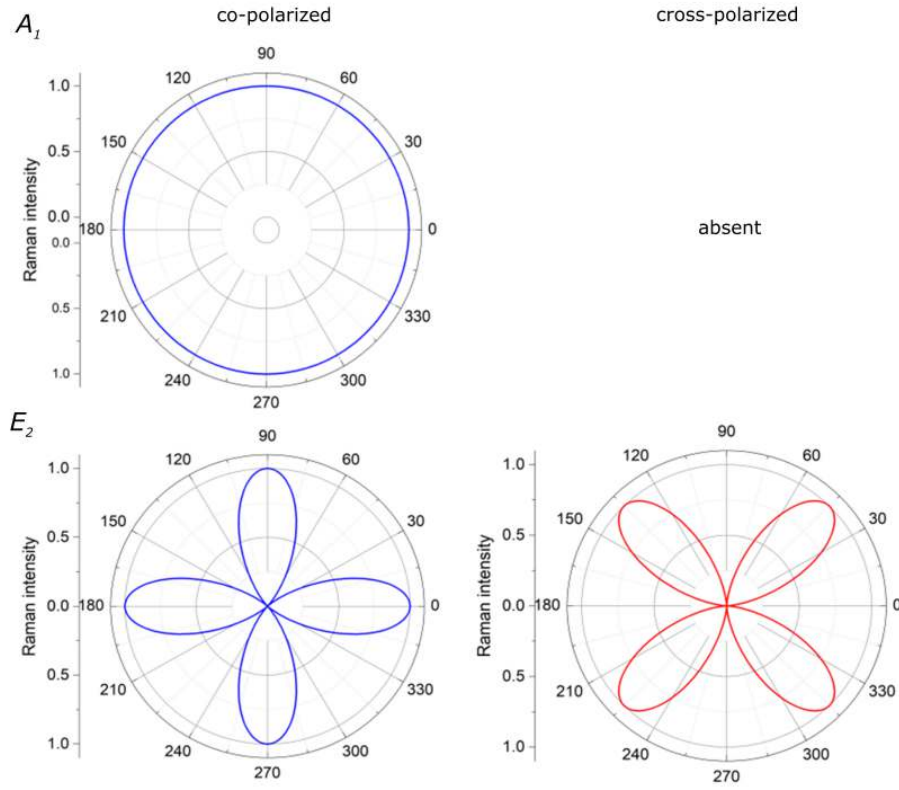
Figure 5.16: Calculated Raman mode intensity in copolarization and crosspolarization for the A_1 and E_2 modes in a hexagonal lattice.

elements:

$$
\hat{R} = \begin{pmatrix} ae^{i\phi_a} & 0 & 0 \\ 0 & be^{i\phi_b} & 0 \\ 0 & 0 & ce^{i\phi_c} \end{pmatrix}
$$

where ϕ_a, ϕ_b, ϕ_c are the phases of the tensor elements which are not equal for materials with anisotropic absorption properties [Ribeiro 2015, Zhang 2017b]. The scattering intensity dependence on the polarization angle is modified and depends on the relative phase shifts between the tensor elements. For example, the intensity of the A_1 mode described in Chapter 2 for a non-absorbing material of triclinic symmetry with two non-equivalent in-plane directions can now be expressed as a function of θ as:

$$
I_{co} \propto |a|^2 \left[\left| 1 + \left(\frac{|b|}{|a|} - 1 \right) \sin^2(\theta) \right|^2 + \frac{1}{2} \frac{|b|}{|a|} \sin^2(2\theta)(\cos(\phi_{ab}) - 1) \right] \tag{5.4}
$$

$$I_{cross} \propto |a|^2 \left[\frac{1}{4} \left(\frac{|b|}{|a|} - 1 \right)^2 + \frac{1}{2} \frac{|b|}{|a|} \left(1 - \cos(\phi_{ab}) \right) \right] \sin^2(2\theta) \tag{5.5}$$

Fig. 5.17 shows the calculated polarization dependence of the A_g^1 mode intensity for different degrees of absorption anisotropy defined by ϕ_{ab}. In co-polarization, the shape of the polarization dependence is modified by the anisotropic absorption and additional maxima appear along the direction perpendicular to the main axis of the polar plot. In cross-polarization, a significantly larger intensity can be observed compared to the case with no absorption.

Birefringence has a qualitatively similar effect of modifying the polarization dependence. The polarization states of the incident and scattered light can be altered after passing through the sample [Zhang 2017b]. The polarizations of the incident and scattered light at a finite depth within the sample where the scattering occurs are different from the polarization of the incident beam before entering the sample and the scattered light polarization measured after the signal emerges from the sample [Kranert 2016]. The layer of the material above the point at which the scattering occurs can be treated as an optical element with an anisotropic refractive index. The scattering intensity can be described using a depth-dependent effective Raman tensor with a phase factor dependent on the anisotropy of $\tilde{n}$ [Kranert 2016].
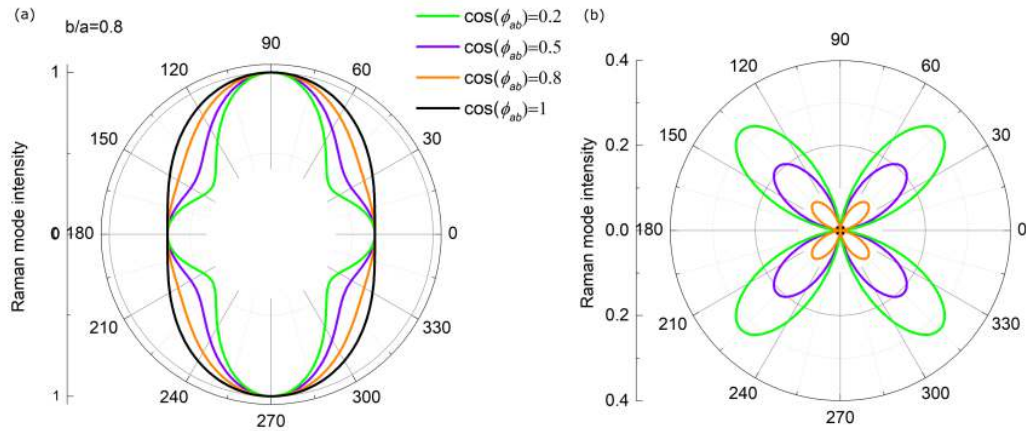
Figure 5.17: Calculated Raman A_1 mode intensity in (a) copolarization and (b) cross-polarization for different values of the phase difference ϕ_{ab} and a/b=0.8.

A model taking into account the influence of multiple reflections and interference on light absorption and propagation of scattered light was suggested [Yoon 2009] and applied to explain for example the anomalous polarization dependence observed in black phosphorus [Kim 2015]. Fig. 5.18 (a) shows a schematic of the multiple reflection interference, the top panel showing the propagation of the incident light and the bottom panel the propagation of the Raman scattered light. Absorption and scattering processes are treated separately in this model. The absorption at depth x in the sample is expressed using the Fresnel coefficients at the interfaces, which are defined based on the complex refractive indices of the layers, and wavelength dependent terms. A similar term is used to express the Raman signal enhancement. The scattering and absorption terms F_{ab} and F_{sc} can be used to define a total enhancement factor F:

$$F \propto N \int_0^{d_1} |F_{ab}F_{sc}|^2 dx \tag{5.6}$$

where N is a normalization factor and the square of the product of the terms is integrated over the whole thickness of the sample d_1. The measured Raman intensity is equal to $I = I_i \cdot F$, where I_i is the intrinsic Raman scattered light intensity. Fig. 5.18 (b) shows the ratio of the enhancement factors along the two perpendicular directions in anisotropic black phosphorus as a function of BP thickness and for different excitation wavelengths. Both these factors strongly influence the enhancement ratio, which means that thickness and excitation energy should be taken into account when interpreting an observed polarization dependence. From Fig. 5.18 (b) it can be seen that the enhancement ratio is close to unity for sample thicknesses up to 50 nm for all excitation wavelengths, while the enhancement becomes strongly anisotropic for thicker samples.
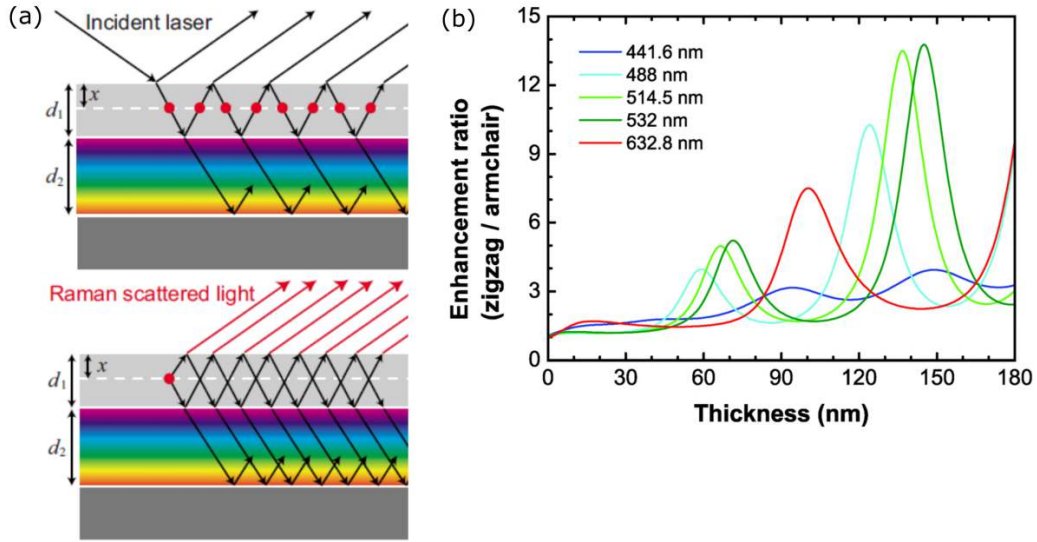
Figure 5.18: (a) Schematic of multiple reflection interference in the absorption (top) and scattering processes (bottom). The light gray layer with thickness d_1 represents the sample material, the colored layer with thickness d_2 the SiO_2 substrate, the dark gray - Si. x is the depth within the sample layer at which the scattering occurs. After [Yoon 2009]. (b) Enhancement ratio obtained by dividing the enhancement factor for the zigzag direction by the factor for the armchair direction for different excitation wavelengths for 90 nm black phosphorus on 300 nm SiO_2 on the Si substrate [Kim 2015].

The anomalous polarization dependence observed by us could be explained by the anisotropy of Raman enhancement factors. The large thickness of the measured flake (around 90 nm) suggests that the polarization state of the incident and scattered light can be significantly altered after passing through the sample due to multiple reflections. The two smaller minima observed in cross-polarization for the lower-energetic modes are oriented along the same axis which can be defined for the 322 cm^{-1} mode in copolarization. A possible explanation is that

this axis defines the direction parallel to the ripples and different Raman enhancement factors can be observed for light polarized parallel and perpendicular to the sample rippling direction. The direction of the axis is parallel to the long edges of the thinner part of flake (Fig. 5.13 (b)). It has been previously observed that franckeite has a preferred cleavage direction along the ripples, resulting in flakes with large length-to-width aspect ratio [Velický 2017b]. The crystalline orientation is most probably the same for the thinner and thicker part of the flake, which would confirm that the observed anisotropy of the Raman intensity is related to the corrugation.

5.6   Conclusions

An anomalous polarization dependence was observed for a 90 nm thick franckeite flake, which could not be explained by considering only the symmetry of the Raman modes. We explain the observed intensity pattern by the presence of optical anisotropy induced by rippling. The unexpected anisotropy of the 322 cm^{-1} A_1 mode in copolarization as well as the anomalous dependence observed for the two other analyzed modes in cross-polarization allowed us to define an optical anisotropy axis, which most likely is parallel to the direction of the one-dimensional rippling of the heterostructure. The observation of this anomalous polarization dependence could provide a means of identifying the rippling direction using Raman spectroscopy. However, as the Raman enhancement factor for anisotropic materials is sensitive to the sample thickness and excitation wavelength, these factors should be considered when using Raman spectroscopy to identify the rippling directions in franckeite.

Chapter 6

Conclusions

With the ongoing trend of miniaturization of electronic devices, semiconducting atomically thin layered materials are natural candidates for a variety of applications. In-plane anisotropy, exhibited by some of these compounds, provides an additional way of tuning the thermal and electrical transport and could be used to realize polarized light emission and detection. There is therefore a strong motivation to gain a better understanding of the fundamental properties of these materials. In this thesis, we have investigated the vibrational and optical properties of three layered materials with in-plane anisotropy: black phosphorus and rhenium disulfide, for which anisotropy results from the low symmetry of their crystal lattices, as well as franckeite, a natural heterostructure for which the incommensurate character of the two constituent lattices results in one-dimensional in-plane rippling.

In the first part of this thesis, we investigated the vibrational properties of black phosphorus using Raman spectroscopy. Compared to other layered materials, BP has exceptionally strong interlayer coupling. The high environmental instability of black phosphorus makes encapsulation a crucial step towards the realization of functional devices. We characterized h-BN/BP/h-BN few-layer thick encapsulated samples to understand how encapsulation can influence their structural and vibrational properties. The Raman line narrowing by around 1 cm^{-1} compared to previous studies was a proof of high material quality and, interestingly, allowed us to make the first experimental observation of the theoretically predicted change of the A_g^1 mode frequency in the surface layers of few layer thick black phosphorus. This frequency change is reflected in the appearance of a new Raman peak around 4 cm^{-1} above the main A_g^1 component for trilayer and and thicker samples. We observed a decrease of the intensity of this peak relative to the intensity of the main A_g^1 component with an increasing number of BP layers, consistent with the assignment of this mode to the vibrations of the atoms in the surface layers. Comparing the experimental observations with the results of theoretical calculations, we discussed the unexpected blueshift of the surface mode in the context of the changes of the lattice constants in the surface layers.

Rhenium disulfide is a material with triclinic symmetry which, in contrast to BP, has good environmental stability. An unresolved controversy exists in the literature concerning the nature of the fundamental bandgap of ReS$_2$. In particular, we were motivated by a theoretical study suggesting the indirect character of the bandgap for all thicknesses of rhenium disulfide apart

from the bilayer, for which a crossover to a direct bandgap in analogy W and Mo based TMDs was predicted. We performed PL characterization of ReS$_2$ as a function of the number of layers and could identify the two previously reported excitonic transitions around 1.55 eV (X$_1$) and 1.57 eV (X$_2$) characterized by strong linear anisotropy of absorption and emission. Based on the monotonous dependence of PL intensity on thickness we concluded that there is no change of the bandgap nature with the number of layers. The PL intensity was comparable for emission from both excitonic states, which given their relative energetic separation of around 20 meV indicates a non-thermalized exciton population. We suggest that a lower-lying state related to a smaller indirect bandgap is responsible for the fast depopulation of the direct states and the departure from the Boltzmann distribution for the number of excitons in the X$_1$ and X$_2$ states. Finally, we can support this conclusion by comparing the experimental observations with the predictions of a kinetic model describing the radiative recombination and scattering of excitons in the direct and indirect states.

The exfoliation of natural heterostructures provides an interesting alternative to the stacking of layers by deterministic placement, which carries the risk of introducing contamination and poor control over the layer orientation. Franckeite is a natural p-type type II heterostructure for which the incommensurate character of the tetragonal and hexagonal-like layers results in a one-dimensional structural deformation. This can lead to the anisotropy of the electrical transport and optical properties. We investigated the polarization dependence of the Raman mode intensity for exfoliated franckeite flakes to establish a method of determining the in-plane rippling direction. We observed an anomalous polarization dependence of the 186 cm^{-1} and 253 cm^{-1} peaks related to the Q-layer and the 322 cm^{-1} H-layer A_g^1 Raman mode. The anisotropy axis observed in these measurements is parallel to one of the cleavage directions of the flakes, which likely corresponds to the direction along the one-dimensional ripples.

Appendices

Appendix A

Publications

Publications based on the results of this thesis:

1. J. M. Urban, M. Baranowski, A. Surrente, D. Włodarczyk, A. Suchocki, G. Long, Y. Wang, Ł. Kłopotowski, N. Wang, D.K. Maude and P. Płochocka
   Observation of A_g^1 Raman mode splitting in few layer black phosphorus encapsulated with hexagonal boron nitride.
   Nanoscale, 2017,9, 19298-19303

2. J. M. Urban, M. Baranowski, A. Kuc, Ł. Kłopotowski, A. Surrente, Y. Ma, D. Włodarczyk, A. Suchocki, D. Ovchinnikov, T. Heine, D. K. Maude, A. Kis, P. Płochocka
   Non equilibrium anisotropic excitons in atomically thin ReS_2.
   2D Materials, 2019,6 015012

3. M. Birowska, J. Urban, M. Baranowski, D. K. Maude, P. Płochocka and Nevill Gonzalez-Szwacki
   The impact of hexagonal boron nitride encapsulation on the structural and vibrational properties of few layer black phosphorus.
   Nanotechnology, 2019, 30(19):195201

Other publications:

1. M. Baranowski, J. M. Urban, N. Zhang, A. Surrente, D. K. Maude, Z. Andaji-Garmaroudi, S. D. Stranks and P. Płochocka
   Static and Dynamic Disorder in Triple-Cation Hybrid Perovskites.
   The Journal of Physical Chemistry C, 2018, 122 (30), pp 17473–17480

2. M. Baranowski, A. Surrente, Ł. Klopotowski, J. M. Urban, N. Zhang, D. K. Maude, K. Wiwatowski, S. Mackowski, Y. C. Kung, D. Dumcenco, A. Kis , and P. Płochocka
   Probing the Interlayer Exciton Physics in a $MoS_2/MoSe_2/MoS_2$ van der Waals Heterostructure.
   Nano Letters, 2017, 17 (10), pp 6360–6365

3. A. Mahboubi Soufiani, Z. Yang, T. Young, A. Miyata, A. Surrente, A. Pascoe, K. Gałkowski, M. Abdi-Jalebi, R. Brenes, J. Urban, N. Zhang, V. Bulovic, O. Portugall,

Y.-B. Cheng, R. J. Nicholas, A. Ho-Baillie, M. A. Green, P. Płochocka and S. D. Stranks
Impact of microstructure on the electron-hole interaction in lead halide perovskites.
Energy & Environmental Science, 2017,10, 1358-1366

Appendix B

Résumé de la thèse en français

Dans cette annexe, nous présentons un résumé en français de ce travail de thèse. Le contenu du résumé ainsi que les figures utilisées sont strictement fidèles à la version anglaise. Aucune information nouvelle n'est donc ici présentée.

B.1   Introduction

Le chapitre 1 est une introduction aux études des matériaux bidimensionnelles et décrit les propriétés des matériaux bidimensionnelles anisotropes étudiés dans cette thèse.

B.1.1   Propriétés des matériaux en couches bidimensionnelles

L'intérêt pour les matériaux bidimensionnels a été suscité par la découverte d'un moyen facile de produire du graphène en une et quelques couches par exfoliation micromécanique [Novoselov 2004]. De nombreux autres matériaux partagent les caractéristiques de la structure stratifiée du graphite (fortes liaisons dans le plan et seulement de faibles interactions van der Waals entre les plans [Novoselov 2005]). Les composés stratifiés comprennent les métaux, les semi-métaux, les isolants ainsi que les semi-conducteurs, et leurs caractéristiques peuvent changer en fonction du nombre de couches [Duong 2017]. La réduction de la dimensionnalité a une forte influence sur les propriétés des matériaux stratifiés et les propriétés d'une monocouche peuvent être radicalement différentes de celles des matières en vrac [Novoselov 2005]. En raison des effets de couplage entre couches et du confinement quantique changeant, la taille et la nature de la bande interdite peuvent être facilement réglées en modifiant le nombre de couches. Les propriétés optoélectroniques des matériaux bidimensionnels sont dominées par les effets excitoniques, qui sont particulièrement robustes en raison de la grande énergie de liaison des exciton et de leurs grandes forces d'oscillateur [Velický 2017c]. Dans les matériaux 2D, la dimensionnalité réduite peut fortement modifier les propriétés excitoniques par rapport au volume. En raison du confinement spatial dans le plan, l'énergie de liaison de l'exciton est augmentée. L'écrantage diélectrique modifié est un autre facteur qui influence fortement l'énergie de liaison de l'exciton dans les matériaux bidimensionnels. La figure B.1 montre l'influence de la réduction des dimensions et de l'écrantage diélectrique sur la structure électronique et l'énergie de liaison d'un exciton.
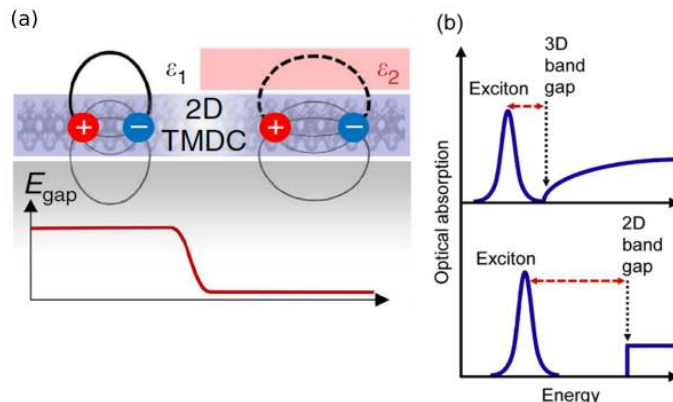
Figure B.1: (a) Influence de l'environnement diélectrique sur l'énergie de bande interdite et sur l'interaction électron-trou. D'après [Raja 2017]. (b) Absorption optique en fonction de l'énergie pour les matériaux en vrac et 2D. D'après [Chernikov 2014].

B.1.2   Matériaux en couches anisotropes

En raison de leur faible symétrie cristalline, certains matériaux ont des propriétés physiques optiques, électroniques, thermiques et mécaniques dépendantes de la direction [Tian 2016]. L'anisotropie dans le plan offre un degré de liberté supplémentaire pour manipuler les propriétés déjà fortement accordables des matériaux en couches. Ces matériaux comprennent parmi d'autres le phosphore noir [Ling 2015], l'arsenic noir [Chen 2018b] et l'antimonène [Wang 2015a], GeSe [Yang 2018], $WTeS_2$ [Zhou 2018], ReS_2 et $ReSe_2$ [Hart 2016] ou hétérostructures dans lesquelles l'anisotropie est un résultat de l'interaction des différents matériaux avec des réseaux incommensurables. Dans cette thèse, nous avons étudié les propriétés de trois matériaux stratifiés à anisotropie dans le plan: le phosphore noir, le disulfure de rhénium et franckéite, une hétérostructure naturelle.

B.1.3   Phosphore noir

Contrairement au graphène et à de nombreux autres matériaux stratifiés, les atomes du phosphore en phosphore noir (BP – black phosphorus) subissent une hybridation sp^3 et forment une structure alvéolaire plissée. L'hybridation spécifique des atomes dans le phosphore noir conduit à une interaction entre couches beaucoup plus forte que pour la plupart des autres matériaux en couches. Les atomes de phosphore se trouvent dans deux plans parallèles et on peut distinguer deux directions non équivalentes dans le plan : zigzag et armchair. La figure B.2 montre la structure cristalline et électronique du phosphore noir. Le couplage entrecouche exceptionnellement fort explique la forte accordabilité de l'énergie de la bande interdite du phosphore noir qui change de 0,3 pour le vrac à environ 2 eV pour une monocouche [Chaves 2017]. Les conséquences de l'hybridation spécifique sont la forte réactivité et l'instabilité environnementale de BP, ce qui constitue un obstacle important du point de vue de la production de dispositifs. L'encapsulation dans des matériaux chimiquement inertes est une approche courante pour prévenir la dégradation du phosphore noir dans les conditions ambiantes.
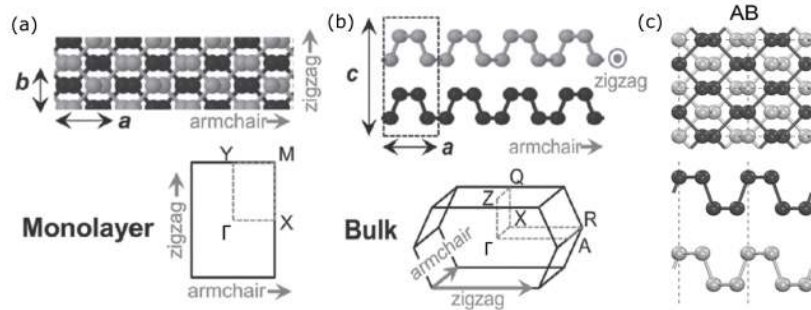
Figure B.2: Vue latérale (à gauche) et d'en haut (à droite) de la structure cristalline de BP et des zones de Brillouin de (a) monolayer et (b) bulk BP et (c) l'ordre d'empilement AB le plus courant. D'après [Chaves 2017].

B.1.4 Disulfure de rhénium

Un autre exemple de matériaux stratifiés à forte anisotropie dans le plan est celui des dichalcogénures de rhénium. Le disulfure (ReS_2) et le diséléniure ($ReSe_2$) de rhénium, contrairement aux dichalcogénures de métaux de transition du groupe VI qui forment les structures H (hexagonales) ou 1T (octaédriques), cristallisent en phase 1T' distordue avec une symétrie triclinique [Jariwala 2016, Tian 2016]. Ils sont stables dans des conditions ambiantes, ce qui les rend intéressants du point de vue des applications. Les atomes de Re forment des chaînes métalliques le long de la direction du cristal *b* [Fang 1997], la structure cristalline est montrée à la figure B.3. L'anisotropie structurelle de ReS_2 entraîne l'anisotropie du transport thermique et électrique. Les propriétés optiques de ReS_2 sont dominées par deux excitons anisotropes énergétiquement non dégénérées [Jariwala 2016] à des énergies d'environ 1,53 eV et 1,57 eV observées en absorption et émission lumineuses fortement anisotrope. Malgré des études intensives, des controverses subsistent concernant la structure électronique et la nature de la bande interdite fondamentale de ReS_2. Il a notamment été mis en question le fait que ReS_2 subisse une transition de la bande interdite indirecte à une bande interdite directe avec une épaisseur décroissante.

B.1.5 Franckéite

La possibilité d'intégrer différents matériaux 2D dans des piles multicouches a ouvert la voie au champ de recherche sur des hétérostructures de van der Waals [Wang 2014, Novoselov 2016]. Les hétérostructures peuvent être formées artificiellement par synthèse ascendante par diverses techniques [Jung 2014] ou par placement déterministe. L'approche de placement déterministe la plus couramment utilisée permet de concevoir des structures dont la composition et les propriétés sont pensées sur mesure. Cette méthode présente toutefois un risque de contamination et de présence d'adsorbats non désirés. Il est également techniquement difficile de contrôler l'orientation correcte des couches. Une autre approche prometteuse est l'exfoliation descend-
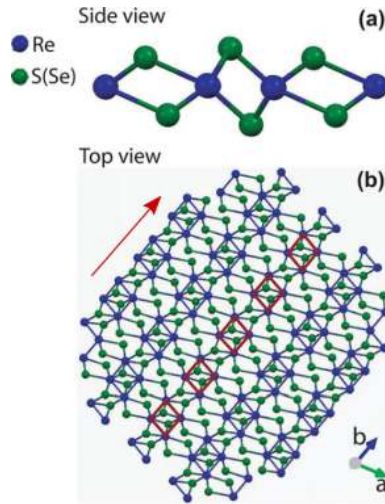
Figure B.3: Schéma de la structure cristalline du ReX$_2$ 1T' (a) vue latérale et (b) d'en haut. Les atomes de rhénium sont représentés en bleu et les atomes de chalcogénure en vert. La flèche rouge indique la direction des chaînes atomiques de Re. D'après [Jariwala 2016].

ante des hétérostructures naturelles. Plusieurs minéraux d'origine naturelle se cristallisent sous forme stratifiée avec différents types de couches alternantes dans le sens de l'empilement et maintenues ensemble par les forces de van der Waals, comme la cylindrite, la coiraite, la potosiite ou la franckéite [Williams 1988]. Une formule chimique approximative de la franckéite est FeSn$_3$Pb$_5$Sb$_2$S$_{14}$ bien que la composition exacte puisse varier [Wang 1995, Heitz 1961]. Franckéite est composé de couches pseudo-tétragonales (appelées Q ou t) et pseudo-hexagonales (H) superposées dans une séquence HQHQ. La franckéite est un semi-conducteur de type p [Burzuri 2018], la bande de valence est composée principalement d'orbitales de la couche H tandis que la bande de conduction est composée des fonctions d'onde de la couche Q, faisant de la franckeite une hétérostructure de type II [Molina-Mendoza 2017] (Figure B.4). L'incommensurabilité de deux couches voisines introduit une contrainte qui peut être relâchée par une déformation structurelle. Ceci conduit à mettre en avant une autre caractéristique de la franckéite: l'ondulation dans le plan avec une périodicité dans la direction [010]. L'anisotropie et la déformation dans le plan induites par les ondulations peuvent avoir une forte influence sur les propriétés optiques et électroniques du matériau.

B.2 Techniques expérimentales

Le chapitre 2 décrit la mise en place de techniques expérimentales utilisées pour étudier nos échantillons.
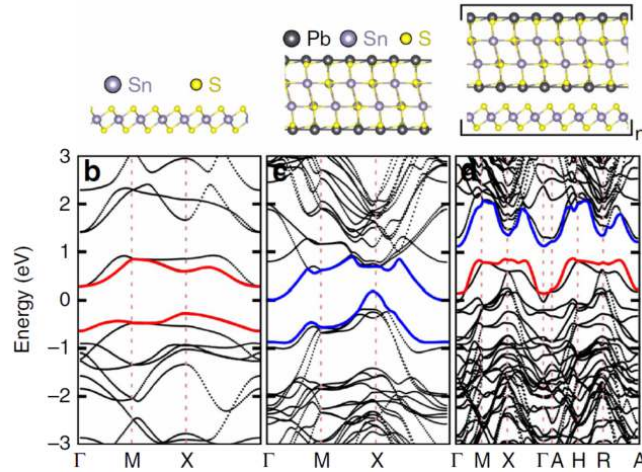
Figure B.4: Structure de bandes électroniques de la couche H (à gauche), de la couche Q (au milieu) et du cristal de franckeite (à droite). Les états de bande fournis par la couche H sont marqués en rouge, les états de bande fournis par la couche Q en bleu. D'après [Molina-Mendoza 2017].

B.2.1 Propriétés optiques des matériaux anisotropes

La première partie du chapitre 2 présente les propriétés optiques des matériaux anisotropes et explique comment l'anisotropie de la susceptibilité diélectrique entraîne le caractère directionnel dépendant de l'absorption et de la propagation de la lumière dans le milieu.

B.2.2 Méthodes spectroscopiques

Les méthodes spectroscopiques utilisées dans cette thèse, en particulier la photoluminescence, la réflectivité et la spectroscopie Raman sont présentées dans la deuxième partie du chapitre 2. Les principes de la spectroscopie Raman y sont expliqués en détail. La figure B.5 (a) montre une illustration schématique des niveaux d'énergie pour différents processus de diffusion de la lumière. Le photon entrant fait passer le système de l'état de base à l'état intermédiaire, à partir duquel il se détend en émettant un photon de même longueur d'onde (diffusion élastique de Rayleigh) ou de longueur d'onde différente (diffusion Raman Stokes- et anti-Stokes). La figure B.5 (b) montre les schémas d'un spectre Raman typique du premier ordre avec les lignes liées aux processus Stokes, Rayleigh et anti-Stokes. Dans la dernière partie,nous décrivons l'installation de -spectroscopie à LNCMI-Toulouse. Le schéma du montage expérimental est illustré à la figure B.6.

B.3 Propriétés vibratoires du phosphore noir encapsulé

Dans le chapitre 3, nous présentons une étude de l'influence de l'encapsulation du h-BN sur les propriétés vibratoires de couches de phosphore noir.
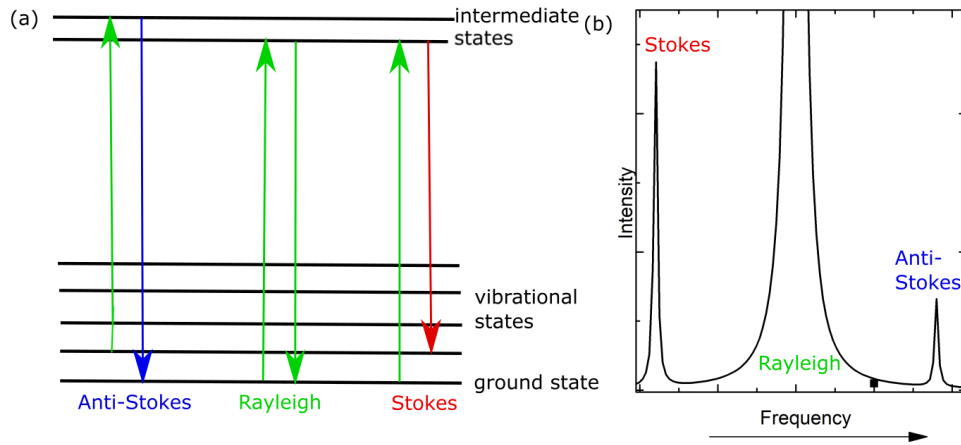
Figure B.5: (a) Le schéma des niveaux d'énergie dans les processus de diffusion élastique et inélastique. Les flèches marquent les photons entrants et diffusés. (b) Le schéma d'un spectre Raman montrant les lignes de Stokes et anti-Stokes et la ligne de Rayleigh à dispersion élastique.
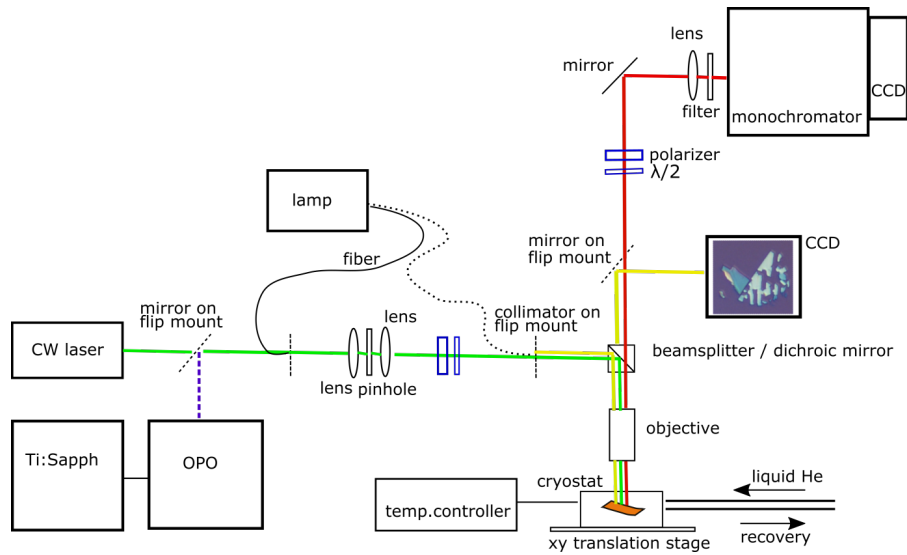
Figure B.6: Montage expérimental utilisé pour la μ-spectroscopie.

B.3.1   Description des échantillons

Les échantillons étudiés dans le cadre de ces travaux étaient des flocons de BP épais de quelques couches encapsulés dans h-BN multicouche et déposés sur des substrats de Si/SiO$_2$. La technique détaillée de production des hétérostructures encapsulées est décrite dans le travaux de [Chen 2015]. La figure B.7 montre les schémas du processus d'encapsulation et la structure de

l'échantillon h-BN/BP/h-BN.
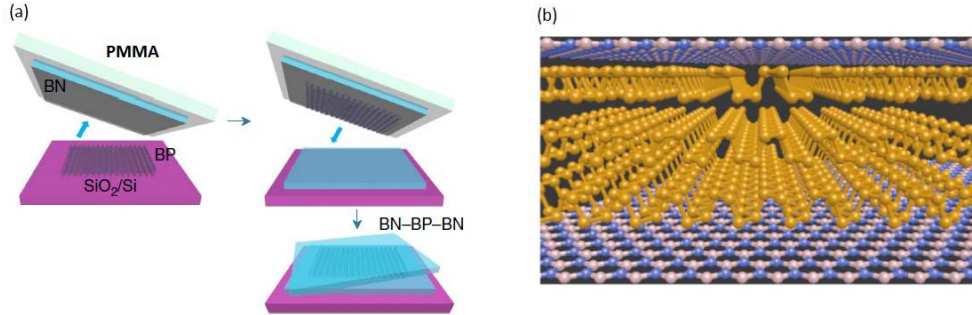
Figure B.7: (a) (a) Schéma du processus de fabrication de l'échantillon encapsulé, d'après [Chen 2015] et (b) structure cristalline du phosphore noir encapsulé en h-BN.

B.3.2 Études μ-Raman du phosphore noir encapsulé

Des mesures de spectroscopie Raman ont été utilisées pour caractériser les échantillons étudiés. Une ligne laser de 532 nm avec une puissance de 630 W a été utilisée pour l'excitation. La figure B.8 (a) montre les schémas des trois modes Raman qui sont observés dans la géométrie de rétrodiffusion avec la direction du mouvement des atomes marqués par des flèches et (b) un spectre Raman typique que nous avons mesuré sur un épais flocon de BP. Le mode A_g^1 autour de 365 cm^{-1} correspond au mouvement des atomes dans la direction z hors plan, le mode A_g^2 autour de 470 cm^{-1} au mouvement principalement dans la direction x (*armchair*) et le mode B_{2g} autour de 440 cm^{-1} pour le mouvement dans la direction y (*zigzag*).
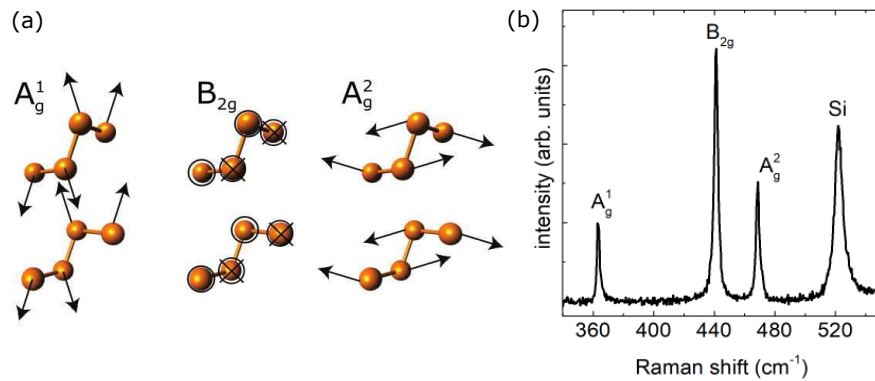
Figure B.8: (a) Les modes vibratoires Raman A_g^1, A_g^2 et B_{2g}. Des flèches marquent les directions du déplacement des atomes. (b) Spectre Raman typique (excitation à 532 nm) d'un flocon de BP épais sur un substrat Si/SiO$_2$.

Il a déjà été noté que des changements par rapport au spectre d'une monocouche peuvent être observés pour un matériau de plusieurs couches. Le pic B_{2g} ne montre que de très faibles variations d'énergie tandis que le pic A_g^2 montre un décalage vers le rouge plus fort et avec une épaisseur croissante. Ceci nous a permis de déterminer l'épaisseur des différentes parties des flocons en fonction du décalage relatif des modes Raman $\Delta(A_g^2 - B_{2g})$, comme montré sur la Fig.B.9.
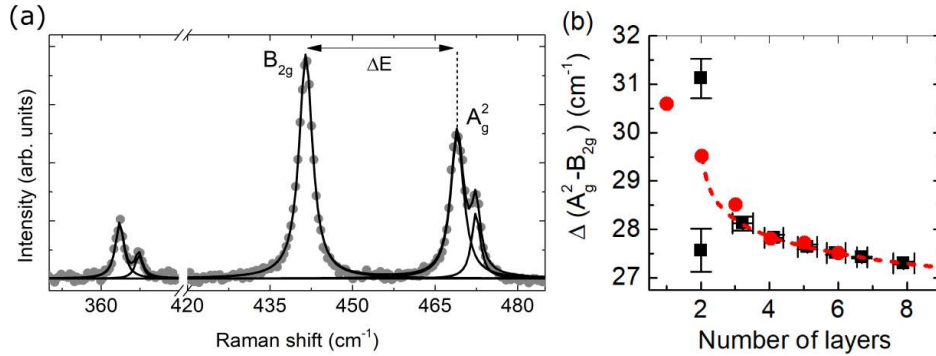
Figure B.9: (a) Spectre Raman d'un mince flocon de BP (points) et les fonctions de Lorentz ajustées (lignes pleines). ΔE est marqué par des flèches. (b) séparation énergétique $\Delta(A_g^2 - B_{2g})$ des modes en fonction du nombre calculé de couches. Les valeurs expérimentales obtenues dans ce travail sont indiquées en noir; les points rouges représentent les données numérisées de [Lu 2014]; la ligne en pointillés indique la fonction ajustée.

Après avoir déterminé le nombre de couches, nous avons pu analyser les différences entre les spectres Raman mesurés pour différentes épaisseurs. Les figures B.10 (a) et (b) montrent les pics Raman en fonction du nombre de couches et des fonctions de Lorentz adaptées. Le pic sur le côté haute énergie d'A_g^2 a déjà été observé auparavant et peut être assigné comme le mode A_g^2 (B_{2u}) résultant de la conversion de Davydov de deux modes actifs à infrarouge en flocons multicouches [Sugai 1985, Phaneuf-L'Heureux 2016, Ribeiro 2018]. Étonnamment, un mode relativement faible montrant une dépendance de l'épaisseur apparaît autour de 3-4 cm^{-1} au côté haute énergie du pic principal A_g^1. Ce nouveau mode a pu être observé pour les échantillons pour les échantillons d'une épaisseur de 3 couches ou plus, mais est absent pour les échantillons bicouches.

L'intensité du mode nouvellement observé par rapport au composant principal du pic A_g^1 diminue en fonction du nombre de couches. Une autre caractéristique intéressante est l'absence de ce mode pour la bicouche. Un changement des fréquences de modes Raman dans les couches superficielles par rapport aux couches intérieures a été théoriquement prédit pour le phosphore noir non encapsulé [Hu 2016]. Les calculs ont suggéré une division des fréquences pour les épaisseurs à partir de trois couches pour les modes A_g^1 et B_{2g} mais pas dans le cas du mode A_g^2. L'effet se produit en raison des différentes caractéristiques de mouvement des atomes dans la surface et dans les couches intérieures. Sur la base de ces observations, nous suggérons que le mode nouvellement observé provient des couches de surface de BP qui sont en contact avec le h-BN encapsulant tandis que la composante basse énergie est liée aux couches internes.
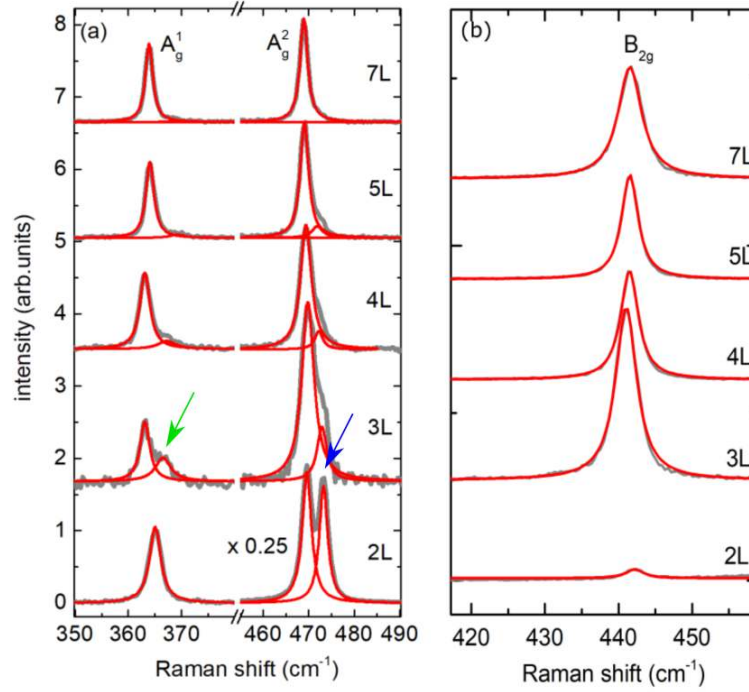
Figure B.10: Les modes (a) A_g^1 et A_g^2 et (b) B_{2g} en fonction du nombre de couches. Les données expérimentales sont affichées en gris et les fonctions Lorentziennes ajustées en rouge. La flèche verte marque le mode nouvellement observé, et la flèche bleue le mode résultant de la séparation de Davydov.

La figure B.11 (a) montre les énergies du mode A_g^1 «intérieur» et «surface» en fonction du nombre de couches obtenues à partir de nos données (rouge), ainsi que calculées théoriquement à partir des références [Hu 2016] (noir) et [Birowska 2019] (vert et bleu) pour BP nu et encapsulé. La différence d'énergie entre les modes «intérieur» et «surface» est comparable pour les données expérimentales et les différentes approches théoriques. Dans le panel (b), les positions et intensités relatives à nos données expérimentales et aux calculs théoriques sont comparées. Une discussion détaillée est présentée dans le chapitre 3.

Nos résultats suggèrent que l'encapsulation, tout en étant un moyen efficace de protéger le matériau, peut également avoir une influence significative sur les propriétés du matériau, en particulier pour les échantillons les plus fins.

B.4 Excitons anisotropes non équilibrés dans ReS₂

Le chapitre 4 présente des études optiques du disulfure de rhénium. Dans la première partie sont exposés les choix présidant à notre étude, et notamment la controverse concernant la nature de la bande interdite de ReS2. Les sections suivantes décrivent la détermination de l'épaisseur et de l'ordre d'empilement des échantillons étudiés en utilisant la spectroscopie Raman ainsi
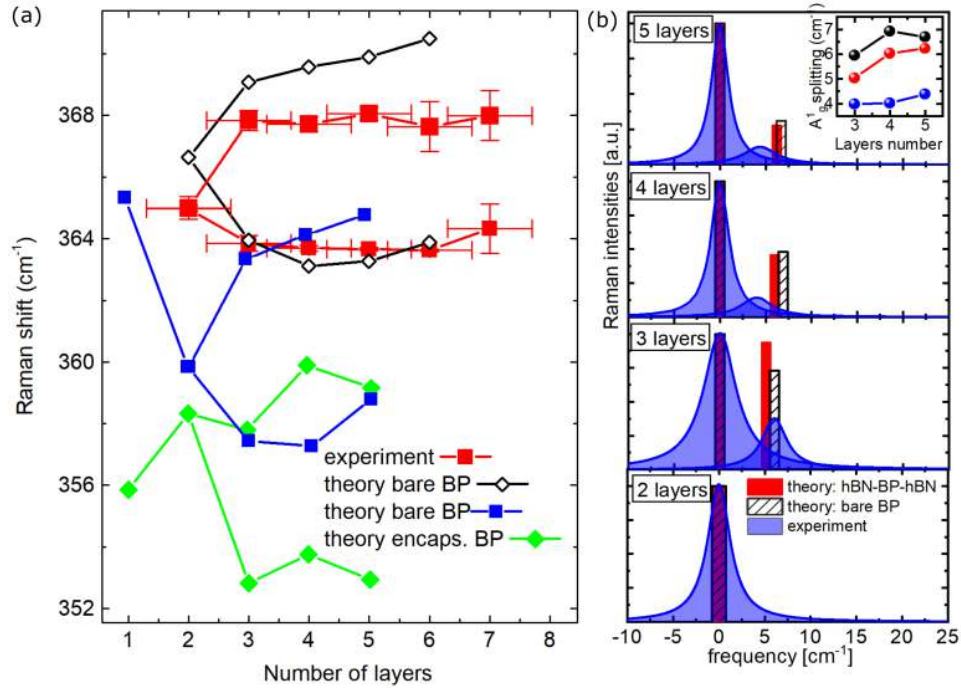
Figure B.11: (a) Énergies des branches intérieures et surface de la vibration A_g^1 en fonction du nombre de couches : de nos données (rouge) et des prévisions théoriques [Hu 2016] (noir) et [Birowska 2019] (bleu - BP nu et vert - BP encapsulé avec h-BN). (b) Intensité relative et division du mode A_g^1 en fonction du nombre de couches sur la base de nos données expérimentales (pics Lorentziens, les intensités sont normalisées à la composante principale A_g^1, les largeurs correspondent au moyen FWHM du pic Raman, la fréquence de la composante principale est fixée à 0) et les calculs pour BP nu (barres noires) et encapsulé (barres rouges). L'encadré montre la différence d'énergie entre les pics intérieurs et de surface en fonction du nombre de couches. D'après [Birowska 2019].

que les mesures de μ-réflectivité et μ-photoluminescence effectuées pour étudier les transitions excitoniques. D'après ces résultats, nous concluons que la photoluminescence observée est une émission liée aux états excitoniques directs. La dernière partie de ce chapitre décrit un modèle cinétique qui peut être utilisé pour expliquer les observations expérimentales et parvenir à des conclusions sur la nature indirecte de la bande interdite fondamentale.

B.4.1 Motivations

Des résultats expérimentaux et théoriques contradictoires existent dans la littérature concernant la nature de la bande interdite fondamentale de ReS_2. Notre étude des propriétés photolumin-escentes du ReS_2 présentée dans ce chapitre a été motivée par les calculs théoriques de A. Kuc et les collaborateurs du groupe du Professeur T. Heine prédisant le caractère indirect de la bande interdite pour toutes les épaisseurs de ReS_2 à l'exception de la bicouche. Les calculs

DFT présentés à la Fig. B.12 suggèrent une diminution de la bande interdite directe au point Γ d'environ 1,5 eV en monocouche à 1,2 eV pour quatre couches, et la présence d'une bande indirecte plus petite pour toutes les épaisseurs à l'exception de la bicouche.
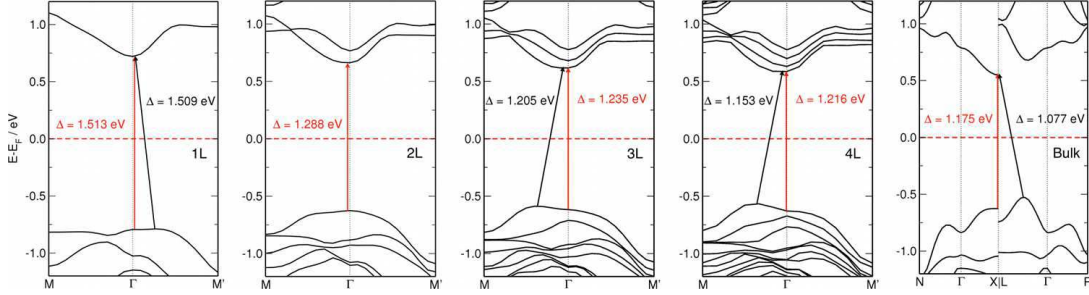
Figure B.12: Structure de bandes électroniques calculée pour différents nombres de couches ReS$_2$. Les flèches rouges marquent la bande interdite directe, les flèches noires la bande interdite fondamentale. D'après [Urban 2019].

B.4.2   Spectroscopie Raman de ReS$_2$

Nous avons étudié des flocons de ReS$_2$ préparés par exfoliation micromécanique et déposés sur un substrat de Si dopé de manière dégénérative recouvert de 270 nm de SiO$_2$. Nous avons effectué une étude de spectroscopie Raman à résolution spatiale sur la surface de plusieurs dizaines de μm en utilisant λ_{exc} =532 nm. Dans notre analyse, nous nous sommes concentrés sur les quatre modes Raman dans la gamme 130-170 cm^{-1} et avons ajusté les spectres dans cette région en utilisant les fonctions lorentziennes. La figure B.13 (a) montre les spectres Raman acquis à différentes positions sur le flocon dont l'image optique est montrée sur la figure B.13 (c). Un contraste optique différent sur la micrographie indique un changement d'épaisseur. Les spectres acquis sur les différentes parties de l'échantillon sont numérotés dans le panneau (a) selon les points marqués en (c). Dans le panneau (b), les schémas des modes vibrationnels A_g^1 et A_g^4 d'après [McCreary 2017] sont affichés.

Les modes A_g^1 et A_g^4 se déplacent dans des directions opposées en fonction de l'épaisseur. Sur la base de la différence d'énergie observée, que nous avons comparée aux résultats d'études Raman précédentes [Qiao 2016], nous avons pu identifier l'ordre d'empilement anisotrope dans notre échantillon et attribuer un certain nombre de couches à chaque partie du flocon. La figure B.14 (b) montre la différence d'énergie entre ceux deux modes ΔE en fonction du nombre de couches déterminé par [Qiao 2016] pour le polytype anisotrope et isotrope de ReS$_2$ ainsi que des points de données obtenus à partir des spectres acquis par nous-mêmes sur différentes régions de l'échantillon. Une fonction exponentielle a été ajustée aux données expérimentales et sur la base de cette dépendance, le nombre estimé de couches a été calculé pour tous les spectres de la carte Raman. La figure B.14 (c) montre le décalage des modes A_g^1 et A_g^4 par rapport à la valeur en vrac en fonction du nombre de couches.
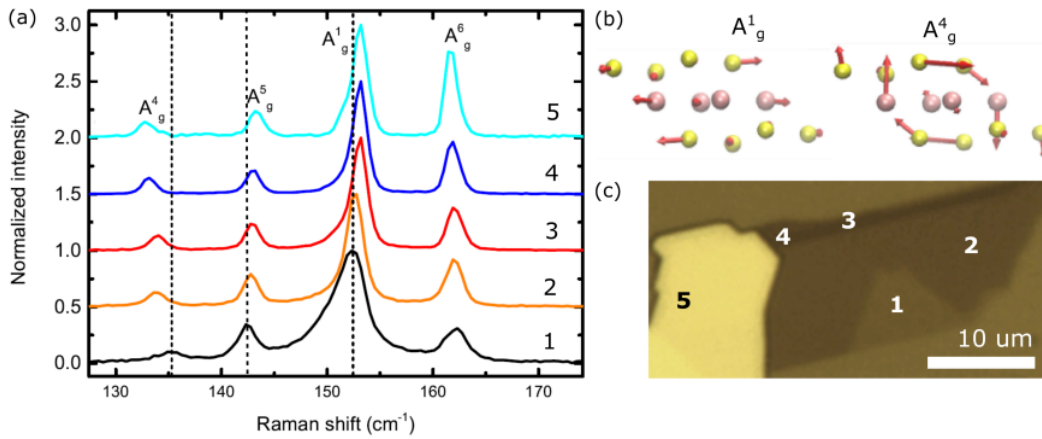
Figure B.13: (a) Spectres Raman acquis par excitation à 532 nm en différentes positions sur le flocon ReS$_2$ montrant les quatre pics caractéristiques dans la gamme 130-170 cm^{-1}. Les spectres sont normalisés à l'intensité du mode A_g^1. (b) Vecteurs propres des modes Raman A_g^1 et A_g^4. Reproduit de [McCreary 2017]. (c) Image optique du flocon avec les positions marquées où les spectres indiqués dans le panneau (a) ont été acquis.
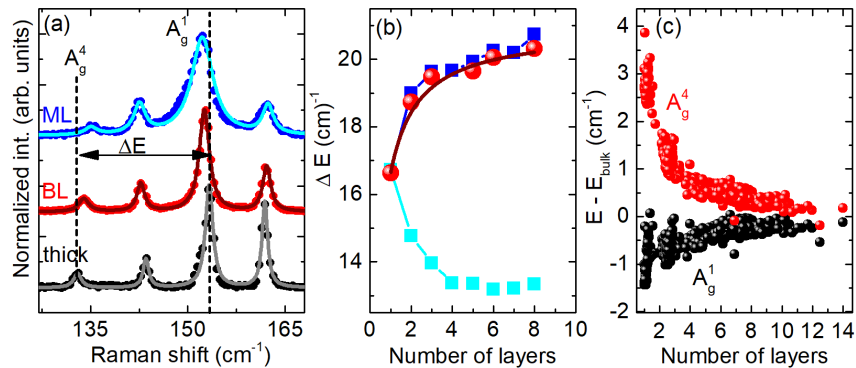
Figure B.14: (a) Spectres Raman montrant les modes A_g^1 et A_g^4 pour différentes épaisseurs; (b) décalage relatif entre les pics A_g^1 et A_g^4 en fonction du nombre de couches pour l'ordre d'empilement isotrope (bleu clair) et anisotrope (bleu foncé) de la référence [Qiao 2016], des points de données expérimentales de ce travail (en rouge) et une fonction exponentielle ajustée; (c) les décalages des énergies de pic A_g^1 et A_g^4 relatifs aux énergies de ReS$_2$ en vrac en fonction du nombre de couches calculé.

B.4.3 Photoluminescence et réflectivité

Des mesures de photoluminescence et de contraste de la réflectivité ont été effectuées pour identifier les transitions excitoniques et caractériser l'absorption et l'émission en fonction de la polarisation linéaire de détection et d'excitation, le nombre de couches ReS$_2$ et de la température. La figure B.15 montre un contraste de réflectivité non polarisé et un spectre de photoluminescence d'un épais flocon de ReS$_2$ à 4 K. Les deux transitions excitoniques les plus basses X$_1$ et X$_2$ peuvent également être identifiées en PL à des énergies d'environ 1,55 eV et 1,565 eV, avec un déplacement de Stokes de 10 méV environ. Les flèches marquent les transitions dans le spectre de photoluminescence, l'émission liée à l'état excitonique X$_1$ permet d'observer deux maxima proches. Il est intéressant de noter que l'intensité des émissions X$_1$ et X$_2$ se situe dans une plage similaire.
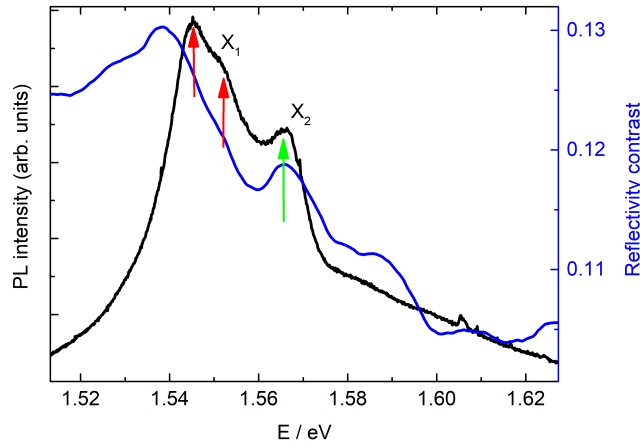
Figure B.15: Spectre de photoluminescence et de contraste de la réflectivité non polarisé pour un flocon épais de ReS$_2$. Les flèches marquent les deux pics que l'on peut distinguer dans l'émission X$_1$ et l'émission X$_2$.

Ensuite, nous avons effectué des mesures de photoluminescence sur le flocon épais en analysant la polarisation linéaire lors de la détection. La figure B.16 (a) montre les spectres pour deux angles de détection choisis et les fonctions ajustées. La figure B.16 (b) montre la dépendance angulaire des intensités d'émission X$_1$ et X$_2$. La dépendance de polarisation observée est en accord avec les études antérieures des deux états excitoniques les plus bas.

La figure B.17 (a) montre les spectres PL acquis sur des régions d'épaisseurs différentes. Un décalage vers le bleu et une diminution de l'intensité de l'émission peuvent être observés pour une diminution de l'épaisseur. La figure B.17 (b) montre les énergies des maxima des émissions X$_1$ et X$_2$ et leur séparation en fonction du nombre de couches. Notre observation est en accord avec les études précédentes qui ont montré une diminution monotone de l'intensité PL et un décalage vers le bleu de l'émission PL avec une épaisseur décroissante [Tongay 2014, Aslan 2016].
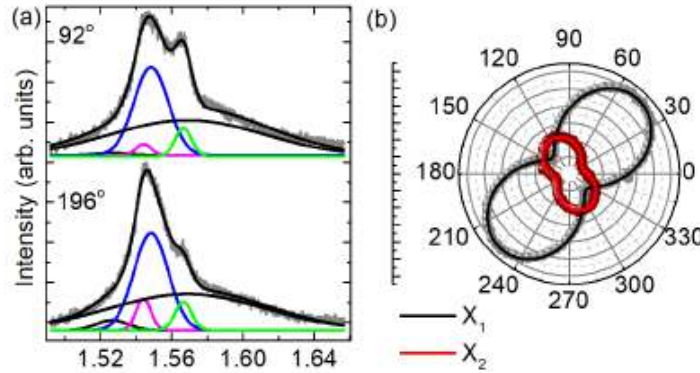
Figure B.16: (a) Spectres de photoluminescence pour deux angles de détection de polarisation et ajustements des cinq pics et de l'ajustement cumulatif. Le pic 1 et pic 2 (magenta et bleu) correspondent à la transition X_1, et le pic 3 (vert) à la transition X_2. (b) Diagramme polaire des intensités de transition X_1 et X_2 (l'intensité X_1 est la somme de la surface des pics 1 et 2).
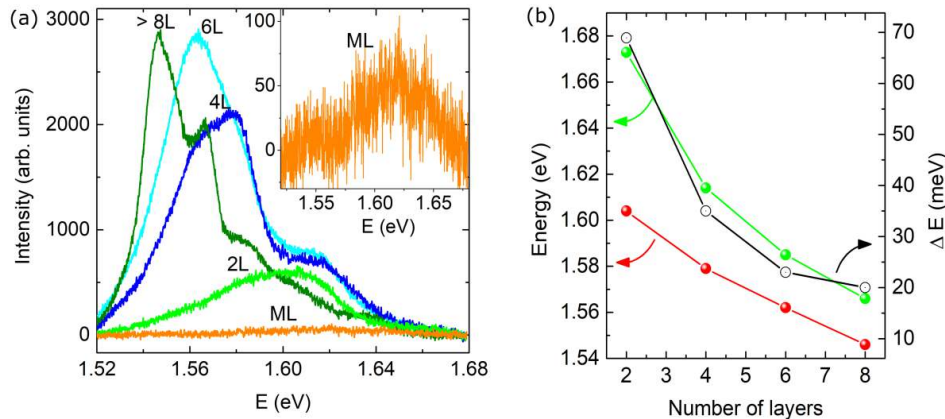
Figure B.17: (a) Spectre de photoluminescence pour différentes épaisseurs de ReS2; (b) les énergies des émissions X_1 et X_2 et leur séparation énergétique en fonction du nombre de couches.

La figure B.18 (a) montre une carte de l'intensité de photoluminescence intégrée sur toute la gamme spectrale. Une augmentation de l'intensité d'émission avec le nombre de couches est visible. La figure B.18 (b) montre l'intensité intégrée en fonction du nombre de couches. La dépendance monotone suggère que la nature de la bande interdite ne change pas avec l'épaisseur pour ReS_2.

B.4.4   Modèle cinétique

Pour décrire nos résultats de manière quantitative et expliquer la nature de l'émission observée, nous proposons un modèle cinétique pour la génération, la recombinaison et la diffusion des
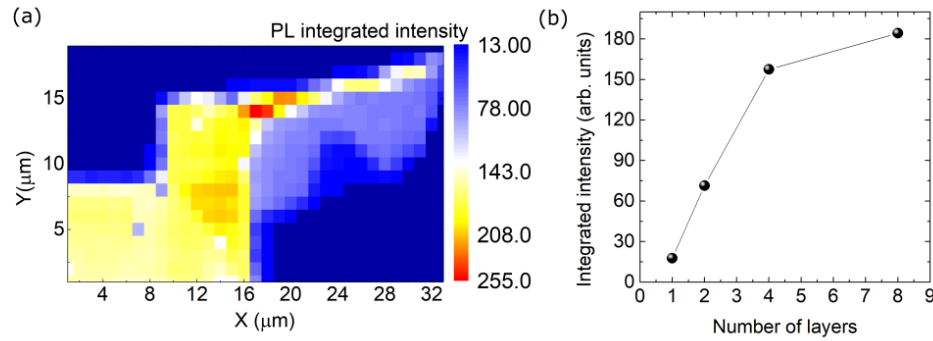
Figure B.18: (a) Intensité de photoluminescence intégrée en fonction de la position spatiale. (b) Intensité intégrée en fonction du nombre de couches.

excitons dans les états X_1 et X_2. Un schéma du modèle des états excitoniques est présenté par la figure B.19. Deux états excitoniques directs X_1 et X_2 se trouvent au-dessus d'un état X_I lié à une bande interdite indirecte. Sous excitation optique à onde continue, des excitons sont créés avec un taux de génération g dans les deux états X_1 et X_2. Un exciton à l'état X_2 peut subir une recombinaison radiative, décrite par une constante de temps τ_r, et diffuser dans l'état direct inférieur X_1 avec une constante de temps τ_x ou dans l'état indirect avec une constante de temps τ_s. Un exciton dans l'état X_1 peut aussi se recombiner radiativement ou se diffuser à l'état indirect. Nous pourrions décrire les processus de création et de recombinaison en termes d'équations de taux décrivant l'évolution de la population d'excitons dans les trois états.
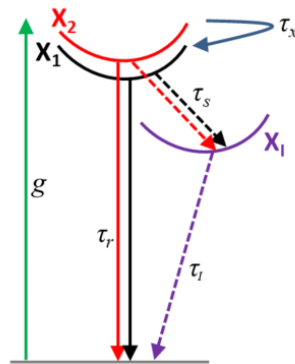
Figure B.19: Le modèle des états excitoniques proposé. X_1 et X_2 sont les états excitoniques directs et X_I est un état excitonique lié à la bande interdite indirecte.

L'intensité de photoluminescence observée dépend du nombre d'excitons dans un état ainsi que de la probabilité de la recombinaison radiative de cet état. La figure B.20 montre le rapport calculé du nombre d'excitons dans les états X_1 et X_2 (N_1/N_2), le rapport de probabilité de

recombinaison radiative P_1/P_2 et le rapport d'intensité d'émission prévue I_1/I_2 en fonction du rapport de temps de recombinaison et diffusion τ_r/τ_x. Cette dépendance a été calculée pour différentes valeurs de τ_x/τ_s. Sur la base de ce modèle, en supposant une plage physiquement plausible de rapports de temps de recombinaison et diffusion ($\tau_r/\tau_x > 1$), nous pourrions conclure que le rapport d'intensité de photoluminescence observé expérimentalement pour le flocon épais ne peut pas être expliqué en supposant l'absence de la bande indirecte (correspondant au τ_s infini, ligne rouge sur figure B.20). Nous suggérons donc un caractère indirect du bandap fondamental pour ReS_2 indépendamment du nombre de couches.
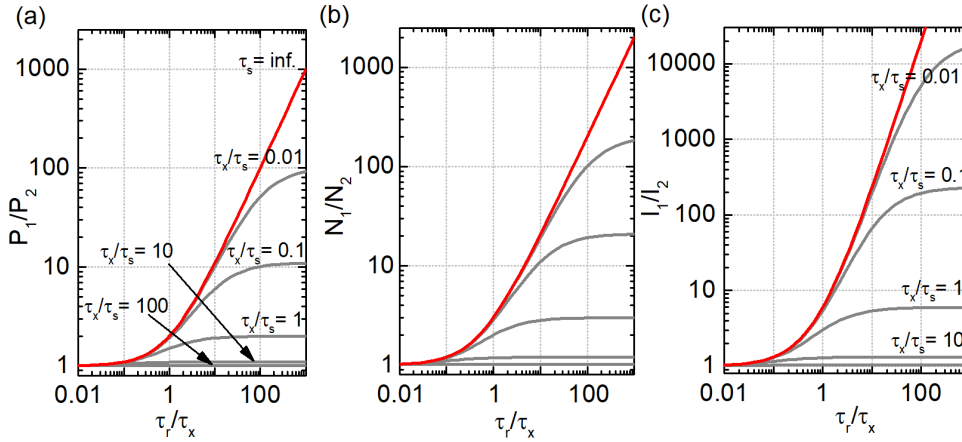
Figure B.20: (a) Probabilité d'émission radiative des états X_1 et X_2; (b) nombre d'excitons dans les états X_1 et X_2; (c) rapport d'intensité de photoluminescence prévu des états X_1 et X_2 en fonction de τ_r/τ_x. La ligne rouge représente la prédiction pour la bande interdite directe ($\tau_s = \infty$) tandis que les lignes grises montrent les prédictions dans la présence d'une bande interdite indirecte pour différents rapports du temps de diffusion entre les états excitoniques directs et l'état indirect τ_x/τ_s.

B.5 Dépendance anormale à la polarisation de la diffusion Raman dans la franckéite

Le chapitre 5 présente nos études de spectroscopie Raman polarimétrique sur la franckéite, menées dans le but de trouver une méthode de détermination de la direction de l'ondulation de l'hétérostructure anisotrope.

B.5.1 Description des échantillons

De minces couches de franckeite ont été préparées par exfoliation mécanique à partir de cristaux en vrac provenant d'une roche naturelle. Les couches ont été exfoliées sur un substrat PDMS et déposées sur un substrat SiO_2/Si de 292 nm [Gant 2017]. Sur la base des mesures AFM (figure

B.21), nous avons pu déterminer l'épaisseur du flocon sur lequel nous avons effectué les mesures par spectroscopie Raman à 87 nm.
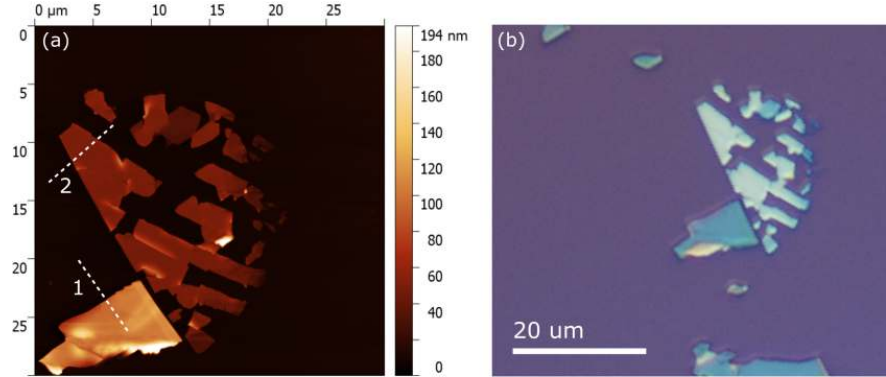
Figure B.21: (a) Image de topographique AFM du flocon étudié avec des profils marqués qui ont été utilisés pour estimer l'épaisseur; (b) Micrographie optique du même flocon.

B.5.2 Spectroscopie polarimétrique Raman

Les mesures ont été effectuées à température ambiante. Pour l'excitation, la ligne CW 532 nm d'un laser à l'état solide a été utilisée à une puissance de 2 mW. Pour les mesures à résolution de polarisation, un séparateur de faisceau non polarisant a été utilisé pour éviter les artefacts de polarisation introduits par le miroir dichroïque. La figure B.22 montre un spectre obtenu en faisant la moyenne des spectres pour une gamme complète d'angles d'excitation mesurés sur la partie la plus épaisse du flocon acquis dans la configuration de détection parallèle et perpendiculaire. La caractéristique la plus importante est le pic à $253\,\mathrm{cm}^{-1}$ avec une épaule du côté droit à $277\,\mathrm{cm}^{-1}$. Ces bandes ont été interprétées comme des modes liés au spectre des stibnites de la phase Q [Ray 2017]. Le pic autour de $300\,\mathrm{cm}^{-1}$ provient très probablement du substrat. La position du mode à $322\,\mathrm{cm}^{-1}$ correspond bien à l'énergie de la vibration A_g^1 observée dans SnS$_2$ [Molina-Mendoza 2017]. L'attribution des deux modes de plus basse énergie n'est pas directe, car ils ont été précédemment attribués à différents modes ou à leurs combinaisons à partir des couches Q et H.

La figure B.23 montre les cartes d'intensité Raman en fonction de l'angle d'excitation pour la configuration de polarisation parallèle et croisée. Les modes montrent une modulation claire de l'intensité avec le sens d'excitation.

Afin de décrire quantitativement la dépendance de l'intensité selon la polarisation, les spectres ont été ajustés en utilisant les pics de Lorentz correspondant aux 5 modes franckéite et le mode provenant du substrat. La hauteur des pics a été extraite comme mesure de l'intensité de la bande et tracée à la figure B.24 pour les trois modes franckeite à 186, 253 et $322\,\mathrm{cm}^{-1}$ pour lesquels une dépendance de polarisation claire a pu être résolue. La figure B.25 montre l'exemple d'un ajustement d'un spectre et les axes de polarisation définis par l'intensité maximale observée en polarisation parallèle superposée sur la micrographie de flocon. La dépendance de polarisation observée ne peut pas être expliquée uniquement sur la base de la
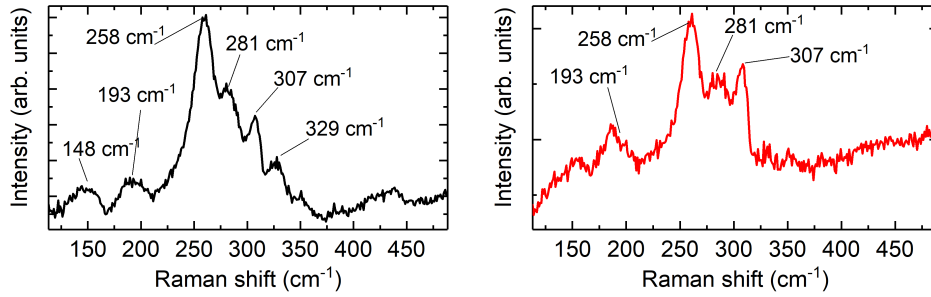
Figure B.22: Spectre Raman des flocons de franckeite d'environ 90 nm épais avec des modes caractéristiques marqués en polarisation (a) parallèle et (b) perpendiculaire en moyennes sur toute la gamme des directions d'excitation.
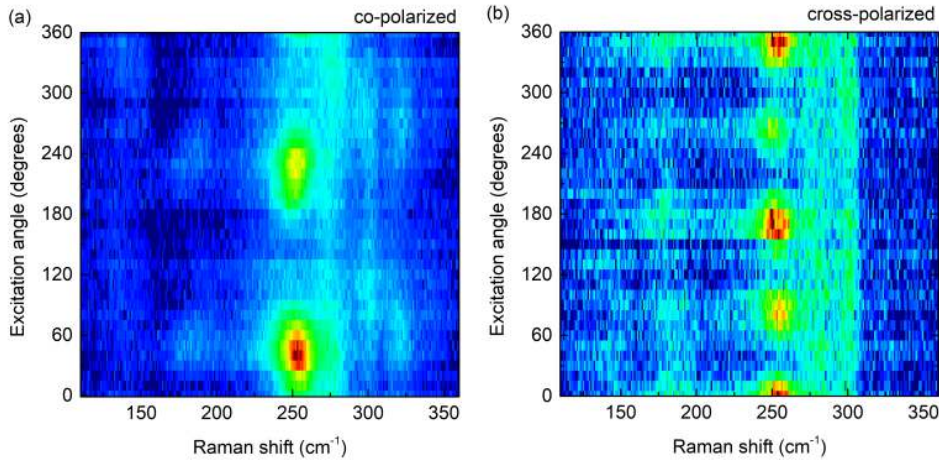
Figure B.23: Cartes montrant l'intensité du mode Raman en fonction de l'angle d'excitation pour la polarisation parallèle (a) et croisée (b).

symétrie des modes Raman. Nous suggérons que l'anisotropie optique, induite par l'ondulation unidimensionnelle, est responsable de la dépendance à la polarisation anormale, notamment la double anisotropie du mode A_1 322 cm^{-1} en polarisation parallèle et les différentes intensités des maxima à orientation perpendiculaire en polarisation croisée pour les modes a 186 et 253 cm^{-1}. L'axe de cette anisotropie est parallèle à l'une des directions de clivage, qui, comme discuté plus en détail au chapitre 5, est très probablement parallèle aux ondulations.

B.6   Conclusions

Avec la tendance actuelle à la miniaturisation des dispositifs électroniques, les matériaux semi-conducteurs en couches minces sont des candidats naturels pour une variété d'applications.
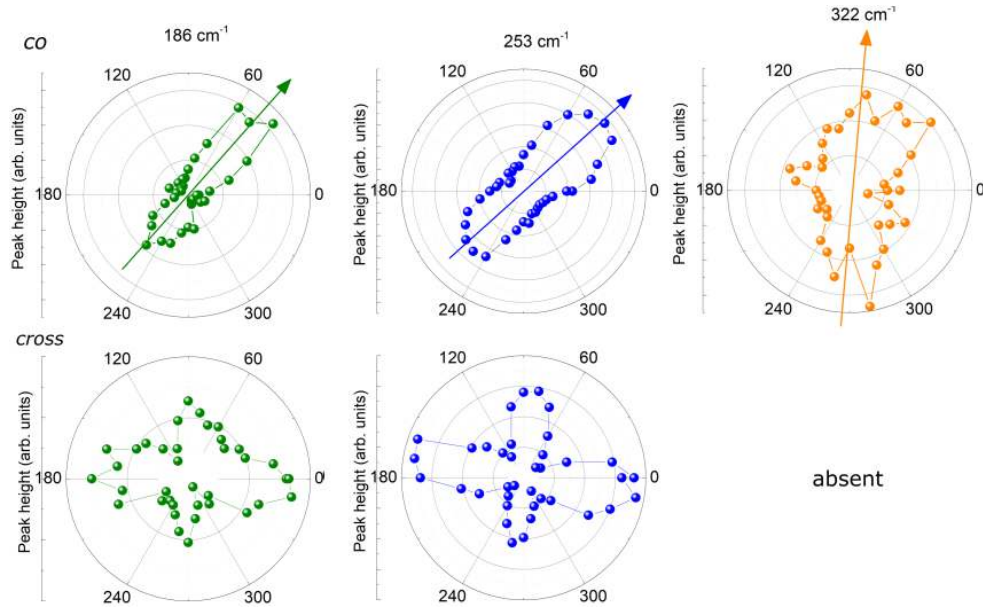
Figure B.24: Diagrammes polaires montrant l'intensité du mode $186\,\mathrm{cm}^{-1}$ (vert), $253\,\mathrm{cm}^{-1}$ (bleu foncé) et $322\,\mathrm{cm}^{-1}$ (orange) en fonction de l'angle d'excitation en polarisation parallèle (haut) et en polarisation croisée (bas). Le mode $322\,\mathrm{cm}^{-1}$ n'a pas été observé en polarisation croisée. Les flèches marquent les directions approximatives de l'intensité maximale.
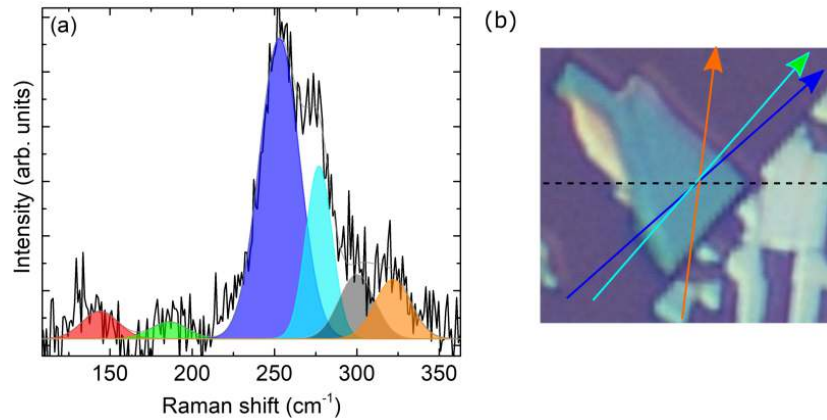
Figure B.25: (a) Exemple d'ajustement d'un spectre pour un angle d'excitation de $0°$ avec des pics lorentziens; (b) Micrographie optique du flocon. La direction $0°$ est marquée avec la ligne pointillée et les directions d'intensité maximale dérivées des diagrammes polaires pour les modes $186\,\mathrm{cm}^{-1}$ (vert), $253\,\mathrm{cm}^{-1}$ (bleu foncé) et $322\,\mathrm{cm}^{-1}$ (orange) sont indiquées par les flèches.

L'anisotropie dans le plan, présentée par certains de ces composés, fournit un moyen supplémentaire d'accorder les caractéristiques de dispositifs – tel que le transport thermique et électrique – et pourrait être utilisée pour réaliser l'émission et la détection de lumière polarisée. Ce sont là des enjeux importants et motivant notre tentative de mieux comprendre les propriétés fondamentales de ces matériaux.

Dans la première partie de cette thèse, nous avons étudié les propriétés vibratoires du phosphore noir par spectroscopie Raman. Nous avons caractérisé des échantillons encapsulés h-BN/BP/h-BN en quelques couches épaisses pour comprendre comment l'encapsulation peut influencer leurs propriétés structurelles et vibratoires. Nous avons pu confirmer que le h-BN assure une protection efficace du matériau instable dans les conditions ambiantes. Le rétrécissement de la ligne Raman d'environ $1\,\mathrm{cm}^{-1}$ par rapport aux études précédentes a fourni une preuve de la haute qualité du matériau et nous a permis de faire la première observation expérimentale du changement théoriquement prévu de la fréquence du mode A_g^1 dans les couches de surface de quelques couches de phosphore noir épais. Ce changement de fréquence se manifeste par l'apparition d'un nouveau pic Raman d'environ $4\,\mathrm{cm}^{-1}$ au-dessus du composant principal A_g^1 pour les échantillons d'une épaisseur de trois couches ou plus. En comparant les observations expérimentales aux résultats de calculs théoriques, nous avons discuté du décalage bleu inattendu de la fréquence modale dans le contexte des changements des constantes de réseau dans les couches de surface et de la déformation induite par le h-BN encapsulant.

Le disulfure de rhénium est un matériau à symétrie triclinique qui, contrairement à BP, présente une bonne stabilité environnementale. Une controverse non résolue existe dans la littérature quant à la nature de l'écart fondamental de ReS_2. Motivés par une étude théorique suggérant le caractère indirect de la bande interdite pour toutes les épaisseurs de disulfure de rhénium à l'exception de la bicouche, nous avons effectué une caractérisation de photoluminescence de ReS_2 en fonction du nombre de couches. Nous avons pu identifier deux transitions excitoniques, précédemment rapportées autour de 1,55 eV (X_1) et 1,57 eV (X_2), caractérisées par une forte anisotropie linéaire d'absorption et d'émission ainsi que par la dépendance monotone de l'intensité d'émission sur l'épaisseur. Nous avons conclu qu'il n'y a aucun changement du type de bande interdite avec l'épaisseur. L'intensité du PL était comparable pour les émissions des deux états excitoniques, ce qui est surprenant étant donné leur séparation énergétique relative d'environ 20 meV. Nous proposons qu'un état plus bas lié à une bande interdite indirecte soit responsable du dépeuplement rapide des états directs. Nous avons pu soutenir cette conclusion en comparant les observations expérimentales avec un modèle cinétique décrivant la recombinaison radiative et la diffusion des excitons dans les états directs et indirects.

Les hétérostructures naturelles offrent une alternative intéressante à l'empilement artificiel des couches. La franckéite est une hétérostructure de type *p* de type II pour laquelle le caractère incommensurable des couches tétragonales et hexagonales entraîne une déformation structurelle unidimensionnelle. Nous avons étudié la dépendance de polarisation de l'intensité du mode Raman pour les couches minces de franckeite exfoliées afin d'établir une méthode pour déterminer la direction de l'ondulation dans le plan. Nous avons observé une dépendance de polarisation anormale des modes Raman de $186\,\mathrm{cm}^{-1}$ et $253\,\mathrm{cm}^{-1}$ pour la couche Q et de $322\,\mathrm{cm}^{-1}$ pour la couche H A_g^1. L'axe d'anisotropie observé dans ces mesures est parallèle à la direction pour laquelle l'ondulation unidimensionnelle pourrait être attendue d'après les directions de clivage observées.

Bibliography

[Ahmed 2017] Taimur Ahmed, Sivacarendran Balendhran, Md Nurul Karim, Edwin L. H. Mayes, Matthew R. Field, Rajesh Ramanathan, Mandeep Singh, Vipul Bansal, Sharath Sriram, Madhu Bhaskaran and Sumeet Walia. *Degradation of black phosphorus is contingent on UV–blue light exposure.* npj 2D Materials and Applications, vol. 1, no. 1, December 2017. (Cited on page 12.)

[Alsaffar 2017] Fadhel Alsaffar, Sarah Alodan, Abdul Alrasheed, Abdulrahman Alhussain, Noura Alrubaiq, Ahmad Abbas and Moh. R. Amer. *Raman Sensitive Degradation and Etching Dynamics of Exfoliated Black Phosphorus.* Scientific Reports, vol. 7, no. 1, December 2017. (Cited on page 12.)

[Arora 2017] Ashish Arora, Jonathan Noky, Matthias Drüppel, Bhakti Jariwala, Thorsten Deilmann, Robert Schneider, Robert Schmidt, Osvaldo Del Pozo-Zamudio, Torsten Stiehm, Arnab Bhattacharya, Peter Krüger, Steffen Michaelis de Vasconcellos, Michael Rohlfing and Rudolf Bratschitsch. *Highly Anisotropic in-Plane Excitons in Atomically Thin and Bulklike 1T' ReSe$_2$.* Nano Letters, vol. 17, no. 5, pages 3202–3207, May 2017. (Cited on pages 70, 76, 78 and 80.)

[Aslan 2016] Ozgur Burak Aslan, Daniel A. Chenet, Arend M. van der Zande, James C. Hone and Tony F. Heinz. *Linearly Polarized Excitons in Single- and Few-Layer ReS$_2$ Crystals.* ACS Photonics, vol. 3, no. 1, pages 96–101, January 2016. (Cited on pages 16, 17, 18, 70, 71, 77, 79, 80 and 127.)

[Avsar 2015] Ahmet Avsar, Ivan J. Vera-Marun, Jun You Tan, Kenji Watanabe, Takashi Taniguchi, Antonio H. Castro Neto and Barbaros Özyilmaz. *Air-Stable Transport in Graphene-Contacted, Fully Encapsulated Ultrathin Black Phosphorus-Based Field-Effect Transistors.* ACS Nano, vol. 9, no. 4, pages 4138–4145, April 2015. (Cited on page 7.)

[Baranowski 2018] M. Baranowski, J. M. Urban, N. Zhang, A. Surrente, D. K. Maude, Zahra Andaji-Garmaroudi, S. D. Stranks and P. Plochocka. *Static and Dynamic Disorder in Triple-Cation Hybrid Perovskites.* The Journal of Physical Chemistry C, vol. 122, no. 30, pages 17473–17480, 2018. (Cited on page 89.)

[Benameur 2011] M. M. Benameur, B. Radisavljevic, J. S. Héron, S. Sahoo, H. Berger and A. Kis. *Visibility of dichalcogenide nanolayers.* Nanotechnology, vol. 22, no. 12, page 125706, 2011. (Cited on page 68.)

[Birowska 2019] Magdalena Birowska, Joanna Urban, Michał, Baranowski, Duncan K Maude, Paulina Płochocka and Nevill Gonzalez Szwacki. *The impact of hexagonal boron nitride encapsulation on the structural and vibrational properties of few layer black phosphorus.* Nanotechnology, 2019. (Cited on pages 14, 52, 53, 54, 55, 56, 123 and 124.)

[Bonch-Bruevich 1968] V. L. Bonch-Bruevich and E. G. Landsberg. *Recombination mechanisms.* physica status solidi (b), vol. 29, no. 1, pages 9–43, 1968. (Cited on page 86.)

[Boukhvalov 2015] D. W. Boukhvalov, A. N. Rudenko, D. A. Prishchenko, V. G. Mazurenko and M. I. Katsnelson. *Chemical modifications and stability of phosphorene with impurities: a first principles study.* Physical Chemistry Chemical Physics, vol. 17, no. 23, pages 15209–15217, 2015. (Cited on page 8.)

[Bridgman 1914] P. W. Bridgman. *Two new modifications of phosphorus.* Journal of the American Chemical Society, vol. 36, no. 7, pages 1344–1363, 1914. (Cited on page 7.)

[Burzuri 2018] Enrique Burzuri, Mariano Vera-Hidalgo, Emerson Giovanelli, Julia Villalva, Andres Castellanos-Gomez and Emilio M. Pérez. *Simultaneous assembly of van der Waals heterostructures into multiple nanodevices.* Nanoscale, vol. 10, pages 7966–7970, 2018. (Cited on pages 21 and 118.)

[Cai 2015a] Yongqing Cai, Qingqing Ke, Gang Zhang, Yuan Ping Feng, Vivek B. Shenoy and Yong-Wei Zhang. *Giant Phononic Anisotropy and Unusual Anharmonicity of Phosphorene: Interlayer Coupling and Strain Engineering.* Advanced Functional Materials, vol. 25, no. 15, pages 2230–2236, April 2015. (Cited on page 11.)

[Cai 2015b] Yongqing Cai, Gang Zhang and Yong-Wei Zhang. *Electronic Properties of Phosphorene/Graphene and Phosphorene/Hexagonal Boron Nitride Heterostructures.* The Journal of Physical Chemistry C, vol. 119, no. 24, pages 13929–13936, June 2015. (Cited on page 14.)

[Calman 2016] E. V. Calman, C. J. Dorow, M. M. Fogler, L. V. Butov, S. Hu, A. Mishchenko and A. K. Geim. *Control of excitons in multi-layer van der Waals heterostructures.* Applied Physics Letters, vol. 108, no. 10, page 101901, 2016. (Cited on page 19.)

[Cao 2015] Y. Cao, A. Mishchenko, G. L. Yu, E. Khestanova, A. P. Rooney, E. Prestat, A. V. Kretinin, P. Blake, M. B. Shalom, C. Woods, J. Chapman, G. Balakrishnan, I. V. Grigorieva, K. S. Novoselov, B. A. Piot, M. Potemski, K. Watanabe, T. Taniguchi, S. J. Haigh, A. K. Geim and R. V. Gorbachev. *Quality Heterostructures from Two-Dimensional Crystals Unstable in Air by Their Assembly in Inert Atmosphere.* Nano Letters, vol. 15, no. 8, pages 4914–4921, August 2015. (Cited on pages 13 and 58.)

[Cardona 1982] M. Cardona and G. Güntherodt. Light scattering in solids ii: basic concepts and instrumentation. Topics in applied physics. Springer-Verlag, 1982. (Cited on page 30.)

[Carvalho 2016] Alexandra Carvalho, Min Wang, Xi Zhu, Aleksandr S. Rodin, Haibin Su and Antonio H. Castro Neto. *Phosphorene: from theory to applications.* Nature Reviews Materials, vol. 1, no. 11, November 2016. (Cited on page 8.)

[Cassabois 2016] G. Cassabois, P. Valvin and B. Gil. *Hexagonal boron nitride is an indirect bandgap semiconductor.* Nature Photonics, vol. 10, pages 262 EP –, Jan 2016. Article. (Cited on page 2.)

[Castellanos-Gomez 2014] Andres Castellanos-Gomez, Leonardo Vicarelli, Elsa Prada, Joshua O Island, K L Narasimha-Acharya, Sofya I Blanter, Dirk J Groenendijk, Michele Buscema, Gary A Steele, J V Alvarez, Henny W Zandbergen, J J Palacios and Herre S J van der Zant. *Isolation and characterization of few-layer black phosphorus.* 2D Materials, vol. 1, no. 2, page 025001, June 2014. (Cited on pages 7, 12, 39, 47 and 58.)

[Chaves 2017] Andrey Chaves, Wei Ji, J Maasen, T Dumitrica and Tony Low. *Theoretical Overview of Black Phosphorus.* In 2D Materials: Properties and Devices, pages 381– 412. Cambridge University Press, 2017. (Cited on pages 8, 9, 10, 12, 116 and 117.)

[Chen 2015] Xiaolong Chen, Yingying Wu, Zefei Wu, Yu Han, Shuigang Xu, Lin Wang, Weiguang Ye, Tianyi Han, Yuheng He, Yuan Cai and Ning Wang. *High-quality sandwiched black phosphorus heterostructure and its quantum oscillations.* Nature Communications, vol. 6, no. 1, December 2015. (Cited on pages 13, 43, 44, 120 and 121.)

[Chen 2017] Xiaolong Chen, Xiaobo Lu, Bingchen Deng, Ofer Sinai, Yuchuan Shao, Cheng Li, Shaofan Yuan, Vy Tran, Kenji Watanabe, Takashi Taniguchi, Doron Naveh, Li Yang and Fengnian Xia. *Widely tunable black phosphorus mid-infrared photodetector.* Nature Communications, vol. 8, no. 1, December 2017. (Cited on page 7.)

[Chen 2018a] Chen Chen, Xiaolong Chen, Yuchuan Shao, Bingchen Deng, Qiushi Guo, Chao Ma and Fengnian Xia. *Valley-Selective Linear Dichroism in Layered Tin Sulfide.* ACS Photonics, August 2018. (Cited on page 16.)

[Chen 2018b] Yabin Chen, Chaoyu Chen, Robert Kealhofer, Huili Liu, Zhiquan Yuan, Lili Jiang, Joonki Suh, Joonsuk Park, Changhyun Ko, Hwan Sung Choe, José Avila, Mianzeng Zhong, Zhongming Wei, Jingbo Li, Shushen Li, Hongjun Gao, Yunqi Liu, James Analytis, Qinglin Xia, Maria C. Asensio and Junqiao Wu. *Black Arsenic: A Layered Semiconductor with Extreme In-Plane Anisotropy.* Advanced Materials, vol. 30, no. 30, page 1800754, July 2018. (Cited on pages 2, 7 and 116.)

[Chenet 2015] Daniel A. Chenet, O. Burak Aslan, Pinshane Y. Huang, Chris Fan, Arend M. van der Zande, Tony F. Heinz and James C. Hone. *In-Plane Anisotropy in Mono- and Few-Layer ReS$_2$ Probed by Raman Spectroscopy and Scanning Transmission Electron Microscopy.* Nano Letters, vol. 15, no. 9, pages 5667–5672, September 2015. (Cited on pages 32, 62, 63 and 65.)

[Chernikov 2014] Alexey Chernikov, Timothy C. Berkelbach, Heather M. Hill, Albert Rigosi, Yilei Li, Ozgur Burak Aslan, David R. Reichman, Mark S. Hybertsen and Tony F. Heinz. *Exciton Binding Energy and Nonhydrogenic Rydberg Series in Monolayer WS$_2$.* Physical Review Letters, vol. 113, no. 7, August 2014. (Cited on pages 4, 5, 6 and 116.)

[Choi 2017] Wonbong Choi, Nitin Choudhary, Gang Hee Han, Juhong Park, Deji Akinwande and Young Hee Lee. *Recent development of two-dimensional transition metal dichalcogenides and their applications.* Materials Today, vol. 20, no. 3, pages 116–130, 2017. (Cited on page 2.)

[Cudazzo 2011] Pierluigi Cudazzo, Ilya V. Tokatly and Angel Rubio. *Dielectric screening in two-dimensional insulators: Implications for excitonic and impurity states in graphane.* Physical Review B, vol. 84, no. 8, August 2011. (Cited on page 5.)

[Cui 2015] Qiannan Cui, Jiaqi He, Matthew Z. Bellus, Mirzojamshed Mirzokarimov, Tino Hofmann, Hsin-Ying Chiu, Matthew Antonik, Dawei He, Yongsheng Wang and Hui Zhao. *Transient Absorption Measurements on Anisotropic Monolayer ReS₂.* Small, vol. 11, no. 41, pages 5565–5571, November 2015. (Cited on pages 16, 70 and 71.)

[Cui 2016] Fangfang Cui, Cong Wang, Xiaobo Li, Gang Wang, Kaiqiang Liu, Zhou Yang, Qingliang Feng, Xing Liang, Zhongyue Zhang, Shengzhong Liu, Zhibin Lei, Zonghuai Liu, Hua Xu and Jin Zhang. *Tellurium-Assisted Epitaxial Growth of Large-Area, Highly Crystalline ReS₂ Atomic Layers on Mica Substrate.* Advanced Materials, vol. 28, no. 25, pages 5019–5024, 2016. (Cited on page 80.)

[Cui 2017] Yudong Cui, Feifei Lu and Xueming Liu. *Nonlinear Saturable and Polarization-induced Absorption of Rhenium Disulfide.* Scientific Reports, vol. 7, no. 1, December 2017. (Cited on page 70.)

[Dai 2014] Jun Dai and Xiao Cheng Zeng. *Bilayer Phosphorene: Effect of Stacking Order on Bandgap and Its Potential Applications in Thin-Film Solar Cells.* The Journal of Physical Chemistry Letters, vol. 5, no. 7, pages 1289–1293, April 2014. (Cited on page 8.)

[Das 2019] Sonali Das, Deepak Pandey, Jayan Thomas and Tania Roy. *The Role of Graphene and Other 2D Materials in Solar Photovoltaics.* Advanced Materials, vol. 31, no. 1, page 1802722, 2019. (Cited on page 2.)

[Dietzek 2011] Benjamin Dietzek, Dana Cialla, Michael Schmitt and Jürgen Popp. Introduction to the fundamentals of raman spectroscopy, pages 21–42. Springer Berlin Heidelberg, Berlin, Heidelberg, 2011. (Cited on pages 32 and 33.)

[Ding 2018] Li Ding, Muhammad Shoufie Ukhtary, Mikhail Chubarov, Tanushree H. Choudhury, Fu Zhang, Rui Yang, Ao Zhang, Jonathan A. Fan, Mauricio Terrones, Joan M. Redwing, Teng Yang, Mingda Li, Riichiro Saito and Shengxi Huang. *Understanding Interlayer Coupling in TMD-hBN Heterostructure by Raman Spectroscopy.* IEEE Transactions on Electron Devices, pages 1–9, 2018. (Cited on page 43.)

[Doganov 2015] Rostislav A. Doganov, Steven P. Koenig, Yuting Yeo, Kenji Watanabe, Takashi Taniguchi and Barbaros Özyilmaz. *Transport properties of ultrathin black phosphorus on hexagonal boron nitride.* Applied Physics Letters, vol. 106, no. 8, page 083505, February 2015. (Cited on page 13.)

[Dong 2016] Shan Dong, Anmin Zhang, Kai Liu, Jianting Ji, Y. G. Ye, X. G. Luo, X. H. Chen, Xiaoli Ma, Yinghao Jie, Changfeng Chen, Xiaoqun Wang and Qingming Zhang. *Ultralow-Frequency Collective Compression Mode and Strong Interlayer Coupling in Multilayer Black Phosphorus.* Physical Review Letters, vol. 116, no. 8, February 2016. (Cited on pages 10, 12 and 42.)

[Dressel 2002] Martin Dressel and George Grüner. Electrodynamics of solids: Optical properties of electrons in matter. Cambridge University Press, 2002. (Cited on page 26.)

[Dresselhaus 2018] M. Dresselhaus, G. Dresselhaus, S.B. Cronin and A.G.S. Filho. Solid state properties: From bulk to nano. Graduate Texts in Physics. Springer Berlin Heidelberg, 2018. (Cited on pages 25 and 29.)

[Du 2015] Haiwei Du, Xi Lin, Zhemi Xu and Dewei Chu. *Recent developments in black phosphorus transistors.* Journal of Materials Chemistry C, vol. 3, no. 34, pages 8760–8775, 2015. (Cited on page 9.)

[Duong 2017] Dinh Loc Duong, Seok Joon Yun and Young Hee Lee. *van der Waals Layered Materials: Opportunities and Challenges.* ACS Nano, vol. 11, no. 12, pages 11803–11830, December 2017. (Cited on pages 1, 2, 4, 11 and 115.)

[Echeverry 2018] J. P. Echeverry and I. C. Gerber. *Theoretical investigations of the anisotropic optical properties of distorted 1 T ReS$_2$ and ReSe$_2$ monolayers, bilayers, and in the bulk limit.* Physical Review B, vol. 97, no. 7, February 2018. (Cited on pages 16 and 72.)

[Edmonds 2015] M. T. Edmonds, A. Tadich, A. Carvalho, A. Ziletti, K. M. O'Donnell, S. P. Koenig, D. F. Coker, B. Özyilmaz, A. H. Castro Neto and M. S. Fuhrer. *Creating a Stable Oxide at the Surface of Black Phosphorus.* ACS Applied Materials & Interfaces, vol. 7, no. 27, pages 14557–14562, July 2015. (Cited on page 12.)

[Falin 2017] Aleksey Falin, Qiran Cai, Elton J.G. Santos, Declan Scullion, Dong Qian, Rui Zhang, Zhi Yang, Shaoming Huang, Kenji Watanabe, Takashi Taniguchi, Matthew R. Barnett, Ying Chen, Rodney S. Ruoff and Lu Hua Li. *Mechanical properties of atomically thin boron nitride and the role of interlayer interactions.* Nature Communications, vol. 8, page 15815, June 2017. (Cited on page 13.)

[Fang 1997] C. M. Fang, G. A. Wiegers, C. Haas and R. A. De Groot. *Electronic structures of ReS$_2$, ReSe$_2$ and TcS$_2$, and in the real and the hypothetical undistorted structures.* Journal of Physics: Condensed Matter, vol. 9, no. 21, page 4411, 1997. (Cited on pages 14 and 117.)

[Favron 2015] Alexandre Favron, Etienne Gaufrès, Frédéric Fossard, Anne-Laurence Phaneuf-L'Heureux, Nathalie Y-W. Tang, Pierre L. Lévesque, Annick Loiseau, Richard Leonelli, Sébastien Francoeur and Richard Martel. *Photooxidation and quantum confinement effects in exfoliated black phosphorus.* Nature Materials, vol. 14, no. 8, pages 826–832, August 2015. (Cited on pages 12, 39, 42, 55 and 57.)

[Favron 2018] Alexandre Favron, Félix Antoine Goudreault, Vincent Gosselin, Julien Groulx, Michel Côté, Richard Leonelli, Jean-Francis Germain, Anne-Laurence Phaneuf-L'Heureux, Sébastien Francoeur and Richard Martel. *Second-Order Raman Scattering in Exfoliated Black Phosphorus.* Nano Letters, vol. 18, no. 2, pages 1018–1027, February 2018. (Cited on pages 43 and 55.)

[Feng 2015] Yanqing Feng, Wei Zhou, Yaojia Wang, Jian Zhou, Erfu Liu, Yajun Fu, Zhenhua Ni, Xinglong Wu, Hongtao Yuan, Feng Miao, Baigeng Wang, Xiangang Wan and Dingyu Xing. *Raman vibrational spectra of bulk to monolayer ReS$_2$ with lower symmetry.* Physical Review B, vol. 92, no. 5, August 2015. (Cited on pages 62 and 63.)

[Fermi 1932] Enrico Fermi. *Quantum Theory of Radiation.* Rev. Mod. Phys., vol. 4, pages 87–132, Jan 1932. (Cited on page 28.)

[Florian 2018] Matthias Florian, Malte Hartmann, Alexander Steinhoff, Julian Klein, Alexander W. Holleitner, Jonathan J. Finley, Tim O. Wehling, Michael Kaniber and Christopher Gies. *The Dielectric Impact of Layer Distances on Exciton and Trion Binding Energies in van der Waals Heterostructures.* Nano Letters, vol. 18, no. 4, pages 2725–2732, April 2018. (Cited on page 4.)

[Fox 2010] M. Fox. Optical Properties of Solids. OUP Oxford, 2010. (Cited on pages 2, 3, 4 and 7.)

[Frisenda 2018] Riccardo Frisenda, Efrén Navarro-Moratalla, Patricia Gant, David Pérez De Lara, Pablo Jarillo-Herrero, Roman V. Gorbachev and Andres Castellanos-Gomez. *Recent progress in the assembly of nanodevices and van der Waals heterostructures by deterministic placement of 2D materials.* Chem. Soc. Rev., vol. 47, pages 53–68, 2018. (Cited on page 20.)

[Froehlicher 2015] Guillaume Froehlicher, Etienne Lorchat, François Fernique, Chaitanya Joshi, Alejandro Molina-Sánchez, Ludger Wirtz and Stéphane Berciaud. *Unified Description of the Optical Phonon Modes in N-Layer MoTe$_2$.* Nano Letters, vol. 15, no. 10, pages 6481–6489, Oct 2015. (Cited on pages 56 and 57.)

[Gant 2017] Patricia Gant, Foad Ghasemi, David Maeso, Carmen Munuera, Elena López-Elvira, Riccardo Frisenda, David Pérez De Lara, Gabino Rubio-Bollinger, Mar Garcia-Hernandez and Andres Castellanos-Gomez. *Optical contrast and refractive index of natural van der Waals heterostructure nanosheets of franckeite.* Beilstein Journal of Nanotechnology, vol. 8, pages 2357–2362, 2017. (Cited on pages 96, 97 and 130.)

[Gehlmann 2017] Mathias Gehlmann, Irene Aguilera, Gustav Bihlmayer, Slavomír Nemšák, Philipp Nagler, Pika Gospodarič, Giovanni Zamborlini, Markus Eschbach, Vitaliy Feyer, Florian Kronast, Ewa Młyńczak, Tobias Korn, Lukasz Plucinski, Christian Schüller, Stefan Blügel and Claus M. Schneider. *Direct Observation of the Band Gap Transition in Atomically Thin ReS$_2$.* Nano Letters, vol. 17, no. 9, pages 5187–5192, September 2017. (Cited on page 18.)

[Geim 2013] A. K. Geim and I. V. Grigorieva. *Van der Waals heterostructures.* Nature, vol. 499, no. 7459, pages 419–425, July 2013. (Cited on pages 1 and 2.)

[Gołasa 2017] Katarzyna Gołasa, Magda Grzeszczyk, Maciej R. Molas, Małgorzata Zinkiewicz, Łukasz Bala, Karol Nogajewski, Marek Potemski, Andrzej Wysmołek and Adam Babiński. *Resonant quenching of Raman scattering due to out-of-plane A_{1g}/A'_1 modes in few-layer MoTe$_2$.* Nanophotonics, vol. 6, no. 6, January 2017. (Cited on page 54.)

[Gomes 2015] Lídia C. Gomes and A. Carvalho. *Phosphorene analogues: Isoelectronic two-dimensional group-IV monochalcogenides with orthorhombic structure.* Physical Review B, vol. 92, no. 8, August 2015. (Cited on page 2.)

[Grzeszczyk 2018] M. Grzeszczyk, K. Gołasa, M. R. Molas, K. Nogajewski, M. Zinkiewicz, M. Potemski, A. Wysmołek and A. Babiński. *Raman scattering from the bulk inactive*

out-of-plane B_{2g}^1 mode in few-layer $MoTe_2$. Scientific Reports, vol. 8, no. 1, page 17745, 2018. (Cited on page 56.)

[Gupta 2017] Garima Gupta, Sangeeth Kallatt and Kausik Majumdar. *Direct observation of giant binding energy modulation of exciton complexes in monolayer $MoSe_2$*. Physical Review B, vol. 96, no. 8, August 2017. (Cited on page 7.)

[Gusmao 2018] Rui Gusmao, Zdenek Sofer, Jan Luxa and Martin Pumera. *Layered franckeite and teallite intrinsic heterostructures: shear exfoliation and electrocatalysis*. J. Mater. Chem. A, vol. 6, pages 16590–16599, 2018. (Cited on pages 21 and 22.)

[Gutiérrez-Lezama 2016] Ignacio Gutiérrez-Lezama, Bojja Aditya Reddy, Nicolas Ubrig and Alberto F Morpurgo. *Electroluminescence from indirect band gap semiconductor ReS_2*. 2D Materials, vol. 3, no. 4, page 045016, October 2016. (Cited on pages 18 and 77.)

[Han 2017] Cheng Han, Zehua Hu, Alexandra Carvalho, Na Guo, Jialin Zhang, Fang Hu, Du Xiang, Jing Wu, Bo Lei, Li Wang, Chun Zhang, A H Castro Neto and Wei Chen. *Oxygen induced strong mobility modulation in few-layer black phosphorus*. 2D Materials, vol. 4, no. 2, page 021007, February 2017. (Cited on page 12.)

[Hart 2016] Lewis Hart, Sara Dale, Sarah Hoye, James L. Webb and Daniel Wolverson. *Rhenium Dichalcogenides: Layered Semiconductors with Two Vertical Orientations*. Nano Letters, vol. 16, no. 2, pages 1381–1386, February 2016. (Cited on pages 7 and 116.)

[He 2016] Rui He, Jia-An Yan, Zongyou Yin, Zhipeng Ye, Gaihua Ye, Jason Cheng, Ju Li and C. H. Lui. *Coupling and Stacking Order of ReS_2 Atomic Layers Revealed by Ultralow-Frequency Raman Spectroscopy*. Nano Letters, vol. 16, no. 2, pages 1404–1409, 2016. (Cited on pages 14 and 63.)

[Heitz 1961] F Heitz, Marie-Thérèse Le Bihan and M Coulon. *Contribution à l'étude structurale d'un sulfure de plomb, d'antimoine et d'étain : la Frankeite*. Bulletin de Minéralogie, vol. 84, no. 4, pages 350–353, 1961. (Cited on pages 20 and 118.)

[Henriksen 2002] René B. Henriksen, Emil Makovicky, S. L. S. Stipp, Camilla Nissen and Carrick M. Eggleston. *Atomic-scale observations of franckeite surface morphology*. American Mineralogist, vol. 87, no. 10, pages 1273–1278, Oct 2002. (Cited on pages 22 and 23.)

[Ho 1997] C. H. Ho, P. C. Liao, Y. S. Huang, T. R. Yang and K. K. Tiong. *Optical absorption of ReS_2 and $ReSe_2$ single crystals*. Journal of Applied Physics, vol. 81, no. 9, pages 6380–6383, May 1997. (Cited on pages 18 and 70.)

[Ho 1998] C. H. Ho, Y. S. Huang, K. K. Tiong and P. C. Liao. *Absorption-edge anisotropy in ReS_2 and $ReSe_2$ layered semiconductors*. Physical Review B, vol. 58, no. 24, page 16130, 1998. (Cited on pages 18, 19, 70, 75 and 83.)

[Ho 2002] C. H. Ho, P. C. Yen, Y. S. Huang and K. K. Tiong. *Photoreflectance study of the excitonic transitions of rhenium disulphide layer compounds*. Phys. Rev. B, vol. 66, page 245207, Dec 2002. (Cited on pages 70, 72, 75 and 82.)

[Ho 2004] C.H. Ho and C.E. Huang. *Optical property of the near band-edge transitions in rhenium disulfide and diselenide.* Journal of Alloys and Compounds, vol. 383, no. 1, pages 74 – 79, 2004. Proceedings of the 14th International Conference on Solid Compounds of Transition Elements (SCTE 2003). (Cited on pages 70 and 72.)

[Ho 2007] C.H. Ho, M.H. Hsieh, C.C. Wu, Y.S. Huang and K.K. Tiong. *Dichroic optical and electrical properties of rhenium dichalcogenides layer compounds.* Journal of Alloys and Compounds, vol. 442, no. 1-2, pages 245–248, September 2007. (Cited on page 70.)

[Ho 2017] Ching-Hwa Ho, Zhan-Zhi Liu and Min-Han Lin. *Direct and indirect light emissions from layered $ReS_{2-x}Se_x$ (0 <= x <= 2).* Nanotechnology, vol. 28, no. 23, page 235203, June 2017. (Cited on pages 16, 17, 18 and 77.)

[Ho 2019] Ching-Hwa Ho and Zhan-Zhi Liu. *Complete-series excitonic dipole emissions in few layer ReS_2 and $ReSe_2$ observed by polarized photoluminescence spectroscopy.* Nano Energy, vol. 56, pages 641 – 650, 2019. (Cited on pages 16, 17 and 77.)

[Hong 2018] Qilin Hong, Feng Xiong, Wei Xu, Zhihong Zhu, Ken Liu, Xiaodong Yuan, Jianfa Zhang and Shiqiao Qin. *Towards high performance hybrid two-dimensional material plasmonic devices: strong and highly anisotropic plasmonic resonances in nanostructured graphene-black phosphorus bilayer.* Optics Express, vol. 26, no. 17, page 22528, August 2018. (Cited on page 7.)

[Hu 2016] Zhi-Xin Hu, Xianghua Kong, Jingsi Qiao, Bruce Normand and Wei Ji. *Interlayer electronic hybridization leads to exceptional thickness-dependent vibrational properties in few-layer black phosphorus.* Nanoscale, vol. 8, no. 5, pages 2740–2750, 2016. (Cited on pages 8, 9, 10, 12, 40, 42, 43, 50, 51, 52, 53, 54, 56, 59, 123 and 124.)

[Huang 2016a] Shengxi Huang, Yuki Tatsumi, Xi Ling, Huaihong Guo, Ziqiang Wang, Garrett Watson, Alexander A. Puretzky, David B. Geohegan, Jing Kong, Ju Li, Teng Yang, Riichiro Saito and Mildred S. Dresselhaus. *In-Plane Optical Anisotropy of Layered Gallium Telluride.* ACS Nano, vol. 10, no. 9, pages 8964–8972, 2016. (Cited on page 104.)

[Huang 2016b] Yuan Huang, Jingsi Qiao, Kai He, Stoyan Bliznakov, Eli Sutter, Xianjue Chen, Da Luo, Fanke Meng, Dong Su, Jeremy Decker, Wei Ji, Rodney S. Ruoff and Peter Sutter. *Interaction of Black Phosphorus with Oxygen and Water.* Chemistry of Materials, vol. 28, no. 22, pages 8330–8339, November 2016. (Cited on page 12.)

[Huo 2017] Nengjie Huo, Yujue Yang and Jingbo Li. *Optoelectronics based on 2D TMDs and heterostructures.* Journal of Semiconductors, vol. 38, no. 3, page 031002, March 2017. (Cited on page 2.)

[Island 2015] Joshua O Island, Gary A Steele, Herre S J van der Zant and Andres Castellanos-Gomez. *Environmental instability of few-layer black phosphorus.* 2D Materials, vol. 2, no. 1, page 011002, January 2015. (Cited on page 12.)

[Island 2016] J.O. Island and A. Castellanos-Gomez. *Black Phosphorus-Based Nanodevices.* In Semiconductors and Semimetals, volume 95, pages 279–303. Elsevier, 2016. (Cited on pages 2 and 9.)

[Island 2017] Joshua O Island, Aday J Molina-Mendoza, Mariam Barawi, Robert Biele, Eduardo Flores, José M Clamagirand, José R Ares, Carlos Sánchez, Herre S J van der Zant, Roberto D'Agosta, Isabel J Ferrer and Andres Castellanos-Gomez. *Electronics and optoelectronics of quasi-1D layered transition metal trichalcogenides.* 2D Materials, vol. 4, no. 2, page 022003, April 2017. (Cited on page 2.)

[Ivchenko 1995] E. L. Ivchenko. Pure and applied chemistry, volume 67, chapitre Spectroscopy of spin-polarized excitons in semiconductors, page 463. 2019 1995. 3. (Cited on page 83.)

[Jadczak 2019] J. Jadczak, J. Kutrowska-Girzycka, T. Smolenski, P. Kossacki, Y. S. Huang and L. Bryja. *Exciton binding energy and hydrogenic Rydberg series in layered ReS$_2$.* Scientific Reports, vol. 9, no. 1, page 1578, 2019. (Cited on pages 16, 72 and 82.)

[Jang 2017] Hyejin Jang, Christopher R. Ryder, Joshua D. Wood, Mark C. Hersam and David G. Cahill. *3D Anisotropic Thermal Conductivity of Exfoliated Rhenium Disulfide.* Advanced Materials, vol. 29, no. 35, page 1700650, 2017. (Cited on pages 15 and 16.)

[Jariwala 2016] Bhakti Jariwala, Damien Voiry, Apoorv Jindal, Bhagyashree A. Chalke, Rudheer Bapat, Arumugam Thamizhavel, Manish Chhowalla, Mandar Deshmukh and Arnab Bhattacharya. *Synthesis and Characterization of ReS$_2$ and ReSe$_2$ Layered Chalcogenide Single Crystals.* Chemistry of Materials, vol. 28, no. 10, pages 3352–3359, May 2016. (Cited on pages 14, 15, 69, 117 and 118.)

[Jung 2014] Yeonwoong Jung, Jie Shen, Yong Sun and Judy J. Cha. *Chemically Synthesized Heterostructures of Two-Dimensional Molybdenum/Tungsten-Based Dichalcogenides with Vertically Aligned Layers.* ACS Nano, vol. 8, no. 9, pages 9550–9557, 2014. PMID: 25153809. (Cited on pages 20 and 117.)

[Keldysh, L. V. 1979] Keldysh, L. V. *Coulomb interaction in thin semiconductor and semimetal films.* JETP Lett., vol. 29, page 658, 1979. (Cited on page 4.)

[Kelly 2017] Adam G. Kelly, Toby Hallam, Claudia Backes, Andrew Harvey, Amir Sajad Esmaeily, Ian Godwin, João Coelho, Valeria Nicolosi, Jannika Lauth, Aditya Kulkarni, Sachin Kinge, Laurens D. A. Siebbeles, Georg S. Duesberg and Jonathan N. Coleman. *All-printed thin-film transistors from networks of liquid-exfoliated nanosheets.* Science, vol. 356, no. 6333, pages 69–73, 2017. (Cited on page 2.)

[Kim 2015] Jungcheol Kim, Jae-Ung Lee, Jinhwan Lee, Hyo Ju Park, Zonghoon Lee, Changgu Lee and Hyeonsik Cheong. *Anomalous polarization dependence of Raman scattering and crystallographic orientation of black phosphorus.* Nanoscale, vol. 7, pages 18708–18715, 2015. (Cited on pages 104, 106 and 107.)

[Kim 2016] Jiho Kim, Seung Kwan Baek, Keun Soo Kim, Young Jun Chang and E.J. Choi. *Long-term stability study of graphene-passivated black phosphorus under air exposure.* Current Applied Physics, vol. 16, no. 2, pages 165–169, February 2016. (Cited on page 13.)

[Kistanov 2018] Andrey Kistanov, Yongqing Cai, Kun Zhou, Sergey Dmitriev and Yong-Wei Zhang. *Effects of Graphene/BN Encapsulation, Surface Functionalization and Molecular Adsorption on the Electronic Properties of Layered InSe: A First-Principles Study.* Physical Chemistry Chemical Physics, 2018. (Cited on page 7.)

[Knox 1963] Robert S. Knox. Theory of excitons. Academic Press, New York, 1963. (Cited on page 2.)

[Koenig 2014] Steven P. Koenig, Rostislav A. Doganov, Hennrik Schmidt, A. H. Castro Neto and Barbaros Özyilmaz. *Electric field effect in ultrathin black phosphorus.* Applied Physics Letters, vol. 104, no. 10, page 103106, March 2014. (Cited on page 12.)

[Korn 2011] T. Korn, S. Heydrich, M. Hirmer, J. Schmutzler and C. Schüller. *Low-temperature photocarrier dynamics in monolayer MoS$_2$.* Applied Physics Letters, vol. 99, no. 10, page 102109, September 2011. (Cited on page 88.)

[Korona 1996] K. P. Korona, A. Wysmołek, K. Pakuła, R. Stępniewski, J. M. Baranowski, I. Grzegory, B. Łucznik, M. Wróblewski and S. Porowski. *Exciton region reflectance of homoepitaxial GaN layers.* Applied Physics Letters, vol. 69, no. 6, pages 788–790, 1996. (Cited on page 73.)

[Kozawa 2014] Daichi Kozawa, Rajeev Kumar, Alexandra Carvalho, Kiran Kumar Amara, Weijie Zhao, Shunfeng Wang, Minglin Toh, Ricardo M. Ribeiro, AH Castro Neto and Kazunari Matsuda. *Photocarrier relaxation pathway in two-dimensional semiconducting transition metal dichalcogenides.* Nature communications, vol. 5, page 4543, 2014. (Cited on pages 87 and 88.)

[Kranert 2016] Christian Kranert, Chris Sturm, Rüdiger Schmidt-Grund and Marius Grundmann. *Raman Tensor Formalism for Optically Anisotropic Crystals.* Phys. Rev. Lett., vol. 116, page 127401, Mar 2016. (Cited on pages 104 and 106.)

[Kuriakose 2018] Sruthi Kuriakose, Taimur Ahmed, Sivacarendran Balendhran, Vipul Bansal, Sharath Sriram, Madhu Bhaskaran and Sumeet Walia. *Black phosphorus: ambient degradation and strategies for protection.* 2D Materials, vol. 5, no. 3, page 032001, April 2018. (Cited on page 12.)

[Lafond 1997] A. Lafond, A. Nader, Y. Moëlo, A. Meerschaut, A. Briggs, S. Perrin, P. Monceau and J. Rouxel. *X-Ray structure determination and superconductivity of a new layered misfit compound with a franckeite-like stacking, [(Pb,Sb)S]$_{2.28}$NbS$_2$.* Journal of Alloys and Compounds, vol. 261, no. 1, pages 114 – 122, 1997. (Cited on page 20.)

[Lédée 2017] Ferdinand Lédée, Gaëlle Trippé-Allard, Hiba Diab, Pierre Audebert, Damien Garrot, Jean-Sébastien Lauret and Emmanuelle Deleporte. *Fast growth of monocrystalline thin films of 2D layered hybrid perovskite.* CrystEngComm, vol. 19, no. 19, pages 2598–2602, 2017. (Cited on page 2.)

[Lee 2010] Changgu Lee, Hugen Yan, Louis E. Brus, Tony F. Heinz, James Hone and Sunmin Ryu. *Anomalous Lattice Vibrations of Single- and Few-Layer MoS$_2$.* ACS Nano, vol. 4, no. 5, pages 2695–2700, May 2010. (Cited on page 42.)

[Lee 2015] Jae-Ung Lee, Minjung Kim and Hyeonsik Cheong. *Raman Spectroscopic Studies on Two-Dimensional Materials.* Applied Microscopy, vol. 45, no. 3, pages 126–130, September 2015. (Cited on page 42.)

[Leite 1966] R. C. C. Leite and S. P. S. Porto. *Enhancement of Raman Cross Section in CdS due to Resonant Absorption.* Phys. Rev. Lett., vol. 17, pages 10–12, Jul 1966. (Cited on page 30.)

[Lezama 2015] Ignacio Gutiérrez Lezama, Ashish Arora, Alberto Ubaldini, Céline Barreteau, Enrico Giannini, Marek Potemski and Alberto F. Morpurgo. *Indirect-to-Direct Band Gap Crossover in Few-Layer MoTe$_2$.* Nano Letters, vol. 15, no. 4, pages 2336–2342, April 2015. (Cited on page 9.)

[Li 2014] Likai Li, Yijun Yu, Guo Jun Ye, Qingqin Ge, Xuedong Ou, Hua Wu, Donglai Feng, Xian Hui Chen and Yuanbo Zhang. *Black phosphorus field-effect transistors.* Nature Nanotechnology, vol. 9, no. 5, pages 372–377, May 2014. (Cited on page 9.)

[Li 2016] Likai Li, Fangyuan Yang, Guo Jun Ye, Zuocheng Zhang, Zengwei Zhu, Wenkai Lou, Xiaoying Zhou, Liang Li, Kenji Watanabe, Takashi Taniguchi, Kai Chang, Yayu Wang, Xian Hui Chen and Yuanbo Zhang. *Quantum Hall effect in black phosphorus two-dimensional electron system.* Nature Nanotechnology, vol. 11, no. 7, pages 593–597, July 2016. (Cited on page 13.)

[Li 2018a] Liang Li, Weike Wang, Penglai Gong, Xiangde Zhu, Bei Deng, Xingqiang Shi, Guoying Gao, Huiqiao Li and Tianyou Zhai. *2D GeP: An Unexploited Low-Symmetry Semiconductor with Strong In-Plane Anisotropy.* Advanced Materials, vol. 30, no. 14, page 1706771, April 2018. (Cited on page 2.)

[Li 2018b] Shuaishuai Li, Tao Wang, Xiaoshuang Chen, Wei Lu, Yiqun Xie and Yibin Hu. *Self-powered photogalvanic phosphorene photodetectors with high polarization sensitivity and suppressed dark current.* Nanoscale, 2018. (Cited on page 7.)

[Liang 2009] C.H. Liang, Y.H. Chan, K.K. Tiong, Y.S. Huang, Y.M. Chen, D.O. Dumcenco and C.H. Ho. *Optical anisotropy of Au-doped ReS$_2$ crystals.* Journal of Alloys and Compounds, vol. 480, no. 1, pages 94–96, July 2009. (Cited on pages 18, 70 and 72.)

[Liao 2018] Mengzhou Liao, Ze-Wen Wu, Luojun Du, Tingting Zhang, Zheng Wei, Jianqi Zhu, Hua Yu, Jian Tang, Lin Gu, Yanxia Xing, Rong Yang, Dongxia Shi, Yugui Yao and Guangyu Zhang. *Twist angle-dependent conductivities across MoS$_2$/graphene heterojunctions.* Nature Communications, vol. 9, no. 1, page 4068, 2018. (Cited on page 20.)

[Lin 2015] Yung-Chang Lin, Hannu-Pekka Komsa, Chao-Hui Yeh, Torbjörn Björkman, Zheng-Yong Liang, Ching-Hwa Ho, Ying-Sheng Huang, Po-Wen Chiu, Arkady V. Krasheninnikov and Kazu Suenaga. *Single-Layer ReS$_2$: Two-Dimensional Semiconductor with Tunable In-Plane Anisotropy.* ACS Nano, vol. 9, no. 11, pages 11249–11257, Nov 2015. (Cited on page 14.)

[Ling 2015] Xi Ling, Han Wang, Shengxi Huang, Fengnian Xia and Mildred S. Dresselhaus. *The renaissance of black phosphorus.* Proceedings of the National Academy of Sciences, vol. 112, no. 15, pages 4523–4530, April 2015. (Cited on pages 7, 10 and 116.)

[Liu 2015] Erfu Liu, Yajun Fu, Yaojia Wang, Yanqing Feng, Huimei Liu, Xiangang Wan, Wei Zhou, Baigeng Wang, Lubin Shao, Ching-Hwa Ho, Ying-Sheng Huang, Zhengyi Cao, Laiguo Wang, Aidong Li, Junwen Zeng, Fengqi Song, Xinran Wang, Yi Shi, Hongtao

Yuan, Harold Y. Hwang, Yi Cui, Feng Miao and Dingyu Xing. *Integrated digital inverters based on two-dimensional anisotropic ReS$_2$ field-effect transistors.* Nature Communications, vol. 6, pages 6991 EP –, May 2015. Article. (Cited on page 15.)

[Liu 2016a] Erfu Liu, Mingsheng Long, Junwen Zeng, Wei Luo, Yaojia Wang, Yiming Pan, Wei Zhou, Baigeng Wang, Weida Hu, Zhenhua Ni, Yumeng You, Xueao Zhang, Shiqiao Qin, Yi Shi, Kenji Watanabe, Takashi Taniguchi, Hongtao Yuan, Harold Y. Hwang, Yi Cui, Feng Miao and Dingyu Xing. *High Responsivity Phototransistors Based on Few-Layer ReS$_2$ for Weak Signal Detection.* Advanced Functional Materials, vol. 26, no. 12, pages 1938–1944, 2016. (Cited on page 15.)

[Liu 2016b] Fucai Liu, Shoujun Zheng, Xuexia He, Apoorva Chaturvedi, Junfeng He, Wai Leong Chow, Thomas R. Mion, Xingli Wang, Jiadong Zhou, Qundong Fu, Hong Jin Fan, Beng Kang Tay, Li Song, Rui-Hua He, Christian Kloc, Pulickel M. Ajayan and Zheng Liu. *Highly Sensitive Detection of Polarized Light Using Anisotropic 2D ReS$_2$.* Advanced Functional Materials, vol. 26, no. 8, pages 1169–1177, 2016. (Cited on pages 15 and 70.)

[Liu 2016c] Yuan Liu, Nathan O. Weiss, Xidong Duan, Hung-Chieh Cheng, Yu Huang and Xiangfeng Duan. *Van der Waals heterostructures and devices.* Nature Reviews Materials, vol. 1, page 16042, Jul 2016. Review Article. (Cited on page 2.)

[Liu 2016d] Zizhuo Liu and Koray Aydin. *Localized Surface Plasmons in Nanostructured Monolayer Black Phosphorus.* Nano Letters, vol. 16, no. 6, pages 3457–3462, June 2016. (Cited on page 7.)

[Liu 2017] Xiaolong Liu, Christopher R. Ryder, Spencer A. Wells and Mark C. Hersam. *Resolving the In-Plane Anisotropic Properties of Black Phosphorus.* Small Methods, vol. 1, no. 6, page 1700143, June 2017. (Cited on pages 7, 9 and 10.)

[Long 2016] Gen Long, Denis Maryenko, Junying Shen, Shuigang Xu, Jianqiang Hou, Zefei Wu, Wing Ki Wong, Tianyi Han, Jiangxiazi Lin, Yuan Cai, Rolf Lortz and Ning Wang. *Achieving Ultrahigh Carrier Mobility in Two-Dimensional Hole Gas of Black Phosphorus.* Nano Letters, vol. 16, no. 12, pages 7768–7773, December 2016. (Cited on pages 7, 9 and 13.)

[Lorchat 2016] Etienne Lorchat, Guillaume Froehlicher and Stéphane Berciaud. *Splitting of Interlayer Shear Modes and Photon Energy Dependent Anisotropic Raman Response in N-Layer ReSe$_2$ and ReS$_2$.* ACS Nano, vol. 10, no. 2, pages 2752–2760, 2016. PMID: 26820232. (Cited on page 63.)

[Loudon 2001] R. Loudon. *The Raman effect in crystals.* Advances in Physics, vol. 50, no. 7, pages 813–864, 2001. (Cited on page 32.)

[Lu 2014] Wanglin Lu, Haiyan Nan, Jinhua Hong, Yuming Chen, Chen Zhu, Zheng Liang, Xiangyang Ma, Zhenhua Ni, Chuanhong Jin and Ze Zhang. *Plasma-assisted fabrication of monolayer phosphorene and its Raman characterization.* Nano Research, vol. 7, no. 6, pages 853–859, June 2014. (Cited on pages 39, 42, 47, 48 and 49.)

[Luo 2013a] Xin Luo, Yanyuan Zhao, Jun Zhang, Minglin Toh, Christian Kloc, Qihua Xiong and Su Ying Quek. *Effects of lower symmetry and dimensionality on Raman spectra*

in two-dimensional WSe₂. Phys. Rev. B, vol. 88, page 195313, Nov 2013. (Cited on pages 41 and 42.)

[Luo 2013b] Xin Luo, Yanyuan Zhao, Jun Zhang, Qihua Xiong and Su Ying Quek. *Anomalous frequency trends in MoS₂ thin films attributed to surface effects*. Phys. Rev. B, vol. 88, page 075320, Aug 2013. (Cited on pages 56 and 57.)

[Luo 2014] Xi Luo, Yaghoob Rahbarihagh, James C. M. Hwang, Han Liu, Yuchen Du and Peide D. Ye. *Temporal and Thermal Stability of Al₂O₃-Passivated Phosphorene MOS-FETs*. IEEE Electron Device Letters, vol. 35, no. 12, pages 1314–1316, December 2014. (Cited on page 7.)

[Luo 2015a] Xin Luo, Xin Lu, Gavin Kok Wai Koon, Antonio H. Castro Neto, Barbaros Özyilmaz, Qihua Xiong and Su Ying Quek. *Large Frequency Change with Thickness in Interlayer Breathing Mode—Significant Interlayer Interactions in Few Layer Black Phosphorus*. Nano Letters, vol. 15, no. 6, pages 3931–3938, June 2015. (Cited on pages 8, 12, 40, 43 and 57.)

[Luo 2015b] Zhe Luo, Jesse Maassen, Yexin Deng, Yuchen Du, Richard P. Garrelts, Mark S Lundstrom, Peide D. Ye and Xianfan Xu. *Anisotropic in-plane thermal conductivity observed in few-layer black phosphorus*. Nature Communications, vol. 6, no. 1, December 2015. (Cited on pages 9 and 10.)

[Mak 2010] Kin Fai Mak, Changgu Lee, James Hone, Jie Shan and Tony F. Heinz. *Atomically Thin* MoS₂*: A New Direct-Gap Semiconductor*. Phys. Rev. Lett., vol. 105, page 136805, Sep 2010. (Cited on page 9.)

[Mak 2012] Kin Fai Mak, Keliang He, Jie Shan and Tony F. Heinz. *Control of valley polarization in monolayer MoS₂ by optical helicity*. Nature Nanotechnology, vol. 7, pages 494 EP –, Jun 2012. (Cited on page 2.)

[Makovicky 2011] E. Makovicky, M. Dusek, V. Petrícek and D. Topa. *The crystal structure of franckeite, $Pb_{21.7}Sn_{9.3}Fe_{4.0}Sb_{8.1}S_{56.9}$*. American Mineralogist, vol. 96, no. 11-12, pages 1686–1702, Nov 2011. (Cited on pages 22, 23 and 24.)

[Mauro 2018] Brotons-Gisbert Mauro, Martínez-Pastor Juan P., Ballesteros Guillem C., Gerardot Brian D. and Sánchez-Royo Juan F. Nanophotonics, volume 7, chapitre Engineering light emission of two-dimensional materials in both the weak and strong coupling regimes, page 253. 2019 2018. 1. (Cited on page 2.)

[McCreary 2017] Amber McCreary, Jeffrey R. Simpson, Yuanxi Wang, Daniel Rhodes, Kazunori Fujisawa, Luis Balicas, Madan Dubey, Vincent H. Crespi, Mauricio Terrones and Angela R. Hight Walker. *Intricate Resonant Raman Response in Anisotropic ReS₂*. Nano Letters, vol. 17, no. 10, pages 5897–5907, October 2017. (Cited on pages 63, 64, 66, 67, 69, 125 and 126.)

[Meckbach 2018] L Meckbach, U Huttner, L C Bannow, T Stroucken and S W Koch. *Interlayer excitons in transition-metal dichalcogenide heterostructures with type-II band alignment*. Journal of Physics: Condensed Matter, vol. 30, no. 37, page 374002, aug 2018. (Cited on page 21.)

[Meng] Xianghai Meng, Yongjian Zhou, Ke Chen, Richard H. Roberts, Wenzhi Wu, Jung-Fu Lin, Ray T. Chen, Xiaochuan Xu and Yaguo Wang. *Anisotropic Saturable and Excited-State Absorption in Bulk ReS2.* Advanced Optical Materials, vol. 6, no. 14, page 1800137. (Cited on page 70.)

[Meyer 2010] M. Meyer, P. G. Etchegoin and E. C. Le Ru. *Electronic structure, Raman tensors, and resonance phenomena in a simple molecular model.* American Journal of Physics, vol. 78, no. 3, pages 300–306, 2010. (Cited on page 32.)

[Mitioglu 2014] A. A. Mitioglu, P. Plochocka, G. Deligeorgis, S. Anghel, L. Kulyuk and D. K. Maude. *Second-order resonant Raman scattering in single-layer tungsten disulfide* WS_2. Phys. Rev. B, vol. 89, page 245442, Jun 2014. (Cited on page 32.)

[Moelo 1997] Yves Moelo, Alain Lafond, Catherine Deudon, Nathalie Coulon, Maryse Lancin and Alain Meerschaut. *Un nouveau chalcogénure composite á feuillets désaccordés dans le systeme Pb-Fe-Nb-S, (Pb_2FeS_3)0,58NbS_2.* Comptes Rendus de l'Académie des Sciences - Series IIB - Mechanics-Physics-Chemistry-Astronomy, vol. 325, no. 5, pages 287 – 296, 1997. (Cited on page 20.)

[Mohamed 2018] Nur Baizura Mohamed, Keisuke Shinokita, Xiaofan Wang, Hong En Lim, Dezhi Tan, Yuhei Miyauchi and Kazunari Matsuda. *Photoluminescence quantum yields for atomically thin-layered ReS_2: Identification of indirect-bandgap semiconductors.* Applied Physics Letters, vol. 113, no. 12, page 121112, 2018. (Cited on page 19.)

[Molina-Mendoza 2017] Aday J. Molina-Mendoza, Emerson Giovanelli, Wendel S. Paz, Miguel Angel Niño, Joshua O. Island, Charalambos Evangeli, Lucía Aballe, Michael Foerster, Herre S. J. van der Zant, Gabino Rubio-Bollinger, Nicolás Agraït, J. J. Palacios, Emilio M. Pérez and Andres Castellanos-Gomez. *Franckeite as a naturally occurring van der Waals heterostructure.* Nature Communications, vol. 8, page 14409, February 2017. (Cited on pages 20, 21, 22, 23, 94, 95, 100, 104, 118, 119 and 131.)

[Molina-Sánchez 2011] A. Molina-Sánchez and L. Wirtz. *Phonons in single-layer and few-layer MoS_2 and WS_2.* Physical Review B, vol. 84, no. 15, October 2011. (Cited on page 42.)

[Momida 2018] Hiroyoshi Momida, Gustav Bihlmayer, Stefan Blügel, Kouji Segawa, Yoichi Ando and Tamio Oguchi. *Topological interface states in the natural heterostructure ($PbSe$)$_5$(Bi_2Se_3)$_6$ with Bi_{Pb} defects.* Phys. Rev. B, vol. 97, page 035113, Jan 2018. (Cited on page 20.)

[Moody 2016] Galan Moody, John Schaibley and Xiaodong Xu. *Exciton dynamics in monolayer transition metal dichalcogenides.* JOSA B, vol. 33, no. 7, pages C39–C49, 2016. (Cited on pages 87 and 88.)

[Mueller 2018] Thomas Mueller and Ermin Malic. *Exciton physics and device application of two-dimensional transition metal dichalcogenide semiconductors.* npj 2D Materials and Applications, vol. 2, no. 1, page 29, 2018. (Cited on page 7.)

[Na 2014] Junhong Na, Young Tack Lee, Jung Ah Lim, Do Kyung Hwang, Gyu-Tae Kim, Won Kook Choi and Yong-Won Song. *Few-Layer Black Phosphorus Field-Effect Transistors with Reduced Current Fluctuation.* ACS Nano, vol. 8, no. 11, pages 11753–11762, November 2014. (Cited on pages 7 and 9.)

[Nagler 2016] Philipp Nagler, Gerd Plechinger, Christian Schüller and Tobias Korn. *Observation of anisotropic interlayer Raman modes in few-layer ReS$_2$.* physica status solidi (RRL) - Rapid Research Letters, vol. 10, no. 2, pages 185–189, February 2016. (Cited on page 63.)

[Nayak 2017] Pramoda K. Nayak, Yevhen Horbatenko, Seongjoon Ahn, Gwangwoo Kim, Jae-Ung Lee, Kyung Yeol Ma, A-Rang Jang, Hyunseob Lim, Dogyeong Kim, Sunmin Ryu, Hyeonsik Cheong, Noejung Park and Hyeon Suk Shin. *Probing Evolution of Twist-Angle-Dependent Interlayer Excitons in MoSe$_2$/WSe$_2$ van der Waals Heterostructures.* ACS Nano, vol. 11, no. 4, pages 4041–4050, 2017. PMID: 28363013. (Cited on page 20.)

[Nemilentsau 2016] Andrei Nemilentsau, Tony Low and George Hanson. *Anisotropic 2D Materials for Tunable Hyperbolic Plasmonics.* Physical Review Letters, vol. 116, no. 6, February 2016. (Cited on page 7.)

[Nguyen 2004] T. A. Nguyen, S. Mackowski, H. E. Jackson, L. M. Smith, J. Wrobel, K. Fronc, G. Karczewski, J. Kossut, M. Dobrowolska, J. K. Furdyna and W. Heiss. *Resonant spectroscopy of II-VI self-assembled quantum dots: Excited states and exciton–longitudinal optical phonon coupling.* Phys. Rev. B, vol. 70, page 125306, Sep 2004. (Cited on page 4.)

[Novoselov 2004] K. S. Novoselov, A. K. Geim, S. V. Morozov, D. Jiang, Y. Zhang, S. V. Dubonos, I. V. Grigorieva and A. A. Firsov. *Electric Field Effect in Atomically Thin Carbon Films.* Science, vol. 306, no. 5696, pages 666–669, 2004. (Cited on pages 1 and 115.)

[Novoselov 2005] K. S. Novoselov, D. Jiang, F. Schedin, T. J. Booth, V. V. Khotkevich, S. V. Morozov and A. K. Geim. *Two-dimensional atomic crystals.* Proceedings of the National Academy of Sciences of the United States of America, vol. 102, no. 30, pages 10451–10453, 2005. (Cited on pages 1, 2 and 115.)

[Novoselov 2016] K. S. Novoselov, A. Mishchenko, A. Carvalho and A. H. Castro Neto. *2D materials and van der Waals heterostructures.* Science, vol. 353, no. 6298, 2016. (Cited on pages 1, 19 and 117.)

[Ovchinnikov 2016] Dmitry Ovchinnikov, Fernando Gargiulo, Adrien Allain, Diego José Pasquier, Dumitru Dumcenco, Ching-Hwa Ho, Oleg V. Yazyev and Andras Kis. *Disorder engineering and conductivity dome in ReS$_2$ with electrolyte gating.* Nature Communications, vol. 7, page 12391, August 2016. (Cited on page 16.)

[Padilha 2014] J. E. Padilha, H. Peelaers, A. Janotti and C. G. Van de Walle. *Nature and evolution of the band-edge states in* MoS$_2$*: From monolayer to bulk.* Phys. Rev. B, vol. 90, page 205420, Nov 2014. (Cited on page 18.)

[Palummo 2015] Maurizia Palummo, Marco Bernardi and Jeffrey C. Grossman. *Exciton Radiative Lifetimes in Two-Dimensional Transition Metal Dichalcogenides.* Nano Letters, vol. 15, no. 5, pages 2794–2800, 2015. (Cited on page 7.)

[Pankove, J. I. 1971] Pankove, J. I. Optical processes in semiconductors. Englewood Cliffs, N.J. : Prentice-Hall, 1971. (Cited on pages 7 and 18.)

[Phaneuf-L'Heureux 2016] Anne-Laurence Phaneuf-L'Heureux, Alexandre Favron, Jean-Francis Germain, Patrick Lavoie, Patrick Desjardins, Richard Leonelli, Richard Martel and Sebastien Francoeur. *Polarization-Resolved Raman Study of Bulk-like and Davydov-Induced Vibrational Modes of Exfoliated Black Phosphorus.* Nano Letters, vol. 16, no. 12, pages 7761–7767, December 2016. (Cited on pages 39, 41, 42, 45, 49, 54, 55, 57 and 122.)

[Prada 2015] Elsa Prada, J. V. Alvarez, K. L. Narasimha-Acharya, F. J. Bailen and J. J. Palacios. *Effective-mass theory for the anisotropic exciton in two-dimensional crystals: Application to phosphorene.* Physical Review B, vol. 91, no. 24, June 2015. (Cited on pages 4 and 5.)

[Pradhan 2015] Nihar R. Pradhan, Amber McCreary, Daniel Rhodes, Zhengguang Lu, Simin Feng, Efstratios Manousakis, Dmitry Smirnov, Raju Namburu, Madan Dubey, Angela R. Hight Walker, Humberto Terrones, Mauricio Terrones, Vladimir Dobrosavljevic and Luis Balicas. *Metal to Insulator Quantum-Phase Transition in Few-Layered ReS₂.* Nano Letters, vol. 15, no. 12, pages 8377–8384, 2015. PMID: 26599563. (Cited on pages 62 and 63.)

[Prando 2017] Giacomo Prando. *The natural way.* Nature Nanotechnology, vol. 12, page 191, Mar 2017. (Cited on pages 20 and 22.)

[Pumera 2017] Martin Pumera and Zdeněk Sofer. *2D Monoelemental Arsenene, Antimonene, and Bismuthene: Beyond Black Phosphorus.* Advanced Materials, vol. 29, no. 21, page 1605299, June 2017. (Cited on page 2.)

[Qiao 2014] Jingsi Qiao, Xianghua Kong, Zhi-Xin Hu, Feng Yang and Wei Ji. *High-mobility transport anisotropy and linear dichroism in few-layer black phosphorus.* Nature Communications, vol. 5, no. 1, December 2014. (Cited on pages 7, 9, 10 and 12.)

[Qiao 2016] Xiao-Fen Qiao, Jiang-Bin Wu, Linwei Zhou, Jingsi Qiao, Wei Shi, Tao Chen, Xin Zhang, Jun Zhang, Wei Ji and Ping-Heng Tan. *Polytypism and unexpected strong interlayer coupling in two-dimensional layered ReS₂.* Nanoscale, vol. 8, no. 15, pages 8324–8332, 2016. (Cited on pages 14, 15, 16, 63, 65, 66, 67, 68, 69, 71, 125 and 126.)

[Qiu 2017a] Diana Y. Qiu, Felipe H. da Jornada and Steven G. Louie. *Environmental Screening Effects in 2D Materials: Renormalization of the Bandgap, Electronic Structure, and Optical Spectra of Few-Layer Black Phosphorus.* Nano Letters, vol. 17, no. 8, pages 4706–4712, August 2017. (Cited on page 14.)

[Qiu 2017b] M. Qiu, Z. T. Sun, D. K. Sang, X. G. Han, H. Zhang and C. M. Niu. *Current progress in black phosphorus materials and their applications in electrochemical energy storage.* Nanoscale, vol. 9, no. 36, pages 13384–13403, 2017. (Cited on page 7.)

[Quereda 2016] Jorge Quereda, Pablo San-Jose, Vincenzo Parente, Luis Vaquero-Garzon, Aday J. Molina-Mendoza, Nicolás Agraït, Gabino Rubio-Bollinger, Francisco Guinea, Rafael Roldlán and Andres Castellanos-Gomez. *Strong Modulation of Optical Properties in Black Phosphorus through Strain-Engineered Rippling.* Nano Letters, vol. 16, no. 5, pages 2931–2937, 2016. PMID: 27042865. (Cited on page 24.)

[Rahman 2017] Mohammad Rahman, Kenneth Davey and Shi-Zhang Qiao. *Advent of 2D Rhenium Disulfide (ReS$_2$): Fundamentals to Applications.* Advanced Functional Materials, vol. 27, no. 10, page 1606129, 2017. (Cited on pages 14 and 15.)

[Raja 2017] Archana Raja, Andrey Chaves, Jaeeun Yu, Ghidewon Arefe, Heather M. Hill, Albert F. Rigosi, Timothy C. Berkelbach, Philipp Nagler, Christian Schüller, Tobias Korn, Colin Nuckolls, James Hone, Louis E. Brus, Tony F. Heinz, David R. Reichman and Alexey Chernikov. *Coulomb engineering of the bandgap and excitons in two-dimensional materials.* Nature Communications, vol. 8, page 15251, May 2017. (Cited on pages 4, 5, 6 and 116.)

[Ray 2017] Kyle Ray, Alexander E. Yore, Tong Mou, Sauraj Jha, Kirby K. H. Smithe, Bin Wang, Eric Pop and A. K. M. Newaz. *Photoresponse of Natural van der Waals Heterostructures.* ACS Nano, vol. 11, no. 6, pages 6024–6030, 2017. PMID: 28485958. (Cited on pages 21, 22, 23, 95, 100, 104 and 131.)

[Ribeiro 2015] Henrique B. Ribeiro, Marcos A. Pimenta, Christiano J. S. de Matos, Roberto Luiz Moreira, Aleksandr S. Rodin, Juan D. Zapata, Eunézio A. T. de Souza and Antonio H. Castro Neto. *Unusual Angular Dependence of the Raman Response in Black Phosphorus.* ACS Nano, vol. 9, no. 4, pages 4270–4276, April 2015. (Cited on page 105.)

[Ribeiro 2018] Henrique B. Ribeiro, Marcos A. Pimenta and Christiano J.S. de Matos. *Raman spectroscopy in black phosphorus.* Journal of Raman Spectroscopy, vol. 49, no. 1, pages 76–90, January 2018. (Cited on pages 40, 41, 42, 43, 45, 49, 54 and 122.)

[Robert 2016] C. Robert, D. Lagarde, F. Cadiz, G. Wang, B. Lassagne, T. Amand, A. Balocchi, P. Renucci, S. Tongay, B. Urbaszek and X. Marie. *Exciton radiative lifetime in transition metal dichalcogenide monolayers.* Physical Review B, vol. 93, no. 20, May 2016. (Cited on pages 87 and 88.)

[Rol 2007] F. Rol, S. Founta, H. Mariette, B. Daudin, Le Si Dang, J. Bleuse, D. Peyrade, J.-M. Gérard and B. Gayral. *Probing exciton localization in nonpolar GaN/AlN quantum dots by single-dot optical spectroscopy.* Phys. Rev. B, vol. 75, page 125306, Mar 2007. (Cited on page 4.)

[Roldán 2015] Rafael Roldán, Andrés Castellanos-Gomez, Emmanuele Cappelluti and Francisco Guinea. *Strain engineering in semiconducting two-dimensional crystals.* Journal of Physics: Condensed Matter, vol. 27, no. 31, page 313201, August 2015. (Cited on page 2.)

[Rytova 1967] N S. Rytova. *The screened potential of a point charge in a thin film.* Moscow University Physics Bulletin, vol. 3, no. 3, page 18, 1967. (Cited on page 4.)

[Schaibley 2016] John R. Schaibley, Hongyi Yu, Genevieve Clark, Pasqual Rivera, Jason S. Ross, Kyle L. Seyler, Wang Yao and Xiaodong Xu. *Valleytronics in 2D materials.* Nature Reviews Materials, vol. 1, pages 16055 EP –, Aug 2016. Review Article. (Cited on page 2.)

[Scott 1969] J. F. Scott, R. C. C. Leite and T. C. Damen. *Resonant Raman Effect in Semi-conductors.* Phys. Rev., vol. 188, pages 1285–1290, Dec 1969. (Cited on page 30.)

[Sereni 2010] Paolo Sereni, Maurizio Musso, Peter Knoll, Peter Blaha, Karlheinz Schwarz and Günther Schmidt. *Polarization-Dependent Raman Characterization of Stibnite (Sb_2S_3).* AIP Conference Proceedings, vol. 1267, no. 1, pages 1131–1132, 2010. (Cited on page 96.)

[Shen 2018] Wanfu Shen, Chunguang Hu, Jin Tao, Jun Liu, Shuangqing Fan, Yaxu Wei, Chunhua An, Jiancui Chen, Sen Wu, Yanning Li, Jing Liu, Daihua Zhang, Lidong Sun and Xiaotang Hu. *Resolving the optical anisotropy of low-symmetry 2D materials.* Nanoscale, 2018. (Cited on page 7.)

[Shim 2016] Jaewoo Shim, Aely Oh, Dong-Ho Kang, Seyong Oh, Sung Kyu Jang, Jaeho Jeon, Min Hwan Jeon, Minwoo Kim, Changhwan Choi, Jaehyeong Lee, Sungjoo Lee, Geun Young Yeom, Young Jae Song and Jin-Hong Park. *High-Performance 2D Rhenium Disulfide (ReS_2) Transistors and Photodetectors by Oxygen Plasma Treatment.* Advanced Materials, vol. 28, no. 32, pages 6985–6992, 2016. (Cited on page 15.)

[Shulenburger 2015] L. Shulenburger, A.D. Baczewski, Z. Zhu, J. Guan and D. Tománek. *The Nature of the Interlayer Interaction in Bulk and Few-Layer Phosphorus.* Nano Letters, vol. 15, no. 12, pages 8170–8175, December 2015. (Cited on pages 9, 11 and 12.)

[Silva-Guillén 2017] J. A. Silva-Guillén, E. Canadell, P. Ordejón, F. Guinea and R. Roldán. *Anisotropic features in the electronic structure of the two-dimensional transition metal trichalcogenide TiS_3: electron doping and plasmons.* 2D Materials, vol. 4, no. 2, page 025085, 2017. (Cited on page 2.)

[Sim 2016] Sangwan Sim, Doeon Lee, Minji Noh, Soonyoung Cha, Chan Ho Soh, Ji Ho Sung, Moon-Ho Jo and Hyunyong Choi. *Selectively tunable optical Stark effect of anisotropic excitons in atomically thin ReS_2.* Nature Communications, vol. 7, page 13569, November 2016. (Cited on page 70.)

[Sim 2018] Sangwan Sim, Doeon Lee, Artur V. Trifonov, Taeyoung Kim, Soonyoung Cha, Ji Ho Sung, Sungjun Cho, Wooyoung Shim, Moon-Ho Jo and Hyunyong Choi. *Ultrafast quantum beats of anisotropic excitons in atomically thin ReS_2.* Nature Communications, vol. 9, no. 1, December 2018. (Cited on pages 15, 16 and 17.)

[Son 2017] Youngwoo Son, Daichi Kozawa, Albert Tianxiang Liu, Volodymyr B Koman, Qing Hua Wang and Michael S Strano. *A study of bilayer phosphorene stability under MoS_2 -passivation.* 2D Materials, vol. 4, no. 2, page 025091, May 2017. (Cited on page 13.)

[Song 2016a] Q. J. Song, Q. H. Tan, X. Zhang, J. B. Wu, B. W. Sheng, Y. Wan, X. Q. Wang, L. Dai and P. H. Tan. *Physical origin of Davydov splitting and resonant Raman spectroscopy of Davydov components in multilayer MoTe 2.* Physical Review B, vol. 93, no. 11, page 115409, 2016. (Cited on page 54.)

[Song 2016b] Qingjun Song, Xingchen Pan, Haifeng Wang, Kun Zhang, Qinghai Tan, Pan Li, Yi Wan, Yilun Wang, Xiaolong Xu, Miaoling Lin, Xiangang Wan, Fengqi Song and Lun Dai. *The In-Plane Anisotropy of WTe2 Investigated by Angle-Dependent and Polarized*

Raman Spectroscopy. Scientific Reports, vol. 6, pages 29254 EP –, Jul 2016. Article. (Cited on page 34.)

[Song 2017] Qingjun Song, Haifeng Wang, Xingchen Pan, Xiaolong Xu, Yilun Wang, Yanping Li, Fengqi Song, Xiangang Wan, Yu Ye and Lun Dai. *Anomalous in-plane anisotropic Raman response of monoclinic semimetal 1 T'-MoTe$_2$.* Scientific Reports, vol. 7, no. 1, page 1758, 2017. (Cited on pages 32 and 104.)

[Spiece 2018] Jean Spiece. *Quantitative mapping of nanothermal transport via Scanning Thermal Microscopy.* PhD thesis, Lancaster University, 2018. (Cited on page 21.)

[Spizzirri 2010] P. G. Spizzirri, J.-H. Fang, S. Rubanov, E. Gauja and S. Prawer. *Nano-Raman spectroscopy of silicon surfaces.* arXiv preprint arXiv:1002.2692, 2010. (Cited on page 99.)

[Staiger 2015] Matthias Staiger, Roland Gillen, Nils Scheuschner, Oliver Ochedowski, Felix Kampmann, Marika Schleberger, Christian Thomsen and Janina Maultzsch. *Splitting of monolayer out-of-plane A_1' Raman mode in few-layer WS$_2$.* Physical Review B, vol. 91, no. 19, May 2015. (Cited on page 54.)

[Steinberg] David Steinberg, Alexandre S. M. V. Oré, Juan D. Zapata, E. A. Thoroh de Souza and Christiano J. S. de Matos. In Latin America Optics and Photonics Conference. (Cited on page 95.)

[Steinberg 2018] David Steinberg, Alexandre S. M. V. Oré, Juan D. Zapata, E. A. Thoroh de Souza and Christiano J. S. de Matos. *Third harmonic generation in mechanically exfoliated franckeite.* In Latin America Optics and Photonics Conference, page Th3E.3. Optical Society of America, 2018. (Cited on page 22.)

[Stelzner 1893] A. W. Stelzner. *Über Franckeit, ein neues Erz aus Bolivia.* Neues Jahrbuch für Mineralogie, vol. 2, no. 37, page 114, 1893. (Cited on page 20.)

[Sugai 1985] S. Sugai and I. Shirotani. *Raman and infrared reflection spectroscopy in black phosphorus.* Solid state communications, vol. 53, no. 9, pages 753–755, 1985. (Cited on pages 49 and 122.)

[Sun 2013] Qi C. Sun, Dipanjan Mazumdar, Lena Yadgarov, Rita Rosentsveig, Reshef Tenne and Janice L. Musfeldt. *Spectroscopic Determination of Phonon Lifetimes in Rhenium-Doped MoS$_2$ Nanoparticles.* Nano Letters, vol. 13, no. 6, pages 2803–2808, June 2013. (Cited on page 57.)

[Sun 2016] Yajing Sun, Dong Wang and Zhigang Shuai. *Indirect-to-Direct Band Gap Crossover in Few-Layer Transition Metal Dichalcogenides: A Theoretical Prediction.* The Journal of Physical Chemistry C, vol. 120, no. 38, pages 21866–21870, September 2016. (Cited on page 9.)

[Sun 2017] Jie Sun, Na Lin, Cheng Tang, Hao Ren and Xian Zhao. *A first principles study of the interaction between two-dimensional black phosphorus and Al$_2$O$_3$ dielectric.* RSC Advances, vol. 7, no. 23, pages 13777–13783, 2017. (Cited on page 14.)

[Surrente 2016] A. Surrente, A. A. Mitioglu, K. Galkowski, L. Klopotowski, W. Tabis, B. Vign-
          olle, D. K. Maude and P. Plochocka. *Onset of exciton-exciton annihilation in single-layer
          black phosphorus.* Physical Review B, vol. 94, no. 7, August 2016. (Cited on page 58.)

[Tan 2012] P. H. Tan, W. P. Han, W. J. Zhao, Z. H. Wu, K. Chang, H. Wang, Y. F. Wang,
          N. Bonini, N. Marzari, N. Pugno, G. Savini, A. Lombardo and A. C. Ferrari. *The shear
          mode of multilayer graphene.* Nature Materials, vol. 11, pages 294 EP –, Feb 2012.
          (Cited on page 43.)

[Tan 2017a] Chaoliang Tan, Xiehong Cao, Xue-Jun Wu, Qiyuan He, Jian Yang, Xiao Zhang,
          Junze Chen, Wei Zhao, Shikui Han, Gwang-Hyeon Nam, Melinda Sindoro and Hua
          Zhang. *Recent Advances in Ultrathin Two-Dimensional Nanomaterials.* Chemical Re-
          views, vol. 117, no. 9, pages 6225–6331, May 2017. (Cited on page 1.)

[Tan 2017b] Dezhi Tan, Hong En Lim, Feijiu Wang, Nur Baizura Mohamed, Shinichiro Mouri,
          Wenjin Zhang, Yuhei Miyauchi, Mari Ohfuchi and Kazunari Matsuda. *Anisotropic
          optical and electronic properties of two-dimensional layered germanium sulfide.* Nano
          Research, vol. 10, no. 2, pages 546–555, February 2017. (Cited on page 7.)

[Tan 2018] Sherman Jun Rong Tan, Ibrahim Abdelwahab, Leiqiang Chu, Sock Mui Poh, Yan-
          peng Liu, Jiong Lu, Wei Chen and Kian Ping Loh. *Quasi-Monolayer Black Phosphorus
          with High Mobility and Air Stability.* Advanced Materials, vol. 30, no. 6, page 1704619,
          2018. (Cited on page 9.)

[Terrones 2014] H. Terrones, E. Del Corro, S. Feng, J. M. Poumirol, D. Rhodes, D. Smirnov,
          N. R. Pradhan, Z. Lin, M. A. T. Nguyen, A. L. Elías, T. E. Mallouk, L. Balicas,
          M. A. Pimenta and M. Terrones. *New First Order Raman-active Modes in Few Layered
          Transition Metal Dichalcogenides.* Scientific Reports, vol. 4, pages 4215 EP –, Feb 2014.
          Article. (Cited on page 56.)

[Thygesen 2017] Kristian Sommer Thygesen. *Calculating excitons, plasmons, and quasi-
          particles in 2D materials and van der Waals heterostructures.* 2D Materials, vol. 4,
          no. 2, page 022004, June 2017. (Cited on pages 2, 4 and 7.)

[Tian 2016] He Tian, Jesse Tice, Ruixiang Fei, Vy Tran, Xiaodong Yan, Li Yang and Han Wang.
          Low-symmetry two-dimensional materials for electronic and photonic applications. Nano
          Today, vol. 11, no. 6, pages 763–777, December 2016. (Cited on pages 7, 14, 116 and 117.)

[Tiong 1999] K. K. Tiong, C. H. Ho and Y. S. Huang. *The electrical transport properties of
          ReS_2 and $ReSe_2$ layered crystals.* Solid state communications, vol. 111, no. 11, pages
          635–640, 1999. (Cited on page 7.)

[Tongay 2014] Sefaattin Tongay, Hasan Sahin, Changhyun Ko, Alex Luce, Wen Fan, Kai Liu,
          Jian Zhou, Ying-Sheng Huang, Ching-Hwa Ho, Jinyuan Yan, D. Frank Ogletree, Shaul
          Aloni, Jie Ji, Shushen Li, Jingbo Li, F. M. Peeters and Junqiao Wu. *Monolayer behaviour
          in bulk ReS_2 due to electronic and vibrational decoupling.* Nature Communications,
          vol. 5, no. 1, December 2014. (Cited on pages 18, 63, 77, 80 and 127.)

[Tonndorf 2013] Philipp Tonndorf, Robert Schmidt, Philipp Böttger, Xiao Zhang, Janna Börner, Andreas Liebig, Manfred Albrecht, Christian Kloc, Ovidiu Gordan and Dietrich RT Zahn. *Photoluminescence emission and Raman response of monolayer MoS$_2$, MoSe$_2$, and WSe$_2$*. Optics express, vol. 21, no. 4, pages 4908–4916, 2013. (Cited on pages 42 and 54.)

[Tran 2015] Vy Tran, Ruixiang Fei and Li Yang. *Quasiparticle energies, excitons, and optical spectra of few-layer black phosphorus*. 2D Materials, vol. 2, no. 4, page 044014, November 2015. (Cited on page 10.)

[Urban 2017] J. M. Urban, M. Baranowski, A. Surrente, D. Wlodarczyk, A. Suchocki, G. Long, Y. Wang, L. Klopotowski, N. Wang, D. K. Maude and P. Plochocka. *Observation of A_g^1 Raman mode splitting in few layer black phosphorus encapsulated with hexagonal boron nitride*. Nanoscale, vol. 9, no. 48, pages 19298–19303, 2017. (Cited on pages 39 and 84.)

[Urban 2019] J M Urban, M Baranowski, A Kuc, Ł. Kłopotowski, A Surrente, Y Ma, D Włodarczyk, A Suchocki, D Ovchinnikov, T Heine, D K Maude, A Kis and P Płochocka. *Non equilibrium anisotropic excitons in atomically thin ReS$_2$*. 2D Materials, vol. 6, no. 1, page 015012, 2019. (Cited on pages 18, 61, 62 and 125.)

[Utt 2015] Kainen L. Utt, Pablo Rivero, Mehrshad Mehboudi, Edmund O. Harriss, Mario F. Borunda, Alejandro A. Pacheco SanJuan and Salvador Barraza-Lopez. *Intrinsic Defects, Fluctuations of the Local Shape, and the Photo-Oxidation of Black Phosphorus*. ACS Central Science, vol. 1, no. 6, pages 320–327, September 2015. (Cited on page 12.)

[Utyuzh 2010] A. N. Utyuzh, Yu. A. Timofeev and G. N. Stepanov. *Effect of pressure on Raman spectra of SnS$_2$ single crystals*. Physics of the Solid State, vol. 52, no. 2, pages 352–356, Feb 2010. (Cited on page 96.)

[Velický 2017a] Matěj Velický and Peter S. Toth. *From two-dimensional materials to their heterostructures: An electrochemist's perspective*. Applied Materials Today, vol. 8, pages 68–103, September 2017. (Cited on pages 2, 21 and 22.)

[Velický 2017b] Matej Velický, Peter S. Toth, Alexander M. Rakowski, Aidan P. Rooney, Aleksey Kozikov, Colin R. Woods, Artem Mishchenko, Laura Fumagalli, Jun Yin, Viktor Zólyomi, Thanasis Georgiou, Sarah J. Haigh, Kostya S. Novoselov and Robert A. W. Dryfe. *Exfoliation of natural van der Waals heterostructures to a single unit cell thickness*. Nature Communications, vol. 8, pages 14410 EP –, Feb 2017. Article. (Cited on pages 94, 95, 97, 99 and 108.)

[Velický 2017c] Matěj Velický, Peter S. Toth, Alexander M. Rakowski, Aidan P. Rooney, Aleksey Kozikov, Colin R. Woods, Artem Mishchenko, Laura Fumagalli, Jun Yin, Viktor Zólyomi, Thanasis Georgiou, Sarah J. Haigh, Kostya S. Novoselov and Robert A. W. Dryfe. *Exfoliation of natural van der Waals heterostructures to a single unit cell thickness*. Nature Communications, vol. 8, page 14410, February 2017. (Cited on page 115.)

[Venuthurumilli 2018] Prabhu K. Venuthurumilli, Peide D. Ye and Xianfan Xu. *Plasmonic Resonance Enhanced Polarization-Sensitive Photodetection by Black Phosphorus in Near Infrared*. ACS Nano, vol. 12, no. 5, pages 4861–4867, May 2018. (Cited on page 7.)

[Wang 1991] S. Wang and K. H. Kuo. *Crystal lattices and crystal chemistry of cylindrite and franckeite.* Acta Crystallographica Section A, vol. 47, no. 4, pages 381–392, 1991. (Cited on pages 23 and 24.)

[Wang 1995] Wang Wang, P R Buseck and Jingyue Liu. *High-angle annular dark-field microscopy of franckeite.* American Mineralogist, vol. 80, no. 11-12, pages 1174–1178, 1995. (Cited on pages 20, 22 and 118.)

[Wang 2014] Hong Wang, Fucai Liu, Wei Fu, Zheyu Fang, Wu Zhou and Zheng Liu. *Two-dimensional heterostructures: fabrication, characterization, and application.* Nanoscale, vol. 6, pages 12250–12272, 2014. (Cited on pages 19 and 117.)

[Wang 2015a] Gaoxue Wang, Ravindra Pandey and Shashi P. Karna. *Atomically Thin Group V Elemental Films: Theoretical Investigations of Antimonene Allotropes.* ACS Applied Materials & Interfaces, vol. 7, no. 21, pages 11490–11496, June 2015. (Cited on pages 7 and 116.)

[Wang 2015b] Xiaomu Wang, Aaron M. Jones, Kyle L. Seyler, Vy Tran, Yichen Jia, Huan Zhao, Han Wang, Li Yang, Xiaodong Xu and Fengnian Xia. *Highly anisotropic and robust excitons in monolayer black phosphorus.* Nature Nanotechnology, vol. 10, no. 6, pages 517–521, June 2015. (Cited on pages 10 and 11.)

[Wang 2018] Xingzhi Wang, Nannan Mao, Weijun Luo, Hikari Kitadai and Xi Ling. *Anomalous Phonon Modes in Black Phosphorus Revealed by Resonant Raman Scattering.* The Journal of Physical Chemistry Letters, vol. 9, no. 11, pages 2830–2837, 2018. (Cited on page 104.)

[Webb 2017] James L. Webb, Lewis S. Hart, Daniel Wolverson, Chaoyu Chen, Jose Avila and Maria C. Asensio. *Electronic band structure of ReS$_2$ by high-resolution angle-resolved photoemission spectroscopy.* Physical Review B, vol. 96, no. 11, September 2017. (Cited on page 18.)

[Wen 2017] Wen Wen, Yiming Zhu, Xuelu Liu, Hung-Pin Hsu, Zhen Fei, Yanfeng Chen, Xinsheng Wang, Mei Zhang, Kuan-Hung Lin, Fei-Sheng Huang, Yi-Ping Wang, Ying-Sheng Huang, Ching-Hwa Ho, Ping-Heng Tan, Chuanhong Jin and Liming Xie. *Anisotropic Spectroscopy and Electrical Properties of 2D ReS$_{2(1-x)}$Se$_{2x}$ Alloys with Distorted 1T Structure.* Small, vol. 13, no. 12, page 1603788, March 2017. (Cited on page 16.)

[White 1998] William B. White and Steven I. Boldish. *Optical band gaps of selected ternary sulfide minerals.* American Mineralogist, vol. 83, no. 7-8, pages 865–871, 08 1998. (Cited on pages 21, 96 and 97.)

[Wieting 1972] T. J. Wieting and J. L. Verble. *Interlayer Bonding and the Lattice Vibrations of β-GaSe.* Physical Review B, vol. 5, page 1473, 1972. (Cited on page 42.)

[Williams 1988] T. B. Williams and B. G. Hyde. *Electron microscopy of cylindrite and franckeite.* Physics and Chemistry of Minerals, vol. 15, no. 6, pages 521–544, Aug 1988. (Cited on pages 20 and 22.)

[Wood 2014] Joshua D. Wood, Spencer A. Wells, Deep Jariwala, Kan-Sheng Chen, EunKyung Cho, Vinod K. Sangwan, Xiaolong Liu, Lincoln J. Lauhon, Tobin J. Marks and Mark C. Hersam. *Effective Passivation of Exfoliated Black Phosphorus Transistors against Ambient Degradation.* Nano Letters, vol. 14, no. 12, pages 6964–6970, December 2014. (Cited on page 12.)

[Wu 2015] Juanxia Wu, Nannan Mao, Liming Xie, Hua Xu and Jin Zhang. *Identifying the Crystalline Orientation of Black Phosphorus Using Angle-Resolved Polarized Raman Spectroscopy.* Angewandte Chemie International Edition, vol. 54, no. 8, pages 2366–2369, 2015. (Cited on page 32.)

[Wu 2019] Juanxia Wu, Shishu Zhang, Lianming Tong and Jin Zhang. Raman spectroscopy of anisotropic two-dimensional materials, pages 53–80. Springer Singapore, Singapore, 2019. (Cited on pages 30, 32, 33, 34 and 62.)

[Wurstbauer 2017] Ursula Wurstbauer, Bastian Miller, Eric Parzinger and Alexander W Holleitner. *Light–matter interaction in transition metal dichalcogenides and their heterostructures.* Journal of Physics D: Applied Physics, vol. 50, no. 17, page 173001, mar 2017. (Cited on page 2.)

[Xia 2014] Fengnian Xia, Han Wang and Yichen Jia. *Rediscovering black phosphorus as an anisotropic layered material for optoelectronics and electronics.* Nature Communications, vol. 5, no. 1, December 2014. (Cited on pages 7 and 9.)

[Xiao 2017] Jun Xiao, Mervin Zhao, Yuan Wang and Xiang Zhang. *Excitons in atomically thin 2D semiconductors and their applications.* Nanophotonics, vol. 6, no. 6, January 2017. (Cited on page 4.)

[Xie 2015] L. M. Xie. *Two-dimensional transition metal dichalcogenide alloys: preparation, characterization and applications.* Nanoscale, vol. 7, no. 44, pages 18392–18401, 2015. (Cited on page 2.)

[Xiong] Yan Xiong, HuaWei Chen, David Wei Zhang and Peng Zhou. *Electronic and Optoelectronic Applications Based on ReS$_2$.* physica status solidi (RRL) Rapid Research Letters, vol. 0, no. 0, page 1800658. (Cited on page 15.)

[Yang 2017] He Yang, Henri Jussila, Anton Autere, Hannu-Pekka Komsa, Guojun Ye, Xianhui Chen, Tawfique Hasan and Zhipei Sun. *Optical Waveplates Based on Birefringence of Anisotropic Two-Dimensional Layered Materials.* ACS Photonics, vol. 4, no. 12, pages 3023–3030, 2017. (Cited on page 7.)

[Yang 2018] Yusi Yang, Shun-Chang Liu, Yang Wang, Mingsheng Long, Chen-Min Dai, Shiyou Chen, Bo Zhang, Zhe Sun, Zhaoyang Sun, Chunguang Hu, Shishu Zhang, Lianming Tong, Gengmin Zhang, Ding-Jiang Xue and Jin-Song Hu. *In-Plane Optical Anisotropy of Low-Symmetry 2D GeSe.* Advanced Optical Materials, page 1801311, December 2018. (Cited on pages 7 and 116.)

[Yao 2018] Wei Yao, Eryin Wang, Changhua Bao, Yiou Zhang, Kenan Zhang, Kejie Bao, Chun Kai Chan, Chaoyu Chen, Jose Avila, Maria C. Asensio, Junyi Zhu and Shuyun

Zhou. *Quasicrystalline 3° twisted bilayer graphene as an incommensurate superlattice with strong interlayer coupling.* Proceedings of the National Academy of Sciences, vol. 115, no. 27, pages 6928–6933, 2018. (Cited on pages 19 and 20.)

[Yoon 2009] Duhee Yoon, Hyerim Moon, Young-Woo Son, Jin Sik Choi, Bae Ho Park, Young Hun Cha, Young Dong Kim and Hyeonsik Cheong. *Interference effect on Raman spectrum of graphene on SiO_2/Si.* Phys. Rev. B, vol. 80, page 125422, Sep 2009. (Cited on pages 106 and 107.)

[Yu 2016] Sheng Yu, Hao Zhu, Kwesi Eshun, Chen Shi, Min Zeng and Qiliang Li. *Strain-engineering the anisotropic electrical conductance in ReS_2 monolayer.* Applied Physics Letters, vol. 108, no. 19, page 191901, 2016. (Cited on page 15.)

[Yuan 2015] Hongtao Yuan, Xiaoge Liu, Farzaneh Afshinmanesh, Wei Li, Gang Xu, Jie Sun, Biao Lian, Alberto G. Curto, Guojun Ye, Yasuyuki Hikita, Zhixun Shen, Shou-Cheng Zhang, Xianhui Chen, Mark Brongersma, Harold Y. Hwang and Yi Cui. *Polarization-sensitive broadband photodetector using a black phosphorus vertical p–n junction.* Nature Nanotechnology, vol. 10, no. 8, pages 707–713, August 2015. (Cited on page 7.)

[Zaslow 1967] B. Zaslow and Melvin E. Zandler. *Two-Dimensional Analog to the Hydrogen Atom.* American Journal of Physics, vol. 35, no. 12, pages 1118–1119, 1967. (Cited on page 4.)

[Zelewski 2017] Szymon J. Zelewski and Robert Kudrawiec. *Photoacoustic and modulated reflectance studies of indirect and direct band gap in van der Waals crystals.* Scientific Reports, vol. 7, no. 1, December 2017. (Cited on pages 18, 19 and 84.)

[Zeng 2012] Hualing Zeng, Junfeng Dai, Wang Yao, Di Xiao and Xiaodong Cui. *Valley polarization in MoS_2 monolayers by optical pumping.* Nature Nanotechnology, vol. 7, pages 490 EP –, Jun 2012. (Cited on page 2.)

[Zhang 2013] Yi Zhang, Tay-Rong Chang, Bo Zhou, Yong-Tao Cui, Hao Yan, Zhongkai Liu, Felix Schmitt, James Lee, Rob Moore, Yulin Chen, Hsin Lin, Horng-Tay Jeng, Sung-Kwan Mo, Zahid Hussain, Arun Bansil and Zhi-Xun Shen. *Direct observation of the transition from indirect to direct bandgap in atomically thin epitaxial $MoSe_2$.* Nature Nanotechnology, vol. 9, pages 111 EP –, Dec 2013. (Cited on page 9.)

[Zhang 2014] Shuang Zhang, Jiong Yang, Renjing Xu, Fan Wang, Weifeng Li, Muhammad Ghufran, Yong-Wei Zhang, Zongfu Yu, Gang Zhang, Qinghua Qin and Yuerui Lu. *Extraordinary Photoluminescence and Strong Temperature/Angle-Dependent Raman Responses in Few-Layer Phosphorene.* ACS Nano, vol. 8, no. 9, pages 9590–9596, September 2014. (Cited on page 58.)

[Zhang 2015] Enze Zhang, Yibo Jin, Xiang Yuan, Weiyi Wang, Cheng Zhang, Lei Tang, Shanshan Liu, Peng Zhou, Weida Hu and Faxian Xiu. *ReS2-Based Field-Effect Transistors and Photodetectors.* Advanced Functional Materials, vol. 25, no. 26, pages 4076–4082, 2015. (Cited on page 15.)

[Zhang 2016] Jia Lin Zhang, Songtao Zhao, Cheng Han, Zhunzhun Wang, Shu Zhong, Shuo Sun, Rui Guo, Xiong Zhou, Cheng Ding Gu, Kai Di Yuan, Zhenyu Li and Wei Chen.

Epitaxial Growth of Single Layer Blue Phosphorus: A New Phase of Two-Dimensional Phosphorus. Nano Letters, vol. 16, no. 8, pages 4903–4908, August 2016. (Cited on page 7.)

[Zhang 2017a] Kailiang Zhang, Yulin Feng, Fang Wang, Zhengchun Yang and John Wang. *Two dimensional hexagonal boron nitride (2D-hBN): synthesis, properties and applications*. Journal of Materials Chemistry C, vol. 5, no. 46, pages 11992–12022, 2017. (Cited on page 13.)

[Zhang 2017b] Shishu Zhang, Nannan Mao, Na Zhang, Juanxia Wu, Lianming Tong and Jin Zhang. *Anomalous Polarized Raman Scattering and Large Circular Intensity Differential in Layered Triclinic ReS$_2$*. ACS Nano, vol. 11, no. 10, pages 10366–10372, 2017. (Cited on pages 104, 105 and 106.)

[Zhang 2017c] Yu Zhang, Yun Zheng, Kun Rui, Huey Hoon Hng, Kedar Hippalgaonkar, Jianwei Xu, Wenping Sun, Jixin Zhu, Qingyu Yan and Wei Huang. *2D black phosphorus for energy storage and thermoelectric applications*. Small, vol. 13, no. 28, page 1700661, 2017. (Cited on page 7.)

[Zhang 2018] Nan Zhang, Alessandro Surrente, Michał, Baranowski, Duncan K. Maude, Patricia Gant, Andres Castellanos-Gomez and Paulina Plochocka. *Moiré Intralayer Excitons in a MoSe$_2$/MoS$_2$ Heterostructure*. Nano Letters, vol. 18, no. 12, pages 7651–7657, 2018. PMID: 30403876. (Cited on page 19.)

[Zhao 2013] Weijie Zhao, R. M. Ribeiro, Minglin Toh, Alexandra Carvalho, Christian Kloc, A. H. Castro Neto and Goki Eda. *Origin of Indirect Optical Transitions in Few-Layer MoS$_2$, WS$_2$, and WSe$_2$*. Nano Letters, vol. 13, no. 11, pages 5627–5634, 2013. PMID: 24168432. (Cited on page 18.)

[Zhao 2015] Huan Zhao, Jiangbin Wu, Hongxia Zhong, Qiushi Guo, Xiaomu Wang, Fengnian Xia, Li Yang, Pingheng Tan and Han Wang. *Interlayer interactions in anisotropic atomically thin rhenium diselenide*. Nano Research, vol. 8, no. 11, pages 3651–3661, Nov 2015. (Cited on page 80.)

[Zhong 2015] Hong-Xia Zhong, Shiyuan Gao, Jun-Jie Shi and Li Yang. *Quasiparticle band gaps, excitonic effects, and anisotropic optical properties of the monolayer distorted 1 T diamond-chain structures ReS$_2$ and ReSe$_2$*. Physical Review B, vol. 92, no. 11, September 2015. (Cited on page 18.)

[Zhou 2018] Wei Zhou, Jingzhe Chen, Heng Gao, Tao Hu, Shuangchen Ruan, Alessandro Stroppa and Wei Ren. *Anomalous and Polarization-Sensitive Photoresponse of T$_d$-WTe$_2$ from Visible to Infrared Light*. Advanced Materials, page 1804629, December 2018. (Cited on pages 7 and 116.)

[Zhu] Yue Zhu, Lele Peng, Zhiwei Fang, Chunshuang Yan, Xiao Zhang and Guihua Yu. *Structural Engineering of 2D Nanomaterials for Energy Storage and Catalysis*. Advanced Materials, vol. 30, no. 15, page 1706347. (Cited on page 2.)

[Ziletti 2015] A. Ziletti, A. Carvalho, D. K. Campbell, D. F. Coker and A. H. Castro Neto. *Oxygen Defects in Phosphorene*. Physical Review Letters, vol. 114, no. 4, January 2015. (Cited on page 12.)